



Technische Universität München

Lehrstuhl für Anorganische Chemie mit Schwerpunkt Neue Materialien

Investigation on solubility and reactivity of empty and endohedral *Zintl*
clusters in liquid ammonia

Benedikt Justus Lutz Witzel

Vollständiger Abdruck der von der Fakultät für Chemie der Technischen Universität München zur
Erlangung des akademischen Grades eines

Doktors der Naturwissenschaften (Dr. rer. nat.)

genehmigten Dissertation.

Vorsitzender: apl. Prof. Dr. Wolfgang Eisenreich

Prüfer der Dissertation:

1. Prof. Dr. Thomas F. Fässler
2. Prof. Dr. Tom Nilges

Die Dissertation wurde am 16.01.2020 bei der Technischen Universität München
eingereicht und durch die Fakultät für Chemie am 05.02.2020 angenommen.

Der experimentelle Teil dieser Arbeit wurde in der Zeit von Dezember 2015 bis Dezember 2019 am Lehrstuhl für Anorganische Chemie mit Schwerpunkt Neue Materialien der Technischen Universität München unter wissenschaftlicher Leitung von Herrn Univ.-Prof. Dr. Thomas F. Fässler durchgeführt.

Ich erkläre hiermit an Eides statt, dass ich die vorliegende Arbeit ohne unzulässige Hilfe Dritter und ohne Benutzung anderer als der angegebenen Hilfsmittel angefertigt habe. Die aus anderen Quellen direkt oder indirekt übernommen Daten und Konzepte sind unter Angabe des Literaturzitats gekennzeichnet.

Garching, den 14.01.2020

Für alle die mich unterstützen.

“Remember, kids, the only difference between screwing around and science is writing it down.”

Adam Savage

Danksagung

Mein besonderer Dank gilt meinem Doktorvater

Prof. Dr. Thomas F. Fässler

für die Möglichkeit, meine Promotion am Lehrstuhl für Anorganische Chemie mit Schwerpunkt Neue Materialien durchzuführen und für konstruktive Anregungen, Kritik und Unterstützung.

Mein weiterer Dank gilt

Manuela Donaubauer

für die Hilfe bei sämtlichen organisatorischen Problemen und ihr offenes Ohr und ihre Hilfsbereitschaft bei Fragen aller Art

Dr. Wilhelm Klein und **Dr. Viktor Hlukhyy**

für die Hilfe bei der Arbeit an den Diffraktometern und der Lösung von kristallographischen Problemen

Dr. Marina Boyko

für die Hilfe bei der Synthese von endohedralen Phasen und der Kooperation die zu einer Publikation führte

Jasmin Dums

für DFT-Berechnungen an den endohedralen Phasen

Jasmin Haberl und **Andreas Wimmer**

für die ICP-OES-Messungen an meinen Ionentauscheransätzen

Dr. Sebastian Geier und **Christoph Wallach** für die vielen Raman Messungen

Dr. Maria Matthews und **Dr. Gabriele Raudaschl-Sieber** für die NMR Messungen

Dr.-Ing. Torben Dankwort, Christian-Albrechts Universität zu Kiel für die TEM Messungen

Einer besonderen Gruppe von Doktoranden des Arbeitskreises Fässler, dem sogenannten „**Quality Squad**“. Ohne dieses wäre meine Zeit niemals so schön gewesen. Auf euch Jungs – **Christoph Wallach, Felix Geitner, Sebastian Geier, Stefan Strangmüller, Thomas Wylezich.**

Meinem Laborkollegen **Lorenz Schiegerl** für die angenehme Zusammenarbeit.

Außerdem dem **Arbeitskreis Fässler** und **Nilges** in seiner Gesamtheit für die angenehme Zeit.

Mein besonderes Dankeschön gilt meiner Freundin **Denise** und meiner Familie, **meinen Eltern** und meiner **Schwester**.

für deren Rückhalt und die Unterstützung jedweder Art während des Studiums und der Promotion.

Abstract

Currently a global shift from fossil fuels to green energy is under way. Because of this, renewable energy production and storage are central themes of many research areas. Special interest is given to the investigation of novel materials with improved properties compared to the current technology.

Group 14 nanoparticles and nanostructured materials are promising candidates in this field due to their intrinsic semi-conducting nature and tunable characteristics. Tetrels often form binary intermetallic compounds like A_4E_4 ($A = \text{Na-Cs}$, $E = \text{Si-Pb}$), A_4E_9 ($A = \text{Na-Cs}$, $E = \text{Ge-Pb}$) and $A_{12}E_{17}$ ($A = \text{Na-Cs}$, $E = \text{Si-Sn}$) which are made up of four atomic and nine atomic clusters that are of interest for the synthesis of such materials.

This work focuses on two main subjects – the research of new tetrel allotropes through ion exchange of alkalimetal counterions of the previously mentioned clusters and subsequent oxidization, possibly forming element structures, as well as the examination of endohedral *Zintl* clusters – both in solid state and solution. The first part of this work is about establishing a systematic approach to ion exchange on *Zintl* phases. Several solvents are tested in order to determine the best solution medium for the different clusters at hand. For bare clusters like $[E_4]^{4-}$ and $[E_9]^{4-}$ these are polar, protic solvents like liquid ammonia, ethylenediamine and dimethylformamide and for substituted clusters like $[\text{Ge}_9[\text{Si}(\text{SiMe}_3)_3]_3]^-$ it is acetonitrile (acn). The exchange characteristics of bare and substituted clusters are comparable in acn and liquid ammonia which is why the substituted cluster is used as a model system to determine the parameters more quickly, since experiments in liquid ammonia are complicated and time consuming. Exchange times are investigated with the result that after eight hours a plateau is reached and after 24 hours the exchange is completed. The ratio of reactant to ion exchange resin is kept at 1/20 to ensure complete exchange in the given time frame. When conducting exchange reactions in liquid ammonia a special glass vessel was designed and implemented in order to moderate the delayed boiling which, if kept unchecked, leads to decomposition of the reaction solution. Having established these parameters, experiments on K_4E_4 ($E = \text{Si, Ge}$), K_4E_9 ($E = \text{Ge, Sn}$) and $K_{12}\text{Si}_{17}$ were conducted. The silicide phases proved to be too volatile and showed reactions with the exchange resin leading to gas expulsion in liquid ammonia which is undesirable using

such a solvent which is why no further experiments using silicides are conducted. With germanides the reaction can be done without the safety issues, however the cluster structure does not remain intact. The only successful exchange with the retention of the cluster structure was done using stannides, which lead to $\text{Li}_4\text{Sn}_9 \cdot 17 \text{NH}_3$. Using substituted clusters, the silylated germanide $\text{Li}[\text{Ge}_9[\text{Si}(\text{SiMe}_3)_3]_3]$ is characterized in bulk using NMR spectroscopy and crystalized as $[\text{Li}(\text{B}12\text{crwon}4)_2][\text{Ge}_9[\text{Si}(\text{SiMe}_3)_3]_3]$, characterized using single crystal X-ray diffraction. All attempts in stabilizing the bare $[\text{Ge}_9]$ cluster were unsuccessful, whether it was by using a polymer matrix or oxidations of the cluster to reduce the amount of alkali metal ions needed to balance the charge. Several experiments yielded germanium nanoparticles in the range of 10 to 100 nm. The size is dependent of what ion (H^+ , Li^+ , Na^+) is loaded onto the exchange resin thus the size can be tailored to desired specifications, however the yield of particles is so small that no further investigation is conducted.

Several new compounds containing endohedral *Zintl* clusters are found after the solid state precursors are examined using Raman spectroscopy. Experimental Raman spectra are compared to theoretical spectra of reported empty and endohedral clusters, which are gained through the use of DFT methods. The comparison allows classification of which clusters are present in the precursor phases. A plethora of new phases, with the compositions $[\text{TM}@\text{E}_9]$ ($\text{TM} = \text{Fe} - \text{Os}, \text{Co}, \text{Rh}, \text{Ni} - \text{Pt}, \text{Cu}, \text{Ag}; \text{E} = \text{Si}, \text{Ge}, \text{Sn}, \text{Pb}$) are synthesized and screened using this technique. Promising candidates are dissolved in liquid ammonia and three new compounds with new endohedral clusters, $[\text{Co}@\text{Ge}_9]^{5-}$, $[\text{Ru}@\text{Sn}_9]^{6-}$, “ $[\text{Rh}@\text{Sn}_9]$ ”, are discovered. $[\text{Co}@\text{Ge}_9]^{5-}$ is the first filled germanium nine-atom cluster, properly characterized using single crystal X-Ray diffraction and the ruthenium filled tin cluster has the highest charge ever found for a nine-atom *Zintl* cluster. A compound containing the $[\text{Co}_2@\text{Ge}_{17}]^{6-}$ cluster is isolated from liquid ammonia after fragmentation reactions of “ K_5CoGe_9 ” and titanium complexes.

Additional compounds, containing previously reported structure motives like $[\text{Co}@\text{Ge}_{10}]^{3-}$ and $[\text{Rh}@\text{Pb}_{12}]^{3-}$, are isolated from liquid ammonia. The Raman analysis of additional solid state precursors indicates the presence $[\text{Ni}@\text{Ge}_9]^{4-}$, a cluster which has only been reported from solution, and $[\text{Pd}@\text{Sn}_9]^{5-}$. No crystallization was realized for either clusters. A plethora of syntheses were conducted trying to substitute the endohedral clusters. Reactions of ternary solid

state phases containing $[\text{Co@Ge}_9]^{5-}$ clusters using main-group reactants mostly yielded previously reported mono- and bisilylated germanides and the reactions using transition metal complexes did not yield any new compound.

Zusammenfassung

Momentan ist ein globaler Wechsel von fossilen Brennstoffen hin zu erneuerbaren Energien zu beobachten. Aus diesem Grund sind die erneuerbare Energiegewinnung und die Speicherung dieser Energie zentrale Themen in vielen Forschungsbereichen. Der Erforschung neuer Materialien mit verbesserten Eigenschaften wird spezielles Interesse entgegengebracht. Aufgrund ihrer Halbleitereigenschaften sind Elemente der vierten Hauptgruppe in Form von Nanopartikeln und nanostrukturierten Materialien in diesem Feld vielversprechende Kandidaten. Tetrele bilden oftmals binäre intermetallische Verbindungen wie A_4E_4 ($A = \text{Na-Cs}$, $E = \text{Si-Pb}$), A_4E_9 ($A = \text{Na-Cs}$, $E = \text{Ge-Pb}$) und $A_{12}E_{17}$ ($A = \text{Na-Cs}$, $E = \text{Si-Sn}$) welche aus isolierten Clustern bestehen, die für die Synthesen von Speichermaterialien geeignet sind.

Die vorliegende Arbeit beschäftigt sich mit zwei Hauptgebieten – zum einem mit der Herstellung von neuen Tetrelallotropen durch Ionentausch der Alkalimetallgegenionen an *Zintl* Phasen und drauffolgender Oxidation von Clustern zu möglichen Elementstrukturen zum anderen von der Untersuchung endohedralear *Zintl* Cluster – im Festkörper und in Lösung. Für den Ionentausch an *Zintl*-Phasen wird ein Verfahren etabliert indem verschiedene Lösungsmittel auf ihre Tauglichkeit für Ionenaustauschreaktionen untersucht wurden. Für isolierte Cluster wie $[E_4]^{4-}$ und $[E_9]^{4-}$ sind stark polare Lösungsmittel wie flüssiger Ammoniak, Ethylendiamin oder Dimethylformamid geeignete Lösungsmittel, während es für substituierte Cluster wie $[\text{Ge}_9[\text{Si}(\text{SiMe}_3)_3]_3]^-$ Acetonitril (acn) ist. Der Ionentausch in flüssigem Ammoniak und acn verhält sich ähnlich. Der substituierte Cluster in acn wird als Modellsystem verwendet, da Reaktionen in flüssigem Ammoniak einen erheblich erhöhten Zeitaufwand darstellen. Austauschzeiten wurden analysiert und zeigen ein Plateau nach acht Stunden und einen kompletten Austausch nach 24 Stunden. Das Verhältnis von Reaktantphase zu Ionentauscherharz wird bei 1/20 gehalten, um den vollständigen Austausch in der gegebenen Zeit zu gewährleisten. Bei Austauschreaktionen in flüssigem Ammoniak wird ein spezielles Glasgefäß verwendet, was die erheblichen Siedeverzüge unterdrückt, die sonst zu einer Zersetzung der Reaktionslösung führen. Mit den festgelegten Parametern werden Experimente mit K_4E_4 ($E = \text{Si, Ge}$), K_4E_9 ($E = \text{Ge, Sn}$) und $K_{12}\text{Si}_{17}$ durchgeführt. Silicide zeigen Gasentwicklung bei der Reaktion in flüssigem Ammoniak, und werden daher als zu gefährlich für weitere Tests eingestuft. Reaktionen mit Germaniden zeigen einen vollständigen Austausch der Ionen,

allerdings bleibt die Clusterstruktur der eingesetzten Phase nicht erhalten. Der einzige Austausch von Ionen, bei dem sich die Reaktantphase nicht zersetzt, gelingt mit K_4Sn_9 , was zu $\text{Li}_4\text{Sn}_9 \cdot 17 \text{NH}_3$ führt. Austauschreaktionen mit subsituierten Clustern ergeben die lithiierte Clustereinheit $\text{Li}[\text{Ge}_9[\text{Si}(\text{SiMe}_3)_3]_3]$ die im Feststoff und Lösung mittels NMR Spektroskopie untersucht wird und als $[\text{Li}(\text{B12crown4})_2][\text{Ge}_9[\text{Si}(\text{SiMe}_3)_3]_3]$ kristallisiert und mit Einkristalldiffraktometrie charakterisiert werden konnte. Sämtliche Versuche, die Germanide gegenüber den eingeführten Lithiumionen zu stabilisieren, verliefen erfolglos, sei es die Einbettung in eine Polymermatrix oder die Oxidation der Cluster, sodass weniger Gegenionen nötig sind. Mehrere Experimente führten zur Bildung von Germaniumnanopartikeln in einem Größenbereich von 10 bis 100 nm. Die Größe der Partikel hängt von der Ionensorte ab, die auf das Tauscherharz geladen werden (H^+ , Li^+ , Na^+). Dadurch lässt sich die Größe der Partikel auf die gewollte Spezifikation einstellen, allerdings ist die Ausbeute dieser Partikel so gering, dass keine weiteren Untersuchungen durchgeführt wurden.

Mehrere neue Verbindungen mit endohedralen *Zintl*-Clustern wurden mittels Ramanspektroskopie in den Festkörpervorstufen nachgewiesen und aus Lösung auskristallisiert. Als erstes wurden die experimentellen Ramanspektren mit denen literaturbekannter leerer und gefüllter Cluster, deren Spektren mittels DFT-Methoden berechnet wurden, verglichen. Die Spektren erlauben eine Zuordnung, welche Cluster in der Vorläuferphase vorliegen. Es wurde eine Fülle an Festkörperphasen der Zusammensetzungen $[\text{TM}@\text{E}_9]$ ($\text{TM} = \text{Fe} - \text{Os}, \text{Co}, \text{Rh}, \text{Ni} - \text{Pt}, \text{Cu}, \text{Ag}; \text{E} = \text{Si}, \text{Ge}, \text{Sn}, \text{Pb}$) synthetisiert und mittels Ramanspektroskopie analysiert. Vielversprechende Kandidaten werden in flüssigem Ammoniak aufgelöst. Aus den Umsetzungen konnten drei neue Verbindungen, die bis heute unbekannte, endohedrale Cluster enthalten - $[\text{Co}@\text{Ge}_9]^{5-}$, $[\text{Ru}@\text{Sn}_9]^{6-}$ und „ $[\text{Rh}@\text{Sn}_9]$ “ - isoliert werden. Der gefüllte Germanium Cluster ist der erste mittels Einkristalldiffraktometrie gut charakterisierte Cluster. Der mit Ruthenium gefüllte Cluster besitzt die höchste Ladung eines Clusters dieser Art. Eine Verbindung die den Cluster $[\text{Co}_2@\text{Ge}_{17}]^{6-}$ enthält wurde nach Fragmentierungsreaktionen von der ternären Phase „ K_5CoGe_9 “ bei Umsetzungen mit Titankomplexen in flüssigem Ammoniak isoliert und kristallographisch charakterisiert. Es wurden weitere Verbindungen aus flüssigem Ammoniak isoliert, die literaturbekannte Struktur motive, wie $[\text{Co}@\text{Ge}_{10}]^{3-}$ und $[\text{Rh}@\text{Pb}_{12}]^{3-}$, enthalten. Ein

Festkörperprekursor, der Hinweise auf die Gegenwart des $[\text{Ni}@\text{Ge}_9]^{4-}$ Clusters enthält, wurde ebenfalls synthetisiert – dieser Cluster war bis jetzt nur aus Lösung kristallisiert werden. Eine Phase, die nach Ramananalyse Hinweise auf die Anwesenheit eines $[\text{Pd}@\text{Sn}_9]^{5-}$ enthält wurde gefunden, eine Kristallisation dieses Clusters aus flüssigem Ammoniak war jedoch nicht möglich. Synthesen, die zu substituierten, endohedralen Clustern führen sollten, waren erfolglos. Reaktionen mit Hauptgruppenreaktanten ergaben nur bereits bekannte mono- und bisilylierte Germanide, während die Reaktion mit Übergangsmetallen keine neuen Verbindungen ergaben.

Table of contents

1.	Introduction	1
1.1.	Tetrel elements in science and application	1
1.2.	<i>Zintl</i> phases – concepts, definitions and rules.....	4
1.2.1.	Bonding situation of <i>Zintl</i> clusters containing group 14 elements.....	5
1.3.	<i>Solubility</i> and reactivity of <i>Zintl</i> phases in solution	9
1.3.1.	Oxidative addition of clusters.....	10
1.3.2.	<i>Zintl</i> clusters featuring exo-bonded Ligands.....	11
1.3.2.1.	<i>Zintl</i> clusters featuring main group ligands	11
1.3.2.2.	<i>Zintl</i> clusters featuring hydrocarbon ligands	13
1.3.2.3.	<i>Zintl</i> clusters featuring protons	17
1.3.2.4.	<i>Zintl</i> clusters featuring transition metal ligands	18
1.3.3.	Endohedral <i>Zintl</i> clusters	24
1.3.4.	Expansion of $[E_9]$ cluster units	32
1.3.5.	Applications of <i>Zintl</i> phases	33
1.3.6.	New tetrel element modifications from <i>Zintl</i> phases.....	34
2.	Motivation	37
3.	Scope and Outline	39
4.	Results and Discussion	41
4.1.	Stability of $K_{12}Si_{17}$ and K_4Ge_9 in liquid ammonia	41
4.2.	Ion exchange on <i>Zintl</i> phases.....	44
4.2.1.	Theoretical background and relevant literature on ion exchange	44
4.2.2.	Standard operating procedures for Amberlyst 15 and <i>Zintl</i> clusters	48
4.2.2.1.	Experimental considerations – quantitative analysis by ICP-OES and ion exchange in liquid ammonia	48
4.2.2.2.	Determining the reaction parameters of Amberlyst 15 and <i>Zintl</i> clusters in solution.....	50
4.2.3.	Ion exchange on <i>Zintl</i> clusters utilizing established parameters.....	54
4.2.3.1.	Ion exchange on <i>Zintl</i> clusters featuring ligands resulting in $Li[Ge_9[Si(SiMe_3)_3]_3]$	54
4.2.3.2.	Ion exchange on bare <i>Zintl</i> clusters resulting in $Li_4Sn_9 \cdot 17 NH_3$	56
4.2.4.	Stabilization experiments of lithiated <i>Zintl</i> phases.....	60
4.2.4.1.	PEO as a lithium ion sequestering agent	60
4.2.4.2.	Counter ion reduction through Cluster oxidation	62

4.2.5.	Formation of germanium nanoparticles using Amberlyst 15 and K_4Ge_9	63
4.2.5.1.	Nanoparticles formed by XER (X = H, Li, Na) and K_4Ge_9	64
4.2.5.2.	Stability of the Ge nanoparticles	66
4.2.6.	Conclusion of ion exchange experiments including bare and silylated <i>Zintl</i> clusters	70
4.3.	Investigations of endohedral <i>Zintl</i> clusters in solid state and solution	71
4.3.1.	Reported Endohedral $[E_9]$ ($E = Ge, Sn, Pb$) units.....	72
4.3.2.	DFT enhanced Raman analysis of $[E_9]$ units.....	74
4.3.2.1.	DFT enhanced Raman analysis of empty $[E_9]$ units ($E = Si, Ge, Sn$)	74
4.3.2.2.	DFT enhanced Raman analysis of reported, endohedral $[E_9]$ ($E = Ge, Sn$) units.....	77
4.3.2.2.1.	Calculated Raman shifts of endohedral $[E_9]$ clusters.....	77
4.3.2.2.2.	Raman analysis of reported $[TM@E_9]$ ($TM = Ni, Co, Cu; E = Ge, Sn$) clusters.....	79
4.3.3.	Synthesis and characterization of novel ternary phases in solid state and solution.....	84
4.3.4.	Crystallization of compounds featuring the new filled $[E_9]$ clusters from liquid ammonia. 85	
4.3.4.1.	Synthesis and characterization of a compound containing the endohedral $[Co@Ge_9]^{5-}$ cluster	85
4.3.4.2.	Synthesis and characterization of a compound containing the endohedral $[Ru@Sn_9]^{6-}$ cluster	91
4.3.4.3.	Synthesis and characterization of a compound containing the endohedral “[Rh@Sn ₉]” cluster	96
4.3.4.4.	Synthesis and characterization of a compound containing the endohedral $[Co@Sn_9]^{5-}$ cluster	100
4.3.4.5.	Presence of hydroxide units $K_5[OH]$ as a way of enhancing cell packing	103
4.3.5.	DFT enhanced Raman analysis of new ternary phases containing endohedral clusters... 105	
4.3.6.	Fragmentation of endohedral clusters in liquid ammonia	108
4.3.6.1.	Synthesis and characterization of a compound containing the endohedral $[Co_2@Ge_{17}]^{6-}$ cluster	109
4.3.6.2.	Synthesis and characterization of compounds containing the endohedral $[Co@Ge_{10}]^{3-}$ cluster	113
4.3.6.3.	Synthesis and characterization of a compound containing the endohedral “[Rh@Pb ₁₂]” cluster	115
4.3.7.	Synthesis trails of ternary solid state phases containing filled cluster units featuring lighter tetrels and late transition metals	117
4.3.7.1.	Synthesis trails of $[TM@E_9]$ units featuring light tetrel elements ($TM = Co, Ni; E = Si, (Si/Ge)$)	117
4.3.7.2.	Synthesis trails of $[Cu@E_9]$ cluster units ($E = Ge, Sn$)	120
4.3.8.	DFT calculations on the clusters $[Co@Ge_9]^{5-}$ and $[Ru@Sn_9]^{6-}$	120

4.3.9.	Synthesis trails with the goal of exo-bonded ligands on endohedral clusters	123
4.3.9.1.	Reactions with main group reactants.....	123
4.3.9.2.	Reactions with transition metal complexes	125
5.	Conclusion.....	126
6.	Experimental Section	129
6.1.	General Techniques	129
6.2.	Solid state precursor syntheses.....	130
6.2.1.	Reaction vessel preparation	130
6.2.2.	Tube furnace.....	131
6.3.	Operating liquid ammonia	132
6.4.	Material list.....	136
6.5.	Analytical Methods	139
6.5.1.	Inductively coupled plasma optical emission spectroscopy (ICP-OES).....	139
6.5.2.	Infrared Spectroscopy (IR)	139
6.5.3.	Nuclear magnetic resonance (NMR).....	139
6.5.3.1.	Solution based NMR	140
6.5.3.2.	Magic angle spinning solid state NMR (MAS NMR).....	140
6.5.4.	Raman spectroscopy.....	140
6.5.5.	X-ray diffraction	141
6.5.5.1.	Single crystal diffraction	141
6.5.5.2.	Preparation of crystals under inert gas	141
6.5.5.3.	Powder X-ray diffraction (PXRD).....	142
6.5.6.	Dynamic scanning calorimetry (DSC).....	143
6.5.7.	Electron spray mass spectrometry (ESI-MS).....	143
6.5.8.	Dynamic light scattering (DLS) & Zeta potential measurements.....	143
6.5.9.	Transmission electron microscopy (TEM).....	144
6.5.10.	Quantum chemical Calculations	145
6.6.	Syntheses	146
6.6.1.	Binary Zintl phases.....	146
6.6.2.	Stability of binary <i>Zintl</i> phases $K_{12}Si_{17}$ and K_4Ge_9 in liquid ammonia.....	146
6.6.3.	Ion exchange experiments using Amberlyst 15 and <i>Zintl</i> phases.....	147
6.6.3.1.	Determination of exchange parameters	147
6.6.3.2.	Lithium ion exchange experiments on bare <i>Zintl</i> phases	149
6.6.3.3.	Lithium ion exchange experiments on <i>Zintl</i> clusters featuring ligands	150

6.6.3.4.	Stabilization of lithium ions towards <i>Zintl</i> clusters using PEO.....	153
6.6.3.5.	Crystallization experiments of lithiated <i>Zintl</i> phases.....	155
6.6.3.6.	Syntheses of Ge nanoparticles using K ₄ Ge ₉ and Amberlyst 15.....	156
6.6.4.	Ternary <i>Zintl</i> Phases.....	156
6.6.4.1.	Syntheses in the ternary system of K-Co- <i>E</i> (<i>E</i> = Ge, Sn)	160
6.6.4.2.	Syntheses in the ternary system of K-TM- <i>E</i> (TM = Co, Ni; <i>E</i> = Si, Ge).....	162
6.6.4.3.	Syntheses in the ternary system of K-Cu- <i>E</i> (<i>E</i> = Ge, Sn)	164
6.6.5.	Reactions of endohedral clusters with transition metal or main group ligands	165
7.	Appendix.....	171
7.1.	ICP-OES data	171
7.2.	Calculated Raman shifts and intensities.....	172
7.3.	Recorded spectra and diffractograms	179
7.3.1.	Reactant phases.....	179
7.3.1.1.	Binary <i>Zintl</i> phases.....	179
7.3.2.	Stability of <i>Zintl</i> phases in liquid ammonia.....	181
7.3.3.	Ion exchange experiments on <i>Zintl</i> phases	184
7.3.4.	Germanium nanoparticles through reaction of K ₄ Ge ₉ and Amberlyst 15	192
7.3.5.	Ternary phases containing Endohedral cluster species.....	196
7.3.6.	ESI-MS spectra	213
7.3.7.	Density functional theory calculations	214
7.3.8.	Dynamic scanning calorimetry.....	215
7.4.	Crystallographic data and structure refinement of new compounds	219
7.4.1.	[Li(B12crown4) ₂][Ge ₉ (Si(SiMe ₃) ₃) ₃]	219
7.4.2.	Li ₄ Sn ₉ · 17 NH ₃	223
7.4.3.	K ₆ [OH][Co@Ge ₉] · 16 NH ₃	226
7.4.4.	K ₇ [OH][Ru@Sn ₉] · 11 NH ₃	229
7.4.5.	C ₁₀₀ H ₂₀₀ K ₈ N ₁₀ O ₂₀ Rh ₄ Sn ₃₆	234
7.4.6.	K ₆ [OH][Co@Sn ₉] · 17 NH ₃	237
7.4.7.	[K(2.2.2-crypt)] ₂ K ₄ [Co ₂ @Ge ₁₇] · 13 NH ₃	241
7.4.8.	[K(2.2.2-crypt)] ₃ [Co@Ge ₁₀] · 3 NH ₃	246
7.4.9.	[K(2.2.2-crypt)] ₃ [Co@Ge ₁₀] · 9 NH ₃	248
7.4.10.	C ₇₂ K ₆ O ₃₆ Pb ₂₃ Rh ₃	250
7.4.11.	[Cs(18-crown-6)][Ge ₉ [Si(SiMe ₃) ₃] ₃][ClSi(SiMe ₃) ₃] ₂	252
7.4.12.	K ₄ [Sn ₉] · 9 dmf.....	254

7.4.13.	$[\text{K}_5(\text{OH})][\text{Ge}_9] \cdot 8 \text{NH}_3$	258
7.4.14.	$[\text{K}(\text{18-crown-6})]_3\text{Ge}_9$	261
7.4.15.	$\text{K}_2[\text{K}(\text{2.2.2-crypt})]_4[\text{Ge}_9\text{-Ge}_9] \cdot 13 \text{NH}_3$	264
8.	References	267
9.	List of publications.....	282

List of Abbreviations

18-crown-6	1,4,7,10,13,16–hexaoxacyclooctadecane
2.2.2–crypt	4,7,13,16,21,24–hexaoxa-1,10-diazabicyclo[8.8.8]hexacosane
2c2e	two-center-two-electron
2D	two-dimensional
3D	three-dimensional
Å	angstrom
A	Alkali metal
<i>a, b, c</i>	crystallographic parameters
Am	1-Chloro-2–methylpropane
Ar ^{L2}	phenyl ligand with w additional organic ligands
acn	acetonitrile
B12crown4	2,3,5,6,8,9-Hexahydro-1,4,7,10-benzotetraoxacyclododecine
BTS	copper oxide catalyst for gas regeNaERation
Bu	butyl
COD	cyclooctadiene
Cp	cyclopentadiene
Cp*	1,2,3,4,5–pentamethylcyclopentadiene
Cpr	But-1-enyl
d	diagonal
DB	double bond
DFT	density functional theory

DLS	dynamic light scattering
dmf	N,N-dimethylformamide
E, E'	tetrel element, element
e	sidelentgh of triangle prism in $[E_9]$ clusters
EDX	energy dispersive X-ray analysis
ESI-MS	electrospray ionization mass spectroscopy
en	ethylenediamine
g	total valence electron number
GB	glovebox
h	height
h	hour(s)
HER	proton exchange resin
HOMO	highest occupied molecular orbital
HSAB	hard and soft acids and bases
Hyp	hypersilyl
i	iso (alkyl group)
ICP-OES	inductively coupled plasma optical emission spectroscopy
IER	ion exchange resin
IR	infrared
K	Kelvin
kg	kilogram
L	ligand

LiER	lithium ion exchange resin
LUMO	lowest unoccupied molecular orbital
<i>M</i>	metal
Me	methyl
Mes	mesityl
min	minute(s)
MO	molecular orbital
n	charge
<i>n</i>	n (linear alkyl)
nm	nanometer
NaER	sodium ion exchange resin
NMR	nuclear magnetic resonance spectroscopy
PBE	DFT-functional after Perdew, Burke, and Ernzerhof
PBE0	hybrid DFT-functional after Perdew, Burke, and Ernzerhof
P-XRD	powder X-ray diffractometry
<i>Pn</i>	pnictide element
ppm	parts per million
Pr	propyl
pyr	pyridine
R	Rest
rpm	rotations per minute
RT	room temperature

s	secondary (alkyl group)
t	time
t	tertiary (alkyl group)
thf	tetrahydrofurane
TM	transition metal
tol	toluene
V	volume
VE	valence electron
XRD	X-ray diffractometry
Z	number of formula units per unit cell
α, β, γ	crystallographic parameters
$\alpha_{1/2/3}$	dihedral angle in [E_9] cluster
μ	my
μm	micrometer
%	percentage

1. Introduction

1.1. Tetrel elements in science and application

The growth of human civilization is accompanied with an increase in energy consumption and most of this energy is still largely generated by burning fossil fuels like coal or gas.^[1] While being aware of this fact, most people have an unchanged attitude^[2] towards the issue of excess use of fossil fuels and the resulting emission of greenhouse gases. This emission already has noticeable effects regarding weather^[3] and increase in temperature.^[4] The level of the greenhouse gas CO₂ in the atmosphere is rapidly increasing, having passed the 400 ppm threshold in 2015 (Figure 1). A decrease in emission rates is not to be expected.^[5]

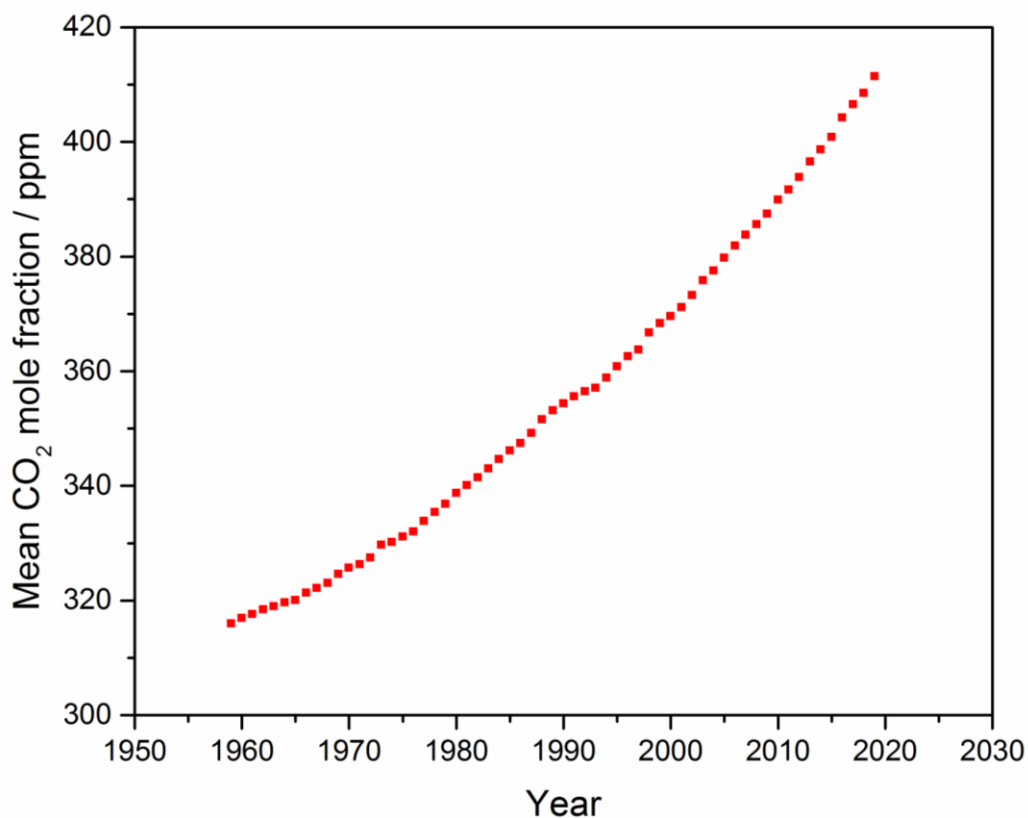


Figure 1: Mean carbon dioxide concentration from 1960 to the beginning of 2020. Recorded at Mauna Loa, Hawaii.^[5]

This current and pressing issue sets the stage for the race towards renewable energy generation and the storage of this, mostly electrical, energy. Being in the focus of media, politics and science the ongoing research of new materials with exceedingly better physical and chemical properties is a necessity. Group 14 elements exhibit an array of different chemical properties which open the possibility for application in science and industry. Elements in this group show completely different chemical behavior depending on the period of the periodic table of elements, to which they belong, like structure, stable oxidation states and electrical conductivity. In carbon, +4 is the preferred oxidation state, while lead is most stable in the form of Pb(II) compounds. Carbon in its diamond form is an insulator while tin and lead are both electric conductors.^[6-7] Especially silicon and germanium proved to be useful candidates as semiconductor materials because of their indirect band gaps (1.12 and 0.67 eV respectively).^[8] As semiconductors, Si and Ge can be used in a wide field of electronics: from photovoltaics,^[9-10] in order to generate energy, to lithium ion batteries,^[11-13] used in energy storage. Both elements can be doped to form positive or negative charge carriers^[14-17] and readily form solid solutions, with compositions of $\text{Ge}_{1-x}\text{Si}_x$,^[18-19] with one another. Because of this fact the characteristics, regarding band gaps, of materials containing silicon or germanium can be tuned to fit the needed application. Germanium has even better qualities regarding Li-ion diffusivity and electron- and hole-mobility^[12, 20-21] compared to silicon which is why it is used in science and has potential in application. However, compared to its lighter homologue the scarcity of germanium and thus its price limits the industrial usage. Silicon can be found in abundance in earth's crust (29% by weight)^[22] and therefore is the more viable option compared to its competitor germanium, found only at an amount of 1.6 ppm.^[23] This is why silicon is found in most daily devices,^[24] not germanium. The heavier homologues of group 14 elements, tin and lead, show less applications as semiconductors and more, as their chemical and physical properties suggest, as metals in alloys. Tin forms alloys such as bronze and brass^[6] as well as solid solutions^[25] with its lighter congeners. Lead is mostly used in accumulators, in alloys or as radiation shielding.^[6]

In order to move away from fossil fuels and toward green energy alternatives the limitations of current technologies have to be expanded and new technologies have to be explored. Using group

14 elements with their inherent semi conductive properties and tunable compositions in nanostructured materials may present as a promising approach to improve current technologies and make green energy generation more appealing. Such nanostructures, especially in the form of clusters, can be synthesized from the elements using high temperatures. Clusters can be extracted subsequently using appropriate solvents. Deltahedral $[E_9]$ ($E = \text{Si, Ge, Sn, Pb}$) clusters are interesting candidates for application purposes with $[\text{Ge}_9]$ already being used a soluble germanium source in inverse opal structures for batteries.^[26-28]

1.2. *Zintl* phases – concepts, definitions and rules

Zintl phases are intermetalloid solid state phases made up of an electropositive and a moderately electronegative component. Between these two components a formal electron exchange takes place. The electropositive component is usually made up of alkali, or alkaline earth metals (except for beryllium) or lanthanides while the (poly)anionic structure consists of p-block metals and semi metals (except for sulfur). Dividing these elements is the *Zintl* line which runs between the third and fourth main group. This separation serves as a guideline of the reactivity for different elements but is not a definitive rule. Because of the high electronegativity difference the binary compounds formed in these cases can be described as having an ionic bonding situation: the complete electron transfer between the two components leads to isolated cations and (complex) anionic structures that are often comparable to isoelectronic elements of the next higher group. Because of the electronegativity of these anionic structures they can be described using a covalent bonding situation following the (8-N) rule. Examples exhibit 1D, 2D and 3D structures like $K_4Ge_4^{[29]}$ containing isolated $[Ge_4]^{4-}$ tetrahedral (same structure as white phosphorus $[P_4]$), $KSb^{[30]}$ containing $[Sb^-]_x$ chains or $Li_7Ge_{12}^{[31]}$ containing complex networks.

Compounds that feature covalently bonded polyanions owe their names to such concepts as the *Zintl-Klemm-Busmann*^[32-34] concept or *Wade-Mingos* rules^[35-38]. Although the structures are complex, with some assumptions it is possible to explain their bonding situations using both of these concepts.^[6]

As mentioned, some of the compounds consisting of electropositive and electronegative components can be classified as *Zintl* phases. Such solids have compositions like A_4E_4 ($A = Na-Cs$, $E = Si^{[39]}$, $Ge^{[29]}$, $Sn^{[40]}$, $Pb^{[41]}$), A_4E_9 ($A = Na-Cs$, $E = Ge^{[42-45]}$, $Sn^{[43, 46]}$, $Pb^{[41, 47-49]}$) and $A_{12}E_{17}$ ($A = Na-Cs$, $E = Si^{[48, 50]}$, $Ge^{[43, 48]}$, $Sn^{[48]}$) and are accessible using high temperature syntheses from the elements. Phases with the composition A_4E_4 and A_4E_9 exclusively contain tetrahedra and nine-atomic clusters respectively, $A_{12}E_{17}$ phases contain both mentioned clusters in a ratio of tetrahedron/nine-atomic cluster 2/1 (Figure 2).

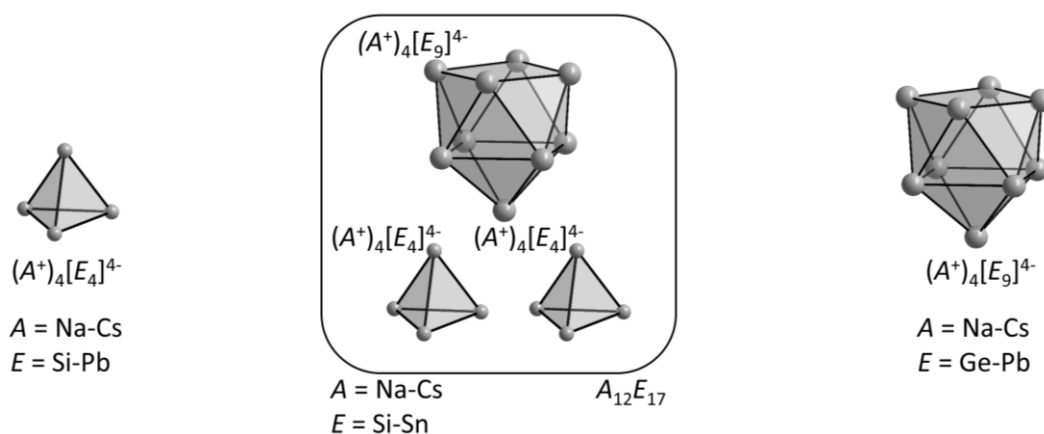


Figure 2: *Zintl* phases of the compositions A_4E_4 , A_4E_9 and $A_{12}E_{17}$ with the respective *Zintl* clusters.

Because of the high charge/atom ratio, clusters are only soluble in highly polar solvents like ethylenediamine (en), dmf or liquid ammonia. Phases containing tetrahedra have a higher charge/atom ratio than those that exclusively contain nine atomic clusters and are considered to have a diminished solubility when compared to each other. Solubility is decreased with decrease in element mass. In solution, charge separation occurs which results in solvated anionic clusters exhibiting uncoordinated tetrel vertex atoms.^[51-54] Besides low solubility the cluster charge also provides these phases with highly reductive properties which may cause problems during reactions in solution.

1.2.1. Bonding situation of *Zintl* clusters containing group 14 elements

The mentioned phases with the compositions A_4E_4 , A_4E_9 and $A_{12}E_{17}$ can be described using either the *Zintl-Klemm-Busmann*^[32-34] concept or *Wade-Mingos* rules^[35-38]. While the *Zintl-Klemm-Busmann* concept is indeed a good approximation for simple structures like $[E_4]^{4-}$ contained in both A_4E_4 and $A_{12}E_{17}$, as structures get more complicated like $[E_9]^{4-}$, it becomes apparent that this concept is too limited. For these more complex anions the *Wade-Mingos* rules appear to be a better approach.

According to the *Zintl-Klemm-Busmann* concept and (8-N) rule, in a *Zintl* phase, the anionic partial structures often adopts the elemental structure of the elements with the same electron count. An example is the $[\text{Si}_4]^{4-}$ unit which when broken down is Si^- which is equivalent to P thus forming a tetrahedron – three bonds for each atom ($8-(4+1) = 3$). An application of this concept to $[\text{Si}_9]^{4-}$ is not possible therefore a more refined method is needed. These clusters can also be described as electron deficient units with delocalized electrons similar to boranes.

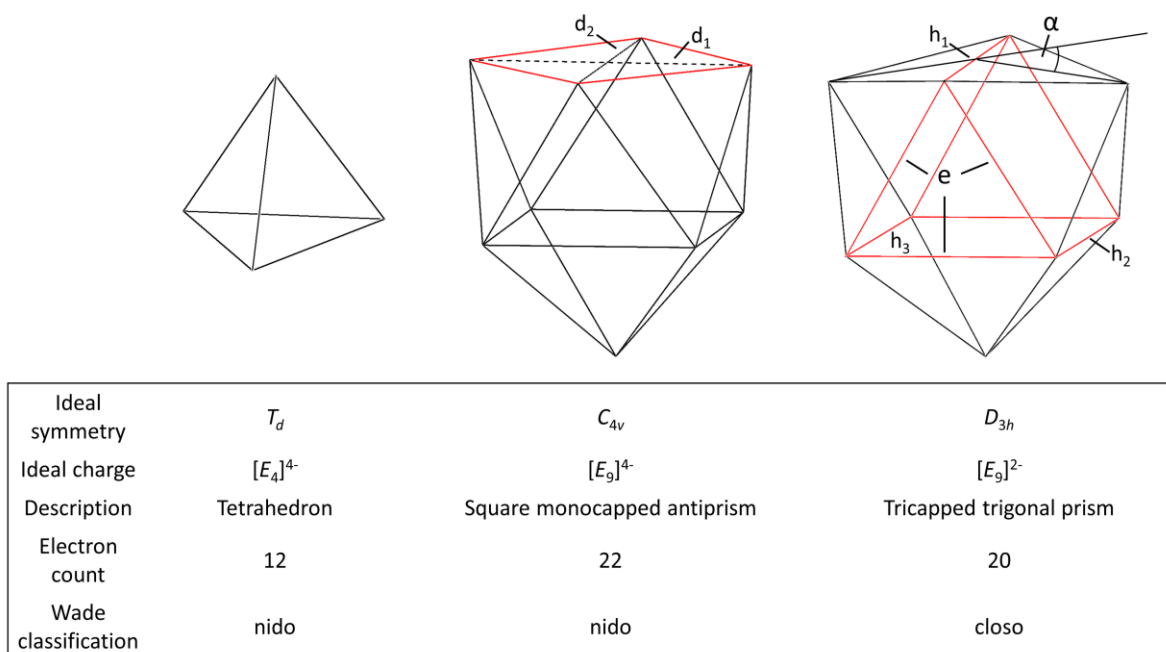


Figure 3: Schematic of different cluster symmetries contained in A_4E_4 , A_4E_9 and $A_{12}E_{17}$. Tetrahedron (nido cluster) contained in A_4E_4 and $A_{12}E_{17}$ (left). Different symmetries of $[\text{E}_9]^{n-}$ namely C_{4v} (nido cluster, middle) and D_{3h} (closo cluster, right) contained in A_4E_9 and $A_{12}E_{17}$. Highlighted in red are the flat, square surface of the monocapped square antiprism and trigonal prism of the tricapped trigonal prism. $d_{1/2}$ – diagonals of the open face in the case of a C_{4v} symmetric $[\text{E}_9]^{n-}$ cluster. $h_{1/2/3}$ – prism heights of a D_{3h} symmetric $[\text{E}_9]^{n-}$ cluster. e – triangle side length of the open face of a D_{3h} symmetric $[\text{E}_9]^{n-}$ cluster. α – angle between the two triangles that make up the open face of a $[\text{E}_9]^{n-}$ cluster.

This similarity comes from the fact, that bonding in these clusters simply cannot be described as a 2 center 2 electron bond because the number of bonds per vertex atom is higher than the available valence electrons. With the similarity between boranes and *Zintl* clusters established, it

is possible to apply the *Wade-Mingos* rules if some further assumptions are made. Firstly, each vertex atom contributes two electrons to the cage framework and secondly every vertex atom has a lone pair that functions as the B-H bond in boranes. $[E_4]^{4-}$ tetrahedra can be thus described as nido cages with $2n + 4 = 12$ skeletal electrons (T_d symmetry), where a closo cluster would be a trigonal bipyramid with $2n + 2 = 12$ electrons.^[55-56] Now an application to $[E_9]$ units is possible. These clusters can be described as two different extreme cases depending on their charge (Figure 3). If the $[E_9]$ cluster exhibits a charge of -4 it can be classified as a nido cluster with $2n + 4 = 22$ electrons. With this charge the cluster has C_{4v} symmetry and the shape of a monocapped, square antiprism. An oxidation of the cluster to $[E_9]^{2-}$ results in a rearrangement towards a closo cluster with $2n + 22 = 20$ electrons and D_{3h} symmetry in the shape of a tricapped, trigonal prism (Figure 3). In order to determine the symmetry of $[E_9]$ clusters several structural criteria have to be considered. The main two are the diagonal ratio d_1/d_2 and the ratio of the three prism heights h_1 , h_2 and h_3 . A quick assessment of these parameters reveals the symmetry, with $d_1/d_2 = 1$ only holds true for a flat open face which is only found in C_{4v} symmetry. Equality of all prisms heights, $h_1 = h_2 = h_3$, is only found in clusters with D_{3h} symmetry (Figure 2). Additional structural information can be deduced from α where if all three lengths are equal the cluster is in D_{3h} configuration. The same holds true for the angle α which can be measured for all three sides of the cluster, whereby for C_{4v} symmetry the angle α equals zero. In solid state the $[E_9]$ unit is exclusively found in its base, nido C_{4v} symmetric form.^[43-50, 57] Other symmetries can only be found in oxidized clusters found in compounds formed in solution.^[55-56, 58-60]

In reality however, most of the found structures lie between these ideal extremes but can be assigned to one or the other using the established structural characteristics. With most of the clusters found in between the two extremes additional symmetries, like C_{2v} , have to be considered.^[55-56, 58, 61-67] Between D_{3h} and C_{4v} lie two distinguishable C_{2v} possibilities, having one elongated and two shortened prism heights. These clusters are often found having a charge of -3 – meaning the cluster is paramagnetic. In order to move from one extreme to another the atoms at the end of one diagonal have to move downwards while elongating the diagonal between them resulting in $d_1/d_2 \neq 1$. At the same time the other diagonal shortens to become the same length

as the prisms heights. Ideally cluster with C_{2v} symmetry have a charge of -3 , possessing 21 electrons which leaves them as a paramagnetic species.^[56]

Calculations show that only small energy barriers between -3.5 kJ/mol and 4.7 kJ/mol separate the different conformations of $[E_9]$ ($E = \text{Si}^{[68]}, \text{Sn}^{[69]}$). With a low energy barrier between cluster conformations the cages can be easily converted from one form to another. A change of electron configuration through oxidation or reduction only results in a minor change of cluster symmetry. The $[E_9]^{n-}$ ($n = 2, 3, 4$) units thus make for a structurally and electronically flexible system with a high potential for redox reactions in solution.^[22, 56]

1.3. Solubility and reactivity of *Zintl* phases in solution

As mentioned before, *Zintl* phases can be dissolved in polar solvents such as en, dmf or liquid ammonia. In solution new reactions are possible: oxidative coupling, filling of cluster cavities and organic or metal based substitution. In order to increase the solubility of these phases and thereby increase the probability of new reactions taking place, sequestering agents are introduced to the solution. One of the first of these agents was [2.2.2]-cryptand, which not only increases the solubility but also the crystallization characteristics of the compounds.^[70-71] This can be explained by the size increase of the coordinated cations exhibiting diameters similar to those of the clusters. Further agents are introduced with 18-crown-6 later on.^[66] With these agents more and more structures containing bare cluster anions were found from solution, ranging from species with different elements and charges (Table 1) to different number of atoms like $[E_5]^{2-}$.^[61, 72-79] Even more exotic constellations like $[E_6]$, $[E_7]$ and $[E_{10}]$ ($E = \text{Ge},^{[80]} \text{Sn},^{[81]} \text{Pb}^{[82]}$) can be found, however these being not bare clusters. Still this shows the potential of fluctuation these clusters have in solution. These different charges and atom constellations indicate that the clusters with different numbers of atoms are in an equilibrium in solution and it is postulated that the amount and type of added agent can determine the species that crystallizes from solution.^[22, 83-84]

Table 1: Crystallized and characterized $[E_4]^{4-}$ and $[E_9]^{n-}$ phases from various solvents.

	$E = \text{Si}$	$E = \text{Ge}$	$E = \text{Sn}$	$E = \text{Pb}$
$[E_4]^{4-}$	[85-86]	[86]	[86-88]	[86-87]
$[E_9]^{4-}$	[89-91]	[92-95]	[76, 96-101]	[102-104]
$[E_9]^{3-}$	[61]	[64-65, 67, 105-106]	[63, 107-109]	[64, 104, 107]
$[E_9]^{2-}$	[110]	[71, 111]	—	—

These clusters show a wide range of redox reactions when in solution, as can be seen from the table above. These reactions take place with just the clusters present and without any additional reaction partners. It is not hard to imagine the possibilities that open up when reacting the clusters with different additional chemicals in a plethora of different solvents. The reactions that these clusters are able to undergo have been and still are an intensely studied topic.^[22, 55-56, 112-120]

1.3.1. Oxidative addition of clusters

Having established the possibility of an equilibrium of differently charged clusters in solution as well as the flexible redox behavior of *Zintl* clusters, the reactivity of clusters with one another in these solutions is of interest. A condensation reaction between clusters would lead to dimers, oligomers and even polymers, the first of which was discovered by Sevov *et al.* in 1999 in the form of $[\text{Ge}_9\text{-Ge}_9]^{6-}$.^[121] Since then many different structures of condensed clusters have been found. Starting from further dimers^[122-125], to trimers^[126-127] and tetramers^[128-129]. Furthermore polymers exist being either solely $[\text{Ge}_9]$ clusters linked together or additional atoms between clusters. Only two examples of a pure $-\text{[Ge}_9\text{]}-$ polymer^[122, 130] are known up to now, whereas chains of $[\text{Ge}_9]$ and different transition metal linkers, like $\text{Hg}^{[52]}$ and $\text{Zn}^{[131-132]}$, are characterized as well. All of these structures consist of $[\text{Ge}_9]$ clusters of different charges, whereas dimers have $[\text{Ge}_9]^{3-}$ units, trimers, tetramers and polymers consist of $-\text{[Ge}_9\text{]}^{2-}$ or $-\text{[Ge}_9\text{-TM}]^{2-}$ units (TM = transition metal). In addition to these structurally characterized polymers there are also calculations investigating the possibility of different new bonding possibilities, like 2D or 3D linked $[\text{Ge}_9]$ units^[133-134] or linked $[\text{Si}_9]^{[135]}$ clusters. The heavier homologues of group 14, tin and lead, have not yielded any structures comparable to these polymers, disregarding the dimeric $[\text{Sn}_9]\text{-Ag-}[\text{Sn}_9]$ anion.^[136-137]

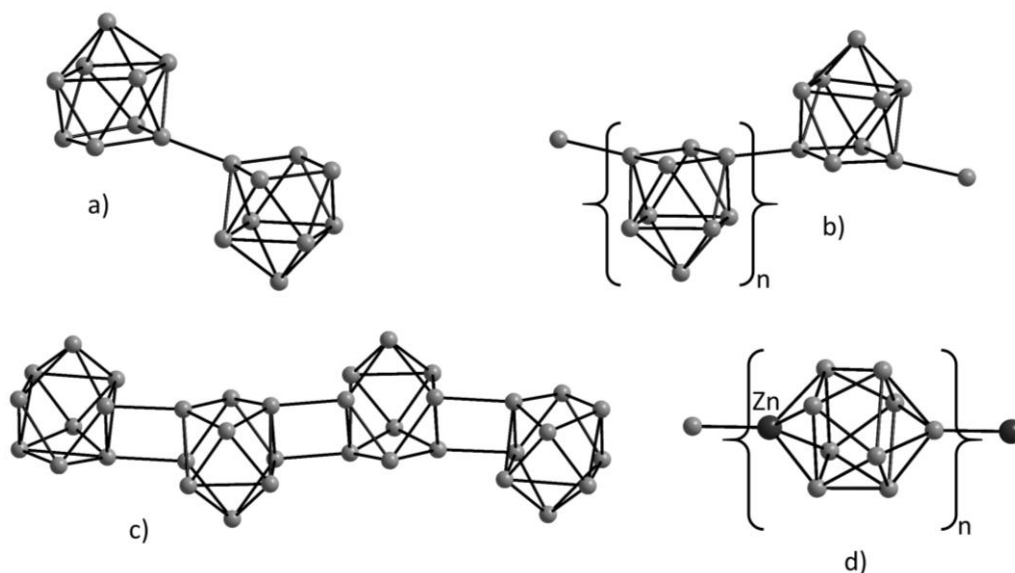


Figure 4: Oligomers and polymers consisting of $[E_9]^{n-}$ Zintl clusters. a) $[Ge_9-Ge_9]^{6-}$ dimer^[121-123]; b) $[Ge_9]^{2-}$ polymer^[122, 130]; c) $[Ge_9]^{2-}$ tetramer^[128]; d) Zn- $[Ge_9]$ polymer^[132]. Grey – germanium.

1.3.2. Zintl clusters featuring exo-bonded Ligands

Reactions including Zintl clusters and a plethora of different agents, ranging from transition metal complexes to main group reactants, have been an abundant research field in the past decades. Over 100 scientific articles investigating the substitution, endohedral nature and even application of clusters in solution or solid state have been published in the last 20 years. In case of clusters like the $[E_9]$ ($E = Si, Ge, Sn, Pb$) species substitution can be understood as the replacement of free lone pairs with different organic or organometallic groups.

1.3.2.1. Zintl clusters featuring main group ligands

Reactions between agents containing main group elements are mainly done using the $[E_9]$ unit with $E = Ge$ being the most used semimetal. Reactions with $E = Si, Sn, Pb$ are less common for different reasons. $[Si_9]$ units can only be extracted from $K_{12}Si_{17}$ and with its low solubility and presence of $[Si_4]$ units that may change reaction characteristics, it is an inherently difficult

reactant. Reactions using $[\text{Sn}_9]$ or $[\text{Pb}_9]$ units are also difficult because of the low stability of the $[\text{E}_9]$ units in solution. Both show fast decomposition from solution yielding elemental metal.

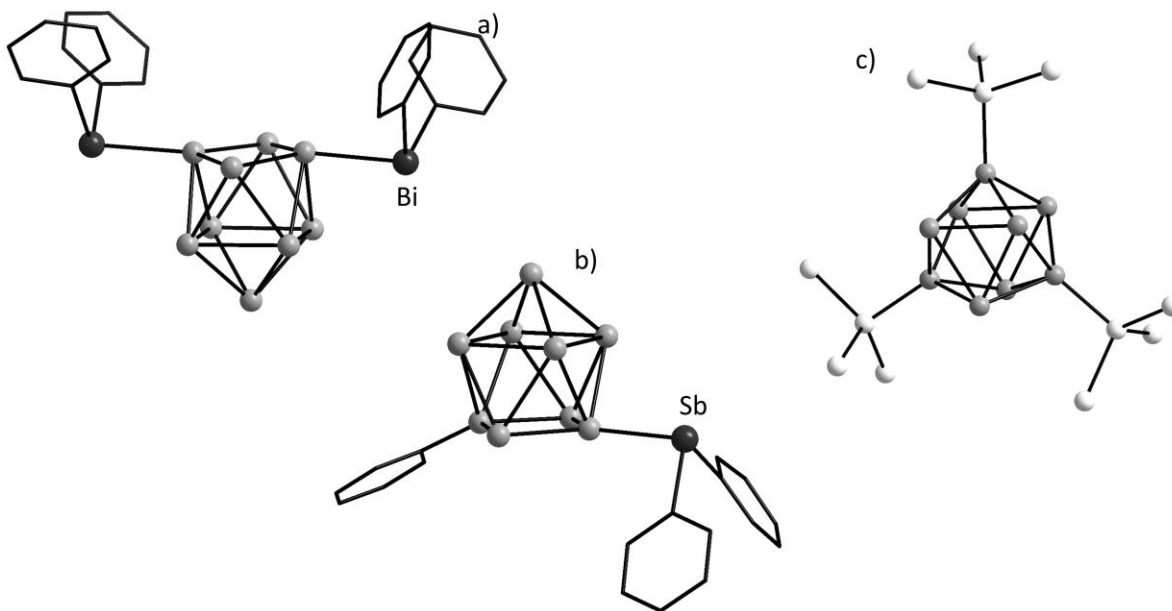


Figure 5: Examples of $[\text{Ge}_9]$ units substituted with different main group element ligands. a) $[\text{Ge}_9(\text{BiPh}_2)_2]^{2-}$ ^[138]; b) $[\text{Ph-Ge}_9\text{-SbPh}_2]^{2-}$ ^[139]; c) $[\text{Ge}_9[\text{Si}(\text{SiMe}_3)_3]_3]^-$ (Methyl groups omitted for clarity).^[140-141] Grey – germanium, white – silicon, Wire and sticks – carbon.

Early examples of substitutions on $[\text{Ge}_9]$ units are $[\text{Ph-Ge}_9\text{-SbPh}_2]^{2-}$ ^[139], $[\text{Ph}_2\text{Sb-Ge}_9\text{-Ge}_9\text{-SbPh}_2]^{4-}$ ^[139] and $[\text{Ph}_2\text{Bi-Ge}_9\text{-BiPh}_2]^{2-}$ ^[138] showing the reactivity of $[\text{Ge}_9]$ towards heavier group 13 elements. The antimony chemistry is further expanded by negative doping of clusters to yield such examples like $[\text{SbGe}_8]\text{-CH=CH}_2$.^[142] In addition to pnictides, some heavier third main group elements are also able to bond to $[\text{Ge}_9]$ units like indium.^[125] In both reactions the reactant coordinates onto the uncapped square of the $[\text{Ge}_9]$ unit and lowers the charge by one as per one “ligand”. Similar reactions are known using group 14 elements resulting in a similar constellation of $[\text{Ge}_9\text{-ER}_3]^{3-}$, $[\text{R}_3\text{E-Ge}_9\text{-ER}_3]^{2-}$ and $[\text{R}_3\text{E-Ge}_9\text{-Ge}_9\text{-ER}_3]^{4-}$ ($\text{E} = \text{Ge}, \text{Sn}$; $\text{R} = \text{Me}, \text{Ph}$).^[83] A major turning point comes in the form of a structure which was synthesized by treating liquid germanium with HBr and $\text{Li}[\text{Si}(\text{SiMe}_3)_3]$ at -78°C to yield $[\text{Ge}_9[\text{Si}(\text{SiMe}_3)_3]_3][\text{Li}(\text{thf})_4]$.^[140] This synthesis was later simplified by using K_4Ge_9 and $\text{Cl}[\text{Si}(\text{SiMe}_3)_3]_3$ to be able to produce $\text{K}[\text{Ge}_9[\text{Si}(\text{SiMe}_3)_3]_3]$ in larger

quantities.^[141] The $[\text{Ge}_9\{\text{Si}(\text{SiMe}_3)_3\}_3]^-$ (Figure 5, c) anion proved to be a major starting point for further reactions involving $[\text{Ge}_9]$ units, by making them soluble in more conventional solvents such as acetonitrile or toluene. Utilizing the solubility of this anion as a starting off point many new structures are synthesized.^[143-146] Even the equivalent anion featuring $[\text{Sn}_9]$ ^[147] instead of $[\text{Ge}_9]$ is synthesized.^[148] These structures included different amounts of $[\text{Si}(\text{SiMe}_3)_3]_3$ ligands^[149] as well as different new silyl ligands.^[150] Another group of inorganic, main group substitution agents are phosphines which show a plethora of compounds with varying steric demand.^[144, 146, 151] In addition to these syntheses calculations are used to investigate new possible synthetic routes using this versatile anion, whether being for novel materials^[152] or new type of ligands.^[153-154]

1.3.2.2. *Zintl* clusters featuring hydrocarbon ligands

The only known $[\text{E}_9]$ *Zintl* clusters which feature organic exo-bonded ligands are $[\text{Ge}_9]$ and $[\text{Sn}_9]$. Between these two units the $[\text{Ge}_9]$ unit is the one for which more structures exist. Again like in the previous chapter, the clusters can be substituted using different ligands but the open square of the $[\text{E}_9]$ unit remains the main attachment point. The characterized compounds can be divided into two categories – clusters with only organic ligands and clusters with two types of ligands. As will be further described in the following chapter 1.3.2.4 when substituting bare $[\text{E}_9]$ clusters, the main location for a ligand is the open, square face. In the field of solely organic ligands there are some mono-substituted, bis-substituted compounds and a particularly high amount of dimeric $[\text{Ge}_9]$ units outfitted with organic molecules. The mono-substituted $[\text{Ge}_9\text{-R}]$ units include ligands such as $\text{R} = -\text{mes}$ ^[155], $-\text{CH}=\text{CH}_2$ ^[155], $-\text{C}(\text{CH}_3)=\text{CH}-\text{CH}_2\text{CH}_3$ ^[156]. Bis-substitution can also be found with $[\text{Ge}_9-(\text{CH}_2-\text{CH}(\text{CH}_2)_2)_2]^{2-}$ ^[156], $[\text{Ge}_9-(\text{CH}=\text{CH}-\text{Fc})_2]^{2-}$ ^[157] (Fc = Ferrocene) and $[\text{CH}_3\text{CH}_2-\text{Ge}_9\{\text{Si}(\text{SiMe}_3)_3\}]^{2-}$ ^[158] which bridges the gap between purely organic substituted and main group element substituted clusters.

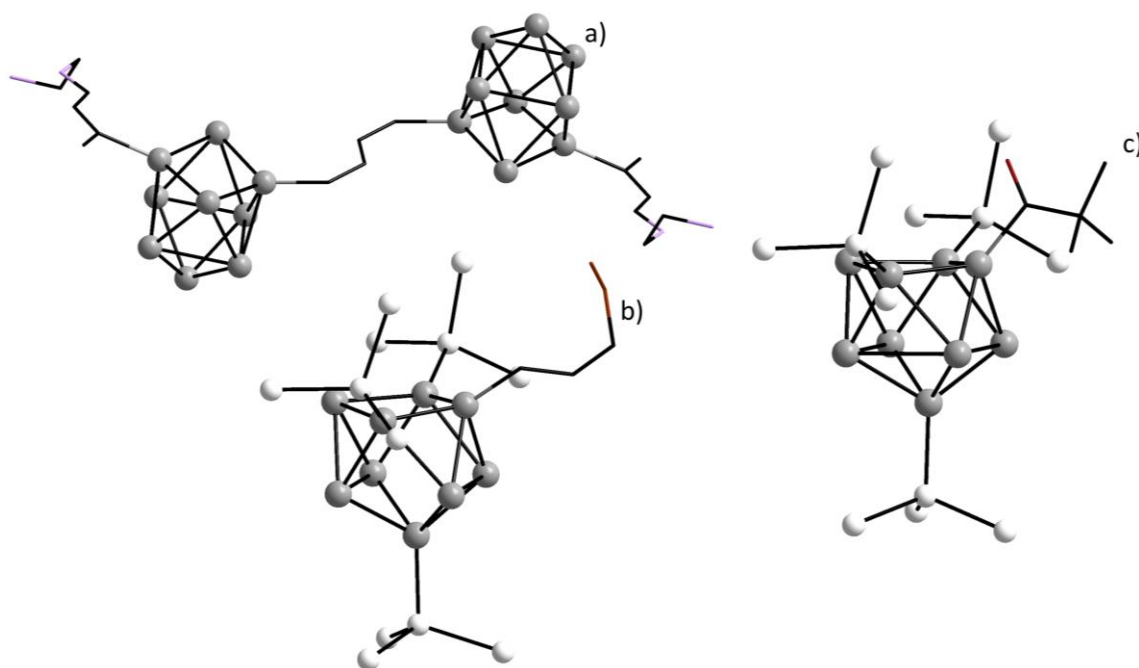


Figure 6: Examples of organic ligands attached to $[\text{Ge}_9]$ clusters. a) *Zintl* triad $[\text{R-Ge}_9\text{-CH=CH-CH=CH-Ge}_9\text{-R}]^{4-}$ ($\text{R} = -\text{C}(\text{CH}_3)=\text{CH-CH=N}(\text{CH}_2)_2\text{NH}_2$ ((2*Z*,4*E*)-7-amino-5-aza-hepta-2,4-dien-2-yl);^[159-160] b) $[\text{CH}_2=\text{CH-CH}_2\text{-CH}_2\text{-Ge}_9[\text{Si}(\text{SiMe}_3)_3]_3]$;^[161] c) $[\text{tBu-CO-Ge}_9[\text{Si}(\text{SiMe}_3)_3]_3]$.^[162] Grey balls – germanium, white balls – silicon, black wire and stock – carbon, red wire and stick – C=C, purple wire and stick – nitrogen.

The first $[\text{Ge}_9]$ dimer with different ligands is in the form of $[\text{R-Ge}_9\text{-Ge}_9\text{-R}]^{4-}$ ($\text{R} = -^t\text{Bu}, -^s\text{Bu}, -^n\text{Bu}, -^i\text{Am}$) ($^i\text{Am} = -2\text{-methylbutane}$), with the last three ligands only being characterized using ESI-MS.^[163] The remainder of these dimeric structures are linked by the organic chains and consist of the same central structure theme of $[\text{R-Ge}_9\text{-CH=CH-CH=CH-Ge}_9\text{-R}]$ with many different organic rests. These structures are usually referred to as *traids*.^[159-160] This organic linker contains two double bonds which can be either in *cis,cis* or *cis,trans* conformation. The simplest of these molecules is with $\text{R} = -\text{CH=CH}_2$ which was one the first to be reported.^[160] During the same time another ligand $\text{R} = -\text{C}(\text{CH}_3)=\text{CH-CH=N}(\text{CH}_2)_2\text{NH}_2$ ((2*Z*,4*E*)-7-amino-5-aza-hepta-2,4-dien-2-yl) was investigated.^[159-160]

Heavier clusters like $[\text{Sn}_9]$ can also be substituted using organic ligands. Even mixed tin and germanium clusters can be found with organic ligands attached in the form of $[\text{GeSn}_8\text{-R}]^{3-}$ ($\text{R} = -$

HC=CH₂, -HC=CHCpr) (Cpr = cyclopropyl) and [Ge₂Sn₇-R]³⁻ (R = -HC=CH₂, -HC=CHPh).^[164] These heteroatomic units show similar behavior as [Ge₉] in terms of substitution location on the cluster. Pure [Sn₉] also shows the same location of organic ligands on the open face of the cluster unit with [Sn₉-R]³⁻ (R = -^tBu, -CH=CH₂, -CH=CH-Ph) where all the ligands are located on the open cluster face.^[165] The [Sn₉-R₃] (R = -2,6-(2,4,6-*i*Pr₃C₆H₂)₂C₆H₃) unit is the largest [E₉] cluster solely substituted by organic ligands.^[166]

There even exists a unit similar to [Ge₉[Si(SiMe₃)₃]₃]⁻ mentioned in chapter 1.3.2.1 where only organic ligands are attached to the cluster and the symmetry is considered *D*_{3h} instead of *C*_{4v}. Fewer structures are known of clusters containing organic ligands as well as additional non-organic ligands. There is again the distinction of monomeric and dimeric [Ge₉] compounds. However, because of the preexisting substituents, here the cluster is assumed to exhibit *D*_{3h} configuration resulting in a higher chance of substitution of the open triangle instead of the open square of the cluster. In the first category three reactions need to be considered: a reaction starting from an alkylation [^tBu-CO-Ge₉[Si(SiMe₃)₃]₃] followed by decarbonylation [^tBu-Ge₉[Si(SiMe₃)₃]₃]^[162] as well as a simple alkylation similar to the previously mentioned [CH₂=CH-CH₂-CH₂-Ge₉[Si(SiMe₃)₃]₃].^[161] Finally the only dimeric species is a [Ge₉[Si(SiMe₃)₃]₂] dimer linked *via* (C₆H₄) unit [(Si(SiMe₃)₃)₂Ge₉]-SiMe₂-(C₆H₄)-SiMe₂-(Ge₉[Si(SiMe₃)₃])⁻.^[167]

Table 2: Collection of organically substituted $[E_9]$ ($E = \text{Ge}, \text{Sn}$) units.

Monosubstituted $[E_9]$ units ($E = \text{Ge}, \text{Sn}$)	Organic rest
$[\text{Ge}_9\text{-R}]^{3-}$	$-\text{mes}^{[155]}, -\text{CH}=\text{CH}_2^{[155]}, -\text{C}(\text{CH}_3)=\text{CH}-\text{CH}_2\text{CH}_3^{[156]}$
$[\text{Ge}_2\text{Sn}_7\text{-R}]^{3-}$	$-\text{HC}=\text{CH}_2, -\text{HC}=\text{CHPh}^{[164]}$
$[\text{GeSn}_8\text{-R}]^{3-}$	$-\text{HC}=\text{CH}_2, -\text{HC}=\text{CHCpr}^{[164]}$
$[\text{Sn}_9\text{-R}]^{3-}$	$-t\text{Bu}, -\text{CH}=\text{CH}_2, -\text{CH}=\text{CH-Ph}^{[165]}$
Bissubstituted $[\text{Ge}_9]$ units	Organic rest
$[\text{R-Ge}_9\text{-Ge}_9\text{-R}]^{4-}$	$-t\text{Bu}, -s\text{Bu}^a, -n\text{Bu}^a, -t\text{Am}^a^{[163]}$
$[\text{Ge}_9\text{-R}_2]^{2-}$	$-\text{CH}=\text{CH-CH}_2\text{NH}_2^{[168]}$ $-\text{CH}=\text{CH-Fc}^{[157]}$
<i>Zintl</i> triads	Organic rest
$[\text{R-Ge}_9\text{-CH}=\text{CH-CH}=\text{CH-Ge}_9\text{-R}]^{4-}$	$-\text{CH}=\text{CH}_2^{[160]}$ $-\text{C}(\text{CH}_3)=\text{CH-CH}=\text{N}(\text{CH}_2)_2\text{NH}_2^{[159-160]}$
Multiple substituted $[E_9]$ units ($E = \text{Ge}, \text{Sn}$)	Organic rest
$[\text{Ge}_9[\text{Si}(\text{SiMe}_3)_3]_3]^-$	$-\text{CO-}t\text{Bu}^{[162]}, -t\text{Bu}^{[162]}, -\text{CH}_2\text{-CH}_2\text{-CH}=\text{CH}_2^{[161]}$
$[\text{Ge}_9[\text{Si}(\text{SiMe}_3)_3]_2]^{2-}$	$-\text{SiMe}_2\text{-(C}_6\text{H}_4\text{)-SiMe}_2^{[167]}$
$[\text{Sn}_9\text{-R}_3]$	$-2,6\text{-(2,4,6-}i\text{Pr}_3\text{C}_6\text{H}_2)_2\text{C}_6\text{H}_3^{[166]}$
$[\text{Sn}_{10}\text{-R}_3]^+$	$-\text{Ar}^{\text{mes}}^{[166]}$

a – only characterized by ESI-MS measurements.

1.3.2.3. *Zintl* clusters featuring protons

A rather new field of cluster reactions is that of protons reacting with the $[E_9]$ units in solution. Using highly polar and protonating solvents like liquid ammonia, en or dmf as the primary way of extraction of *Zintl* ions from solids, the potential for protonation is always present. In the last year six new publications were published describing that protonation can occur in solution to almost all $[E_9]$ ($E = \text{Si}, \text{Ge}, \text{Sn}$), and even $[E_4]$ ($E = \text{Si}, \text{Ge}$) units.

The first hint that protonation could be an ever present side reaction possibility was observed by Eichhorn *et al.* in 2012 with the $[\text{HSn}_9]^{3-}$ ion crystallized from en.^[169] They report a juxtaposition of $[\text{HSn}_9]^{3-}$ and $\text{K}_x\text{Sn}_9^{(4-x)-}$ ($x = 1, 2, 3$) in solution using crystallographic methods, NMR and DFT calculations. After this a plethora of new structures have been published including the lighter homologues equivalents $[\text{HGe}_9]^{3-}$ ^[170] and $[\text{HSi}_9]^{3-}$ ^[171-172] as well as mixtures thereof $[\text{H}_2(\text{Si/Ge})_9]^{2-}$ ^[171] and even higher proton counts on silicide clusters $[\text{H}_2\text{Si}_9]^{2-}$ ^[173].

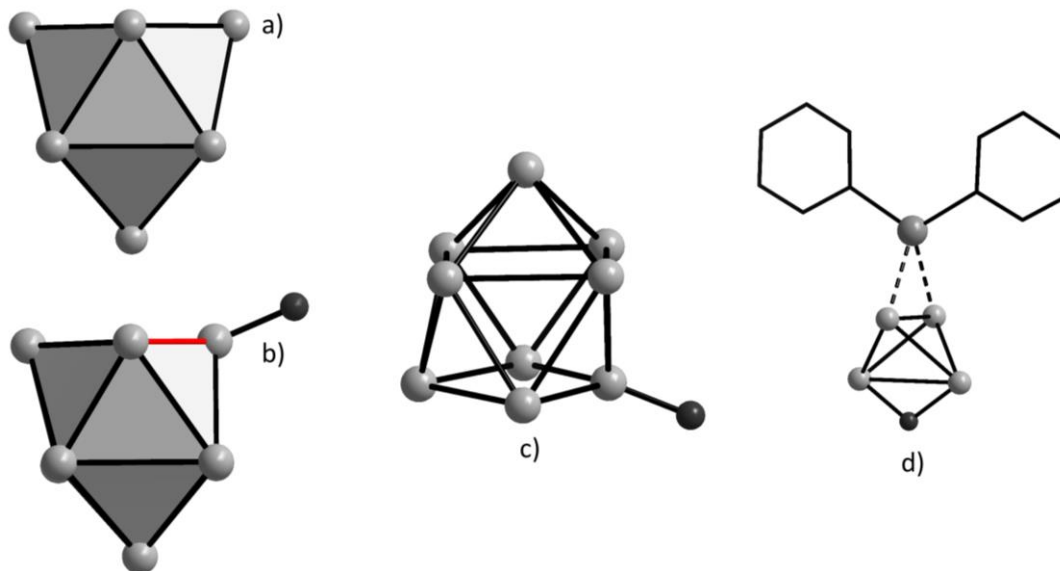


Figure 7: Schematic structures of protonated $[E_9]$ and $[E_4]$ units. a) Unprotonated $[E_9]^{4-}$ cluster with C_{4v} symmetry; b) Protonated, distorted $[\text{HE}_9]^{3-}$ unit; highlighted in red are shortened Ge-Ge bonds c) $[\text{HSi}_9]^{3-}$ cluster with significant distortion to the uncapped square^[171, 173]; d) Protonated $[\text{HGe}_4]\text{-ZnPh}_2$ unit^[174]. Grey – germanium, black – protons, wire and sticks – hydrocarbons.

All these clusters feature one or more proton bound η^1 on the uncapped, square face of the $[E_9]$ unit which significantly alters the symmetry of the cluster. The distances from the coordinated E atom to its two neighboring atoms is shortened resulting in an asymmetric quadrangle (Figure 7, a) and b)).

The shortening of these bond lengths also goes along with increase of the angle between the capped square and the side of the cluster from an acute angle to almost 90° . Refining protons to such clusters units poses several problems. Protons are extremely light and therefore do not interact much with the X-rays used in crystallographic measurement methods. Because of that finding the correct electron density in structures to reliably determine whether a proton is present is difficult. Because of this additional analytics are needed to prove the presence of protons in structures like $^1\text{H-NMR}$. The distortions that come as a result of the protonation can be helpful in determining whether a cluster is protonated or not in a more quick and simple fashion for future structures.

$[E_4]$ clusters are also found to be subject to protonation, however there is only a single crystallographically characterized structure - a $[\text{Ge}_4]^{4-}$ cluster with an additional ZnPh_2 ligand (Figure 7, d). All other investigations are limited to NMR and DFT calculations.^[75] The structure contains the $[\text{HGe}_4]^{3-}$ unit in which the proton is bonded η^2 as opposed to η^1 on the $[E_9]$. This in turn leads to an elongation of the bonds next to the proton rather than a shortening.

1.3.2.4. *Zintl* clusters featuring transition metal ligands

Transition metals ligands on *Zintl* clusters, as with using main group elements, can be best summarized in two categories – substitution on bare clusters and substitution of already functionalized clusters.

For the substitution of bare clusters a small trend can be observed - $[E_9]$ units consisting of heavier group 14 elements such as Sn and Pb are often substituted by early transition metal complexes, containing for example Cr, Mo, W, while their lighter homologues like Ge and Si more often do so with later transition metals.

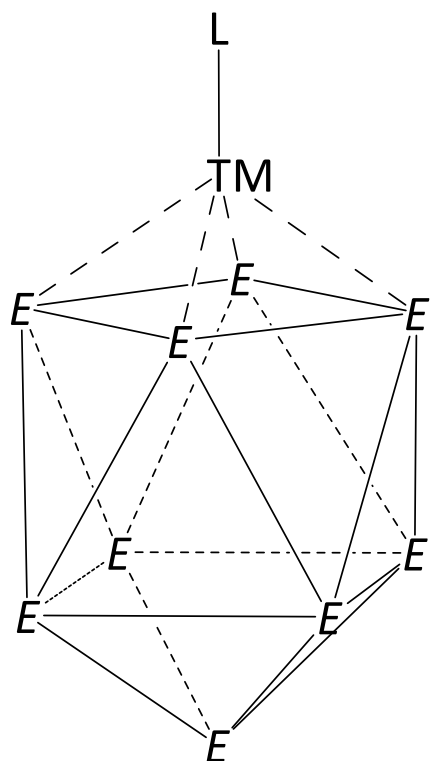


Figure 8: Schematic depiction of the typical bonding situation of a bare $[E_9]$ unit with a transition metal (TM) and its ligand (L).

Table 3: Transition metal complexes of $[E_9]$ units ($E = \text{Si, Ge, Sn, Pb}$) attached on the open, basal face of the cluster.

$[E_9]$	TM-L
$E = \text{Si}$	$\text{Zn}(\text{C}_6\text{H}_5)^{-[175]}$
	$\text{Ni}(\text{CO})_2^{[176]}$
$E = \text{Ge}$	$\text{Zn}(\text{C}_6\text{H}_5)^{-[175]}$
	$\text{Zn-Zn-}[\text{Ge}_9]^{[132]}$
	$\text{Cu}(\text{PR}_3)^{3-} (\text{R} = i\text{Pr, Cy})^{[177]}$
	$\text{Au}_3-[\text{Ge}_9]^{[178]}$
	$[\text{M}(\text{CO})_5]_3 (\text{M} = \text{Cr, Mo, W})^{[179]}$
	$\text{Ni}(\text{CO})^{[180]}$
	$[\text{Pd}(\text{Ph})_3]^{[181]}$
$E = \text{Sn}$	$\text{Fe}(\text{CO})_3^{\text{a}[182]}$
	$\text{TiCp}_2(\text{NH}_3)^{[183]\text{b}}$
	$\text{Cr}(\text{CO})_3^{[184]}$
	$\text{Mo}(\text{CO})_3^{[185]}$
	$\text{W}(\text{CO})_3^{[185]}$
	$\text{Ir}(\text{COD})^{[186]}$
	$\text{Zn}(\text{C}_6\text{H}_5)^{-[175]}$
$E = \text{Pb}$	$\text{Mo}(\text{CO})_3^{[185]}$
	$\text{W}(\text{CO})_3^{[185]}$
	$\text{Zn}(\text{C}_6\text{H}_5)^{-[175]}$
	$\text{Cd-Cd-}[\text{Pb}_9]^{[132]}$

^a – in this case the clusters fragments and a $[\text{Ge}_8]$ fragment is coordinated with the transition metal complex. ^b – In this structure the $\text{TiCp}_2(\text{NH}_3)$ is bound η^1 to the $[\text{Sn}_9]$ unit.

However this is not a definitive rule and exceptions can be found. As mentioned before on a bare cluster without any preexisting substitutions the coordination most likely occurs on the open square face of the $[E_9]$ unit. A possible reason for this is the fact that it features the most open space of the cluster in C_{4v} symmetry. This structure motif can be seen in almost all the structures with bare $[E_9]$ units (Figure 8). Basically all reactions yielding these compounds utilize strong ligands, such as CO and $(C_6H_5)^-$, attached to the transition metal. This is done to be able to draw as much of the electron density away from the transition metal as possible in order to have a stable bond to the cluster. With the exception of $[(Ni(CO))_2(Si_9)_2]$ and $[Ge_9]-Au_3-[Ge_9]$ all of the structures mentioned in Table 3 share the same motif of the transition metal coordinating on the uncapped square of the $[E_9]$ cluster. With the dimeric $[Si_9]$ species, the coordination is still on the square but it is only a η^2 instead of a η^4 binding situation.

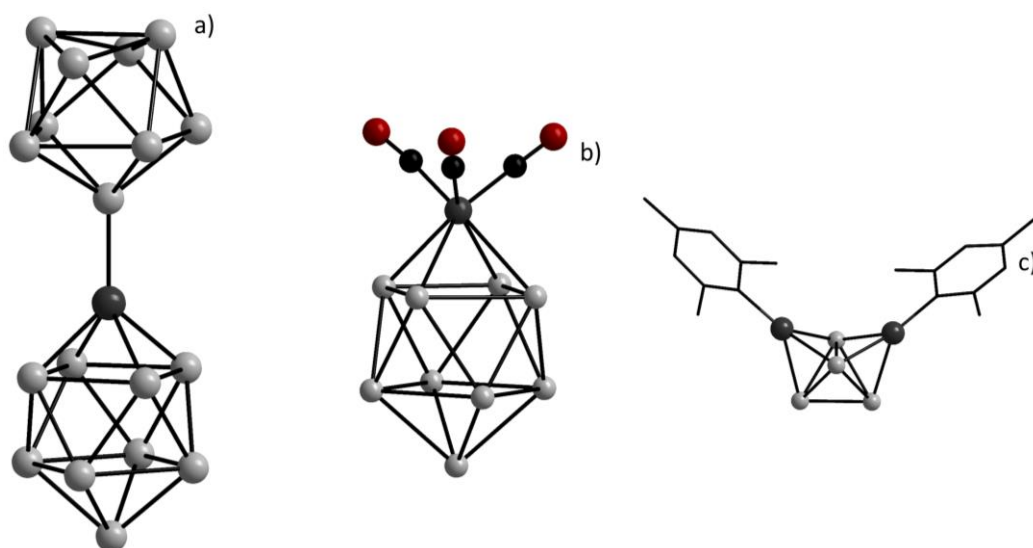


Figure 9: Bare $[E_9]$ and $[E_4]$ cluster substituted with transition metal complexes. a) $[Ge_9]-Cu-[Ge_9]^{7-}$ ^[177]; b) $[[Sn_9]-Cr(CO)_3]^{4-}$ ^[184]; c) $[[Si_4]-(CuMes)_2]^{4-}$ ^[187]

Because of its reduced solubility, the amount of coordinated $[E_4]$ clusters is far less than the larger $[E_9]$ cluster. Some structures exist with the bulk being of the lighter group 14 elements Si and Ge. Again the trend, of the lighter elements preferably crystalizing with the later transition metals, as

described before, is confirmed. There are two structures containing $[E_4]$ ($E = \text{Si}, \text{Ge}$)^[187-188] coordinated by CuMes in a η^3 fashion (Figure 9, c) and even mixed clusters $[(\text{Si}/\text{Ge})_4]-(\text{CuMes})_2$.^[189-190]

Another mixed compound containing a tetrahedron is found as $[\text{Cd}_3(\text{Ge}_3\text{P})_3]_3^{3-}$.^[191] Further examples of tetrahedral can be found $[\text{Ge}_4]-(^t\text{Bu}_3\text{Si})_4$ as early as 1996.^[192] Examples in solid state exist as well with infinite $-\text{[Au-(Ge}_4)]-$ chains in M_3AuGe_4 ($\text{M} = \text{K}, \text{Rb}, \text{Cs}$)^[193], dimeric $[(\text{Ge}_4)-\text{Zn}-(\text{Ge}_4)]$ in $\text{M}_{14}\text{ZnGe}_{16}$ ($\text{M} = \text{K}, \text{Rb}$)^[188] and $-\text{[Cd-(Pb}_4)]-$ oligomers in $\text{K}_6\text{Pb}_8\text{Cd}$.^[194] Beside the coordination to bare clusters there is also the possibility of using already substituted clusters and reacting them with transition metal complexes. For this the most used template is the aforementioned trisubstituted $[E_9\text{R}_3]^-$ unit. Prime candidate are the $[\text{Ge}_9[\text{Si}(\text{SiMe}_3)_3]_3]^-$ anion and variations of it. These variations include different ligands or even $[\text{Sn}_9]$ as a central unit. With three ligands already in place this square is blocked by the steric requirements of the ligands (Figure 10, a). With the threefold ligand coordination the symmetry changes from C_{4v} towards D_{3h} thus opening the top and bottom face of the trigonal prism of the cluster for coordination (Figure 10, b).

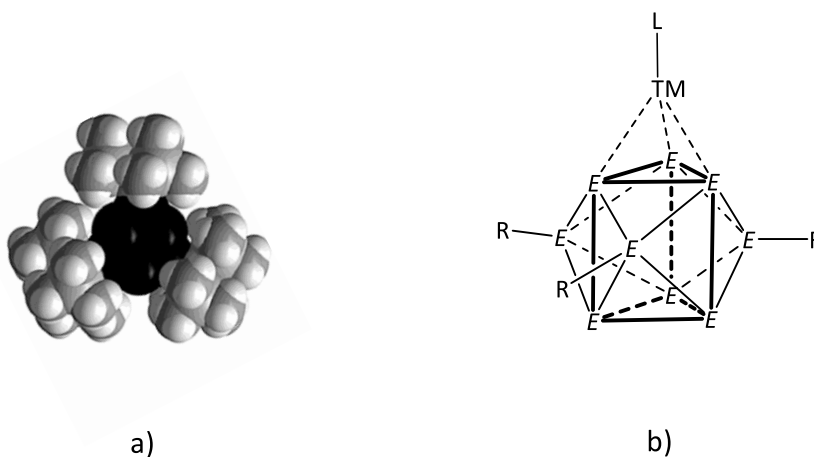


Figure 10: Possible coordination sites of substituted $[E_9]$ units. a) Space filling model of the $[\text{Ge}_9[\text{Si}(\text{SiMe}_3)_3]_3]^-$ anion showing the steric requirements of the ligands, Ge – black, silyl groups – grey; b) Ideal structure motif of a $[E_9\text{R}_3]^-$ with the transition metal (TM) and its ligand (L) bonded in η^3 mode.

This is necessary because steric ligands are arranged in equatorial positions and thus the transition metal ligand has to coordinate in an axial fashion. With respect to this the coordination of one cluster to one transition metal complex as well as the binding of multiple units of the aforementioned motif together are observed. Structures of the first category, singly substituted cluster units with one transition metal complex attached, can be found in Table 4. Several different types of multiple coordination between the singly substituted unit exist, the first being a dimerization which can be interpreted as the singly substituted clusters situation (Figure 10, b) where L is another substituted cluster unit $[E_9R_3]$ (Table 4). Two structure components exhibiting a somewhat inverted situation are known, at first two transition metal complexes coordinating to one cluster unit $[(dppe)Ni]_2-(Ge_9[Si(SiMe_3)_3]_3)^+$.^[195] Secondly a structure being a dimer of $[E_9R_2]$ -TM-L linked together by another two TM-L (TM = Cu; L = $-P(iPr)_3$) units with $[Cu-P(iPr)_3]_4[Ge_9(SiPh_3)_2]_2$.^[196] Several oligomers exist as well, which can be described as basic singly coordinated cluster situation being a monomer unit which is bonded together several times.

Table 4: Zintl clusters with exo-bonded transition metal complexes.

<i>E</i> = Ge		
	R = Si(SiMe ₃) ₃	R = Si(<i>i</i> Pr) ₃ ^[197] ; Si(<i>i</i> Bu) ₃ ^[198]
[<i>E</i> ₉ R ₃]-L	TiCp ₂ (MeCN) ^[199]	
	–TM–(NHC ^{Dipp}) (TM = Cu, Au) ^[200]	
	FeCp(CO) ₂ ^[201]	–Cu(NHC ^{Dipp}) ^[197-198]
	–Ni(dppe) ^[195]	
	–ZnCp* ^[196]	
	–Cu–P(<i>i</i> Pr) ₃ ^[196]	
<i>E</i> = Ge		
	R = Si(SiMe ₃) ₃	R = Ge(SiMe ₃) ₃ /Si(SiMe ₃) ₃ = 1/2
[<i>E</i> ₉ R ₃]-L-[<i>E</i> ₉ R ₃]	Mn ^[195]	
	Pd ^[202]	Zn ^[205]
	Cu, ^[203] Ag, ^[200, 203] Au ^{[203]a}	
	Zn ^[196, 204] , Cd ^[204] , Hg ^{[204]b}	
<i>E</i> = Ge		<i>E</i> = Sn
	R = Si(SiMe ₃) ₃	R = Si(SiMe ₃) ₃
L ₁ -[<i>E</i> ₉ R ₃]-L ₂ -[<i>E</i> ₉ R ₃]- L ₃	L ₁ = ∅; L ₂ = Cu; L ₃ = Cu-PPh ₃ ^[202]	L ₁ = (SiMe ₃) ₃ SiAu; L ₂ = Au; L ₃ =
	L ₁ = (SiMe ₃) ₃ SiZn; L ₂ = Pt; L ₃ = ZnSi(SiMe ₃) ₃ ^[206]	AuSi(SiMe ₃) ₃ ^[207]

^a – a similar structure exists with R = Si(*i*Bu)₃^[198]; ^b – The same structure exists with R = [Si(SiMe₃)₂(SiPh₃)].^[208]

1.3.3. Endohedral *Zintl* clusters

Examining the change of a clusters exterior yielded an abundance of new structures, but an at least equal amount of time was used researching the possibilities of changing the inside of clusters. Usually a filled unit consists of the host shell and at least one guest atom, most frequently a transition metal. The smallest unit in the class of filled *Zintl* clusters is the $[E_9]$ cluster ($E = \text{Ge}, \text{Sn}, \text{Pb}$) while more configurations are possible like $[E_x]$ ($x = 10, 12, 16, 17, 18$).^[112, 120] Even larger units such as onion, or matryoshka, compounds are also known with them featuring multiple shells (Figure 11, d).

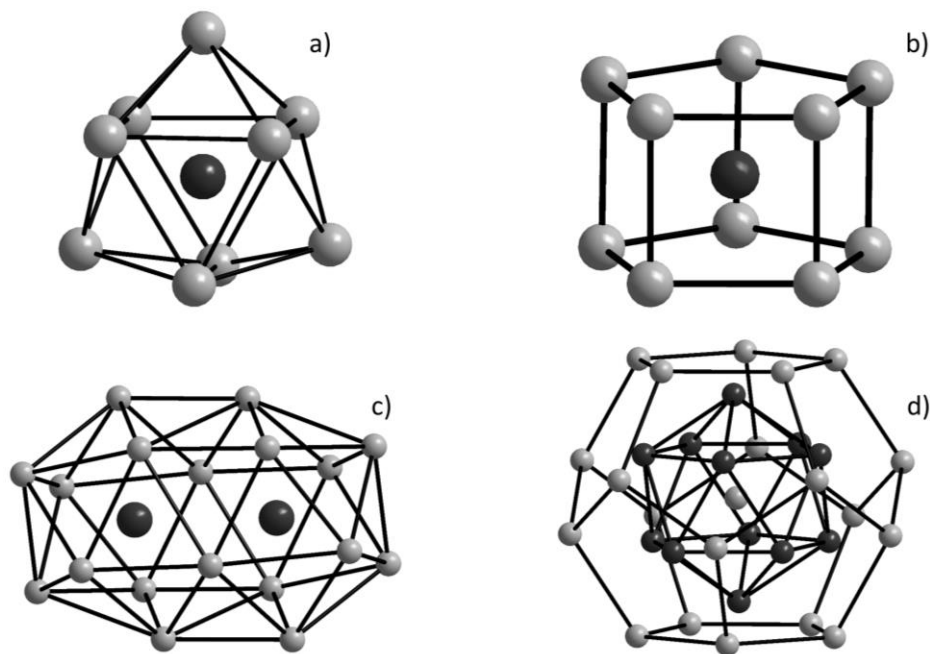


Figure 11: Frequently found structure motif of endohedral *Zintl* clusters. a) $[\text{Cu}@\text{Sn}_9]^{3-}$ ^[209]; b) $[\text{Co}@\text{Ge}_{10}]^{3-}$ ^[210]; $[\text{Pd}_2@\text{Sn}_{18}]^{4-}$ ^[211], $[\text{Sn}@\text{Cu}_{12}@\text{Sn}_{20}]^{12-}$ ^[212]. Grey – cage atoms (Ge or Sn – check sum formula); black – endohedral atoms (Co or Cu – check sum formula).

The smallest known endohedral *Zintl* cluster is the $[E_9]$ cluster (Figure 11, a), of which there are several examples of different group 14 element clusters filled with late transition metals (Table 5). Filling an $[E_9]$ cluster, i.e. formation of an endohedral cluster, is possible through two distinct

ways – firstly by solid state reaction resulting in a phase with the endohedral species already present, or secondly using preexisting *Zintl* phases and dissolving them together with an appropriate transition metal agent. The usual electronic configuration of such a cluster is $[(TM)^{n+/-}@E_9]^{4-}$, because the central atom is regarded as having d^{10} configuration which formally does not participate in any electron transfer to the cage. This leaves a broad range of possible cluster charges from highly negative of -6 in $[Ru@Sn_9]$ to a more moderate -3 in $[Cu@Sn_9]$ ^[209]. Possible center metals range from group 8 to group 11 but no clear trend of symmetry change, being either C_{4v} or D_{3h} , can be attributed to overall cluster charge or transition metal ion size in the known structures. Some examples like $[Ni@Sn_9]^{4-}$ and $[Co@Sn_9]^{5-}$ show different symmetries while retaining the same basic structure^[213] and depending on reaction properties^[214] suggesting that the central atoms are not the only symmetry-directing factor for the $[E_9]$ unit.

Table 5: List of endohedral and structurally characterized $[TM@E_9]^{n-}$ units crystallized from solution and displayed with the ideal charge as for a d^{10} configuration of the transition metal.

	$E = Ge$	$E = Sn$	$E = Pb$
$[TM@E_9]^{n-}$		$[Ru@Sn_9]^{6-c}$	
		$[Co@Sn_9]^{4.68-[216]a}$	
	$[Co@Ge_9]^{5-c}$	$[Co@Sn_9]^{4.79-[217]a}$	$[Cu@Pb_9]^{3-[209]}$
	$[Ni@Ge_9]^{3-[215]}$	$[Ni@Sn_9]^{4-[213-214, 218]}$	
		$[Pt@Sn_9]^{3-[219]b}$	
		$[Cu@Sn_9]^{3-[209]}$	

^a – Ideal charge of a $[Co@Sn_9]$ cluster would be -5 but due to only partially occupied Co position the real charge is diminished. The occupancy in the solid state phase can be considered full for both $[Co@Sn_9]^{5-}$ and $[Ni@Sn_9]^{4-}$.^[213] ^b – A proton is bound to the platinum included in the cluster which results in the charge of -3, whereas the ideal charge would -4. Also the structure of this cluster is characterized by NMR techniques rather than single crystal diffraction. ^c – this cluster is discussed in this work.

These endohedral $[E_9]$ units can be found bare or with additional ligands on the outside of the cluster. A special case is $[Sn_9]$ which has the most characterized bare and substituted cluster, including a protonated species^[219]. This may be due to the fact that tin is located in the fifth period of the periodic system which means it forms cluster which are large and stable enough to form such endohedral compounds. Germanium, being situated one period above, seems to be too small to host larger ions inside while lead may be less suitable due to its generally unstable nature in solution. $[Co@Sn_9]$ is especially interesting because it is the first endohedral species used a reactant for further syntheses, resulting in ternary functionalized species like $[Co@Sn_9NiCO]^{3-}$ or $[Co@Sn_9AuPh]^{3-}$ ^[220]. This opens up new possibilities for research in this field. $[Ge_9]$ and $[Pb_9]$ only feature two and one filled species respectively while to date no filled $[Si_9]$ species has been found.

Table 6: Bare and substituted, structurally characterized $[TM@E_{10}]^{n-}$ clusters.

$[TM@E_{10}]^{n-}$	$E = Ge$	$E = Sn$	$E = Pb$
Transition metals		$[Fe@Sn_{10}]^{3-}$ ^[222]	
	$[Co@Ge_{10}]^{3-}$ ^[210]	$[Rh@Sn_{10}]^{3-}$ ^[223]	$[Ni@Pb_{10}]^{2-}$
	$[Fe@Ge_{10}]^{3-}$ ^[221]	$[Ni@In_{10}]^{10-}$ ^{[224]a}	[225-227]
		$[Zn@In_{10}]^{8-}$ ^{[224]a}	
R- $[TM@E_{10}]^{n-}$		$[Ni@Sn_9Ti]^{3-}$ ^[214]	
	$[Ni@(Ge_9Ni-CCPh)]^{3-}$ ^[180]	$[Pd@(Sn_9Sn-Cy_3)]^{3-}$ ^[229]	
	$[Ni@(Ge_9Ni-CO)]^{2-}$ ^[180, 228]	$[Pd@(Sn_9Pd-SnCy_3)]^{3-}$ ^[229]	\emptyset
	$[Ni@(Ge_9Pd-PPh_3)]^{2-}$ ^[181]	$[Pt@(Sn_9Pt-PCy_3)]^{2-}$ ^[230]	
	$[Ni@(Ge_9Ni-PPh_3)]^{2-}$ ^[228]	$[Ni@(Sn_9Ni-CO)]^{3-}$ ^[230]	

^a – $[E_{10}]$ units from solid state phases.

The next larger endohedral *Zintl* unit is $[E_{10}]$. Where the general shape of an $[E_9]$ unit stays more or less the same, only slight changes occurring during the change from C_{4v} to D_{3h} , the conformation of an $[E_{10}]$ unit changes considerably depending on which ion is encapsulated. The two most prominent shapes are a pentagonal prism^[210, 221] (ideal symmetry D_{5h}) (Figure 11, b) and

a bicapped, square antiprism^[214, 224-225] (ideal symmetry D_{4d}). Other symmetries, found in reported clusters, include a tetracapped trigonal prism^[180, 224] (ideal symmetry C_{3v}), pentagonal antiprism (ideal symmetry D_{5v}) and a monocapped, square antiprism where the middle square is expanded by one atom^[222] (no ideal symmetry). Many theoretical studies have been conducted concerning the best symmetry for all $[TM@E_{10}]$ units where a promising candidate might be D_{5h} but different factors like inclusion element size and number of metal d orbital back bonding^[222] suggest a more complex issue. Experimental data corroborates this fact by showing how many of the clusters crystallize differently. To date no reliable formation mechanism has been found for any of the cluster anions obtained from solution based syntheses. Speculations range from the combination of two $[E_5]$ units and a Co^+ ion to redox reactions between $[E_9]$ clusters.^[210]

Further increase of the cage size results in a filled $[E_{12}]$ units which can also adapt a substantial amount of different cluster symmetries. Reported clusters show that the most obvious is the icosahedron^[186, 226, 231] (ideal symmetry I_h) but shapes like a pentagonal prism with an added dumbbell^[116, 232] (pseudo- D_{2d}) and a tetracapped, quadrangle prism (ideal symmetry D_{2h}) are possible^[233].

Table 7: Bare $[TM@E_{12}]^{n-}$ units from solution and in solid state phases.

$[TM@E_{12}]^{n-}$	$E = Ge$	$E = Sn$	$E = Pb$
Transition metals		$[Rh@Sn_{12}]^{3- [223]}$	$[Mn@Pb_{12}]^{3- [233]}$
	$[Ru@Ge_{12}]^{3- [232]}$	$[Ir@Sn_{12}]^{3- [186]}$	$[Rh@Pb_{12}]^{3- [236]}$
	$[Li@Ge_{12}]^{7- [234]a}$	$[Ca@Sn_{12}]^{12- [235]a}$	$[Pt@Pb_{12}]^{2- [226-227, 231]}$
		$[Sr@Sn_{12}]^{12- [235]a}$	$[Pd@Pb_{12}]^{2- [226]}$
			$[Ni@Pb_{12}]^{2- [226-227]}$

^a – $[E_{12}]$ units from solid state phases.

This category of clusters shows a trend of only the two heaviest homologues of the group 14 elements being favorable for an $[E_{12}]$ with only one $[Ge_{12}]$ unit existing in $[Ru@Ge_{12}]^{3-}$. Some

theoretical studies have been conducted suggesting some stable $[E_{12}]$ units with lighter elements like Ge^[237-238] and even Si^[238-239] but such species have yet to be discovered. The heavier congener have not been left out of these theoretical studies with possible noble gas^[240] or rare earth inclusions^[241], the viability of which can be questionable. Most characterized compounds found from solution have been synthesized using *Zintl* phases as precursors and a transition metal agent but as before with $[E_{10}]$ units a formation mechanism is hard to formulate. A possible mechanism comes from Fässler *et al.* with an a coordination of the $[Sn_9]^{4-}$ ion with Ir(COD) (COD = cyclooctadiene) with subsequent oxidation through DPPE (DPPE = 1,2-Bis(diphenylphosphino)ethan) and heat to yield $[Ir@Sn_{12}]^{3-}$. The oxidation through DPPE has been explained through NMR studies before and after the reaction.^[186] This shows a possible path of how such units as the $[E_{12}]$ can form in solution but an exact mechanism of how an $[E_9]$ unit is increased in size to an $[E_{12}]$ has yet to be found. The next larger group of endohedral cluster can be summarized as the only differ in size by one atom between themselves – $[E_{16}]$, $[E_{17}]$ and $[E_{18}]$. All of these compounds are found from solution by use of preexisting phases dissolved with transition metal agents as before. These clusters are big enough to host more than one transition metal each consisting of the cage and two guest atoms. All of them share a common structure motif of being more elongated and cigar-shaped as opposed to the mostly spherical structure of smaller units. This is to accommodate the increased number of included atoms and give them sufficient space (Figure 11, c). There is only one example of $[E_{16}]$ with $[Co_2@Ge_{16}]^{4-}$ ^[242] which was first analyzed using ESI-MS.^[243] As for $[E_{17}]$ two distinct conformations exist: One consisting of two $[E_9]$ units joined on one vertex atom, the other being the same shape as the $[E_{18}]$ unit depicted in Figure 11. $[Ni_2@Ge_{17}]^{4-}$ (A structure found by Christoph Wallach, M. Sc., Chair of Inorganic Chemistry with Focus on Novel Materials), $[Co_2@Ge_{17}]^{6-}$ (This structure is discussed in this work), $[Ni_2@Sn_{17}]^{4-}$ ^[244], $[Co_2@Sn_{17}]^{5-}$ ^[216-217] can be assigned to the first conformation while $[Pt_2@Sn_{17}]^{2-}$ ^[219] looks like the latter. Three examples are known for $[E_{18}]$ with $[Pd_2@Ge_{18}]^{4-}$ ^[245], $[Ni-Ni@Ge_{18}]^{4-}$ ^[215] and $[Pd_2@Sn_{18}]^{4-}$ ^[211, 246]. These examples exhibit the same motif of single large cavity encompassing two, or three, metal atoms. While only one example of a filled $[E_{16}]$ unit exists numerous theoretical studies are conducted^[243, 247-248] trying to pave the way to more of these compounds.

Close resemblances exist between these cluster structures even with a differing number of cluster atoms. $[\text{Ni}_2@\text{Sn}_{17}]^{4-}$ is similar to $[(\text{Ni-Ni-Ni})@(\text{Ge}_9)_2]^{4-}$ ^[215] whereas both have cluster units joined on one vertex atom. This is also the only example with multiple small cavities instead of one larger one. Both $[E_{18}]$ units mentioned share the same structure motif of one big cavity including two guest atoms. Here as well a close similarity to $[(\text{Ni-Ni-Ni})@(\text{Ge}_9)_2]^{4-}$ ^[215] can be found by removing the middle Ni atom and joining both $[\text{Ge}_9]$ shells together the $[E_{18}]$ structure can be approximated. One structure worth mentioning that defies classification in the aforementioned groups is $[\text{Rh}_3@\text{Sn}_{24}]^{5-}$ by Sun *et al.*^[223] It can best be described by three $[\text{Rh}@\text{Sn}_{10}]^{3-}$ units joined via their three bottom edges.

Table 8: Collection of $[E_{16}]$, $[E_{17}]$ and $[E_{18}]$ crystallized and characterized from solid state phases and solution.

	$E = \text{Ge}$	$E = \text{Sn}$
$[E_{16}]$	$[\text{Co}_2@\text{Ge}_{16}]^{4-}$ ^[242-243]	\emptyset
		$[\text{Co}_2@\text{Sn}_{17}]^{5-}$ ^[216-217]
$[E_{17}]$	$[\text{Co}_2@\text{Ge}_{17}]^{6-a}$	$[\text{Rh}_2@\text{Sn}_{17}]^{6-}$ ^[223]
	$[\text{Ni}_2@\text{Ge}_{17}]^{4-b}$	$[\text{Ni}_2@\text{Sn}_{17}]^{4-}$ ^[244]
		$[\text{Pt}_2@\text{Sn}_{17}]^{2-}$ ^[219]
$[E_{18}]$	$[\text{Pd}_2@\text{Ge}_{18}]^{4-}$ ^[245]	$[\text{Pd}_2@\text{Sn}_{18}]^{4-}$ ^[211, 246]
	$[\text{Ni-Ni-Ni}@\text{Ge}_{18}]^{4-}$ ^[215]	$([\text{Ni}@\text{Sn}_9]-\text{In}-[\text{Ni}@\text{Sn}_9])^{5-}$ ^[249]

^a – this cluster is discussed in this thesis in section 4.3.6. ^b - This cluster is examined by Christoph Wallach, M. Sc., Chair of Inorganic Chemistry with Focus on Novel Materials.

The largest clusters considered to be endohedral clusters show an interesting characteristic – they consist of multiple layers of shells. A common structure motif consists of a single atom inside an icosahedron which in turn is encapsulated in a pentagonal dodecahedron (Figure 11, d) – $[\text{X}@\text{Y}_{12}@\text{X}_{20}]$ ($\text{X} = \text{As}$ ^[250], Sb ^[251-252], Sn ^[212]; $\text{Y} = \text{Ni}$ ^[250], Cu ^[212], Pd ^[251-252]). Structures containing this

motif are found from solid state syntheses^[212, 253] as well as from solution^[250-252]. Solid state compounds formally have a much higher charge per onion structure of around -20 while compounds formed in solution usually carry a charge of -3 or -4. The high charge of the solid state compounds prevents them from being dissolved and crystallized, or used as reactants in further syntheses, which can be done using related fullerenes. When interpreting the spherical $[\text{Sn}@\text{Cu}_{12}@\text{Sn}_{20}]^{12-}$ ion as a zero dimensional dot, the compound $\text{Na}_{2.8}\text{Cu}_5\text{Sn}_{5.6}$ can be described as infinite 1D tubes consisting of $[\text{Sn}_{0.6}@\text{Cu}_5@\text{Sn}_5]$.^[254] In a string of unconnected Sn atoms lie inside a tube of antiprism like pentagonal rings which in turn is inside a larger tube consisting of Sn atoms. This outside tube lies in a star shape around and is connected with the middle Cu structure.

Group 15 elements also show tendencies to form endohedral clusters under the right circumstances, as shown by structures like $[\text{Sb}@\text{Pd}_{12}@\text{Sb}_{20}]^{12-}$. These pnictogen clusters also show a large amount of possible structural motifs which differs greatly from the tetrel species (Figure 12).

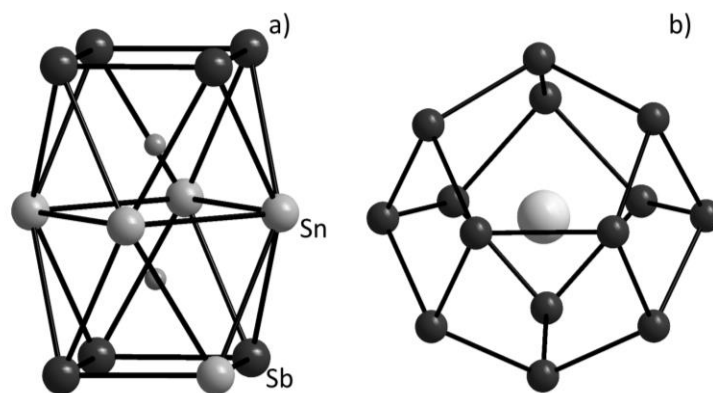


Figure 12: Pnictogen/tetrel endohedral clusters. a) $[\text{Co}_2@\text{Sn}_5\text{Sb}_7]^{3-}$ ^[255]; b) $[\text{Eu}@\text{Sn}_6\text{Bi}_8]^{4-}$.^[256]

Tetrel and pnictogen elements readily form endohedral clusters together where both elements make up the host shell with different transition metals as guests. It is to be noted that because of their closeness in the periodic table some mixtures of elements like for example Sn and Sb are hard to differentiate using crystallographic methods applying X-ray radiation. Additional

analytical methods like EDX or ESI-MS are required in these cases.^[255] Mixed host clusters include such structures as the triple, square antiprism $[\text{Co}_2@\text{Sn}_5\text{Sb}_7]^{3-}$ or the fullerene-type anion $[\text{Eu}@\text{Sn}_6\text{Bi}_8]^{4-}$. The first structure the assignment of atoms is clearly made in the structure where the latter only has mixed positions throughout the shell. A particular interesting structure is $[\text{Ln}@\text{Sb}_{12}]^{3-}$ (Ln = La, Y, Ho, Er, Lu) - it consists of three $[\text{Sb}_4]$ rings connected to form the cluster shell around different elements. The same structure motif can be found in $[\text{U}@\text{Bi}_{12}]^{3-}$ ^[257] the only difference being that the $[\text{Sb}_4]$ units are almost flat whereas the $[\text{Bi}_4]$ units are slightly bent. Further uranium filled cluster are also known and share similar structures to Figure 11 b) and c).^[257] This structure motif can also be found in $[\text{Pd}_3@\text{Sn}_8\text{Bi}_6]^{4-}$ ^[258]. The only difference being the open space on top and bottom of the structure, if the $[\text{Pn}_4]$ units are seen as equatorial, are now capped by one atom each. Interestingly these group 15 and group 15 and 14 mix clusters show a tendency to complexate heavier elements than the pure group 14 clusters.

1.3.4. Expansion of $[E_9]$ cluster units

The previous chapter deals with substituting the outside and filling the inside of different sized clusters and chapter 1.3.1 detailed that cluster units can condensate to form larger oligo- and polymers. Using the right reaction conditions clusters can also expand to form much larger units than the ones present in the starting materials.

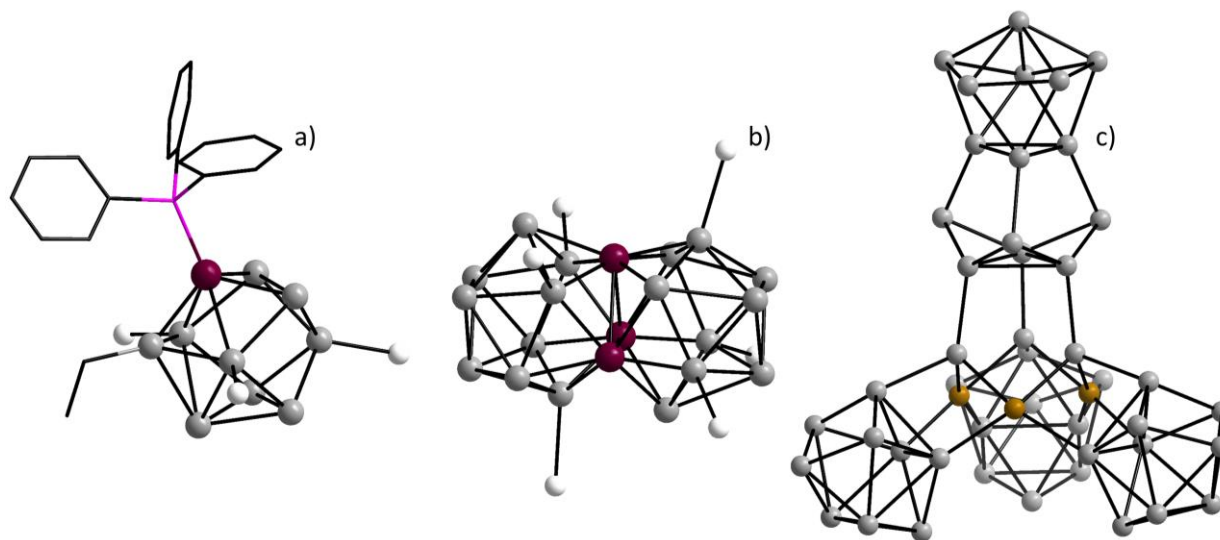


Figure 13: Examples of cluster expansion from K_4Ge_9 and different transition metal agents. a) $[(Ge_9Pd-PCy_3)(Si(SiMe_3)_3)_3Et]^{259}$; b) $[Ge_{18}Pd_3(Sn(iPr)_3)_6]^{2-260}$; c) $[Au_3Ge_{45}]^{9-261}$; $SiMe_3$ and iPr groups omitted for clarity; pink – phosphorus; purple – palladium; yellow – gold; grey – germanium; white – Si or Sn (check sum formula).

Some of these expanded cluster can be seen in Table 6 in chapter 1.3.3. Similar to endohedral clusters, these expansion reactions can be achieved through two different ways – top down or bottom up. Bottom up refers to a synthesis through simple building blocks to directly yield the desired compound while in top down some more complex reactants are synthesized first and then used in a final step. In the case of cluster expansion top down means using *Zintl* phases of the composition K_4E_9 ($E = Ge, Sn$) Examples of cluster expansion using this method can be seen in such structures as $[(Ge_9Pd-PCy_3)(Si(SiMe_3)_3)_3Et]^{259}$ – a neutral species that incorporated a palladium complex into the existing substituted cluster unit. A similar $[Ge_8(Mo(CO)_3)_2]^{4-}$ cluster is

known.^[262] A dimer of substituted $[\text{Ge}_9]$ cluster is reported without any linking agents as $\text{Ge}_{18}[\text{Si}(\text{SiMe}_3)_3]_6$.^[263] Larger “double” units can be found as the staggered^[260] and eclipsed^[264] species of $[\text{Ge}_{18}\text{Pd}_3(\text{E}(\text{iPr})_3)_6]^{2-}$ ($\text{E} = \text{Si}, \text{Sn}$) showing that dimerization is possible. A similar sort of dimerization can be found as a crystal structure in $[\text{Sn}_{14}\text{Ni}(\text{CO})]^{4-}$ consisting of two triangle-joined $[\text{Sn}_9]$ units while the monomer ion $[\text{Sn}_9\text{Ni}_2\text{CO}]^{2-}$ is found in ESI-MS measurements.^[265] An extremely large expansion can be found in $[\text{Au}_3\text{Ge}_{45}]^{9-}$ where four $[\text{Ge}_9]$ units and three gold atoms form a tower like structure.^[261]

The bottom up approach in this context is using E halides ($\text{E} = \text{Ge}, \text{Sn}$) and different transition metal complexes. This method’s yield is similar to the first synthesis of the $[\text{Ge}_9[\text{Si}(\text{SiMe}_3)_3]_3]^{-}$ ^[140] anion and leads to such structures as $(\text{Sn}_{10}\text{Si}(\text{SiMe}_3)[\text{Si}(\text{SiMe}_3)_3]_4)^{2-}$ ^[266], which is very similar to $[\text{Sn}_{10}[\text{Si}(\text{SiMe}_3)_3]_4]^{2-}$,^[267] or $\text{Ge}_{14}\text{Br}_8(\text{PEt}_3)_4$.^[268] With these techniques and with the $[\text{Ge}_9[\text{Si}(\text{SiMe}_3)_3]_3]^{-}$ ion as a base building block even transition metal “doped” structures can be achieved with $([\text{Si}(\text{SiMe}_3)_3]_3\text{Ge}_9\text{-TM}-(\text{CO})_3)^{-}$ ($\text{TM} = \text{Cr}, \text{Mo}, \text{W}$).^[269]

1.3.5. Applications of *Zintl* phases

As shown *Zintl* phases provide an abundant research field for the last three decades but they are still limited in their application. Only a few examples are known where these phases are used in some applied capacity.

A first step towards the goal of using *Zintl* phases in application is that K_4Ge_9 can serve as precursors in the fabrication of thin films. In these they serve as the germanium source for inverse opal structures. With the ability of germanium to form solid solution with its lighter and heavier congeners these opal structures can be tuned for composition. These inverse opal structures can be used in solar cells or batteries as the anode material. The structure serves to alleviate the extreme volume increase and decrease^[270] tetrels undergo when being used in such application.^[27-28] These volumetric changes plague batteries which feature pure silicon or germanium as an anode. When lithiated the tetrel is converted into Li_{15}E_4 ^[271] ($\text{E} = \text{Si}$,^[272] Ge ^[273]) which is not the phase with the highest lithium content (that would be Li_{22}E_5 ($\text{E} = \text{Si}$,^[274] Ge ^[275])) seems to be the most stable in the context of a battery. It should be noted that $\text{Li}_{22}\text{Si}_5$ could be

misinterpreted and is in actuality $\text{Li}_{17}\text{Si}_4$.^[276-277] Similarly to *Zintl* phases an electron transfer between lithium and the poly anionic clusters present in this class of $\text{Li}/E/P$ ($E = \text{Si}$,^[278-281] Ge ,^[282] Sn ^[283]) compounds takes place. While not strictly *Zintl* phases, because of the non-stoichiometric nature, it is worth noting these *Zintl* “adjacent” phases.

These phases show the potential to be used in batteries – either as a composite cathode material or solid state electrolyte. Besides the application in batteries the $[\text{Ge}_9]$ cluster can also be used in photoluminescence or photo catalysis.^[10] This is mainly in the form of mesoporous germanium which shows improved properties with regards to band gaps.^[284-287] The $[\text{Ge}_9]$ cluster is used in the synthesis of the mesoporous germanium via a self-assembly process which enables the tuning of pore diameters and thus the band gap. A more niche application of *Zintl* phases is the usage as a precursor for Si or Ge nanoparticles. The precursors often consist of *Zintl* phases of the composition A_4E_4 and $A_{12}E_{17}$ ($A = \text{Na}, \text{K}$; $E = \text{Si}$,^[288-289] Ge ^[288, 290]) – both featuring the $[E_4]$ cluster. Aside from forming the particles themselves it also possible to coat nanoparticles with a desired tetrel element – germanium on top of silicon nanoparticle precursors. This can be done using $[\text{Ge}_9]$ clusters functionalized with ethylene groups which can be attached to the hydrogen terminated Si particles.^[291]

While usage in solar cells is yet to be seen the phases do show great potential in batteries where they show great capacity, capacity retention and intrinsic rate capabilities.^[26]

1.3.6. New tetrel element modifications from *Zintl* phases

Another one of the limited applications of *Zintl* phases is the possibility of synthesizing new tetrel element modifications. This was shown first in 1982 by Nesper *et al.* using the *Zintl* phase $\text{Li}_7\text{Ge}_{12}$ as a starting material.^[292] Using protic solvents and mild oxidation with subsequent heating two new germanium allotropes can be isolated – *allo*-Ge and 4H-Ge respectively. Using benzophenone to oxidize the germanium the lithium is removed from the 2D networks contained in $\text{Li}_7\text{Ge}_{12}$ which in turn forms new bonds resulting in a 3D network, *allo*-Ge. Heating this newly formed network to 147 °C resulted in 4H-Ge which can be described as showing modified diamond structure with alternating chair- and boat-configuration instead of only chair (Figure 14).

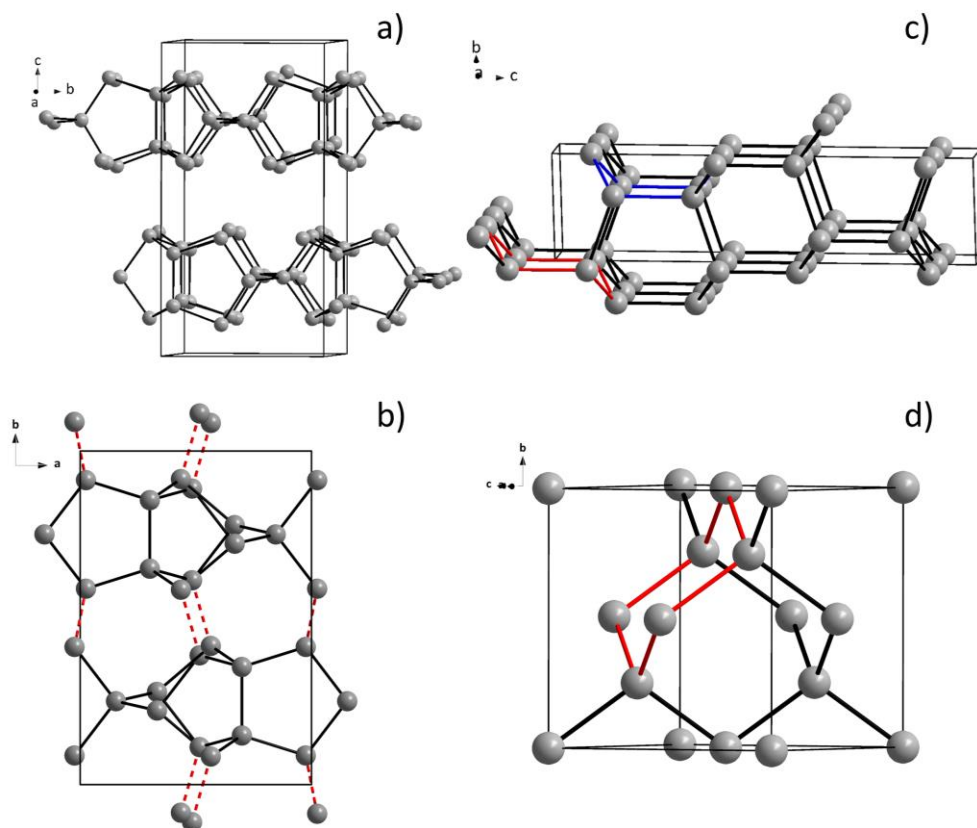


Figure 14: a) Extended unit cell of $\text{Li}_7\text{Ge}_{12}$; b) Connection between the 2D layers of $\text{Li}_7\text{Ge}_{12}$ during oxidation reaction forming *allo*-Ge;^[31] c) structure of 4H-Ge, highlighted in red – chair conformation, blue – boat configuration; d) structure of α -Ge, highlighted in red – exclusively present chair configuration.

Under the similar reaction conditions the lighter element silicon can be isolated in its new modification of *allo*-Si.^[293] While a multitude of follow up research was done on *allo*- and 4H-germanium during the last years, no reproduction of *allo*-Si is possible making the existence this new silicon modification questionable.^[294] Further work on possible new allotropes of silicon^[295-296] was done by Strobel *et al.* in the direction of clathrates.^[297-298] New syntheses paths are researched for *allo*-^[31] as well as 4H-germanium^[299] while the structure of both is reinvestigated.^[31, 299-302] *allo*-germanium is also investigated for its electrochemical properties as a anode material.^[303] A more recent demonstration of this phenomenon is the oxidation of $[\text{Ge}_9]$

Zintl clusters using ionic liquids resulting in a guest free germanium clathrate.^[42] While not explicitly a new modification of germanium, it consists only of germanium with no other elements being present and thus it is close to being a new allotrope. An additional allotrope of germanium was found recently in the form of Ge(oP32) through a similar oxidation using ionic liquids.^[304] Since $[\text{Ge}_9]^{4-}$ cluster prove to be able to form new allotropes in form of this clathrate the possibility of them also forming an allotrope that features the same nine-atomic unit is not so farfetched. This has been investigated using DFT methods and shown that it in theory it is possible to have 1D and 2D structures consisting of the $[\text{Ge}_9]$ unit.^[134] In addition to these DFT calculations some high-temperature and –pressure phases are suspected to also be a pathway towards new allotropes.^[305]

All of these reactions have mild removal of light alkali metal ions, i.e. Li and Na, in common, whether it is through mild oxidation agents, benzophenone or through ionic liquids. This common trait may be an indication that more reactions are possible to form new element modifications out of *Zintl* phases, especially $[\text{E}_9]$ ($\text{E} = \text{Si}, \text{Ge}, \text{Sn}, \text{Pb}$) clusters. While the species of $[\text{E}_9]$ cluster is well researched, as detailed in the previous chapters, only a handful of these clusters are known with Li^+ as their counter ion. The examples include $\text{Li}_4\text{E}_9 \cdot 17 \text{NH}_3$ ($\text{E} = \text{Sn}, \text{Pb}$)^[306] and $[\text{Li}(\text{thf})_4][\text{Ge}_9(\text{Si}(\text{SiMe}_3)_3)_3]$.^[140] In contrast a plethora of Li-E ($\text{E} = \text{Si}$,^[272, 274, 276, 294, 307-311] Ge ,^[273, 275, 312-318] Sn ,^[319-330] Pb ^[331-335]) phases are known

2. Motivation

Chemistry plays, today more than ever, an essential part of the future of energy generation and storage. This is nowhere more evident than in the application and research of tetrel elements compounds which have a solidified place in batteries, optoelectronics and solar cells. With the ability to fine tune the features of these materials, whether it be composition or structure, tetrel elements provide a great potential for even more and better materials.

One group of compounds consisting of tetrel elements and alkali metals are *Zintl* phases which, when dissolved in the appropriate solvent, can provide a plethora of polyanions for many reactions. The modification of structure and composition can serve as a way of insight of characteristics of compounds between bulk and molecules. Deltahedral, $[E_9]$ or $[E_4]$ ($E = \text{Si, Ge, Sn, Pb}$), *Zintl* clusters in particular already show the potential for an abundance of different reaction types, whether substitution or filling, because of the delocalized bonds throughout the whole unit.^[112, 115, 336] The variable structure which can easily rearrange between D_{3h} , with an ideal charge of -2, and C_{4v} , with an ideal charge of -4, cages and fast exchange of atomic positions because of bond fluctuations make the abundance of reactions possible.^[337] The $[E_9]$ units present themselves as electron-delocalized and electron-deficient systems with exceptional reactive properties, which range from condensation and substitution to expansion reactions. A particularly interesting property of *Zintl* phases is the possibility of the formation of element modifications through the removal of the cations present in the structures. This was first reported for $\text{Li}_7\text{Ge}_{12}$ in which case two new modifications of germanium – *allo*-Ge and 4H-Ge – were found. The first modification can be attained through mild oxidation in a protic solvent and subsequent heating creates the second one.^[292] The same reaction was realized for silicon shortly after^[293], however the viability of this reaction is still contested.^[294] These new germanium allotropes were investigated on their electrochemical^[303] and structural properties as well as possible new syntheses paths^[31, 299-300]. A more recent example is the formation of a guest free germanium clathrate from $[\text{Ge}_9]$ clusters and while not explicitly described as a new allotrope it has all the characteristics of one.^[42] The formation of this clathrate as well as theoretical studies^[134] suggest the possibility of a truly new modification of germanium made from $[\text{Ge}_9]$ units. With the

existence of $[E_9]$ ($E = \text{Si, Sn, Pb}$) units this might even be possible for the lighter and heavier congeners of the tetrel elements. The common denominators of both syntheses resulting in new germanium modifications are the mild oxidation of the used reactants which results in removal of light alkali metals, i.e. lithium and sodium. Whether it be using mild oxidation agents and protic solvents or ionic liquids the result is the formation of new bonds. These bonds are created in order to compensate the negative charge left by the absence of the removed cations thus creating new allotropes. The requirement for this oxidation is the presence of light alkali metals like lithium or sodium. These ions can be either used in the initial synthesis of the desired phase or be brought in retroactively using ion exchange.

The main part of this thesis is focused on the discovery of new silicon or germanium allotropes which feature the $[E_9]$ unit. In order to gain the desired phases the synthesis method mentioned prior is employed: removal of lithium ions and soft oxidation. The first step of this is the synthesis of solid state phases with lithium ions and $[E_9]$ units. Thus this work focuses on the development of new path ways to yield compounds consisting of *Zintl* clusters, mainly $[E_9]$ and $[E_4]$ ($E = \text{Si, Ge, Sn}$) or mixtures thereof, and lithium ions. Special consideration is given to phases containing Si and Ge clusters. The establishment of standard operating procedures regarding ionic exchange time, ratio of reactants and solvent compatibility is a focus.

With the focus of this work being on discovering new tetrel modifications featuring cluster units, an additional project is the synthesis of new compounds containing endohedral clusters. These clusters feature a cluster host with a transition metal guest which changes the charge of the clusters. The variable charge on the cluster is a viable option that can be integrated in the ion exchange studies as a way to gain new bimetallic structures rather than new element modifications. The endohedral phases are synthesized in solid state reactions, analyzed using PXRD and Raman and crystallized to analyze the new structures. After this bulk phase analysis is possible which opens the possibility of ion exchange experiments.

3. Scope and Outline

This thesis is divided into two major parts – the investigation of ion exchange to generate the reactants for the synthesis of new tetrel element allotropes and the syntheses and characterization of new solid state phases containing endohedral clusters.

First the stability of the mentioned *Zintl* phases in liquid ammonia, namely after evaporation, is studied to ensure that the phases are stable enough to be used in the experiments (Section 4.1).

The application of ion exchange agents on *Zintl* phases of the composition of $K_{12}Si_{17}$ and K_4E_9 ($E = Ge, Sn$) is detailed next. An overview of the ionic exchange technique is given as well as characterized structures synthesized using this technique (Section 4.2.1).

Then standard operating procedures are investigated in order to find the optimal solvents, reactant ratios and reaction times (Section 4.2.2).

With the parameters in place a proof of concept is conducted using a test environment using the $[Ge_9[Si(SiMe_3)_3]_3]^-$ ion, which has proven to be a dependable test medium (Section 4.2.3.1).

The application of the system on the phases $K_{12}Si_{17}$, K_4E_4 ($E = Si, Ge$) and K_4E_9 ($E = Ge, Sn$) is conducted (Section 4.2.3.2).

With several issues with the adaptation of the ion exchange from the test environment to the actual phases several stabilization techniques are discussed (4.2.4).

The unexpected development of germanium nanoparticles from a specific mixture is investigated in Section 4.2.5.

In the second part of the thesis the synthesis and characterization of new phases containing endohedral cluster is discussed. Especially clusters of the composition $[TM@E_9]^{n-}$ ($TM = Fe, Ru, Os, Co, Rh, Ir, Ni, Pd, Pt, Cu, Ag$; $E = Ge, Sn, Pb$; $n = 6, 5, 4, 3$) are of interest in this section. Their synthesis, characterization in the solid state phase as well as in solution are investigated.

Firstly a short overview of already known endohedral clusters of $[TM@E_9]^{n-}$ composition is given as well as the synthesis methods applied which can be divided in two major approaches – strictly solid state or through solution based methods (Section 4.3.1).

DFT enhanced Raman analytics are introduced in order to determine whether a solid phase contains endohedral cluster (Section 4.3.2). First a detailed study of known and new clusters, empty and filled, using this technique is given (Sections 4.3.2.1 - 4.3.2.2). Reported, endohedral clusters are synthesized and analyzed using the method detailed in the previous section (Section 4.3.2.2.2).

Newly synthesized endohedral clusters, like $[Co@Ge_9]^{5-}$, $[Ru@Sn_9]^{6-}$ and “[Rh@Sn₉]”, their symmetry and Raman behavior is studied and solution experiments are described in section 4.3.4. Further DFT enhanced Raman analysis of ternary solid state compounds can be found in section 4.3.5 while experiments on fragmentation of endohedral clusters, resulting in clusters like $[Co_2@Ge_{17}]^{6-}$, $[Co@Ge_{10}]^{3-}$ and $[Rh@Pb_{12}]^{3-}$, are described in section 4.3.6.

The syntheses trials of compounds containing endohedral clusters with lighter tetrel elements and late transition metals are discussed in section 4.3.7.

The structures of the clusters of $[Co@Ge_9]^{5-}$ and $[Ru@Sn_9]^{6-}$ are optimized using DFT methods and their charge distribution, MO situation and charge distribution are calculated in Section 4.3.8.

Lastly the substitution experiments, using main group as well as transition metal complexes, are discussed in Section 4.3.9 and a conclusion is given in Section 5.

The last section contains the experimental parameters (Section 6.1), analyses (Section 6.5), syntheses (Section 6.6), and crystallographic data (Section 7.4) as well as the appendix with spectra and diffractograms (Section 7.3).

4. Results and Discussion

4.1. Stability of $K_{12}Si_{17}$ and K_4Ge_9 in liquid ammonia

Before ion exchange experiments can be conducted, the stability of the *Zintl* phases $K_{12}Si_{17}$ and K_4Ge_9 towards liquid ammonia needs to be confirmed. These phases readily dissolve in liquid ammonia, but no information exists whether the phases decompose during solvent evaporation. In order to analyze the composition of the phases after solvation with liquid ammonia the phases are dissolved, filtered and the solvent is removed. The filtration process is described in more detail in section 6.3. The synthesis parameters of the binary phases can be found in section 6.6.1. Experimental details can be found in section 6.6.2.

Both the undissolved residue of the filtration (referred to as “residue” from this point on) as well as the solid product gained after the removal of liquid ammonia and drying *in vacuo* of the filtrate (referred to as “filtrate” from this point on) are analyzed using PXRD, Raman and DSC.^[43, 338] Raman and PXRD measurements are done before and after the DSC analysis. The filtrates are analyzed first and the residues second.

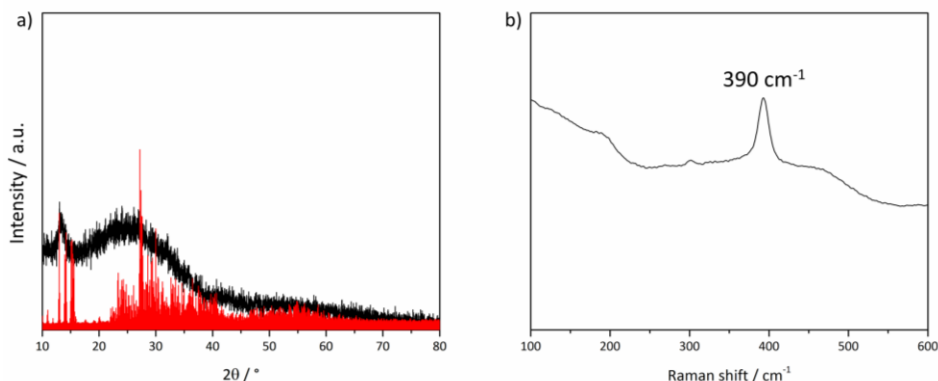


Figure 15: a) X-ray powder diffractogram measured (black) of filtrated $K_{12}Si_{17}$ and calculated (red) of $K_{12}Si_{17}$. The calculated diffractogram is based on single crystal data.^[48] The diffractogram is measured using Cu- $K\alpha_1$ radiation. b) Raman spectrum of filtrated $K_{12}Si_{17}$, after the removal of liquid ammonia, with all visible signals attributed to the $[Si_9]$ cluster in $K_{12}Si_{17}$ (Figure 72).^[48]

PXRD analysis of the filtrate shows the possibility that $K_{12}Si_{17}$ is still present however the signal to noise ratio makes it difficult to determine reliably. In the Raman spectrum the main signal of the $K_{12}Si_{17}$ phase, can be seen while no other signals are present (Figure 15; a spectrum of the reactant phase can be found in Figure 72 and in a publication of Dr. Lorenz Schieger^[173]). Together the analyses indicate the possibility that $K_{12}Si_{17}$ stays intact during the solvation, filtration and precipitation processes. When analyzing the sample using DSC a broad signal at 450 °C and a small signal around 570 °C can be found (Figure 139). Analysis of the sample after the DSC measurement shows the presence of elemental silicon in both the PXRD and Raman while the PXRD also shows the signals of $K_{12}Si_{17}$ and silicon (Figure 76). This indicates that $K_{12}Si_{17}$ decomposes during the heating process to 1000 °C. It is possible that the signals at 450 °C and 570 °C are a result of that decomposition. DSC analysis to lower temperatures like 500 °C may inhibit the decomposition. It is known that silicon can have side reactions with niobium,^[338] but the temperatures present are not high enough to facilitate this. When $K_{12}Si_{17}$ is extracted in en and annealed at 600 °C no signals of $K_{12}Si_{17}$ or silicon can be found in Raman spectroscopy.^[339] All known examinations point to the fact that $K_{12}Si_{17}$ decomposes during a heating process after solvation.

Analyzing the residue using PXRD and Raman show signals that can be attributed to $K_{12}Si_{17}$, although there is again a high signal to noise ratio in the PXRD (Figure 77). After the DSC analysis (Figure 140) PXRD shows a match of the calculated and measured diffractogram of $K_{12}Si_{17}$. The Raman shows only one signal which can be attributed to $K_{12}Si_{17}$ (Figure 78). In summary, $K_{12}Si_{17}$ shows increased amorphous behavior after the solvation process and remains stable in liquid ammonia but shows decomposition during heating to 1000 °C.

Analyzing the filtrate of K_4Ge_9 using PXRD and Raman spectroscopy the main signals of K_4Ge_9 can be observed (Figure 16). However the amorphous nature makes it difficult to safely determine the purity of the sample. Subsequent DSC measurements reveal no significant signals in the range between room temperature and 1000 °C (Figure 141). Analysis of the sample after the DSC measurement shows the presence of signals attributed to K_4Ge_9 in both PXRD and Raman (Figure 79). This proves the stability of K_4Ge_9 towards liquid ammonia after solvation.

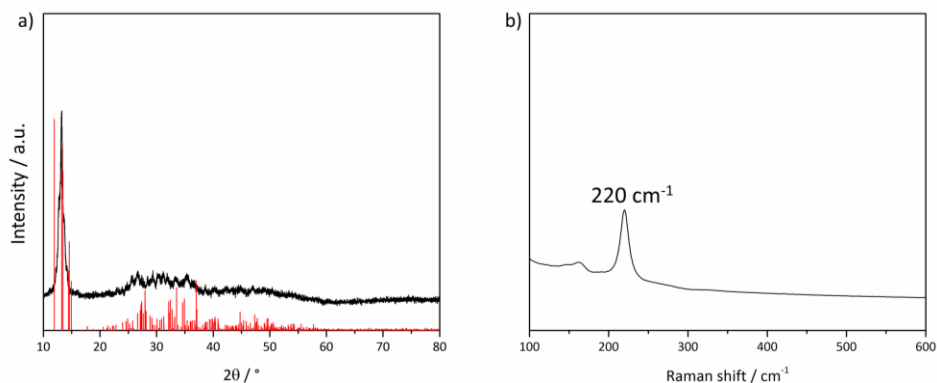


Figure 16: a) X-ray powder diffractogram measured (black) of filtrated K_4Ge_9 and calculated (red) of K_4Ge_9 . The calculated diffractogram is based on single crystal data.^[44] The diffractogram is measured using $Cu-K_{\alpha 1}$ radiation. b) Raman spectrum of filtrated K_4Ge_9 with all visible signals attributed to K_4Ge_9 .^[43]

The analysis of the residue shows an amorphous morphology, in both PXRD and Raman (Figure 80). This amorphous morphology remains after the DSC analysis (Figure 142, Figure 81). Analysis after the DSC shows an acceptable agreement of the signals with $K_{12}Ge_{17}$, which contains both $[Ge_4]^{4-}$ as well as $[Ge_9]^{4-}$ clusters (Figure 81). Since K_4Ge_9 shows no signs of any reactions or decomposition when heated to 1000 °C, the presence of $[Ge_4]^{4-}$ in the sample has to be a result of exposure to liquid ammonia in combination with the heating in the DSC.

In summary it can be said that both $K_{12}Si_{17}$ as well as K_4Ge_9 are stable after the solvation with liquid ammonia. This solvation results in very amorphous samples which can be made more crystalline by tempering. This tempering however can result in decomposition in the case of $K_{12}Si_{17}$. There is also a possibility of side reactions of K_4Ge_9 with liquid ammonia that result in $[Ge_4]^{4-}$ clusters.

4.2. Ion exchange on *Zintl* phases

The main goal of the experiments featured in this part of the thesis is to synthesize compounds containing lithium ions and isolated *Zintl* clusters, like $[E_9]$ and $[E_4]$ ($E = \text{Si, Ge, Sn}$). Theoretically this can be achieved through two different ways, either by bottom up synthesis of the phases using the desired tetrel elements and lithium or by lithiating preexisting phases containing heavier alkali metals and clusters. The problem with the first method is the fact that silicon or germanium tend to form networks^[314, 316, 340-341] or isolated, highly charged units, when Li^+ is present as a counter ion. Larger highly charged units as well as networks tend to be insoluble even in highly polar solvents like liquid ammonia. In addition none of the phases show the desired $[E_9]$ or $[E_4]$ clusters units. Since the presence of clusters is desirable in the context of this work the method of direct high temperature synthesis is dismissed. In order to gain the desired compounds, ion exchange is chosen as a method to introduce lithium ions to the isolated clusters (Figure 17). The syntheses of compounds containing isolated *Zintl* clusters are well researched so producing large quantities of reactants is possible.

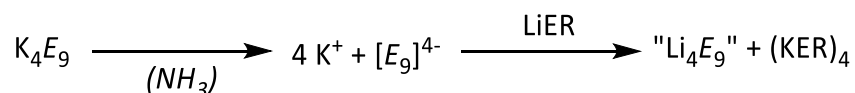


Figure 17: Hypothetical reaction pathway for lithiating $[E_9]$ ($E = \text{Ge, Sn}$) clusters using ion exchange resin (ER).

4.2.1. Theoretical background and relevant literature on ion exchange

Ion exchange experiments were conducted as early as 150 years ago when it was noticed that the composition of sulfates would change after being passed through soil.^[342-343] The first synthetic ion exchange resins are a polycondensate of phenol and formaldehyde, used as a cation exchanger, and a polyamine, used as an anion exchanger.^[344] Ion exchangers can be used in three distinct applications – substitution, separation and removal. Both anions as well as cations can be loaded on different polymer matrices for subsequent ion exchange in a multitude of solvents.^[345]

The principle of ion exchange is based on different factors such as affinity of ions toward the functional groups found on the polymer matrix, reaction equilibrium, polymer base, temperature and solvent. The affinity of ions towards the exchange resin can be explained by the HSAB concept – softer ions are more affine toward the resin.^[6] Reaction equilibria can be pushed to the product side by increasing the amount of reactants.

Table 9: Structural, chemical and physical characteristics of Amberlyst 15.^[346]

Amberlyst 15 (H ⁺)	
Matrix	Polystyrene-divinylbenzene
Functional groups	–(SO ₃) [–]
Structure	Insoluble, macroporous beads
Ion loading capacity	4.7 mmol/g
Working pH range	0-14
Maximum operating temperature	120 °C
Bead size	0.4 – 0.5 mm
Average pore diameter	300 Å
Surface area	53 m ²

A regularly used base matrix for ion exchange is polystyrene crosslinked with divinylbenzene (Figure 18, b). Linear polystyrene is made from styrene by either radical, cationic or anionic polymerization often using catalysts (Figure 18, a). The linear polymer is a clear moldable plastic

which is soluble in certain solvents, like toluene, and has a well-defined softening point. By cross linking the polymer with vinylbenzene the structure becomes rigid and insoluble. Amberlyst 15 is such a cross linked polystyrene polymer and thus useable in many different conventional solvents because of its insolubility. The basic structure of Amberlyst 15 is crosslinked vinylbenzene with a benzyl-sulfonate as a functional group (Figure 16 c).

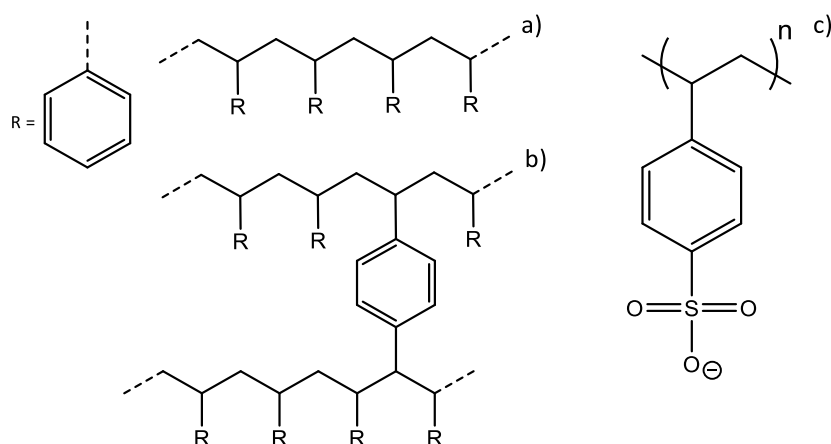


Figure 18: Schematic depiction of polystyrene a) linear and b) crosslinked. c) shows the functional group of Amberlyst 15.

Amberlyst 15 is usually found in the form of spherical beads formed by monomer droplets aggregating as micelles in the suspending medium, which generally is water. The polymer beads come in a size of about half a millimeter and can be used in a temperature range of up to 120 °C, where higher temperatures result in thermal decomposition of the polymer. The maximum capacity of Amberlyst 15 is 4.7 mmol per 1 g in its dry form. The polymer shows a good pH stability and can be used in extremely basic or acidic environments (Table 9). All of these characteristics make it a suitable candidate for ion exchange experiments in many different applications.

In 1967 Hume *et al.* proved ion exchange to be possible in liquid ammonia using Dowex 50W, which is a sulfonated polystyrene polymer, crosslinked by vinyl benzene just as Amyberlyt 15

is.^[347] After this discovery ozonides, because they readily dissolve in liquid ammonia, were used in conjunction with Amberlyst 15 in ion exchange experiments (Table 10).

Table 10: Novel compounds containing ozonides isolated from liquid ammonia using ion exchange through the means of Amberlyst 15 resin.

Starting reactant	Ion loaded on Amberlyst 15	Final composition
CsO ₃	Li ⁺	LiO ₃ ^[348]
	Na ⁺	NaO ₃ ^[349]
	Ba ²⁺	Cs ₂ Ba(O ₃) ₄ ^[350]
	[((C ₆ H ₅) ₃ P) ₂ N] ⁺	[((C ₆ H ₅) ₃ P) ₂ N]O ₃ ^[351]
	[(((CH ₃) ₂ N) ₃ PN) ₄ P] ⁺	[(((CH ₃) ₂ N) ₃ PN) ₄ P]O ₃ ^[351]
	[(((CH ₃) ₂ N) ₃ PN) ₄ P] ⁺	[(((CH ₃) ₂ N) ₃ PN) ₄ P]O ₃ ^[351]

The ozonides found have all been synthesized from CsO₃ which features the biggest alkali metal ion cesium thus facilitating the ion exchange. Smaller ions like Li⁺, Na⁺ and Ba²⁺ where successfully exchanged and crystallized as well as several larger phosphine based ions. Compounds containing larger ions, like the last three in Table 10, are isolated from the surface of the ion exchange resin. This explains the exchange contradicting the normal direction.

Ozonides and *Zintl* phases are comparable in terms of sensitivity to air and moisture as well as their readiness to dissolve in liquid ammonia. Since ozonides are stable in the presence of Amberlyst 15 in liquid ammonia the same can be approximated for dissolved *Zintl* phases and the extracted *Zintl* clusters. Thus transferability of the ion exchange technique to form new compounds containing light alkali metals and *Zintl* clusters can be approximated.

4.2.2. Standard operating procedures for Amberlyst 15 and *Zintl* clusters

In order to generate reproducible results using Amberlyst 15 as an exchange agent for *Zintl* phases and their extracted *Zintl* clusters, standard operating procedures regarding reaction parameters have to be established and new analytical methods have to be examined.

4.2.2.1. Experimental considerations – quantitative analysis by ICP-OES and ion exchange in liquid ammonia

The analytical challenges of these experiments can be separated into two categories: analysis of the alkali metals and analyzing the *Zintl* clusters. Analysis of the *Zintl* clusters can be done using Raman spectroscopy and powder X-ray diffraction. *Zintl* phases and the contained clusters show characteristic signals and are well researched using both methods.

The next problem is how to quantitatively determine the lithium content of the phase after the exchange. Detection methods like EDX do not have sufficient detection thresholds for this task because of the limited detection range of some spectrometers and the fact that lithium is a very light element which makes its detection difficult and the results are rarely quantitative. For this reason inductively coupled plasma optical emission spectroscopy (ICP-OES) is used to determine the lithium and potassium contents found in the *Zintl* phases. ICP-OES is advantageous for alkali metals which have very characteristic emission spectra. Special consideration has to be given to the orientation of the detector in relation to the plasma stream used to ionize the sample. In order to reliably detect alkali metals emission lines it is imperative that an equatorial detector is used instead of an axial one. Alkali metals electrons are easily excited to emit their characteristic spectral lines but are equally quick to return to the ground state. This makes it difficult to detect the emitted light with a detector in line with and behind the plasma. However a detector, or a mirror for redirection of emitted light, placed at a 90 degree angle to the plasma makes detection of the lines possible and repeatable. This placement can be optimized further by placing the mirror at the precise location where each element is ionized which decreases the detection level but increases the width of the detection area.^[352-353]

The first subject of determining standard operating procedures is the choice of reactants for the exchange experiments using *Zintl* phases, which come in many different compositions of A_4E_4 , A_4E_9 , $A_{12}E_{17}$ ($A = \text{Na} - \text{Cs}$, $E = \text{Si} - \text{Pb}$). Main attention is given to phases containing $E = \text{Si}$, Ge , Sn and the compositions A_4E_4 and A_4E_9 ($A = \text{K}$, Cs). In order to perform ion exchange experiments on these phases they have to be dissolved. Liquid ammonia is a frequently used solvent for these phases because of their polar bond characteristics. Liquid ammonia is difficult to handle on its own but the difficulty is increased because of the macroporous structure of Amberlyst 15. With the high inner surface area of 53 m^2 of the beads the potential for delayed boiling is increased.

This delayed boiling is so significant in experiments utilizing liquid ammonia that it is possible the solution is thrust up the reaction vessel. The reaction vessel is never fully submerged in the cooling mixture needed for ammonia to be in liquid form. With delayed boiling as significant as with Amberlyst 15 it can be expected that the ammonia solution is thrust onto the room temperature glass. This results in two things, firstly that the solution decays and no longer takes part in the exchange reaction. The more troublesome second result is that at room temperature ammonia is a gas which the solutions turns into on contact with the room temperature glass. This is not only detrimental to the experiment but a safety hazard as well. This delayed boiling cannot be suppressed by slow cooling or heating or special care when handling these experiments. A solution for this problem is found by containing the ER in a separate glass cylinder inside the reaction vessel. This glass cylinder is filled with the appropriate amount of ER and closed using Whatman filters. With this the ion exchange can still take place with the solution being able to permeate through the filters and onto the ER. The delayed boiling is inhibited by the fact that the gas is expelled in a controlled, slow fashion through the openings of the cylinder in contrast to being expelled all at once (Figure 57).

4.2.2.2. Determining the reaction parameters of Amberlyst 15 and *Zintl* clusters in solution

As mentioned before the reaction parameters need to be optimized regarding proper solvents, reactant equivalents and exchange times. Special interest is given to phases containing $[E_9]$ units with $E = \text{Si, Ge, Sn}$. Experimental conditions can be found in section 6.6.3.1 and ICP-OES data in section 7.1. In order to determine reaction parameters only phases containing $[\text{Ge}_9]$ clusters and the silylated cluster $\text{K}[\text{Ge}_9[\text{Si}(\text{SiMe}_3)_3]_3]$ are used. $[\text{Ge}_9]$ clusters are used in the solvents dmf, en and liquid ammonia while $\text{K}[\text{Ge}_9[\text{Si}(\text{SiMe}_3)_3]_3]$ serves as a comparison in solvents like acn. Exchange reactions featuring additional phases are described in section 4.2.3.

The first step in the determination of a good exchange system is the choice of alkali metal which acts as a cation in the phases. The cation exchange, as established before, can be described using the HSAB concept. Larger cations thus adhere better to the polymer than smaller ions. Phases containing $[\text{Ge}_9]^{4-}$ can be found with alkali metals Na, K, Rb and Cs as counter ions. In order to lithiate phases containing $[\text{Ge}_9]$ clusters, in theory larger ions are beneficial to the exchange reaction. This can be tested using Cs_4Ge_9 and $\text{K}_4\text{Ge}_9 - \text{Zintl}$ phases featuring alkali metals with different ion radii. The phase containing cesium ions should be the more suitable candidate to use in the cation exchange experiments, because of the radius difference between Cs^+ (165 pm) and K^+ (133 pm).

To test this K_4Ge_9 and Cs_4Ge_9 are dissolved in liquid ammonia alongside the ion exchange resin loaded with lithium ions. The exchange time was set at 24 hours, as a baseline, after which the exchange is finished and the suspension is filtrated. The ratio of reactant to LiER was 1/20 meaning 20 equivalents of LiER per one alkali metal ion in the reactant, equaling a total of 80 equivalents. The analysis of this experiment shows that the exchange of both ions after the time is similar with only a difference of 4% (Figure 19, middle). Cs_4Ge_9 is much more difficult to synthesize because of handling elemental cesium. Additionally the synthesis has to be done in tantalum ampoules where as K_4Ge_9 can be synthesized in bulk in a reusable steel autoclave. A marginal difference of 4% thus does not validate Cs_4Ge_9 as a superior candidate for exchange experiments. Because of this K_4Ge_9 will be used as a source of bare $[\text{Ge}_9]$ clusters for further exchange experiments.

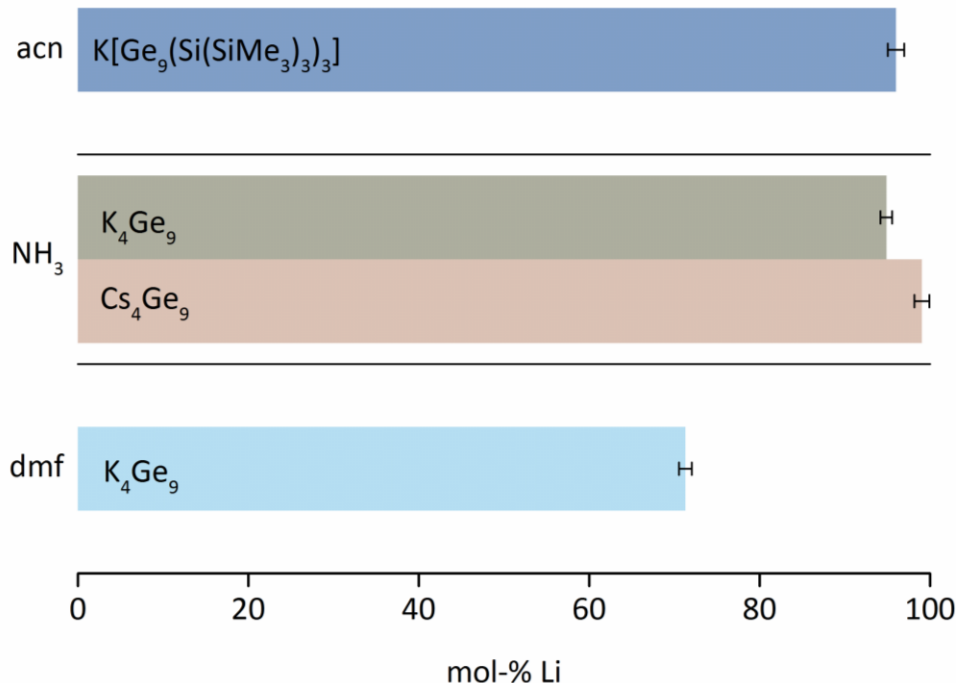


Figure 19: ICP-OES analysis of lithium ion exchange experiments on different *Zintl* phases and in different solvents after 24 hours. Top graph: molar content of lithium ions after exchange of $K[Ge_9[Si(SiMe_3)_3]_3]$ in acn. Middle graph: comparison of Cs_4Ge_9 and K_4Ge_9 as reactants for ion exchange in liquid ammonia. Bottom graph: molar content of lithium after exchange using K_4Ge_9 in dmf.

As mentioned before, these phases are only soluble in highly polar solvents like liquid ammonia, en and dmf. For this reason exchange experiments including *Zintl* phases are limited to these solvents. Even though the solid state phases readily dissolve in en, Amberlyst 15 seems to react with it. This can be seen as soon as the solvent makes contact with the resin resulting in gas expulsion and an increase in temperature. This reaction occurs in mixtures of the solid state phase, en and the ion exchange resin as well as just with en and Amberlyst 15. This shows that the resin and en are not stable in the presence of one another. This rules out the usage of en for any experiments, where Amberlyst 15 or any similar resins are to be used. Comparing the bare clusters dissolved in dmf and liquid ammonia it becomes clear that liquid ammonia is a far superior alternative to dmf because of the diminished exchange rate. In 24 hours the exchange in

liquid ammonia is mostly finished with 96% lithium content while in dmf only 71% lithium can be found (Figure 19).

Because reactions in liquid ammonia are time consuming a model system is examined. A comparison between the phase K_4Ge_9 and $K[Ge_9[Si(SiMe_3)_3]_3]$ is tested. If ion exchange is similar for these two compounds $K[Ge_9[Si(SiMe_3)_3]_3]$ could be used to test exchange parameters instead of K_4Ge_9 . The silylated cluster is soluble in acn and thus reactions can be done quicker and with less hassle. Comparing the exchange of K_4Ge_9 in liquid ammonia with $K[Ge_9[Si(SiMe_3)_3]_3]$ in acn a close accordance can be observed (Figure 19). Both experiments show almost equivalent exchange after the 24 hour period. This fact opens the possibility of using $K[Ge_9[Si(SiMe_3)_3]_3]$ as a model for further investigation on the cation exchange system, which presents multiple positive factors.

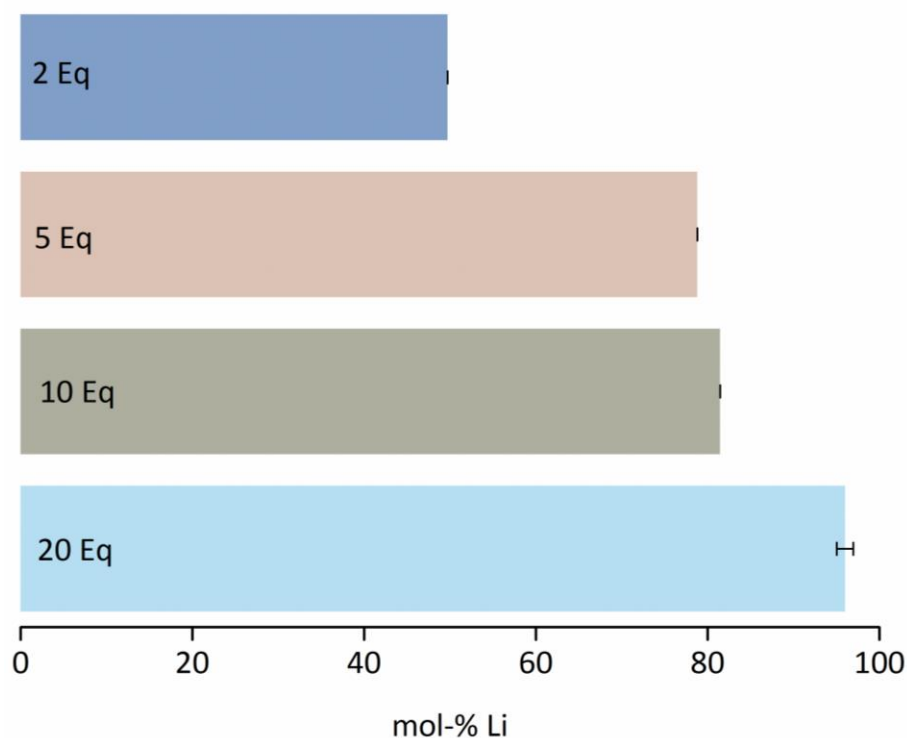


Figure 20: Comparison of equivalents of LiER per alkali metal ion. The exchange reaction is done using $K[Ge_9[Si(SiMe_3)_3]_3]$ in acn with different amounts of LiER in a period of 24 hours.

Firstly the handling of $\text{K}[\text{Ge}_9[\text{Si}(\text{SiMe}_3)_3]_3]$ in acn is simpler than handling liquid ammonia. Furthermore more experiments can be done in a shorter time frame because the reaction and filtration can be done using standard techniques instead of the specialized ammonia equipment. Using this model system the next investigation is aimed at figuring out the amount of LiER per alkali metal ion needed to ensure full ion exchange in a reasonable time frame. The start configuration for this was 20 equivalents per alkali metal in the reactant. In addition to these 20 equivalents, two, five and ten equivalents were tested to see if the amount of LiER can be reduced. Analyzing the results of using different amounts of LiER on the system of $\text{K}[\text{Ge}_9[\text{Si}(\text{SiMe}_3)_3]_3]$ in acn during an exchange time of 24 hours, the results show that 20 equivalents are the only suitable amount for a proper exchange of ions. Two, five and ten equivalents do not show an acceptable exchange in the chosen time frame (Figure 20).

The last variable to be considered is the exchange time of the reaction. For this the model system was tested at one, two, four, eight, 24 and 48 hours using $\text{K}[\text{Ge}_9[\text{Si}(\text{SiMe}_3)_3]_3]$ and 20 equivalents in acn in order to eluate the time it takes for the exchange to be completed.

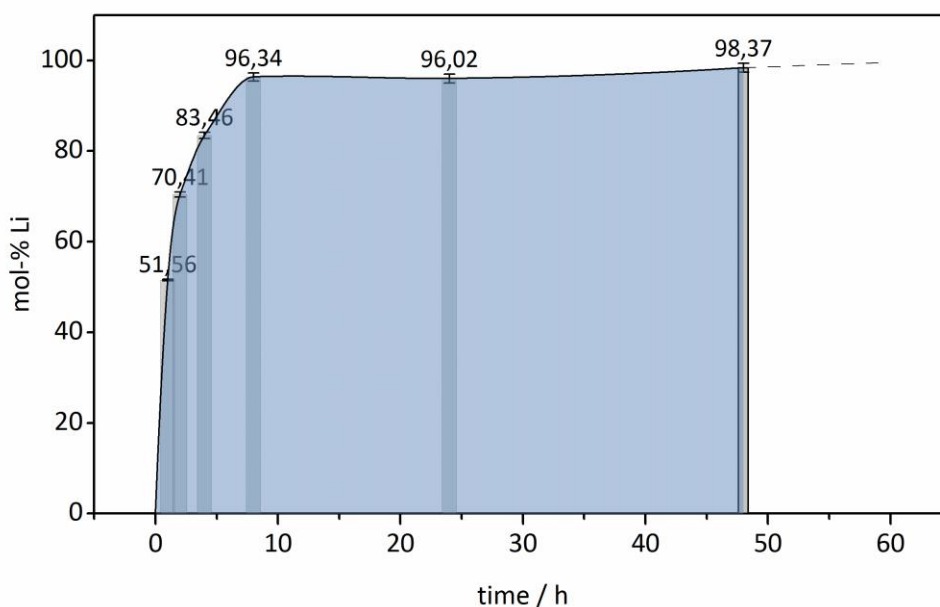


Figure 21: Experiment analyzing the amount of time needed for the ion exchange to be completed. $\text{K}[\text{Ge}_9[\text{Si}(\text{SiMe}_3)_3]_3]$ and 20 equivalents of LiER loaded with lithium ions are used in acn over different periods of time.

Analyzing the experiment a plateau is reached at around eight hours. This shows that the minimum exchange time given should at least be eight hours. More time is usually given, often reactions are done overnight, to ensure the maximum amount of ions is exchanged. Shorter reaction times are not desirable because of the possibility of a mixture of ions remaining in the compound. Combining the results of all the test experiments a concise list of parameters can be summarized for the Amberlyst 15 system (Table 11).

Table 11: Minimum exchange times and necessary equivalents of LiER in different solvents regarding $\text{K}[\text{Ge}_9[\text{Si}(\text{SiMe}_3)_3]_3]$ and phases containing $[\text{Ge}_9]$ clusters.

Solvent	Minimum exchange time / h	LiER equivalents
acn	24	20
$\text{NH}_3(\text{l})$	48	

4.2.3. Ion exchange on *Zintl* clusters utilizing established parameters

With the new reaction parameters established, the application on different compounds containing *Zintl* clusters can now be realized. Functionalized clusters are tested first because they feature less alkali metal cations per cluster unit making them an ideal starting point. After this further experiments on bare clusters are conducted.

4.2.3.1. Ion exchange on *Zintl* clusters featuring ligands resulting in $\text{Li}[\text{Ge}_9[\text{Si}(\text{SiMe}_3)_3]_3]$

Utilizing the parameters for exchange reactions established in section 4.2.2 the next step a proof of concept. Experimental conditions can be found in section 6.6.3.3.

First a bulk synthesis of $\text{Li}[\text{Ge}_9(\text{Si}(\text{SiMe}_3)_3)_3]$ is conducted through cation exchange on $\text{K}[\text{Ge}_9(\text{Si}(\text{SiMe}_3)_3)_3]$ in acn. Analysis of this bulk product showed no significant shift of NMR signals, ^1H and ^{29}Si , could be found same as in literature,^[140-141] proving that the cluster is intact after the exchange of cations in the bulk (Figure 60, Figure 62). In addition to the literature known NMR studies, ^7Li -NMR is recorded of $\text{Li}[\text{Ge}_9(\text{Si}(\text{SiMe}_3)_3)_3]$. The solution NMR reveals a single signal at - 2.72 ppm which matches signals of free lithium ions (Figure 61).^[354] ICP-OES analysis shows an almost complete absence of potassium ions and only lithium ions being present (section 6.6.3.3).

Next $[\text{Li}(\text{B12crown4})_2][\text{Ge}_9(\text{Si}(\text{SiMe}_3)_3)_3]$ is crystallized by dissolving $\text{Li}[\text{Ge}_9(\text{Si}(\text{SiMe}_3)_3)_3]$ in acn and adding B12crown4, which is a lithium ion sequestering agent. A single crystal is found analyzed using single crystal X-ray diffraction. Single crystal data can be found in section 7.4 in Table 53. Comparing the bond lengths, Si-Ge (2.381(2) – 2.395(2) Å) and Ge-Ge (2.533(1) – 2.694(1) Å), of the present $[\text{Ge}_9(\text{Si}(\text{SiMe}_3)_3)_3]^-$ anion to the ones known from literature no significant deviations can be found.^[140-141] While B12crown4 is designed to encapsulate one lithium ion, in this instance a single Li^+ ion is fixed in a sandwich-like structure (Figure 22). Similar coordination for lithium have also been reported with Li-O (2.09(1) – 2.43(1) Å) distances matching those found in this work^[355-357] as well as a structure with sodium ions sandwiched in 12crown4 with similar constitution.^[358]

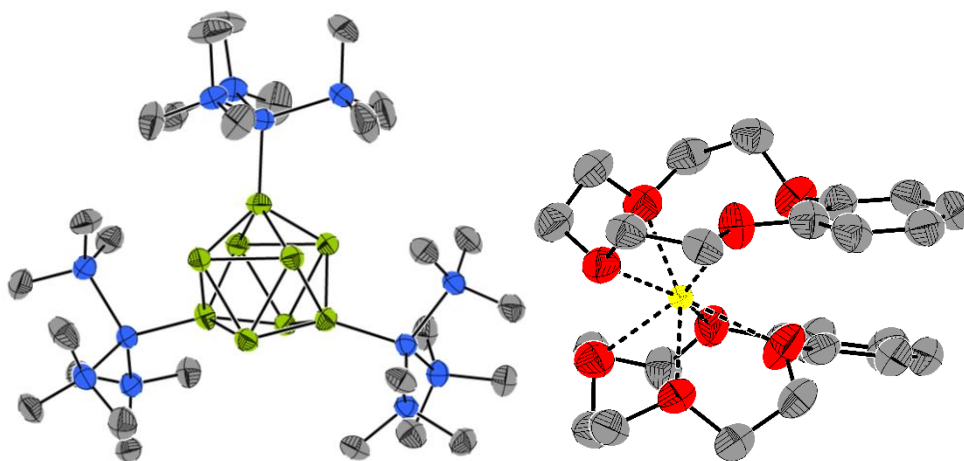


Figure 22: $[\text{Ge}_9(\text{Si}(\text{SiMe}_3)_3)_3]^-$ anion and Li^+ cation, complexed by two B12crown4 units. Thermal ellipsoids are set at 50% probability. Green – germanium, blue – silicon, red – oxygen, yellow – lithium, grey – carbon. Protons are omitted for clarity.

DFT studies suggest that the cavity of B12crown4 might be too small even for lithium ions to fit inside the plane of the ring thus, the coordination always shows an out of plane structure. In this the distance between a Li^+ ion and the oxygen plane is about 0.5 \AA .^[359] This coincides with the fact that the mean Li-O distance is $2.26(2) \text{ \AA}$ while one uncoordinated oxygen O1 has a 0.7 \AA longer distance to Li^+ . The two B12crown4 molecules are rotated approximately 60° in relation to each other's benzyl rings.

4.2.3.2. Ion exchange on bare *Zintl* clusters resulting in $\text{Li}_4\text{Sn}_9 \cdot 17 \text{ NH}_3$

With a reliable system found for silylated clusters trials for bare clusters are performed on phases containing bare $[\text{E}_9]$ ($\text{E} = \text{Si}, \text{Ge}, \text{Sn}$) clusters. Experimental conditions can be found in section 6.6.3.2. All phases are dissolved in liquid ammonia in the presence of LiER, filtrated and analyzed. As before in section 4.1, residue in the context of these reactions means the undissolved residue of a filtration in liquid ammonia. Filtrate refers to the solid yielded after evaporation of liquid ammonia and drying *in vacuo*.

First exchange reactions are conducted with $[\text{Si}_9]^{4-}$ cluster, but since no phase with the composition K_4Si_9 exists, $\text{K}_{12}\text{Si}_{17}$ is used instead. For more data on the exchange characteristics of silicide clusters, K_4Si_4 is also examined in the context of ion exchange. All experiments conducted with silicide phases and Amberlyst 15 result in a rapid gas expulsion and thus have to be stopped prematurely. Since silicide phases have diminished solubility in liquid ammonia compared to germanide or stannide phases, this shortened reaction time is especially bad for the analysis of these experiments.

Since no direct experiment can be conducted on the reactivity of the silicide phase with the lithium ion exchange on Amberlyst 15, an alternative test reaction is conducted. $\text{K}_{12}\text{Si}_{17}$ is dissolved in liquid ammonia and filtrated onto LiBr in order to test the behavior when lithium ions are introduced to the phase. As soon as the solution of $\text{K}_{12}\text{Si}_{17}$ gets into contact with the LiBr, gas expulsion can be observed just as with the LiER. This shows that simply introducing lithium ions is not a suitable method with silicide clusters such as $[\text{Si}_4]^{4-}$ and $[\text{Si}_9]^{4-}$. These clusters seem to exhibit significant reactivity when in contact with the light Li^+ ions. Analyzing solid yielded after

the solvent evaporation of the filtrate shows an amorphous phase in both Raman and PXRD, of which no reliable statements can be made (Figure 82). Analyzing the solid with DSC shows no significant signals (Figure 143). However, the Raman and PXRD after the DSC show elemental silicon^[360] in the Raman and LiBr as well as KBr in the PXRD (Figure 83). No signals of $K_{12}Si_{17}$ or $[Si_9]^{4-}/[Si_4]^{4-}$ can be observed anymore which is probably due to the heating. Nevertheless the reaction with LiBr shows gas expulsion just as with the LiER. This shows that these silicides cannot be simply lithiated by using the established Amberlyst 15 system.

Next the germanide phases K_4Ge_9 and K_4Ge_4 are used in the ion exchange experiments. $K_{12}Ge_{17}$ is not used in this case since there is access to $[Ge_9]^{4-}$ cluster through the K_4Ge_9 phase. All experiments regarding unfunctionalized germanium cluster units have not yielded any crystallized compounds. While the exchange of K^+ and Li^+ ions can be completed, the clusters do not survive this procedure intact (Figure 23).

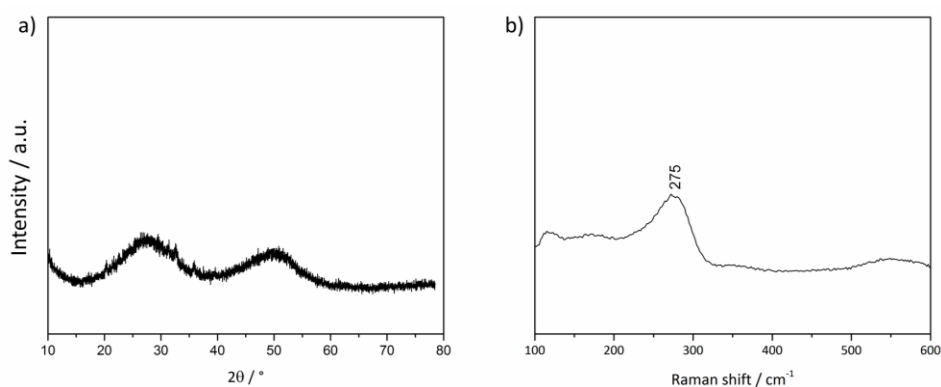


Figure 23: a) PXRD of K_4Ge_9 after lithium ion exchange experiment. Both experiments show only signals that can be attributed to amorphous germanium.^[361-362] b) Raman spectrum of K_4Ge_9 after lithium ion exchange experiment. The only observable signal can be attributed to amorphous germanium.^[27, 363]

The analysis of experiments in liquid ammonia using K_4Ge_9 and Amberlyst 15 show a decomposition of the $[Ge_9]^{4-}$ unit after the solvent is removed. While in solution the $[Ge_9]^{4-}$ cluster appear to be stable judging from the red color of the solution, removal of the solvent leaves black powder as residue which looks noticeably different from solid K_4Ge_9 . Analysis of this

powder using PXRD^[364] and Raman spectroscopy^[363] reveal the presence of only elemental, amorphous germanium (Figure 23). These findings are corroborated by TEM measurements showing only germanium (Figure 85, Figure 86). The TEM shows several larger amorphous agglomerates (Figure 24 a), b). Alongside these amorphous agglomerates, germanium nanoparticles of around 40 nm in diameter (Figure 24 c), d), e) can be found. These areas show crystalline structure which can be attributed to elemental germanium. These amorphous areas are probably a result of the removal of the liquid ammonia. HRTEM shows the larger agglomerates in greater detail (Figure 85). This decomposition is probably due to the smaller size of lithium (ion radius = 76 pm) compared to potassium (ion radius = 138 pm).

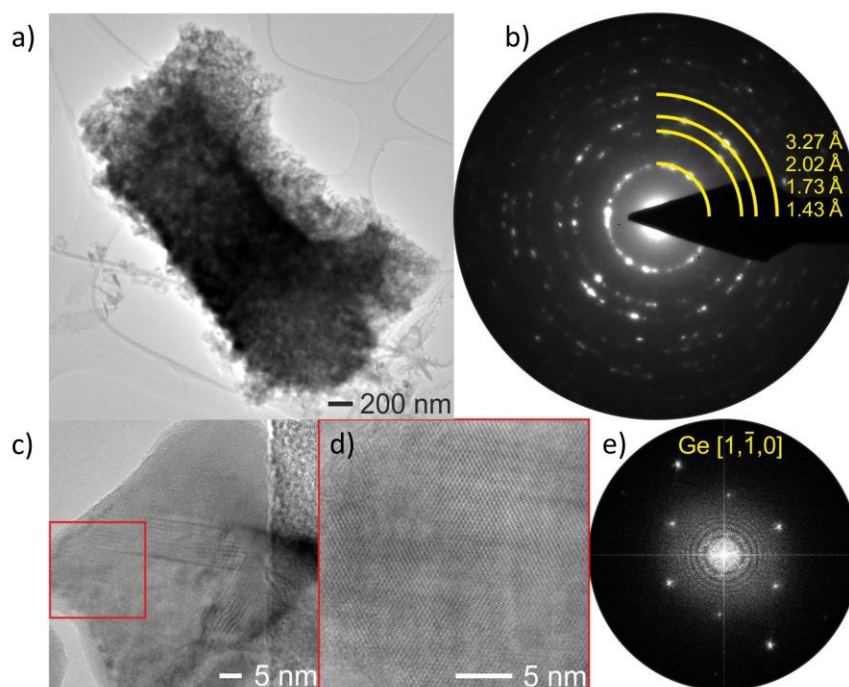


Figure 24: TEM pictures of filtrated K_4Ge_9 after the lithium ion exchange experiment in liquid ammonia. a) Matrix of amorphous germanium. b) Diffraction pattern that can be attributed to elemental germanium. c) TEM picture of a section of crystalline germanium. d) Red enlarged section of crystalline germanium. e) Diffraction pattern that can be attributed to elemental, crystalline germanium.

Next the *Zintl* phase K_4Ge_4 was used to get a better insight to the characteristics of germanides when in contact with lithium ions in liquid ammonia. When analyzing the filtrate of this reaction it becomes clear, that the desired compound with the composition of " Li_4Ge_4 " was not accomplished. Instead analysis of the sample shows only signals of a crystalline amine in the form of $\text{KNH}_2 \cdot \text{NH}_3$ (Figure 84). Raman analysis shows amorphous germanium being present (Figure 84), the same is the case with the reaction of K_4Ge_9 and LiER in liquid ammonia. So again the clusters do not seem to be stable after the exchange of potassium ions for lithium ions and removal of the solvent. TEM analysis shows the sample consists of single crystalline crystals in the μm scale. These crystals show to be rich in potassium, which corroborates the presence of the $\text{KNH}_2 \cdot \text{NH}_3$ (Figure 87, Figure 88).

No crystallization of Li_4Si_9 or Li_4Ge_9 is realized, however the equivalent tin structure was found by Dr. Wilhelm Klein, Chair of Inorganic Chemistry with Focus on novel Materials working on the same project. In this case K_4Sn_9 was dissolved in liquid ammonia and reacted with LiER. This results in a single crystal which when analyzed using single crystal X-ray diffraction reveals to be the compound $\text{Li}_4\text{Sn}_9 \cdot 17 \text{NH}_3$ (Figure 148, Table 56). This structure was first reported by Korber *et al.*^[306] by dissolving the elements in liquid ammonia. Comparing the $[\text{Sn}_9]^{4-}$ units from both, the reproduced and literature known compounds, it demonstrates that both show almost no deviation from one another. The coordination of Li by ammonia molecules is roughly tetrahedral with the Li-N-Li angles ranging from $97.1(1) - 122.0(1)$, yet most of the angles are close to the ideal tetrahedral angle. The Li-N bond lengths ($2.03(1) - 2.10(1) \text{ \AA}$) match the literature lengths. This is also the case for the distances between the single ammonia molecule to its next neighboring, Li-coordinated ammonia molecules matches to the distances found by Korber *et al.*,^[306] indicating weak hydrogen bonding as in cubic solid ammonia.^[365]

In order to have a stable coordination between lithium and the $[\text{Ge}_9]^{4-}$ unit the lithium ions have to be shielded somehow. Making lithium ions softer however is indeed possible as can be seen from the crystallization of $[\text{Li}(\text{B12crown4})_2][\text{Ge}_9[\text{Si}(\text{SiMe}_3)_3]_3]$. The crown ether B12crown4 serves as an agent to enhance ion packing.

4.2.4. Stabilization experiments of lithiated *Zintl* phases

As mentioned in the previous chapter, the *Zintl* phases containing germanium and silicon are not stable against the lithiation using Amberlyst 15. Because of this reason, the phases need to be stabilized using two different methods. One way is the employment of lithium sequestering agents like crown ethers or the oxidation of the cluster species, in order to require less lithium counter ions. The first method is well documented with many crystal structures which contain clusters also containing these sequestering agents. The fact, that $[E_9]^{n-}$ cluster have a variable charge $n = -4, -3, -2$, is also known from structures (Section 1.2) as well as electrochemical measurements.^[110]

4.2.4.1. PEO as a lithium ion sequestering agent

Sequestering the lithium ions in the compound is one way of stabilizing the clusters in order to form a stable bulk compound. One possibility is the usage of polyethyleneoxide (PEO) $(-CH_2-CH_2-O-)_n$ which is known to complexate lithium ions and is in application in lithium ion batteries.^[366-368] The sequestration happens through the creation of pockets of the linear polymer, in which the lithium is situated. This is done via the “functional” ether group of the polymer and usually the lithium is complexated by several oxide groups. PXRD measurements indicate that these pockets can also form channels in which the lithium ions can travel along 2D tunnels.^[369] The lithium ion is still mobile in these pockets and can migrate from one to another, which still holds the possibility of oxidizing the phase to form new germanium allotropes. This mobility is increased by the “softness” and size of the complexing anion.^[366] Experimental conditions can be found in section 6.6.3.4.

Experiments including PEO are done using the model system of $Li[Ge_9[Si(SiMe_3)_3]_3]$ in acn, because there is only one ion to exchange and the substituted cluster is soluble in this solvent as is PEO. The cluster is dissolved in acn together with the PEO, the solvent is removed and the solid is analyzed using NMR spectroscopy and Raman. This can be done for 1H and ^{29}Si for the cluster and 7Li for the lithium ions. The mobility of the lithium ions can be judged by the sharpness of the

^7Li signals. Broader peaks indicate inhibited mobility while sharp signals show increased mobility.^[370-371]

The cluster remains stable in the presence of PEO in acn according to a solution based ^1H -NMR signal at 0.22 ppm. This proves the stability of the silylated cluster towards the addition of PEO (Figure 63).

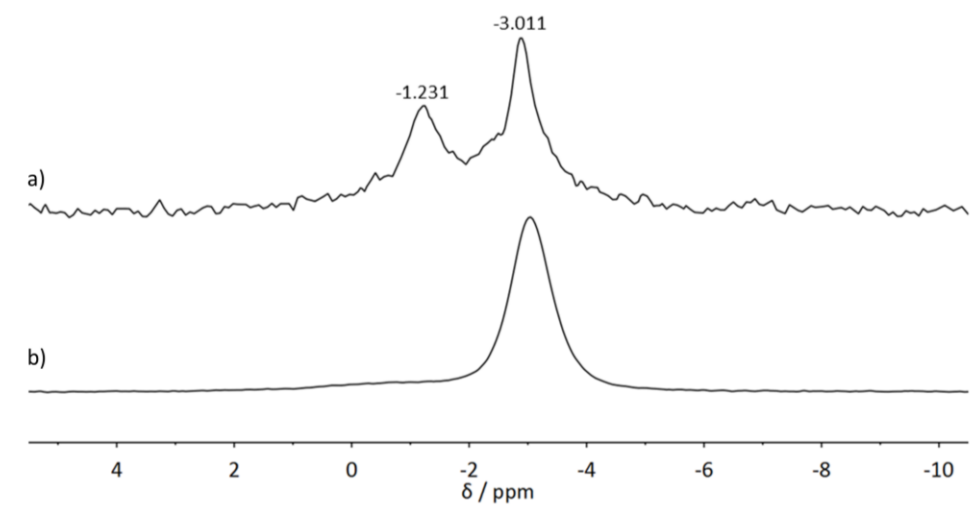


Figure 25: ^7Li -MAS-NMR of $\text{Li}[\text{Ge}_9[\text{Si}(\text{SiMe}_3)_3]_3]$ a) with three equivalents of PEO and b) $\text{Li}[\text{Ge}_9[\text{Si}(\text{SiMe}_3)_3]_3]$ with no added PEO.

Reactions between the silylated cluster, LiER and PEO are conducted and analyzed using MAS-NMR. The switch to MAS-NMR is due to the fact that the reaction yields solutions that cannot be isolated from the precipitate present. The lithium MAS-NMR signal of $\text{Li}[\text{Ge}_9[\text{Si}(\text{SiMe}_3)_3]_3]$ with no added PEO is located at -3.011 ppm (Figure 25). This changes when the PEO is added which results in two observable signals being present in a sample with PEO added. This low field shift agrees with literature where complexed lithium ions generate signals at lower fields.^[372] The presence of two signals indicates the presence of sequestered and unsequestered lithium ions simultaneously. This can also be seen in the experimental observations, where as soon as the PEO/acn solution is added, orange solid precipitates form the orange solution, which indicates some of the lithium ions being coordinated in the polymer. Increase of polymer concentration

does increase the yield of solid, but the solution never becomes completely colorless. Another difficulty is the fact the solution and solid cannot be separated properly. This is due to the fact that the solid is so fine that it clogs up any kind of filter. Separation through the use of a centrifuge was also unsuccessful.

With the model system proving the viability of the usage of PEO as a possible stabilizing agent for *Zintl* clusters against lithium ions, the next step is the adaptation to bare clusters. K_4Ge_9 is dissolved in both liquid ammonia and dmf alongside LiER, filtrated onto PEO. Using different amounts of PEO as a sequestering agent (Section 6.6.3.4) for the introduced lithium, similar results as without the added PEO are observed. The removal of solvent yields a black solid, which when analyzed using Raman spectroscopy, only the presence of amorphous germanium (Figure 93, Figure 94). No NMR measurements are conducted on the samples gained from filtration of liquid ammonia and dmf because of the decomposition of the cluster.

4.2.4.2. Counter ion reduction through Cluster oxidation

Masking the lithium ions using a polymer matrix did not yield the desired results as the bare $[Ge_9]^{4-}$ clusters decomposed. Another way of stabilizing the cluster would be to decrease the amount of lithium ions in the compound because then less ions are present which need to find a way to properly pack in a crystal structure. A decreased amount of lithium ions, as well as shielding from ligands, proved to be a deciding factor in section 4.2.3.1 where exchange and cluster retention was successful with $[Ge_9(Si(SiMe_3)_3)_3]$. A reduction of lithium ions would be achieved by a reduction of negative charge on the cluster, i.e. by oxidation. These kind of oxidations are possible as explained in the introductory chapters of this work. Though this redox behavior is often random, some cases were reported where the reduction of charge was planned, one such case is the isolation of $[Si_9]^{2-}$ by Sevov *et al.*^[110] Here Me_3SnCl is used in liquid ammonia to oxidize the cluster and it is stable afterwards.

Table 38 in section 6.6.3.5 shows the crystallization experiments done using the same technique as Sevov. The *Zintl* phases are dissolved in liquid ammonia with a sequestering agent and oxidized

using Me_3SnCl . Liquid ammonia is removed and the solid is dissolved in acn, filtrated and the exchange is done using LiER. No compound with lithium ions present could be isolated in form of crystals from these experiments.

4.2.5. Formation of germanium nanoparticles using Amberlyst 15 and K_4Ge_9

During several experiments involving Amberlyst 15 and K_4Ge_9 in acn, red solutions are obtained without the usage of sequestering agents. This is surprising because K_4Ge_9 is not generally considered to be soluble in acn without any previous extraction in liquid ammonia or en and the addition of sequestering agents. So in this case the formation of a red solution is investigated more closely.

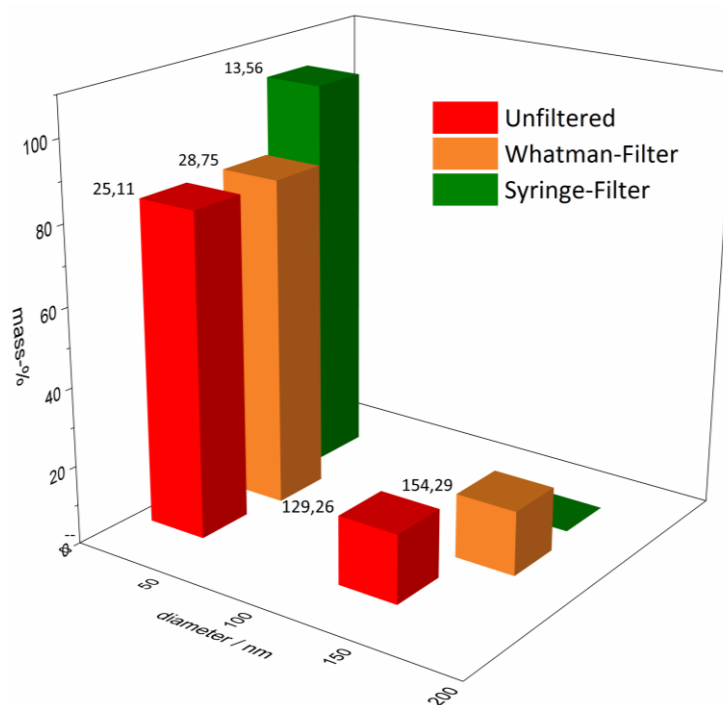


Figure 26: Germanium nanoparticle distribution in the first reactions of K_4Ge_9 and lithium ion loaded Amberlyst 15. Two species of nanoparticles can be observed – one around 25 nm and one around 140 nm which both can be found in the sample simultaneously. This can be inhibited by filtrating using a syringe filter as can be seen by the green graph.

During these investigation this solution proved to be a suspension which was discovered by filtrating the suspension through a syringe filter with a pore dimeter of 200 μm . This caused to particulate matter to become trapped in the filter and only clear, colorless acn to emerge. Further investigations showed the presence of nano particles. The first case of these nanoparticles proved to be a mixture of particles of different sizes (Figure 26). Preliminary analysis of the particle sizes using dynamic light scattering reveals two species can be identified being present simultaneously in any given sample yielded by lithium ion loaded Amberlyst 15 and K_4Ge_9 in acn. These two species are found both when filtrating the sample as well as when just separating the suspension from the Amberlyst 15 beads. Only a filtration with the aforementioned syringe filters can yield the single smaller species isolated in suspension. The potential of nanoparticle syntheses using Amberlyst 15 and K_4Ge_9 animated further research into this field which will be detailed in the following chapters. General synthesis parameters of the nanoparticles syntheses can be found in the experimental section. It has been reported that it is possible to synthesize nanoparticles from *Zintl* phases. Several more deliberate works have been conducted using silicide phase $\text{K}_{12}\text{Si}_{17}$ ^[289] and germanide using $\text{Na}_{12}\text{Ge}_{17}$ ^[290] and A_4Ge_4 ($\text{A} = \text{Na}, \text{K}$).^[373]

The mentioned cases however proof to yield a considerable amount of particles and are designed to do so. In the case of the particles yielded by the reaction between Amberlyst 15 and K_4Ge_9 in acn the yield is so small that only preliminary analysis was done on the system.

4.2.5.1. Nanoparticles formed by XER ($\text{X} = \text{H}, \text{Li}, \text{Na}$) and K_4Ge_9

Further investigations into the possibility of the formation of nanoparticles are conducted with LiER. In addition to this, HER and NaER are used to examine the possible influence of the counter ion on the size of the particles. The experiments are conducted using 40 equivalents of ER in relation to one equivalent of K_4Ge_9 in 10 mL acn and a reaction time of 24 hours (Section 6.6.3.6). The size of the nanoparticles is measured using dynamic light scattering and TEM.

Examining the nanoparticle suspensions gained from reactions of the three species of ER and K_4Ge_9 in acn it is clear that all show the presence of Ge nanoparticles after reaction in solution. Raman spectra measured in suspension (Figure 95, Figure 96, Figure 97) show the characteristic

wide signal of amorphous germanium at around 275 cm^{-1} . Additional signals stem from the suspension medium acn, marked with red diamonds, or the Raman spectrometer. Analysis of the sizes of these particles indicates, that the counter ion of the ER has a definitive effect of the size as well as the size distribution of the Ge nanoparticles created. While H^+ and Na^+ loaded ER show defined particles size (when disregarding one outlier in each analysis), Li^+ loaded ER develops 2 distinct groups of particles as mentioned before (Figure 99, Figure 100).

The mean particle diameter is 32.89 nm (30.90 nm when taking the outlier into consideration) for Ge particles gained from reactions of HER and K_4Ge_9 and 12.54 nm (11.89 nm when taking the outlier into consideration) for Ge particles gained from reactions of NaER and K_4Ge_9 . No uniform size can be determined for nanoparticles formed by reaction of K_4Ge_9 and LiER. All nanoparticles samples are also examined using TEM as to confirm the nanoscale (Figure 89 - Figure 92). This analysis corroborates the fact that all three reactions do indeed yield Ge nanoscale samples.

The nanoscale of the samples can be seen best in the examination of the particles yielded by the exchange reaction using HER. Alongside the nanoparticles, however, there are also amorphous plates and agglomerates.

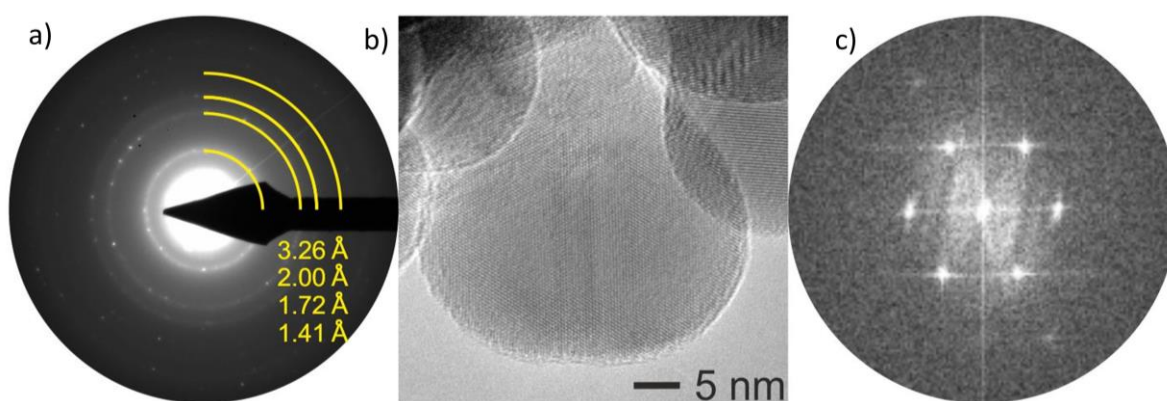


Figure 27: b) TEM analysis after the exchange reaction between K_4Ge_9 and HER in acn. Nanoparticles can clearly be seen at around 40 nm in size. a) & c) The diffraction patterns can be attributed to elemental, crystalline Ge.

This could be a result of the removal of suspension medium (Figure 89). The particles can clearly be seen and characterized as crystalline, elemental germanium. The size of the particles ranges between 20 and 40 nm (Figure 27, Figure 90). Reactions of K_4Ge_9 with LiER or NaER also result in nanoparticles, corroborated by the DLS analysis. In addition to the amorphous platelets, TEM measurements also shows nanoparticles in significantly smaller number. It seems that the removal of the suspension medium causes the particles to decompose or agglomerate into larger, amorphous particles (Figure 91, Figure 92). This effects seems to be more significant in the cases of samples gained from NaER and LiER.

4.2.5.2. Stability of the Ge nanoparticles

Suspensions of Ge nanoparticles seem to be stable at ambient conditions and under inert gas for months. A sample obtained from the reaction of K_4Ge_9 and HER showed no change in particle distribution after 2 months (Figure 102). Prolonged exposure to air, i.e. overnight, shows decomposition as by disappearance of the red color. Water seems to not have any effect, as in the color persists when the particles are exposed to water. Experimental conditions are described in section 6.6.3.6.

Because the Ge nanoparticles present are stable over long periods of time a mechanism must be present that prevents agglomeration. In general nanoparticles can be stabilized in suspension by one of two mechanisms – charge of a particle or surfactant. If a nanoparticle is sufficiently charged the repulsion of the particles will inhibit agglomeration and thus lead to a stable suspension. Generally nanoparticles are considered stable if the charge exceeds -30 mV for negatively charged and +30 mV for positively charged particles.^[374-375] In the case of surfactants the particle is enveloped in some sort of molecule that shrouds its charge and increases the steric real estate of the particles. This in turn leads again to inhibition of agglomeration and to a stable suspension. Most surfactants are polymers with some sort of charge functional group to adhere to the charged particle^[376] – as is Amberlyst 15 with its sulfonic acid group.

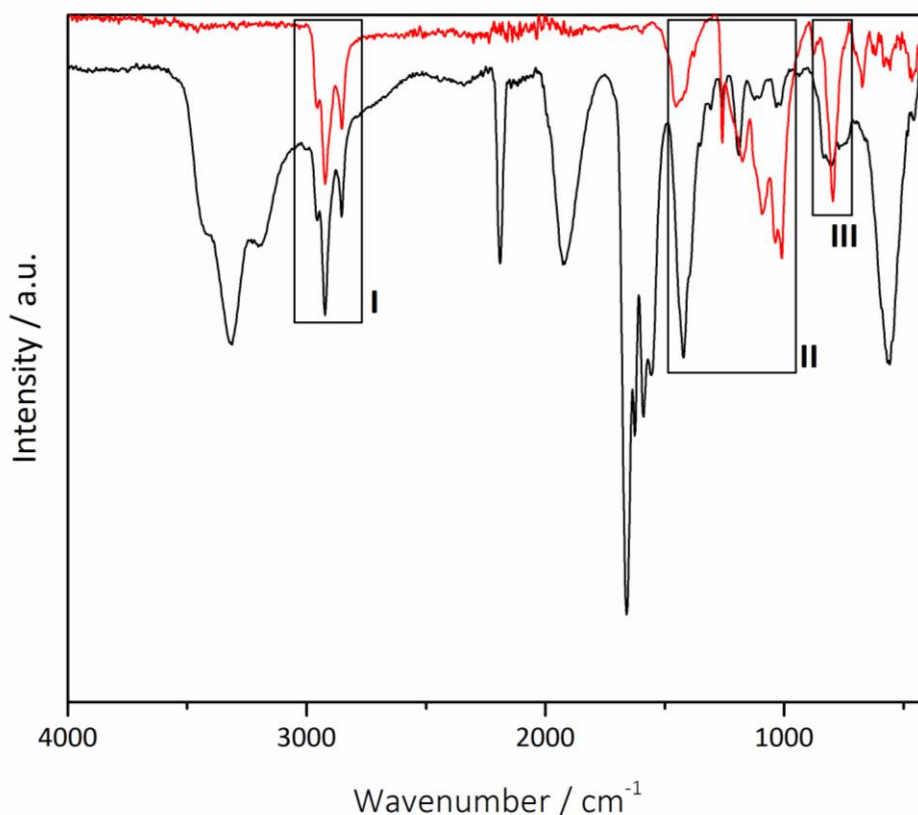


Figure 28: IR spectrum comparing the pure NaER (red) and the dried suspension containing Ge nanoparticles (black).

The ion exchange resin could stabilize the particles by acting as a surfactant. A suitable way to analyze this possibility is to use IR spectrometry. If bands that relate to these kinds of bonds are found in the sample, this indicates that the polymer is, at least in part, the stabilizing agent of these nanoparticles. In order to study this possibility pure NaER and a dried suspension of nanoparticles gained by the reaction of K_4Ge_9 and NaER are analyzed using IR spectroscopy.

Several agreements of the pure NaER and the dried suspension of Ge nanoparticles can be found in the IR spectrum (Figure 28). Looking at the signals at around 3000 cm^{-1} (I) there is an almost perfect match between the pure NaER and the dried nanoparticles. These three signals can be attributed to symmetrical and asymmetrical $-CH_2-$ vibrations of the backbone of the Amberlyst 15 polystyrene and polyvinylbenzene structure. The signals marked II, going from left to right, can be attributed to the aromatic $C=C$ vibrations of the benzene group and the $S=O$ and $S-O$ vibrations

of the sulfonic acid group, which acts as the functional group of the polymer. The signal group marked III also shows good accordance between the pure ER and the dried nanoparticles, however with it being in the fingerprint area of the IR spectrum it is difficult to reliably determine which vibrations can be attributed to these signals.

These similarities show the high probability that Amberlyst 15 contributes to the stability of the germanium in suspension. As mentioned before, surfactants are not the only way of stabilizing particles in suspension, charge can also be an additional factor. In order to determine the charge of the nanoparticles they have to be suspended in water, since Zeta potential measurements are only possible in water with the spectrometer present. This is done by removing the original solvent and resuspending in water by sonication. The resulting suspension is then analyzed for its zeta potential. The measurement shows a clear signal at a mean value of -35.5 mV, which lies over the barrier of -30 mV which corroborates the stability of the particles. A comparison between particles in acn and particles in water is difficult because of possible size difference and change in the composition of the particles. Because of the large difference of measurements in acn and water no further analysis of the particles suspended in water is done. The zeta potential measurement is done to test of the possibility of charged particles. However the results of both the IR and Zeta potential analysis show that the particles are probably stabilized by surfactants as well as charge.

It seems to be the case that some sort of surfactant originating from Amberlyst 15 and the charge of the particles work in conjunction to stabilize the suspension. More experiments on what kind species is on the surface of the particles surface as well as potential measurements are needed to complete the picture of the stability of the particles.

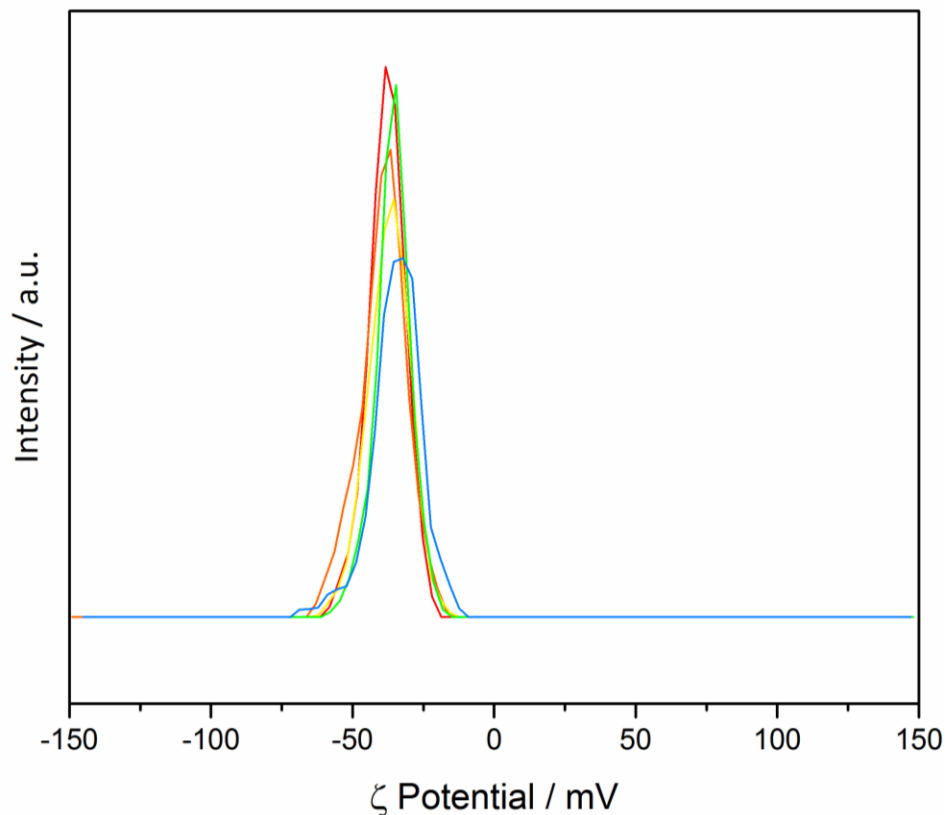


Figure 29: Zeta potential of nanoparticles in aqueous suspension. The nanoparticles are synthesized in acn by reaction of LiER and K_4Ge_9 . The solvent is removed from the suspension and the resulting solid is suspended in water by sonication.

It was shown that the combination of Amberlyst 15 and K_4Ge_9 in acn results in a small quantity of nanoparticles suspended in the reaction medium. The size of the generated nanoparticles depends on the cation loaded onto the ER. The germanium species are stable in suspension for an indefinite amount of time and it is likely that the particles are stabilized by polymer strands from Amberlyst 15. However because of the low yield of the reactions no further investigations were conducted. Further studies are not recommended unless the yield can be substantially increased.

4.2.6. Conclusion of ion exchange experiments including bare and silylated *Zintl* clusters

The first part of this work is dedicated to the examination of the ion exchange using Amberlyst 15 and *Zintl* phases of different compositions. The first step is to establish a repeatable system for the ion exchange experiments – different solvents, reactant ratios and exchange times are tested. The model system of $\text{K}[\text{Ge}_9(\text{Si}(\text{SiMe}_3)_3)_3]$ and LiER are used for this task, because preliminary tests showed that the characteristics of ion exchange using Amberlyst 15 in acn and liquid ammonia are extremely similar. With this the parameters of reactant/ER ratio is set to 1/20 and exchange reactions are conducted for at least 24 hours in order to guarantee complete exchange of ions. ICP-OES was used to determine the amount of different alkali metal ions in the different reactions. Ion exchange on $\text{K}[\text{Ge}_9(\text{Si}(\text{SiMe}_3)_3)_3]$ yielded $\text{Li}[\text{Ge}_9(\text{Si}(\text{SiMe}_3)_3)_3]$ in bulk and subsequently $[\text{Li}(\text{B12crown4})_2][\text{Ge}_9(\text{Si}(\text{SiMe}_3)_3)_3]$ and was the only successful exchange on a germanide. Reactions using these parameters and analysis methods with silicides show gas expulsion in liquid ammonia and were thus deemed too dangerous. Exchange using germanides could be conducted safely however the structure of the clusters are not retained after the exchange. This is most likely due to the size difference of lithium and potassium. The only successful exchange with a *Zintl* phase with a bare cluster is with K_4Sn_9 which yielded $\text{Li}_4\text{Sn}_9 \cdot 17 \text{NH}_3$, which was achieved by Dr. Wilhelm Klein, a member of the Chair of Inorganic Chemistry with Focus on Novel Materials working on the same project. All attempts stabilizing the compounds after the exchange do not yield the desired products, neither by using a polymer matrix to envelop the lithium ions or oxidizing the cluster to reduce the amount of needed counter ions. Finally, some reactions yield germanium nanoparticles which are characterized in size by DLS and TEM. These particles showed size dependence according to the different ions loaded in the ER. However because of the small yield of particles per reaction no further analysis is conducted.

4.3. Investigations of endohedral *Zintl* clusters in solid state and solution

As mentioned before the second part of this thesis deals with the syntheses of new phases containing $[E_9]$ units and lithium ions with the end goal of synthesizing new tetrel modifications. In section 4.2.4.2 the idea of reducing the cluster charge to reduce the amount of cations that need to be exchanged with lithium ions is discussed. Instead of using oxidizing agents like Me_3SnCl in this chapter endohedral clusters are synthesized as possible reactants. These clusters are similar in structure to the $[E_9]$ unit but feature a filled cavity. This cavity usually contains late transition metals like $\text{Co}^{[216-217]}$, $\text{Ni}^{[213, 218]}$ or $\text{Cu}^{[209]}$. With the presence of these metals the overall clusters charge can be increased or decreased resulting in varying amounts counter cations. However as detailed in the previous chapters, the cation exchange proved to be hardly adaptable to *Zintl* clusters like the $[E_9]$ species thus using endohedral clusters as reactants does not promise to be successful. However, as will be detailed in the following chapters, the research of new endohedral, ternary phases yielded interesting results. While not compatible to the end goal of synthesizing new tetrel modifications these results do expand upon previously reported knowledge.

As described in chapter 1.3.3, endohedral clusters show guest-host behavior. The isolated cage-anion serves as the host incorporating the guest transition metal. The cluster shells consist of the heavier tetrel elements Ge, Sn and Pb while only late transition metals are encapsulated. The cluster cages appear in different shapes and sizes ranging from the smallest $[E_9]$ to larger ones like $[E_{18}]$ and even onion like double shell structures as described in the previous chapters (1.3.3).

The $[E_9]$ units in particular are of special interest because they are the smallest known endohedral species and can feature notably high charges for units of that size. Furthermore these clusters exist as empty $[\square@E_9]^{n-}$ and filled forms $[\text{TM}@E_9]^{n-}$. This characteristic is almost solely found in this species. The high charges and examples of empty and endohedral species make these clusters an interesting research field. Recently Sun *et al.* proved that filled clusters can even be specifically targeted for ligand attachment reactions opening a completely new field of reactions.^[220]

Generally these endohedral $[E_9]$ units can be synthesized using two different approaches – either by solid state reaction directly incorporating the transition metal during formation of the cage or

by filling preexisting empty clusters in solution. Using the first synthesis path, only two compounds are known containing $[\text{Co}@\text{Sn}_9]^{5-}$ and $[\text{Ni}@\text{Sn}_9]^{4-}$ in $\text{K}_{13-x}\text{Co}_{1-x}\text{Sn}_{17}$ and $\text{Na}_{12}\text{Ni}_{1-x}\text{Sn}_{17}$ respectively.^[213] The second preparation route yields numerous compounds with the same structure motif of $[\text{TM}@\text{E}_9]^{n-}$. This second synthesis path proves to be quite random at times often in resulting not only in the desired $[\text{TM}@\text{E}_9]^{n-}$ species but also in species with additional ligands attached to the clusters. Usually, the first method results in solid state phases that may or may not contain filled clusters which cannot reliably be determined using PXRD. Only single crystal X-ray diffraction can determine whether the desired product is reached. Using Raman spectroscopy, a new method of screening the bulk phases, is found in order to determine the presence of endohedral units. Preexisting phases as well as new phases are examined applying this spectroscopic method for the first time.

4.3.1. Reported Endohedral $[\text{E}_9]$ ($E = \text{Ge}, \text{Sn}, \text{Pb}$) units

Filled versions of $[\text{E}_9]$ units exist for $E = \text{Ge}, \text{Sn}, \text{Pb}$ with the major part of the compounds containing $[\text{Sn}_9]^{n-}$ clusters. Only two filled $[\text{Ge}_9]$ and one filled $[\text{Pb}_9]$ clusters are known according to literature (Table 12; the second one which exists in addition to $[\text{Ni}@\text{Ge}_9]$ is $[\text{Co}@\text{Ge}_9]$ which is described in section 4.3.4). No filled $[\text{Si}_9]$ units are known most probably due to the overall small size of the cluster, i.e. short bond lengths, units making it difficult for an atom to be situated in the cavity.

When a cluster unit is filled, the volume of said clusters increases, i.e. the $E-E$ bonds are elongated, in order to enlarge the cavity size for the guest atom. These volume increases show different magnitudes depending on the incorporated metal and tetrel element making up the cage. The volume increase is more pronounced the lighter the tetrel element is, germanium having a mean increase of 15.1% while tin shows 9.0% and lead 11.3% increase (Table 12). It should be mentioned that two structures reduce the mean volume increase in tin clusters, $[\text{Co}_{0.68}@\text{Sn}_9]^{4.68-}$ and $[\text{Co}_{0.79}@\text{Sn}_9]^{4.79-}$. Because of the only partial occupancy of the transition metal in the cage, their volume increase is significantly decreased compared to an occupation of 100%. Finding a correlation of transition metal and volume increase is difficult because of the small sample, size

but generally a heavier element seems to induce a higher increase in volume. There is no visible correlation between the cluster symmetry and the incorporated element. Some clusters like $[\text{Cu@Sn}_9]^{3-}$ can even be found in more than one isomer cluster form, namely with D_{3h} and C_{4v} symmetry.^[377]

Generally the transition metals in these filled clusters have d^{10} electron configuration. It is then taken as not partaking in the bonding situation of the cage. Considering this the cluster unit can be described as $[(\text{TM})^y @ (\text{E}_9)^{4-}]^{(4-y)-}$. The range of charge can vary between -6 for $[\text{Ru@Sn}_9]^{6-}$ to -3 $[\text{Cu@Sn}_9]^{3-}$, with the ruthenium species being of the most highly charged $[\text{E}_9]$ units known to date, which is further discussed in this work (4.3.4).

Table 12: Comparison of the volume increase across empty/filled $[\text{E}_9]^{n-}$ clusters ($\text{E} = \text{Ge}, \text{Sn}, \text{Pb}$; $n = 3; 4; 5; 6$).

Cluster	Approx. Symmetry	Volume / \AA^3	Volume increase compared to empty cluster	Reference
$[\text{Ge}_9]^{4-}$	C_{4v}	22.1		[124]
$[\text{Ni@Ge}_9]^{3-}$ ^a	C_s	25.4	15.1 %	[215]
$[\text{Sn}_9]^{4-}$	C_{4v}	32.9		[306]
$[\text{Co}_{0.68}@\text{Sn}_9]^{4.68-}$	C_{4v}	35.4	7.7 %	[216]
$[\text{Co}_{0.79}@\text{Sn}_9]^{4.79-}$	C_{4v}	35.3	7.6 %	[217]
$[\text{Ni@Sn}_9]^{4-}$	C_{4v}	34.8	5.9 %	[218]
$[\text{Cu@Sn}_9]^{3-}$	C_{4v}	36.4	10.6 %	[377]
$[\text{Cu@Sn}_9]^{3-}$	D_{3h}	37.3	13.4 %	[209]
$[\text{Pb}_9]^{4-}$	C_{4v}	37.4		[306]
$[\text{Cu@Pb}_9]^{3-}$	D_{3h}	41.7	11.3%	[209]

^a - Mean value of two crystallographically independent cluster units.

4.3.2. DFT enhanced Raman analysis of $[E_9]$ units

PXRD is often used to analyze *Zintl* compounds. However without data from a single crystal or Rietveld refinement, the collected diffractograms are of limited use. The data is often also plagued by amorphous samples and high absorption. While some information about packing and $[E_4]/[E_9]$ ratio can still be gathered from analyzing the PXRD data, no definitive statement can be made about whether the phase contains endohedral clusters or not. In order to reliably determine if a solid state phase contains the desired filled cluster units, other analytical methods need to be developed. Raman spectroscopy is often used in analyzing phases such as the ones mentioned before. This method carries the benefit of only resulting in data if certain vibrations are triggered. It is literature known that *Zintl* clusters like $[E_4]^{4-}$, $[E_9]^{4-}$ ($E = \text{Si}^{[48, 173]}$, $\text{Ge}^{[57, 378]}$, $\text{Sn}^{[43, 378-379]}$) and mixtures thereof can be successfully and reliably be analyzed using Raman spectroscopy.

4.3.2.1. DFT enhanced Raman analysis of empty $[E_9]$ units ($E = \text{Si}, \text{Ge}, \text{Sn}$)

Concerning the $[E_9]^{4-}$ cluster several vibrational modes are known whereas the main mode is considered to be the cluster breathing mode, i.e. all nine atoms diverging from a hypothetical cluster center (Figure 30, **G**).

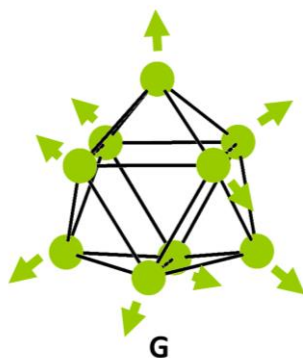


Figure 30: Main mode of $[E_9]$ cluster units where all atoms diverge from a hypothetical cluster center.

If a guest atom is now situated at the center, the energy of the respective mode is subject to change which in turn can be measured using Raman spectroscopy. This makes this method advantageous for analyzing endohedral $[E_9]$ units in solid state phases. The main mode (highest intensity mode) for the $[E_9]$ species is described in Table 13. The mode of $[\text{Si}_9]^{4-}$ is taken by principle of elimination from $\text{K}_{12}\text{Si}_{17}$ since there is no pure K_4Si_9 phase. Filled $[\text{Pb}_x]$ ($x = 9, 10, 12$) units exist but the $[\text{Pb}_9]^{4-}$ unit does not show any significant Raman activity in the investigated range of wave numbers and is thus excluded in this research. When a cluster is filled the energy of the main mode is increased and the signals are clearly distinguishable.

Table 13: Main Raman modes of empty $[E_9]^{4-}$ ($E = \text{Si, Ge, Sn}$) cluster units. Calculated Raman shifts can be found in section 7.2.

$[E_9]^{4-}$	Main Raman mode for empty $[E_9]$ units / cm^{-1} (exp. lit.)	Main Raman mode for empty $[E_9]$ units / cm^{-1} (calc.)
$[\text{Si}_9]^{4-}$	390 ^[48]	395
$[\text{Ge}_9]^{4-}$	220 ^[43]	225
$[\text{Sn}_9]^{4-}$	146 ^[43]	148

Density functional theory is known for the potential to aid in many different fields of chemistry. In addition to MO calculations, DFT can be used to calculate the vibrations of the clusters in a structure. This method can be applied to *Zintl* clusters as well. Using exchange correlation hybrid functional after Perdew, Burke and Ernzerhof (PBE0) and def2–TZVPP basis sets for all considered elements. Structure parameters for single point calculations are taken from respective single crystal structures after optimization. All calculations concerning clusters or spectra thereof are calculated in a vacuum, i.e. clusters are assumed to be without any additional atoms. Calculated Raman shifts are subject to change using appropriate scale factors of up to 5%.^[380] Values treated with scale factors will be marked as such.

In order to gain more insight to the characteristic vibrations of empty and endohedral clusters this technique was used to calculate the vibrations and the resulting Raman spectra. Specifically empty cluster units $[\text{Ge}_9]^{4-}$ and $[\text{Sn}_9]^{4-}$ are used to determine whether these calculations yield reliable Raman spectra for a comparison to solid state phases (synthesis is described in section 6.6.1). Since no phase containing exclusively $[\text{Si}_9]^{4-}$ clusters is known this cluster is excluded in these considerations, however filled $[\text{Si}_9]$ units will be discussed in section 4.3.7.1. The calculations of the clusters are done with isolated clusters meaning other atoms in the structure are removed. Calculations details can be found in section 6.5.10. Calculations of the Raman spectra of said clusters show good agreement, within an error margin of 5% (scale factors are applicable within this range as well),^[380] of Raman shift and intensity for the main signals of both empty units (Figure 31, Table 47, Table 48).

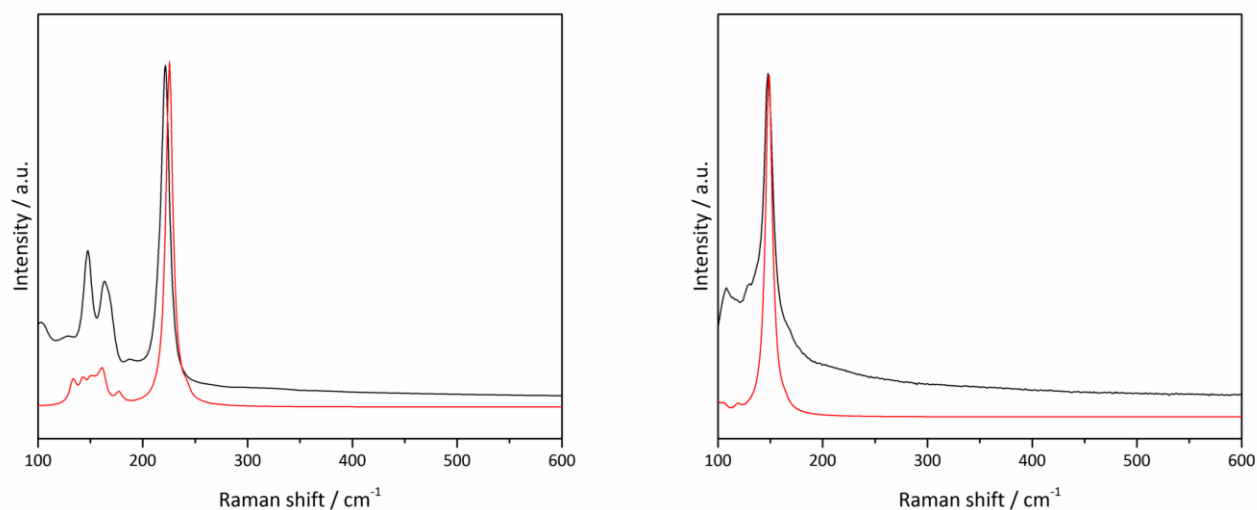


Figure 31: Left: Measured Raman spectrum of K_4Ge_9 (black) and calculated spectrum of $[\text{Ge}_9]^{4-}$ (red). Right: Measured Raman spectrum of K_4Sn_9 (black) and calculated spectrum of $[\text{Sn}_9]^{4-}$ (red).

Exactly calculated Raman shifts can be found in the appendix in section 7.2 in Table 47 and Table 48. This agreement serves as a prove-of-concept for the method of calculating Raman spectra of isolated clusters for comparison with solid state phases.

4.3.2.2. DFT enhanced Raman analysis of reported, endohedral $[E_9]$ ($E = \text{Ge}, \text{Sn}$) units

4.3.2.2.1. Calculated Raman shifts of endohedral $[E_9]$ clusters

The next step is to apply the technique of generating theoretical Raman spectra from empty to filled cluster species. Here the characteristics of the Raman shifts of filled clusters in comparison to unfilled clusters are discussed. As mentioned before the main vibration of the $[E_9]$ unit is the “breathing mode” (**G**, Figure 32). If an atom is present in the $[E_9]$ species this main signal shifts to higher energies by about 20 cm^{-1} for $E = \text{Ge}, \text{Si}$ and 30 cm^{-1} for $E = \text{Sn}$. This results in the main signal of an endohedral $[E_9]$ species being located around 309 cm^{-1} for $[\text{Si}_9]$, 240 cm^{-1} for $[\text{Ge}_9]$ and 175 cm^{-1} for $[\text{Sn}_9]$ (Table 14). The movement of the cage atoms remains the same motion of all atoms diverging away and towards the center of the cluster, with or without a center atom present. This new position of the main mode allows a definitive discernment of the presence of a filled cluster unit through Raman spectroscopy. Known cluster units like $[E_4]$ and $[E_9]$ ($E = \text{Ge}, \text{Sn}$) or combinations thereof show no signals in these regions.^[43] Also other possible impurities like clathrates also do not show signals in this area with the same multiplicity or intensity.^[381-383]

There are also two new modes that appear, when the cluster is filled. The first mode is caused by the uncapped square and capping atom of the cluster moving down, while the central atom moves upward (Figure 32, **A**). The second mode is generated when the central atom moves to one side of the cluster, while the adjacent side moves in the opposite direction (Figure 32, **B**). This vibration can also occur twice at the same time, where the second movement is perpendicular to the first one, which is then called **B'**.

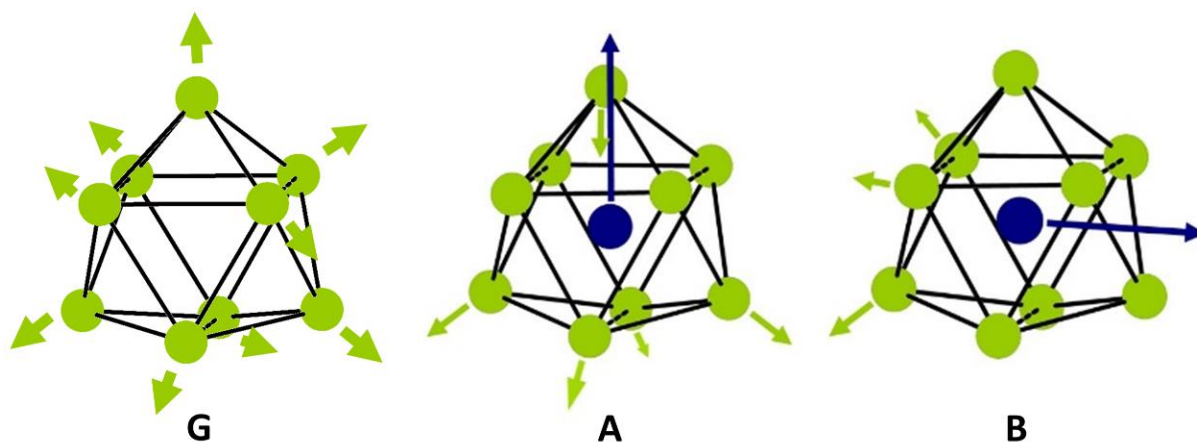


Figure 32: Different Raman modes of empty and filled $[E_9]$ units. **G**: Main Raman mode of an empty $[E_9]$ unit; breathing of the cluster where all atoms diverge from the cluster center. **A**: Raman mode characteristic to endohedral $[E_9]$ species; The uncapped square and capping atom of the cluster move down while the central atom moves upward. **B**: Second characteristic Raman mode, where the central atom moves to one side of the cluster while the adjacent side moves in the opposite direction. This vibration can also occur twice, where the second occurrence is perpendicular to the first one, which is then called **B'**.

These two additional vibrational modes cause signals in an energy range where the empty cluster does not provoke signals. $[Si_9]$ clusters show signals at around $460 - 470 \text{ cm}^{-1}$, $[Ge_9]$ clusters in the range of $340 - 360 \text{ cm}^{-1}$ and for $[Sn_9]$ clusters it is $230 - 270 \text{ cm}^{-1}$ (Table 14). It should be mentioned that these new characteristic vibrational modes, show significantly less intensity than the main cluster breathing mode. Because of this they are not always observed in measured spectra of compounds. With the energy shift of the main mode and the newly created modes resulting in characteristic signals, Raman spectroscopy offers a unique way of analyzing solid bulk phases for their content of endohedral clusters. In order to match the measured signals of the precursor phases to specific modes of empty and filled clusters, the structure of the desired cluster has to be known. This is best accomplished by a crystal structure. Starting from this, the new modes can be calculated using DFT. Reported structures were used to determine the approximate shifts displayed in Table 14.

Table 14: Calculated Raman shifts of filled $[E_9]$ ($E = \text{Si, Ge, Sn}$) units. Values are calculated from literature known examples in case of Ge and Sn. For Si a hypothetical $[\text{Ni}@\text{Si}_9]^{4-}$ cluster was used to calculate the modes and resulting signals.

$[\text{TM}@\text{E}_9]^{4-}$	Main Raman mode area for filled $[\text{E}_9]$ units / cm^{-1} (calc.)	Characteristic endohedral metal modes / cm^{-1} (calc.)
$[\text{TM}@\text{Si}_9]^{4-}$	409	460 - 470
$[\text{TM}@\text{Ge}_9]^{4-}$	235 - 245	340 - 360
$[\text{TM}@\text{Sn}_9]^{4-}$	165 - 178	230 - 270

4.3.2.2.2. Raman analysis of reported $[\text{TM}@\text{E}_9]$ ($\text{TM} = \text{Ni, Co, Cu}$; $E = \text{Ge, Sn}$) clusters

With the approximate area where new signals are to be expected, if endohedral species are present, solid state phases can be synthesized (as described in Table 39 & Table 40) and analyzed using DFT enhanced Raman spectroscopy. Analyzing the measured Raman spectra of the endohedral $[\text{Sn}_9]$ species, the trend that the calculated Raman shifts exhibit can be also seen in the experimental spectra. The Raman shift of the main signal is increased from 146 cm^{-1} for an empty $[\text{Sn}_9]^{4-}$ cluster to around $160 - 170 \text{ cm}^{-1}$ which is the case for all three species (Figure 33).

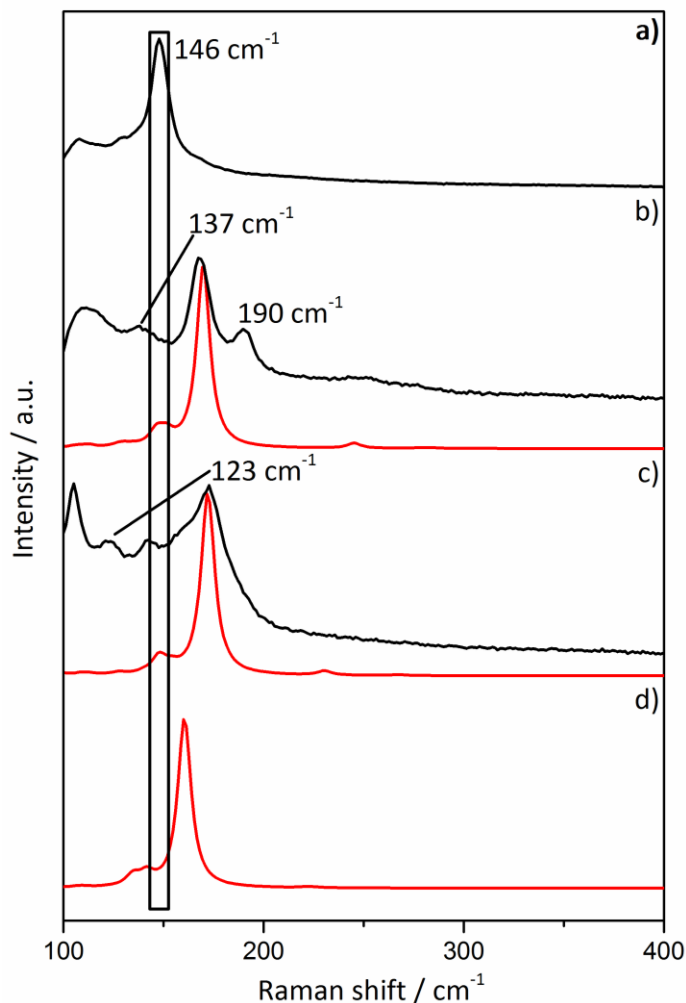


Figure 33: Depiction of filled $[TM@Sn_9]$ ($TM = Co, Ni, Cu$) units compared to the empty $[Sn_9]$ cluster. Measured spectra are depicted in black, calculated spectra in red. a) Measured Raman spectrum of K_4Sn_9 . b) " $K_5Co_3Sn_9$ " (black) and calculated Raman spectrum of $[Co@Sn_9]^{5-}$ (red). c) Measured Raman spectrum of " $K_4Ni_3Sn_9$ " (black) and calculated Raman spectrum of $[Ni@Sn_9]^{4-}$ (red; This spectrum is treated with a scale factor of 1.03.^[380] Table 15 shows the corrected value. Table 49 shows original values). d) Calculated Raman spectrum of $[Cu@Sn_9]^{3-}$ (red).

For $[Cu@Sn_9]^{3-}$ no measured spectrum exists because the reported crystal could not be resynthesized^[209] and no solid state phase exists. Instead Figure 33 a) and d) shows $[Sn_9]^{4-}$ and $[Cu@Sn_9]^{3-}$ in order to emphasize the shift of the main signal. However the calculated spectrum

shows the same behavior as the spectra of $[\text{Co@Sn}_9]^{5-}$ and $[\text{Ni@Sn}_9]^{4-}$ - a shift of the main signal toward higher wave numbers. Because of this it can be approximated that phases containing $[\text{Cu@Sn}_9]^{3-}$ in a solid state phase will exhibit the same signal shift as the other phases.

In the case of the cobalt species (Figure 33 b) the calculated main signal of $[\text{Co@Sn}_9]^{5-}$ shows good accordance with the experiment which corroborates the proven fact that the filled cluster is already present in the solid state phase. The phase also seems to contain empty $[\text{Sn}_4]^{4-}$ and $[\text{Sn}_9]^{4-}$ units in addition to the filled clusters, as can be seen by the signal at 190 cm^{-1} .^[43] This signal corresponds to the $[\text{Sn}_4]^{4-}$ cluster in the context of the phase $\text{K}_{12}\text{Sn}_{17}$. This indicates the presence of empty $[\text{Sn}_9]$ clusters. This suggests that the amount of cobalt used in the synthesis was not enough to fill all cluster units. This is also in line with the fact that compounds crystallized from solution containing cobalt filled clusters exhibit cobalt positions with below 100% occupation in the crystal structure. There is one additional signal at 137 cm^{-1} which cannot be attributed to anything in the context of clusters.

The sample containing $[\text{Ni@Sn}_9]^{4-}$ shows good accordance of the experimental and calculated signal of the filled species. Additional signals include one at 123 cm^{-1} which could be β -tin^[384] and one at 142 cm^{-1} which could hint at the fact that empty $[\text{Sn}_9]$ clusters are present (Figure 33 c). However a signal found in the calculated spectrum is also in the same range which makes the presence of the empty cluster questionable.

For $[\text{Co@Sn}_9]^{5-}$ and $[\text{Ni@Sn}_9]^{4-}$ this analysis shows that the endohedral cluster species is already present in the solid state phase, corroborated by crystals, both from solid state and solution.^[213, 216-217] The example of $[\text{Cu@Sn}_9]^{3-}$ shows a shift of the main signal, the same as with $[\text{Co@Sn}_9]^{5-}$ and $[\text{Ni@Sn}_9]^{4-}$, in relation of the empty unit just as the other filled species. The calculated main signal is in the same range of signals as the other filled tin species which shows that the filling of clusters seem to always have a similar effect concerning Raman spectra.

As mentioned in section 4.3.2.2.1 in addition to the shift of the main cluster mode to higher energies, additional characteristic signals appear with endohedral species present in a sample. These signals, at higher wave number, stem from the vibration and interaction of the cluster host and the transition metal guest (Figure 32). In the case of filled $[\text{Sn}_9]$ cluster the signals appear at

around 260 cm^{-1} . As mentioned before these characteristic signals show a significantly lower intensity than the main signal. Because of this they are often not visible in the experimental spectra. Following is the example of the $[\text{Co@Sn}_9]^{5-}$ cluster where the signals can be detected in the solid state.

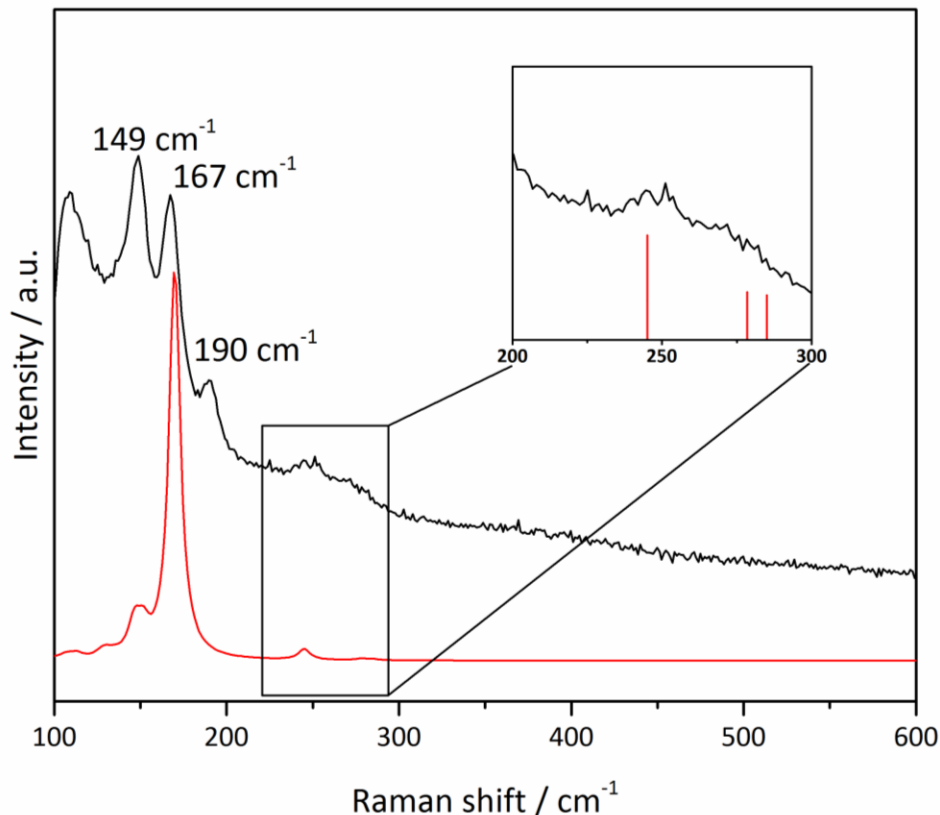


Figure 34: Measured Raman spectrum of “ $\text{K}_5\text{Co}_3\text{Sn}_9$ ” (black) and calculated Raman spectrum of $[\text{Co@Sn}_9]^{5-}$ (red). Enlarged section shows characteristic Raman signals of endohedral clusters. Vertical red lines indicate which vibration causes the signal. From left to right: **A, B, B'**.

Figure 34 shows, as an example, the characteristic lines of a phase with the nominal composition “ $\text{K}_5\text{Co}_3\text{Sn}_9$ ” containing the $[\text{Co@Sn}_9]^{5-}$ cluster. In addition to the signals, 149 cm^{-1} and 190 cm^{-1} , of the filled cluster additional signals which can be attributed to $\text{K}_{12}\text{Sn}_{17}$ can be observed.^[43] It is however possible that the signal at 149 cm^{-1} is a result from the filled cluster which can be seen in Figure 34 from the red line.

In the spectrum new signals appear between 230 and 270 cm^{-1} . No known signals of similar cluster compounds or clathrates appear in this area ruling out the possibility for contamination by any of these species.^[43, 381, 383] As mentioned in section 4.3.2.2.1 the modes resulting in these signals are **A**, **B** and **B'** (Figure 32) and the calculated Raman shift shows good accordance with the experimental data. In addition to the shift of the main signal these characteristic signals again prove the presence of the filled cluster in solid state phases.

Looking at the calculated Raman spectrum of the $[\text{Ni}@\text{Ge}_9]^{4-}$ species a similar effect can be observed where the main signal is shifted to higher energy by about 20 cm^{-1} . This cluster unit was synthesized in solution from K_4Ge_9 and until now no solid state phase containing this filled unit was synthesized. The synthesis of a solid state phase containing the $[\text{Ni}@\text{Ge}_9]^{4-}$ cluster was successful and is discussed in section 4.3.5.

Table 15: Main signals and characteristic signals of endohedral cluster units. Raman shifts of the $[\text{Ni}@\text{Sn}_9]^{4-}$ cluster are treated with a scale factor of 1.03.^[380] Table 15 shows the corrected value. Table 49 shows original values).

Endohedral cluster	Main signal / cm^{-1} (calc.)	Main signal / cm^{-1} (exp.)	Characteristic signal / cm^{-1} (calc.)	Characteristic modes
$[\text{Co}@\text{Sn}_9]^{5-}$	169	167	245, 278, 285	A, B, B'
$[\text{Ni}@\text{Sn}_9]^{4-}$	172	173	230, 267, 268	A, B, B'
$[\text{Cu}@\text{Sn}_9]^{3-}$	160	/	220, 225, 252	A, B, B'

The appearance of new signals in conjunction with the shift of the main cluster signal proves the presence of the endohedral unit in the solid state phases (Table 15). While the modes **A**, **B** and **B'** are the characteristic signals that only the filled $[\text{E}_9]$ clusters can have the shift of the main signal is the more reliable technique to identify the presence of endohedral clusters. This is because the characteristic modes have a significantly reduced intensity compared to the main signals and thus

not always show up in measurements. This solidifies the usage of Raman spectroscopy as a major analysis technique for such phases.

4.3.3. Synthesis and characterization of novel ternary phases in solid state and solution

A collection of all syntheses parameters, including reactant ratios, reaction temperatures and Raman analysis can be found in section 6.6.4. All phases depicted in these tables are analyzed using PXRD and Raman. Diffraction patterns and spectra can be found in section 7.3.5.

Table 39 includes syntheses parameters and analysis of ternary phases synthesized by Dr. Marina Boyko, Chair of Inorganic Chemistry with Focus on Novel Materials, and the author wants to extend his gratitude for the help in this field.^[385] Raman analysis of the phases shows the presence of empty *Zintl* clusters of the compositions $[E_9]^{4-}$ and $[E_4]^{4-}$ ($E = \text{Ge, Sn}$) and mixtures thereof. Additionally some phases also include filled clusters in the form of $[\text{TM}@E_9]$. These phases are marked with the respective cluster that can be found according to Raman analysis. Phases where Raman analysis shows the probable presence of endohedral *Zintl* clusters are dissolved in liquid ammonia for crystallization. Several new compounds containing unprecedented endohedral cluster can be isolated from solution and are discussed in the following chapters. Not all phases containing endohedral clusters, according to Raman analysis, did yield crystals from solution. These phases and the respective Raman analysis are also discussed in the following chapter.

Additional Synthesis including the element combinations K-Co- E ($E = \text{Ge, Sn}$) can be found in Table 40, K-TM- E (TM = Co, Ni; $E = \text{Si, Ge}$) in Table 41, K-Cu- E ($E = \text{Ge, Sn}$) in Table 42.

4.3.4. Crystallization of compounds featuring the new filled $[E_9]$ clusters from liquid ammonia

4.3.4.1. Synthesis and characterization of a compound containing the endohedral $[Co@Ge_9]^{5-}$ cluster

The first cluster species investigated consisted of filled $[Ge_9]$ species since only one is known until now with $[Ni@Ge_9]^{3-}$. This cluster, however, is not characterized well for several reasons. First the charge is surprisingly different from expectation with -3 where it should be -4 which indicates that either the cluster host or the transition metal guest are oxidized. Furthermore the crystal structure determination shows a high wR_2 value which indicates that this structure model is questionable. So in order to expand the class of filled $[Ge_9]$ units several solid state and liquid ammonia experiments are conducted. First the synthesis of a phase containing $[Co@Ge_9]^{5-}$ is attempted. Its heavier homologue $[Co@Sn_9]^{5-}$ as well as a close approximation with $[Co@Ge_{10}]^{3-}$ both exist. Modifying the technique that yielded the phase that contains filled tin cluster, the synthesis of a phase containing the predicted $[Co@Ge_9]^{5-}$ was successful. It is characterized by Raman in the solid state and crystallized from liquid ammonia.^[386]

The synthesis was conducted, as reported in literature^[217], with a heating step to 1000 °C and a quenching step at 550 °C (Table 40). This proved to be sufficient to produce a phase with the nominal composition of “ $K_5Co_{1.2}Ge_9$ ” which contains the desired full cluster as well as the empty $[Ge_9]^{4-}$ (Figure 35).

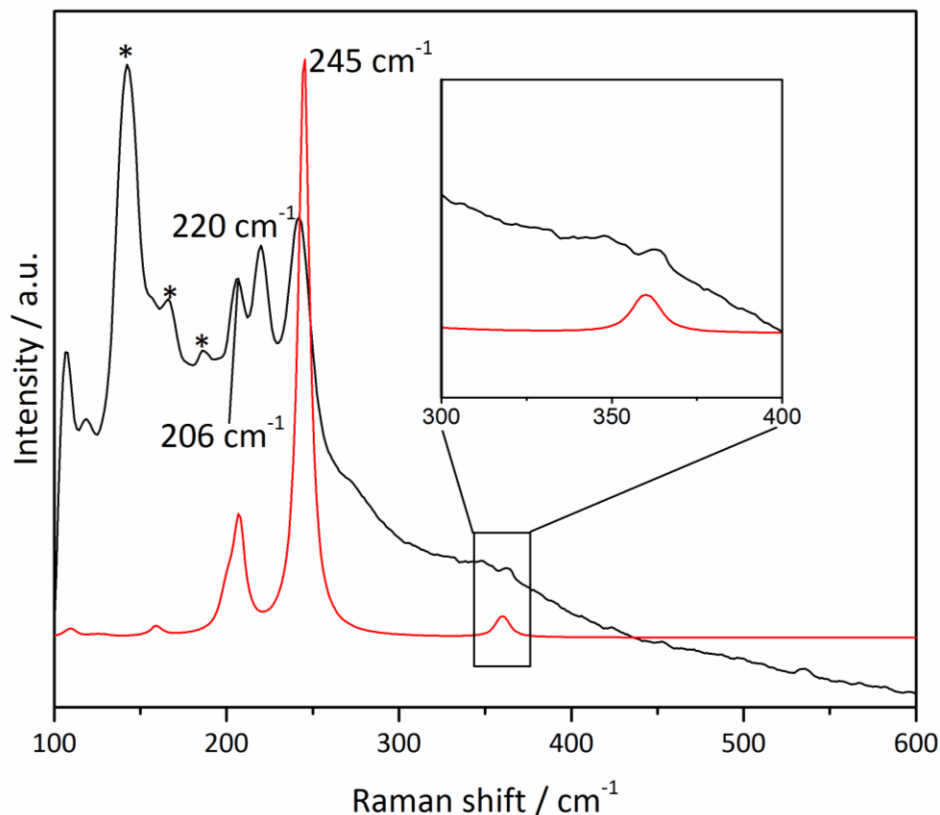


Figure 35: Raman spectrum of “ $\text{K}_5\text{Co}_{1.2}\text{Ge}_9$ ” (black) and $[\text{Co@Ge}_9]^{5-}$ (red). Enlarged part shows characteristic modes of the filled cluster at higher energies. The signals marked with “*” and the signal at 220 cm^{-1} can be attributed to the $[\text{Ge}_9]$ cluster.

Like the literature known examples with filled tin clusters, phases containing the cobalt filled $[\text{Ge}_9]$ cluster show a shift of the main signal towards higher energies as well as characteristic modes at higher energies. Analyzing the Raman spectrum several signals can be observed. A majority below 220 cm^{-1} can be assigned to $[\text{Ge}_9]^{4-}$ except the signal at 206 cm^{-1} which can be attributed to $[\text{Co@Ge}_9]^{5-}$ as seen by the calculated red spectrum (Figure 35). The signal at 245 cm^{-1} , which is the main cluster signal shifted to higher energies by the cobalt atom at the center, can also be attributed to the filled $[\text{Ge}_9]$ cluster. The characteristic signals at approximately 360 cm^{-1} consist of the vibrations **A** and **B**. The vibration of **B'** is shifted to higher energies and its intensity is so minimal compared to rest of the signals that it hardly be observed in the measured spectrum. Having proven the presence of the filled cluster unit in the bulk solid state phase no crystal

structure could be yielded from it. The phase is of purely amorphous nature which makes it difficult to crystallize the sample. Analyzing the sample using PXRD shows the presence of clusters, corroborating the Raman spectroscopy (Figure 103). The best agreement is found for the X-Ray pattern of $K_{12}Ge_{17}$. Additionally it shows that the binary phase CoGe is present in the sample (Figure 103) which is due to an incomplete reaction between the precursor and elemental potassium. DSC analysis shows two distinct signals, one originating from melting and recrystallization of CoGe (Figure 144).^[387] The other signal can only be observed in the first heating cycle which indicates an irreversible process at 541 °C (Figure 144). Raman analysis after the heating cycles shows the absence of any signals of the filled species indicating that the irreversible signals originates from the decomposition of the endohedral cluster (Figure 104). No change can be seen in the PXRD after the DSC, proving the Raman spectroscopy can serve as an important and more sensitive tool.

The sample is dissolved in liquid ammonia with some sequestering agents, 18-crown-6 and 2.2.2-crypt, in order to crystallize a compound that includes the $[Co@Ge_9]^{5-}$ unit, which is successful. The desired unit was isolated as $K_6[OH][Co@Ge_9] \cdot 16 NH_3$ as black single crystals from liquid ammonia and analyzed using single crystal X-ray diffraction (Table 59).

Table 16: Geometrical parameters for the $[\text{Co@Ge}_9]^{5-}$ in $\text{K}_6[\text{OH}][\text{Co@Ge}_9] \cdot 16 \text{ NH}_3$ cluster compared to the unfilled counterpart in $\text{K}_5[\text{OH}][\text{Ge}_9] \cdot 11 \text{ NH}_3$ ^[124].

	$[\text{Ge}_9]^{4-}$	$[\text{Co@Ge}_9]^{5-}$
SE ^a	22	22
h_1^b	1	1.25
h_2^b	1	1.25
h_3^b	1.34	1.28
γ^c	25.02	2.2
α_1^d	177.5	161.5
α_2^d	148.9	154.6
α_3^d	149.0	154.6
d_1 / d_2^e	1.03	1.12
symmetry	$\sim C_{4v}$	$\sim D_{3h}$
Volume / \AA^3	21.3	26.4
Volume change	19.4%	

^a no. of skeleton electrons assuming d^{10} configuration for the central atoms; ^b heights of the best trigonal prism, values are normalized to the shortest height of each tetrel element cluster; ^c angle between the basal faces of the best prism; ^d dihedral angle between the trigonal halves of

the possible planar faces of the best trigonal prism; ^e ratio of diagonals of the most planar square faces. e. g. the ratio of the heights as well as the tilting of the basal faces of the best trigonal prism ($1.0/0^\circ$ for D_{3h}) and the ratio of the diagonals as well as the dihedral angle of the triangular halves of the best square face ($1.0/180^\circ$ for C_{4v}).

Table 17: Interatomic distances of selected endohedral clusters in comparison to $[\text{Co@Ge}_9]^{5-}$.

$d(\text{TM-E}) / \text{\AA}$	
2.331(1) - 2.374(1)	$[\text{Co@Ge}_9]^{5-}$
2.267(3) - 2.410(2)	$[\text{Ni@Ge}_9]^{4-}$ ^[215]
2.479(1) - 2.525(1)	$[\text{Co@Ge}_{10}]^{3-}$ ^[210]
2.553(7) - 2.886(7)	$[\text{Co}_{0.68}\text{@Sn}_9]^{4-}$ ^[216]
2.518(2) - 2.702(2)	$[\text{Co}_{0.79}\text{@Sn}_9]^{4.79-}$ ^[217]

The charge of the filled cluster is undoubtedly -5 which is corroborated by six K^+ cations and one hydroxide anion per formula unit as determined from a single crystal structure determination. The cluster symmetry of $[\text{Co@Ge}_9]^{5-}$ is C_m , but the deviation from D_{3h} symmetry is small (Figure

36). Using the parameters elaborated in section 1.2, Figure 3 the cluster symmetry can be determined. Having almost equal prism heights [$h_1 = \text{Ge1-Ge3} = 3.5720(13) \text{ \AA}$; $h_2 = \text{Ge4-Ge5} = 3.4832(10)$; $h_3 = \text{Ge4}^i\text{-Ge5}^i = 3.4832(10) \text{ \AA}$] and isosceles, nearly coplanar prism triangles (2.2° between the Ge1/Ge5/Ge5^i and Ge2/Ge4/Ge4^i faces), $[\text{Co@Ge}_9]^{5-}$ can best be described as a slightly distorted tri-capped trigonal prism, which is an alternative to C_{4v} in 22 SE clusters (Table 16).^[58, 213] All nine Co-Ge contacts are almost identical between 2.331 \AA and 2.374 \AA which enables all Ge cluster atoms to lie on an almost perfect sphere and as close as possible around Co atom. These distances are also shorter than those in the $[\text{Co@Ge}_{10}]^{3-}$ cluster with Co-Ge bond distances between 2.48 \AA and 2.53 \AA . Similarly to the transition metal distances the Ge-Ge bond lengths are in the narrow range of 2.683 \AA to 2.811 \AA . As its congeners the $[\text{Co@Ge}_9]^{5-}$ unit seems to incorporate a transition metal with d^{10} valence electron configuration which results in the formal charge distribution $[\text{Co}^{1-}@\text{(Ge}_9\text{)}^{4-}]$. Anionic Co is known from several ligand-stabilized complexes,^[388-397] and recently $\text{Co}(-\text{I})$ has been found as guest-ion incorporated in $[\text{Sn}_9]$ Zintl clusters.^[388-391] The volume increase, compared to the empty counterpart $[\text{Ge}_9]^{4-}$, that is inherent with the endohedral nature of this cluster, is the highest to date with 19.4% (Table 16). The Ge-Ge distances are elongated by about 5% which probably is due to the fact that the Ge atoms are in a perfect sphere around the cobalt atom. The cluster seems to be stretched to a maximum with no additional room available to increase the volume further. The interatomic Co-Ge distances within the $[\text{Co@Ge}_9]^{5-}$ cluster lie between 2.35 and 2.37 \AA (Table 17), which is a bit shorter than the respective distances in compounds in the binary Co-Ge system^[398-402] of 2.34 to 2.73 \AA . The shortest distances are observed in monoclinic CoGe ^[401] which is synthesized at high pressures. On the other hand Ge-Ge distances in $[\text{Co@Ge}_9]^{5-}$ $2.683\text{--}2.811 \text{ \AA}$ are in the good agreement with those within the binary Co-Ge system ($2.43\text{--}3.03 \text{ \AA}$).^[398-402] As mentioned before the structure also contains hydroxide as an unintentional impurity, which is most likely caused by contaminated batches of $\text{NH}_3(\text{l})$. The hydroxide anion is coordinated by a distorted square pyramid of five K^+ ions with the hydroxide H atom located at the basal face of the pyramid. In addition, the K^+ ions are also coordinated by several ammonia molecules each, so a $[\text{K}_5(\text{OH})]^{4+}$ complex cation is formed (Figure 149, Figure 150). Similar ions are previously reported in $\text{K}_5[\text{OH}][\text{Ge}_9] \cdot 11 \text{ NH}_3$ ^[124] and in $\text{K}_5[\text{OH}][\text{Sn}_9] \cdot 11 \text{ NH}_3$.^[403]

DFT is used to calculate the optimized structure of $[\text{Co@Ge}_9]^{5-}$ as well as $[\text{Ge}_9]^{4-}$ which leads to D_{3h} and to C_{4v} symmetry respectively. Additionally single point calculations for empty $[\text{Ge}_9]^{4-}$ in C_{4v} and D_{3h} symmetry to derive an orbital interaction diagram, resulting in slightly different HOMO-LUMO gaps of 4.35 eV and 3.66 eV. The geometry is taken from the optimized structure of the filled clusters. The calculated interatomic distances agree well with the experimental data showing deviations of less than 0.06 Å or below 2% for all Ge-Ge and Ge-Co distances for the endohedral cluster which corroborates the structure optimization.

Table 18: HOMO-LUMO gap and point group for the calculated structures

	Point group	Gap / eV
$[\text{Co@Ge}_9]^{5-}$	D_{3h}	3.73
$[\text{Ge}_9]^{4-}$	D_{3h}	3.66
$[\text{Ge}_9]^{4-}$	C_{4v}	4.35

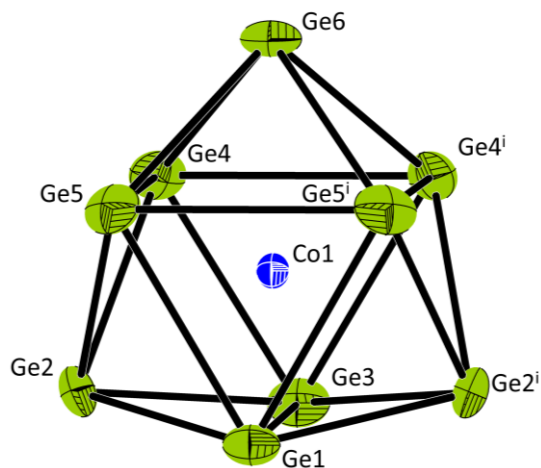


Figure 36: Exemplary endohedral cluster $[\text{Co@Ge}_9]^{5-}$. Thermal ellipsoids are drawn at 50 % probability level; symmetry operations: (i) $x, 0.5-y, z$.

4.3.4.2. Synthesis and characterization of a compound containing the endohedral $[\text{Ru}@\text{Sn}_9]^{6-}$ cluster

Syntheses to yield new endohedral tin clusters are also conducted several of different transition metals and similar molar ratios and temperature programs to the syntheses of the germanium congener (Chapter 6.6.4). One of these trials yields the solid state phase with the nominal composition of “ $\text{K}_4\text{Ru}_3\text{Sn}_7$ ” that contains the filled cluster $[\text{Ru}@\text{Sn}_9]^{6-}$ (Table 39). Again the Raman analysis of the bulk phase confirms the presence of the cluster unit prior to crystallization in the bulk phase. The main mode **G**, like the literature known endohedral tin cluster, is shifted to higher energies in the area of 170 cm^{-1} .

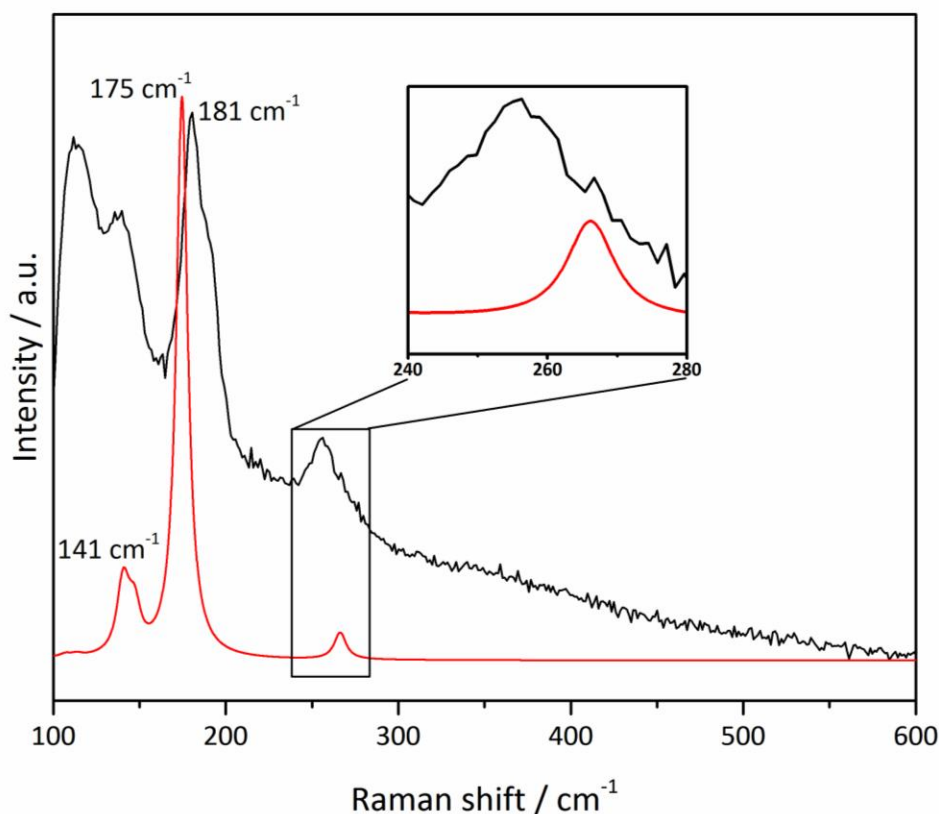


Figure 37: Raman spectrum of “ $\text{K}_4\text{Ru}_3\text{Sn}_7$ ” (black) and $[\text{Ru}@\text{Sn}_9]^{6-}$ (red). Enlarged part shows characteristic modes of the filled cluster at higher energies.

The characteristic signals also appear in the same region as the phases analyzed prior (section 4.3.2.2, Table 15) at around $240 - 280 \text{ cm}^{-1}$. These signal consist of the vibrations **A** and **B** while **B'** is shifted to higher energies around 286 cm^{-1} . A shoulder on the main cluster signal suggests the presence of $\text{K}_{12}\text{Sn}_{17}$, a mix of $[\text{Sn}_4]^{4-}$ and $[\text{Sn}_9]^{4-}$ clusters in the phase, but no other clusters can be identified in the solid state phase. Analyzing the solid state phase using PXRD clusters can be identified. The best agreement of known phases containing clusters is with $\text{K}_{12}\text{Sn}_{17}$, as before with the germanium species (Figure 105). DSC analysis in this case shows no signals and Raman and PXRD after the heating cycles do not show any change as well (Figure 145, Figure 106). This indicates that the filled clusters are stable up to 1000°C and do not decompose like the germanium sample.

Similarly to how the compound containing $[\text{Co}@\text{Ge}_9]^{5-}$ is crystallized, “ $\text{K}_4\text{Ru}_3\text{Sn}_7$ ” is dissolved in liquid ammonia with the sequestering agent 2.2.2-crypt. This yields a single crystal of the compound $\text{K}_7[\text{OH}][\text{Ru}@\text{Sn}_9] \cdot 10 \text{ NH}_3$ containing the anion $[\text{Ru}@\text{Sn}_9]^{6-}$ which is analyzed using single crystal X-ray diffraction (Table 62). The charge of the endohedral cluster in this compound is -6 , which can be derived from the presence of seven K^+ ions and one OH^- anion in the structure, similar to the situation in $\text{K}_6[\text{OH}][\text{Co}@\text{Ge}_9] \cdot 16 \text{ NH}_3$. The unit cell contains two symmetrically independent clusters **I** and **II**, which possess the same shape. Analyses of the geometrical parameters of these two clusters show again almost perfect D_{3h} -symmetric polyhedra, like it is the case in $[\text{Co}@\text{Ge}_9]^{5-}$ (Table 20, Figure 38). The Ru-Sn bond lengths are almost equal with a narrow range $2.641 - 2.700 \text{ \AA}$ (Table 19), same as the Sn-Sn bonding distances $(3.0512(8) - 3.1409(6) \text{ \AA})$.

Table 19: Interatomic distances of selected endohedral clusters in comparison to $[\text{Ru}@\text{Sn}_9]^{6-}$.

$d(TM-E) / \text{\AA}$	
2.612(2) - 2.711(1)	$[\text{Ru}@\text{Sn}_9]^{6-}$
2.651(1) - 2.771(1)	$[\text{Ru}@\text{Ge}_{12}]^{3-}$ [232]
2.553(1) - 2.886(1)	$[\text{Co}_{0.68}@\text{Sn}_9]^{4-}$ [216]
2.518(2) - 2.702(2)	$[\text{Co}_{0.79}@\text{Sn}_9]^{4.79-}$ [217]
2.487(3) - 2.784(2)	$[\text{Ni}@\text{Sn}_9]^{4-}$ [218]
2.611(7) - 2.700(7)	$[\text{Cu}@\text{Sn}_9]^{3-}$ [209]

The tetrel distances are in average elongated compared to those in empty $[\text{Sn}_9]^{4-}$ (typically below 3 Å). The endohedral Ru atom must also provide 10 electrons to the system, formally resulting in Ru(–II) which is again d^{10} configuration going with the trend set by other endohedral nine atomic clusters. While compounds containing Ru(–II) ions are rare, several complexes with isonitrile^[404] and biphosphinine^[405] ligands exist. The only known intermetalloid cluster, $[\text{Ru}@\text{Ge}_{12}]^{3-}$, formally contains Ru(–I).^[232] Comparing the D_{3h} symmetry of $[\text{Ru}@\text{Sn}_9]^{6-}$ to other known filled clusters like Co-filled and Ni-filled 22–electron clusters a discrepancy can be found. All other tin clusters, empty or filled, exhibit C_{4v} like $[\text{Sn}_9]^{4-}$,^[403] $[\text{Ni}@\text{Sn}_9]^{4-}$ ^[213, 218] and for the partially oxidized $[\text{Co}_{0.68}@\text{Sn}_9]^{4-}$ cluster with 21 SE.^[216]

Table 20: Geometrical parameters for the *TM*-centred cluster $[\text{Ru@Sn}_9]^{6-}$ in $\text{K}_7[\text{OH}][\text{Ru@Sn}_9] \cdot 10 \text{ NH}_3$ compared to the unfilled counterparts in $\text{K}_5[\text{OH}][\text{Sn}_9] \cdot 11 \text{ NH}_3$ ^[403].

	$[\text{Sn}_9]^{4-}$	$[\text{Ru@Sn}_9]^{6-}$ (I)	$[\text{Ru@Sn}_9]^{6-}$ (II)
SE ^a	22	22	22
h_1^b	1	1.25	1.25
h_2^b	1	1.26	1.25
h_3^b	1.28	1.28	1.22
γ^c	20.44	1.6	1.7
α_1^d	152.7	155.9	157.6
α_2^d	152.7	154.9	157.6
α_3^d	176.8	159.4	155.0
d_1 / d_2^e	1.03	1.11	1.17
symmetry	$\sim C_{4v}$	$\sim D_{3h}$	$\sim D_{3h}$
Volume / \AA^3	32.9	38.3	38.8
Volume change		16.4%	17.9%

^a no. of skeleton electrons assuming d^{10} configuration for the central atoms; ^b heights of the best trigonal prism, values are normalized to the shortest height of each tetrel element cluster; ^c angle between the basal faces of the best prism; ^d dihedral angle between the trigonal halves of the possible planar faces of the best trigonal prism; ^e ratio of diagonals of the most planar square faces. e. g. the ratio of the heights as well as the tilting of the basal faces of the best trigonal prism ($1.0/0^\circ$ for D_{3h}) and the ratio of the diagonals as well as the dihedral angle of the triangular halves of the best square face ($1.0/180^\circ$ for C_{4v}).

Like the previous structure, $\text{K}_7[\text{OH}][\text{Ru@Sn}_9] \cdot 10 \text{ NH}_3$ features a pyramidally coordinated hydroxide unit and is synthesized by dissolving the phase “ $\text{K}_4\text{Ru}_3\text{Sn}_7$ ” in liquid ammonia. The $[\text{K}_5(\text{OH})]^{4+}$ features the OH group on the basal plane of the pyramid and is coordinated by ammonia molecules (Figure 153, Figure 154). Because of the similarities of $[\text{Co@Ge}_9]^{5-}$ and $[\text{Ru@Sn}_9]^{6-}$ the same DFT calculations are been performed for the latter as well as for the empty

$[\text{Sn}_9]^{4-}$. In accordance to experimental findings the structure optimization leads to a D_{3h} symmetry for $[\text{Ru}@\text{Sn}_9]^{6-}$ and to C_{4v} symmetry for the empty clusters (Table 21).

Table 21: Point group and HOMO-LUMO gap for each calculated structure.

	Point group	Gap / eV
$[\text{Ru}@\text{Sn}_9]^{6-}$	D_{3h}	2.89
$[\text{Sn}_9]^{4-}$	D_{3h}	2.98
$[\text{Sn}_9]^{4-}$	C_{4v}	3.53

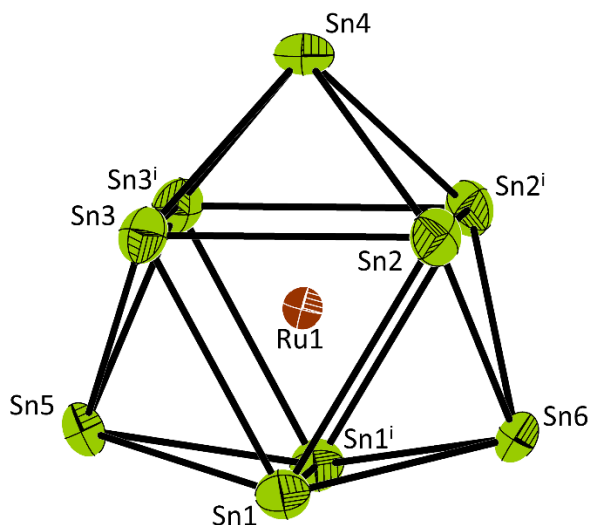


Figure 38: Endohedral cluster $[\text{Ru}@\text{Sn}_9]^{6-}$ (I). Thermal ellipsoids are drawn at 50 % probability level; symmetry operations: (i) $x, 0.5-y, z$.

The single point calculations for the empty cluster $[\text{Sn}_9]^{4-}$ are performed in both D_{3h} and C_{4v} symmetry to derive an orbital interaction diagram, resulting in slightly different HOMO-LUMO gaps of 2.98 eV and 3.53 eV, respectively. The geometry is taken from the optimized structure of the filled clusters. The calculated interatomic distances agree well with the experimental data and show deviations of less than 0.06 Å or below 2 % which corroborates the optimized structure. Analysing the volume increase of the ruthenium filled $[\text{Sn}_9]$ unit the same trend as with the other filled tin clusters can be observed. With an increase of Sn-Sn bond lengths comes a substantial increase of cavity volume of 17.9% for $[\text{Ru}@\text{Sn}_9]^{6-}$ (I) and 16.4% for $[\text{Ru}@\text{Sn}_9]^{6-}$ (II). This equals an average increase of 17.2% for this cluster species compared to the empty $[\text{Sn}_9]^{4-}$ which is the

largest increase in volume ever recorded for a tin cluster. Furthermore it is the second largest volume increase period, with only $[\text{Co@Ge}_9]^{5-}$ having a larger volume increase (Table 12).

4.3.4.3. Synthesis and characterization of a compound containing the endohedral $[\text{Rh@Sn}_9]$ cluster

Analysing the phase with the nominal composition $[\text{Na}_{13}\text{RhSn}_{17}]$ (Table 39) there is a high probability of that phase containing the $[\text{Rh@Sn}_9]^{5-}$ anion. Experimental data shows good agreement with the simulation of the Raman spectrum (Figure 39). No crystal could be isolated from the liquid ammonia solution of $[\text{Na}_{13}\text{RhSn}_{17}]$.

However a single crystal, which after analysis by single crystal diffraction, consists of a compound containing a rhodium filled tin cluster, could be isolated from a liquid ammonia solution of $[\text{K}_5\text{RhSn}_9]$ (for more information on $[\text{K}_5\text{RhSn}_9]$ see Table 39), a phase similar to $[\text{Na}_{13}\text{RhSn}_{17}]$. A rhodium filled tin cluster in conjunction with the previously reported pyramidal hydroxide unit can be found (Table 65). The phase with the nominal composition $[\text{K}_5\text{RhSn}_9]$ was not analyzed using Raman spectroscopy but due to the fact that a compound containing the $[\text{Rh@Sn}_9]$ cluster can be isolated from liquid ammonia strongly suggests the presence of the cluster already in $[\text{K}_5\text{RhSn}_9]$. Due to the low quality of the single crystal the space group determination was unclear. Structure refinement was carried out with space group I_4/mmm but making exact statements about bond lengths or angles is difficult. It was possible to determine the $[\text{Rh@Sn}_9]$ anion. Furthermore R -values are not yet in a range where the structure is definitive. Additionally the refinement is not yet good enough to have a definitive sum formula which makes statements about the charge of the cluster impossible. Because of this the cluster will be henceforth referred to as $[\text{Rh@Sn}_9]$ without a given charge. However the filled cluster can clearly be seen and thus will be discussed to the extent possible.

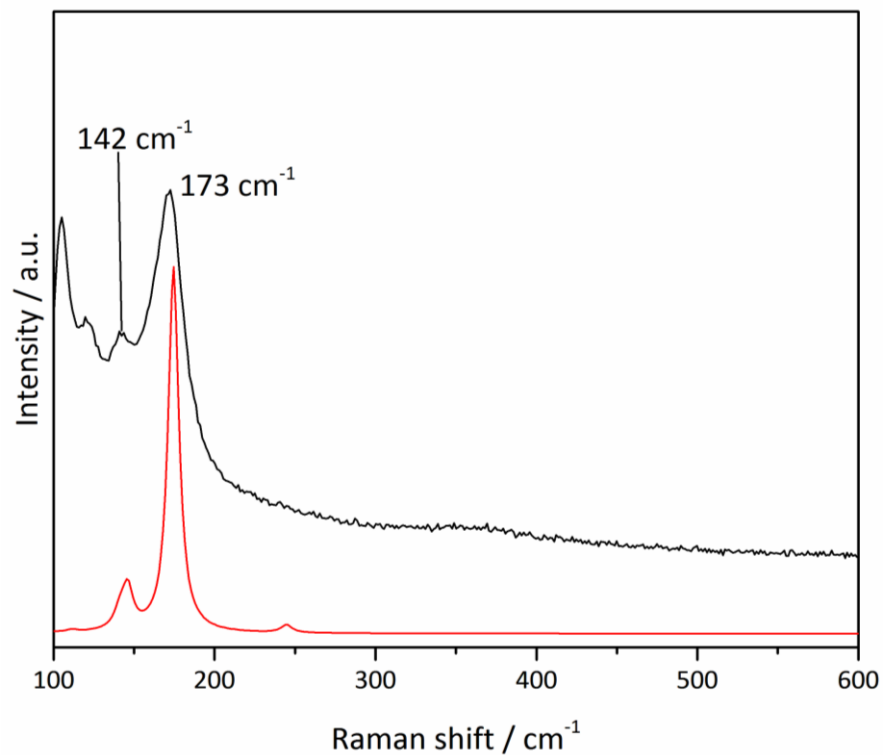


Figure 39: Raman spectrum of “Na₁₃RhSn₁₇” (black) and [Rh@Sn₉]⁵⁻ (red).

As opposed to its congeners, [Rh@Sn₉] shows cluster symmetry that can best be approximated with C_{4v} instead of D_{3h} , which can be seen by the ratio being $d_1/d_2 = 1$ (Figure 40). Further analysis of the geometrical parameters is not done because of the previously mentioned facts.

Beside the cluster a pyramidal hydroxide unit is probably crystallized. As with the previously mentioned clusters, the volume of the cage increases with the expansion of the $E-E$ bond lengths. Here the bond lengths are 2.92 – 3.40 Å which equals an increase in regards to the empty [Sn₉] unit which in turn leads to a volume increase of 14.6%.

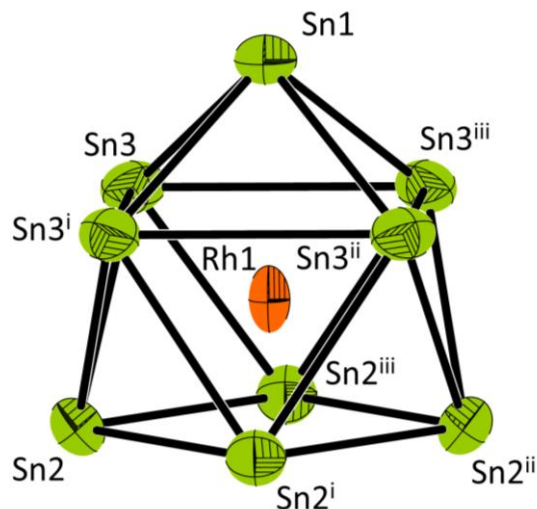


Figure 40: Endohedral cluster $[\text{Rh}@\text{Sn}_9]$. Thermal ellipsoids are drawn at 50 % probability level. Symmetry operations: (i) $y, -x, z$; (ii) $-x, -y, z$; (iii) $-y, x, z$.

The structure refinement suffers from the fact that the symmetry cannot be reliably refined. Refinement with the tetragonal space group I_4/mmm leads to the situation that the fourfold symmetry axis runs through the central atom of the $[\text{Rh}@\text{Sn}_9]$ cluster. The inspection of the electron density reveals that the capping Sn1 as well as all other tin atoms of the cluster are fully occupied, whereas the second capping atom Sn4 is occupied by 24%. This leads to the assumption of a superposition of a $[\text{Rh}@\text{Sn}_9]$ and $[\text{Rh}@\text{Sn}_{10}]$ unit with 76% and 24%, respectively (Figure 41). This reduced occupation of the Sn4 atom also results in different Rh-Sn distances of the capping atoms ($d(\text{Rh1-Sn1}) = 2.771(4) \text{ \AA}$; $d(\text{Rh1-Sn4}) = 3.33(1) \text{ \AA}$).

$[E_{10}]$ units most often appear as a pentagonal prism,^[210, 221-222] but the approximated bicapped, square antiprism is not unprecedented as can be seen by examples like $[\text{Ni}@\text{Pb}_{10}]^{2-}$ ^[225] and $[\text{Rh}@\text{Sn}_{10}]^{3-}$ ^[223]. As mentioned before, since the refinement is not yet finalized no reliable statements about the cluster charge can be made, be it of the clusters individually or in combination.

If rhodium in this cluster also follows the d^{10} trend it would fit the other known endohedral $[E_9]$ units. As found for the other endohedral cluster, Rh(-I) is reported in several complex

conformations.^[406-407] There are several other instances of rhodium inside a cluster unit – $[\text{Rh@Pb}_{12}]^{3-}$ ^[236] and in the recent publication of Sun *et al.*, which features several rhodium filled clusters including $[\text{Rh@Sn}_{10}]^{3-}$, $[\text{Rh@Sn}_{12}]^{3-}$, $[\text{Rh}_2\text{@Sn}_{17}]^{6-}$ and the new triply-fused stannide, $[\text{Rh}_3\text{@Sn}_{24}]^{5-}$.^[223] The Rh-Sn distances (Table 22) are shorter than the distances found in the binary RhSn system (2.70 – 2.99 Å),^[408-411] as is the case for the previously discussed endohedral species. The interatomic distances are also in good agreement with congeners of Rh-Sn clusters known. Even the distances of the $[\text{Rh@Pb}_{12}]^{3-}$ show good agreement even though clusters containing lead usually show increased bond lengths.

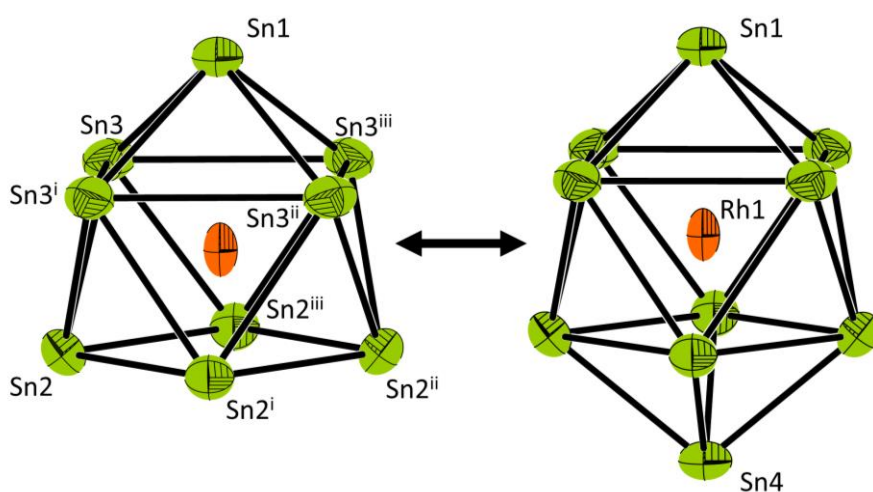


Figure 41: $[\text{Rh@Sn}_9]$ unit in its two configurations. The middle cluster shown is depicting the superposition of the separate units. Symmetry operations: (i) $y, -x, z$; (ii) $-x, -y, z$; (iii) $-y, x, z$.

While the publication of Sun *et al.* contains the larger filled cluster species like $[E_{10}]$, $[E_{12}]$ and $[E_{17}]$ and in ESI-MS measurements even $[\text{Rh@Sn}_8]^-$, the $[E_9]$ species with $[\text{Rh@Sn}_9]$ is missing. The structure and solid state Raman analysis thus would fill the gap and completes this group of clusters. Interestingly the report shows the optimised structure of $[\text{Rh@Sn}_8]^-$ to be a tub form which was first reported by Fässler *et al.*^[183, 412] and shown to be a structural theme in many other clusters.^[118]

Table 22: Interatomic distances of selected endohedral clusters in comparison to $[\text{Rh@Sn}_9]^{5-}$.

$d(TM-E) / \text{\AA}$	
2.6183(1) – 2.7708(4) ^a	$[\text{Rh@Sn}_9]$
2.6792(14) – 2.887(4)	$[\text{Rh@Sn}_{10}]^{3- [223]}$
2.8781(4) – 2.9498(5)	$[\text{Rh@Sn}_{12}]^{3- [223]}$
2.4974(5) – 2.7607(5)	$[\text{Rh}_2\text{@Sn}_{17}]^{6- [223]}$
2.6586(9) – 3.058(1)	$[\text{Rh}_3\text{@Sn}_{24}]^{5- [223]}$
2.984(1) – 3.027(1)	$[\text{Rh@Pb}_{12}]^{3- [236]}$

^a – Distances in this cluster are of the fully occupied Rh and Sn positions only. The Rh-Sn distance the 24% occupied Sn atom is 3.32(1) \AA .

It is difficult to accurately discuss the $[\text{Rh@Sn}_9]$ cluster because of the crystal quality and symmetry problem but this structure clearly shows that the crystallization of such a cluster is possible. Further experiments could yield a sufficiently good crystal to finalize the structure refinement exhibited here.

4.3.4.4. Synthesis and characterization of a compound containing the endohedral $[\text{Co@Sn}_9]^{5-}$ cluster

A new compound with a previously reported structural unit was isolated from liquid ammonia in the form of $\text{K}_6[\text{OH}][\text{Co@Sn}_9] \cdot 17 \text{NH}_3$ (Figure 42, Figure 157, Table 68) and was analyzed using single crystal diffraction. It forms by a reaction of $\text{NHC}^{\text{Dipp}}\text{-Cu-Cl}$ and “ $\text{K}_5\text{Co}_3\text{Sn}_9$ ” in liquid ammonia (Table 40). $\text{NHC}^{\text{Dipp}}\text{-Cu-Cl}$ was provided by Dr. Felix Geitner, Chair of Inorganic Chemistry with Focus on Novel Materials. This chloride ion crystallizes with the structures as a result of the presence of the $\text{NHC}^{\text{Dipp}}\text{-Cu-Cl}$. This is added to the solution to yield compounds similar to the one reported by Dr. Felix Geitner in the form of $\text{NHC}^{\text{Dipp}}\text{-Ag-}[\text{Sn}_9]$.^[137]

Table 23: Geometrical parameters for the *TM*-centred cluster $[\text{Co@Sn}_9]^{5-}$ compared to the unfilled counterparts in $\text{K}_5[\text{OH}][\text{Sn}_9] \cdot 11 \text{NH}_3^{[403]}$ and the filled “[Co@Sn₉]⁵⁻” cluster with the correct electron configuration of d^{10} .

	$[\text{Sn}_9]^{4-}$	“ $[\text{Co@Sn}_9]^{5-}$ ” ^f	$[\text{Co@Sn}_9]^{5-}$
SE ^a	22	22	22
h_1^b	1	1.07	1.07
h_2^b	1	1.11	1.16
h_3^b	1.28	1.28	1.28
γ^c	20.44	14.31	12.47
α_1^d	152.7	152.2	146.4
α_2^d	152.7	151.7	154.6
α_3^d	176.8	171.6	170.8
d_1 / d_2^e	1.03	1.06	1.07
symmetry	$\sim C_{4v}$	$\sim C_{2v}$	$\sim C_{2v}$
Volume / Å ³	32.9	35.3 ^f	36.1
Volume change		7.3%	9.7%

^a no. of skeleton electrons assuming d^{10} configuration for the central atoms; ^b heights of the best trigonal prism, values are normalized to the shortest height of each pure tetrel element cluster; ^c angle between the basal faces of the best prism; ^d dihedral angle between the trigonal halves of the possible planar faces of the best trigonal prism; ^e ratio of diagonals of the most planar square faces. e. g. the ratio of the heights as well as the tilting of the basal faces of the best trigonal prism (1.0/0° for D_{3h}) and the ratio of the diagonals as well as the dihedral angle of the triangular halves of the best square face (1.0/180° for C_{4v}); ^f mean value of $[\text{Co}_{0.68}\text{@Sn}_9]^{4.68-[216]}$ and $[\text{Co}_{0.79}\text{@Sn}_9]^{4.79-[216]}$ clusters.

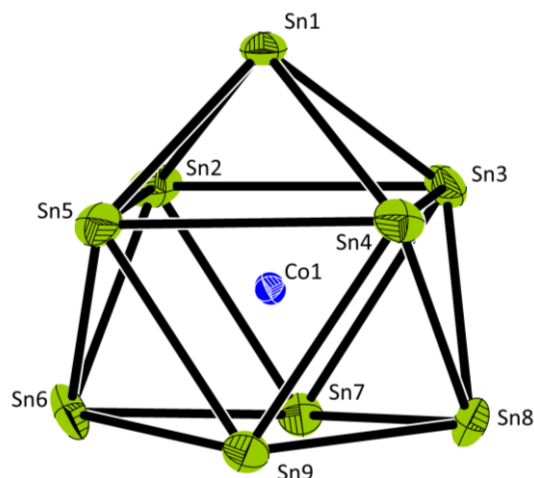


Figure 42: Endohedral cluster $[\text{Co}@\text{Sn}_9]^{5-}$. Thermal ellipsoids are drawn at 50 % probability level.

The compound consists several potassium ions coordinated by ammonia, a hydroxide anion as well as the previously reported, filled $[\text{Co}@\text{Sn}_9]$ cluster unit.^[213, 216-217] Six potassium ions are present to balance the charge of the cluster and the hydroxide ion in the compound. Because of this the cobalt probably exhibits d^{10} in this compound, which is in line with the reported structures and other filled $[\text{E}_9]$ units. In the case of the $[\text{Co}@\text{Sn}_9]$ cluster the cobalt position shows 100% occupancy, unlike the reported compounds where the occupancy is lower.^[216-217] Bond lengths, Sn-Sn (2.9760(6) – 3.7487(6) Å) and Co-Sn (2.5938(8) – 2.6545(7) Å), are not affected by the reduced charge of the cluster and are almost identical to the reported distances.^[213, 217]

When comparing the geometrical parameters of the present cluster to previously reported cobalt filled clusters several differences can be observed. While the unfilled clusters clearly exhibits bonds lengths and angles that show that the clusters has C_{4v} symmetry the examined $[\text{Co}@\text{Sn}_9]^{5-}$ cluster does not. The prism heights and angles show that a deviation from the ideal $d_1/d_2 = 1$ of a C_{4v} symmetric cluster (Table 23). However this deviation is not significant enough to result in D_{3h} symmetry of the cluster which is characterized by $h_1 = h_2 = h_3$. As detailed in chapter 1.2 if the cluster does not show the geometrical signs that can be attributed it to either one of the “extremes” of the possible symmetries, C_{4v} or D_{3h} , the symmetry can be in between the two. This is most likely the case with the present filled cluster which shows geometrical parameters which indicate C_{2v} symmetry.

The volume increase of the $[\text{Co@Sn}_9]^{4-}$ and $[\text{Co@Sn}_9]^{5-}$ clusters is 9.7% and 7.3%, respectively, which can be attributed to the fact that the former cluster has a cobalt position with 100% occupancy while the latter only has around 75% occupancy. Like the previous structures the cluster again crystalizes with a hydroxide ion which is pyramidally shielded by potassium ions.

4.3.4.5. Presence of hydroxide units $\text{K}_5[\text{OH}]$ as a way of enhancing cell packing

An interesting fact is that all newly discovered compounds containing endohedral cluster species are found with a pyramidal $(\text{K}_5[\text{OH}])^{4+}$ (Figure 43) unit in the structure. As mentioned this is most likely the result of contaminated liquid ammonia. Since the phases are synthesized from the same tetrel elements and alkali metal this is also a probable origin of the contamination.

As mentioned before these compounds are not the first ones containing the hydroxide unit. Several structure containing $[\text{E}_9]$ ($\text{E} = \text{Ge}, \text{Sn}$) clusters are known that also contain the pyramidal unit.^[124, 403] The fact that multiple compounds exist with this hydroxide unit leaves the question that maybe this pyramidal unit is beneficial for the crystallization of compounds containing cluster and especially endohedral ones. The hydroxide unit might be aiding the crystallization process supplanting sequestering agents as the more advantageous co-crystallization medium. When comparing the volume of clusters and these pyramidal units a discrepancy can be found. While, depending on the element in question, the cluster volume can vary between 20 and 35 Å³ the volume of the pyramidal unit is constant at around 13 Å³ (Table 24).

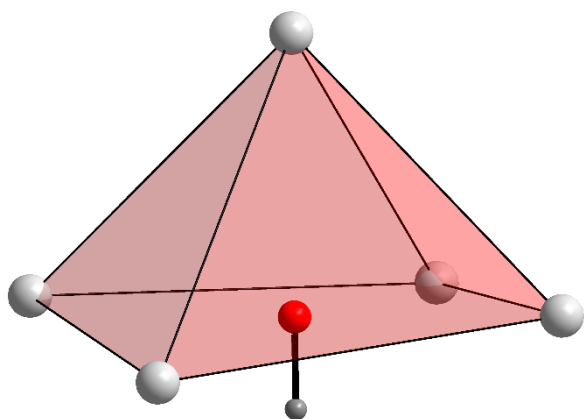


Figure 43: Pyramidal $(K_5[OH])^{4+}$ unit found in several compounds containing endohedral and non-filled clusters. grey – potassium; red – oxygen; dark grey – hydrogen. Atoms are displayed as balls and sticks.

Table 24: Crystallographic units with their respective approximate crystallographic volume in \AA^3

Crystallographic unit	Approx. volume / \AA^3
$[Ge_9]^{4-}$	22
$[Sn_9]^{4-}$	33
$(K[18\text{-crown-6}])^+$	5
$(K[2.2.2\text{-crypt}])^+$	80
$(K_5[OH])^{4+}$	13

The size of sequestering agents such as 18-crown-6 and 2.2.2-crypt varies drastically between 5 \AA^3 and 80 \AA^3 respectively. The extremely low volume can be explained by the almost planar structure of the $[K(18\text{-crown-6})]^+$ ion. With its ability to leave the potassium able to coordinate to any anion structure the volume is not the deciding factor for crystallization. Both agents are known to crystallize well with the cluster species. Taking into consideration the first coordination sphere of the pyramidal unit, consisting of ammonia molecules, the size can be upwards of 100 \AA^3 which is much larger than the cryptand when it is coordinating alkali metal ions. Another aspect that is critical to the crystallization process is the charge of the co-crystallization unit. While the size might be only in approximate agreement with the cluster, the hydroxide unit exhibits an overall charge of +4. Unlike its sequestering congeners, which show the charge of +1 of the alkali metal ion, only one of these units is needed to compensate the charge of a normal $[E_9]^{4-}$ unit. This makes it a prime candidate to crystallize with the endohedral clusters. Because of their high charge these species are hard to dissolve and equally difficult to crystallize. With the addition of such a unit there is only the need for one or two extraneous alkali metal ions, sequestered or not, to stabilize the cluster unit's high charge. Usually this has to be done by the same number of alkali

metals as the charge which is hard to pack efficiently against the single charge carrier of the cluster unit. The charge combined with the size are a possible explanation why the endohedral species frequently co-crystallize with the pyramidal hydroxide unit.

4.3.5. DFT enhanced Raman analysis of new ternary phases containing endohedral clusters

Further synthesis of ternary phases are described in section 6.6.4. The goal was to synthesize new phases containing novel, endohedral clusters or phases containing clusters only characterized from compounds found from solution.

First the synthesis of a solid state phase containing $[\text{Ni}@\text{Ge}_9]^{4-}$ is attempted. Detailed synthesis parameters can be found in chapter 6.6.4.2. Starting point was the combination of K-Ni-Ge in a ratio of 4–1–9 and the same temperature program is as used in the synthesis of “ $\text{K}_5\text{Co}_{1.2}\text{Ge}_9$ ”. This however was not successful in yielding the desired phase. Several trials with different molar ratios and temperature programs are used in order to produce a phase with the right composition (Figure 66, Table 41). The correct temperature range is finally found with holding at 1000 °C for 24 hours and additionally at 650 °C for 30 hours with a molar ratio of K-Ni-Ge/4–3–9. The analysis of the phase is repeated using Raman spectroscopy and the calculated spectrum of $[\text{Ni}@\text{Ge}_9]^{4-}$. The structure data used to calculate the spectrum is taken from literature.^[215] During the calculation the ideal charge was assumed -4 instead of the recorded -3. Comparing the measured spectrum to the calculated spectrum a close resemblance can be found. Like before the synthesized sample contains the desired filled cluster but additionally also the empty $[\text{Ge}_9]^{4-}$ cluster. All signals of the filled cluster can be found in the shifted main signal as well as the characteristic signals at higher energies (Figure 44). The main mode **G** is shifted by about 20 cm^{-1} which is in line with the phase containing $[\text{Co}@\text{Ge}_9]^{5-}$. As before the characteristic mode that is visible in the measured spectrum consist of the vibrations **A** and **B** while the **B'** vibration has an intensity so small compared to the rest that it cannot be observed.

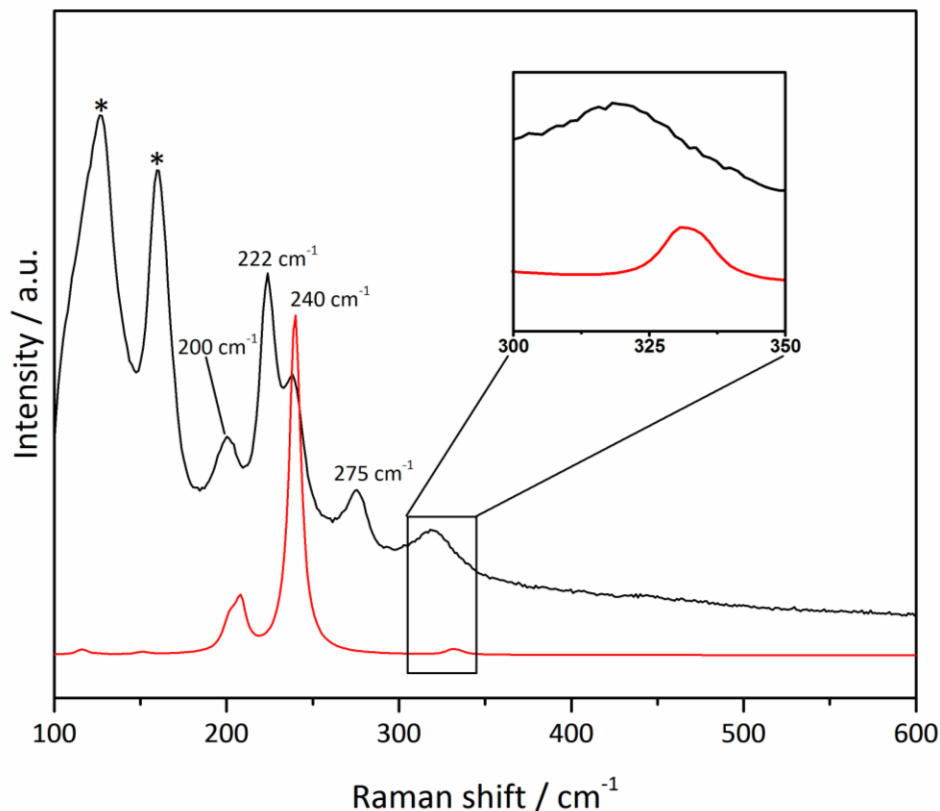


Figure 44: Raman spectrum of “ $K_4Ni_3Ge_9$ ” (black) and $[Ni@Ge_9]^{4-}$ (red). Enlarged part shows characteristic modes of the filled cluster at higher energies. Signals marked with “*” can be attributed $K_{12}Ge_{17}$.

A signal around 275 cm^{-1} can be attributed to either $K_{12}Ge_{17}$ (in addition to signals marked with “*”) or elemental, amorphous germanium. While the synthesis is successful in creating a bulk solid state phase that contains the endohedral cluster unit no crystallization is achieved yet. However as mentioned before a structure of $[Ni@Ge_9]^{3-}$ is already recorded in literature with some crystallographic flaws. This synthesis was only successful once in several tested experiments. All attempts to recreate the synthesis are unsuccessful so far. However, the extremely good agreement of the calculated and measured spectrum still shows that the synthesis is indeed possible and was successful.

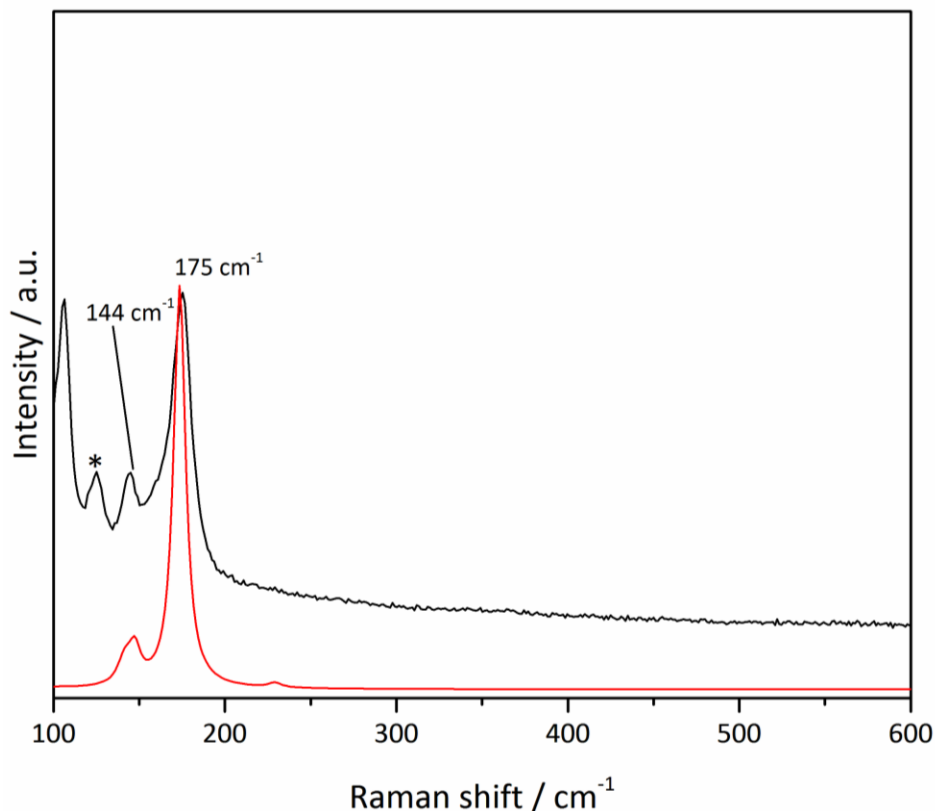


Figure 45: Measured Raman spectrum of “Na₁₂Pd₂Sn₁₇” (black) and calculated spectrum of [Pd@Sn₉]⁴⁻ (red. This spectrum is treated with a scale factor of 1.04.^[380] Table 25 shows corrected values. Table 49 shows original values).

Additionally a phase with the nominal composition of “Na₁₂Pd₂Sn₁₇” (Table 39) was examined using Raman spectroscopy and shows the signals of a filled [Sn₉] cluster in the form of [Pd@Sn₉]⁴⁻ (Figure 45). The cluster charge is assumed to be the ideal -4 resulting from a Pd(0) in the form of [(Pd)^{±0}@(Sn₉)⁴⁻]⁴⁻ and thus not contributing any electrons to the cage unit. As before the cluster shows a shift of the main signal to higher energies by about 30 cm⁻¹ with new signals around 175 cm⁻¹. These new signals show only miniscule intensities compared to the main signal of the cluster unit thus they cannot be observed in the measured spectrum. Regardless of this fact, they consist of the same characteristic vibrations of the cage structure **A**, **B**, **B'**. Unlike the previous cases, this cluster could not be isolated from solution. Several attempts using different sequestering agents like 18-crown-6 and 2.2.2-crypt were unsuccessful in yielding a crystal

structure. However Dr. Marina Boyko was successful in isolating a single crystal from a solid state sample and analysing it using single crystal diffraction, thus corroborating the Raman analysis.^[385]

Summarizing the acquired Raman data everything shows a similar picture compared to the samples characterized in literature. A shift of the main signal occurs and new characteristic modes appear. Both signal groups show good agreement of measured and calculated signals. This technique provides a way to detect endohedral clusters in solid state phases.

Table 25: Main signals and characteristic signals of endohedral cluster units. (Raman shifts of the $[\text{Pd@Sn}_9]^{4-}$ cluster are treated with a scale factor of 1.04.^[380] Table 49 shows original values).

Endohedral cluster	Main signal / cm^{-1} (calc.)	Main signal / cm^{-1} (exp.)	Characteristic signal / cm^{-1} (calc.)	Characteristic modes
$[\text{Co@Ge}_9]^{5-}$	245	242	358, 361, 398	A, B, B'
$[\text{Ni@Ge}_9]^{4-}$	240	238	330, 334, 371	
$[\text{Ru@Sn}_9]^{6-}$	175	181	265, 266, 286	A, B, B'
$[\text{Rh@Sn}_9]^{5-}$	174	173	244, 245, 268	
$[\text{Pd@Sn}_9]^{4-}$	173	175	228, 230, 255	

4.3.6. Fragmentation of endohedral clusters in liquid ammonia

Several new compounds featuring structure motifs with new and reported compositions have been isolated from liquid ammonia and analyzed using single crystal X-ray diffraction. All these compounds have been synthesized through reaction of a nominally endohedral solid state phase in liquid ammonia.

4.3.6.1. Synthesis and characterization of a compound containing the endohedral $[\text{Co}_2@\text{Ge}_{17}]^{6-}$ cluster

A new compound in the form of $[\text{K}(\text{2.2.2-crypt})]_2\text{K}_4[\text{Co}_2@\text{Ge}_{17}] \cdot 13 \text{ NH}_3$, was characterized using single crystal diffraction (Table 71). This new compound contains a cobalt filled germanium cluster was found after the reaction of “ K_5CoGe_9 ” (Table 40) and $\text{TiCp}_2(\text{NH}_3)_2\text{Cl}$ in liquid ammonia. $\text{TiCp}_2(\text{NH}_3)_2\text{Cl}$ was provided by Dr. Felix Geitner, Chair of Inorganic Chemistry with Focus on Novel Materials. The structural motif of this new unit is already known as two nine-atomic cluster joined by one vertex atom $[\text{TM}_2@\text{E}_{17}]^{n-}$ and is mentioned in section 1.3.3. Though the exact formation mechanism cannot be determined reliably the new double cluster is most likely formed through oxidation and fragmentation induced by the titanium complex.

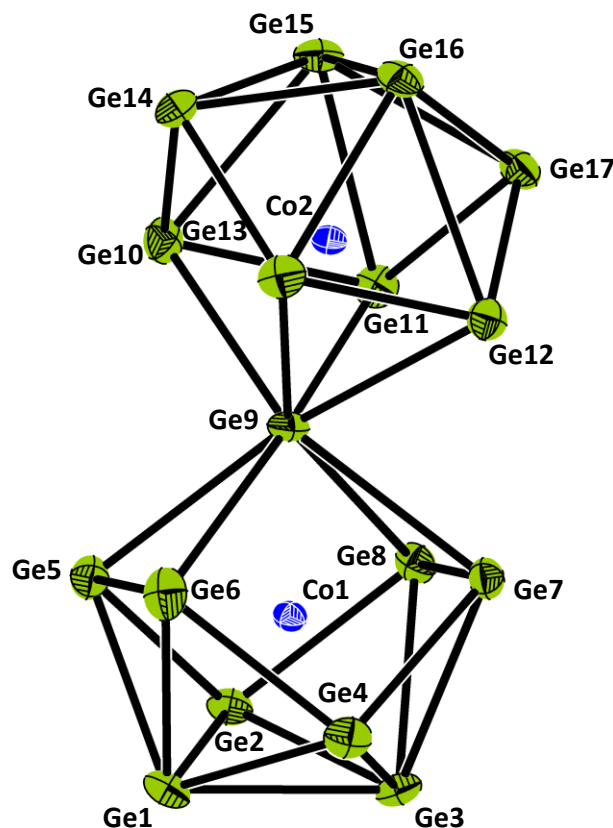


Figure 46: New endohedral cluster $[\text{Co}_2@\text{Ge}_{17}]^{6-}$ isolated from liquid ammonia. Thermal ellipsoids are displayed with 50% probability.

Alongside the $[\text{Co}_2@\text{Ge}_{17}]^{6-}$ four free and two potassium ions coordinated by 2.2.2-crypt, as well as 13 ammonia molecules can be found. $[\text{Co}_2@\text{Ge}_{17}]^{6-}$ and the nickel equivalent are the first compounds which contain a filled, nine atomic germanium cluster doublet. Several compounds containing the heavier congener tin have been found with the same transition metals $\text{Co}^{[216]}$, $\text{Ni}^{[244]}$ and in addition $\text{Rh}^{[223]}$ has been reported.

All the mentioned combined clusters feature two nine-atomic clusters joined on vertex atom with both cavities being filled by one transition metal atom. Another structure motif closely related to the 17 vertex cluster is the 18 vertex where the one extra atom leads to a more cigar shaped cluster which only has one large cavity where both transition metal ions reside. Examples of this are $[\text{Pd}_2@E_{18}]$ ($E = \text{Ge}^{[245]}$, $\text{Sn}^{[211, 246]}$), $[(\text{Ni-Ni-Ni})@\text{Ge}_{18}]^{4- [215]}$ and $[\text{Pt}_2@\text{Sn}_{17}]^{4- [219]}$.

Table 26: Comparison of bond lengths and TM-E-TM angles in several reported and new 17-atomic clusters.

	$d(E-E)_{\text{intra}} / \text{\AA}$	$d(E-E)_{\text{inter}} / \text{\AA}$	$d(\text{TM}-E) / \text{\AA}$	$\angle (\text{TM}-E-\text{TM}) / ^\circ$
$[\text{Co}_2@\text{Ge}_{17}]^{6-}$	2.605(1) –	2.897(1) –	2.192(1) –	168.85(5)
	2.939(1)	4.033(1)	2.462(1)	
$[\text{Ni}_2@\text{Ge}_{17}]^{4-a}$	2.589(1) –	2.5274(6) –	2.147(3) –	180
	2.825(1)	3.4208(2)	2.434(1)	
$[\text{Co}_2@\text{Sn}_{17}]^{5- [216]}$	2.945(1) –	3.107(1) –	2.406(1) –	165.51(5)
	3.2628(9)	4.277(1)	2.769(1)	
$[\text{Rh}_2@\text{Sn}_{17}]^{6- [223]}$	2.9332(7) –	3.2216(6) –	2.4974(8) –	163.89(3)
	3.3051(6)	4.6317(8)	2.7606(6)	
$[\text{Ni}_2@\text{Sn}_{17}]^{4- [244]}$	2.9713(4) –	3.1177(3) –	2.3822(6) –	180
	3.2086(3)	3.6244(4)	2.7403(4)	

^a – the interstitial germanium atom in this case is split into two distinct atoms which makes definitive statements about bond lengths and angles problematic. For the angle analysis an ideal middle atom is used. This cluster is examined by Christoph Wallach, M. Sc., Chair of Inorganic Chemistry with Focus on Novel Materials.

While the 17 vertex double cages all share the same structural motif, several distinct variations exist in between the different structures. The base element can be seen having perfectly lined up nine-atomic cages which means the angle $\text{TM}-E_{\text{central}}-\text{TM}$ is exactly 180° . This is the case with $[\text{Ni}_2@E_{17}]^{4-}$ ($E = \text{Ge}, \text{Sn}$), which leads to the ideal symmetry of D_{2d} .

Comparison of the bond lengths in both the cobalt filled and nickel filled is problematic because of the split position of the middle germanium in the case of the nickel example. The Ge-Ge distances in the clusters however are in the same range of around 2.7 \AA . The same goes for the tin examples already reported in literature – they all show comparable distances in the clusters as well as between the separated cluster units (Table 26). In case of the $\text{TM}-E$ distance the same is true when comparing the different tetrel elements – similar ranges without any major inconsistencies. When comparing the $\text{TM}-E$ distances between the $[\text{Co}@\text{Ge}_9]$ doublet with the isolated $[\text{Co}@\text{Ge}_9]$ cluster an increase in the range can be observed. This is due to the shared vertex atom which lies further away from the central cobalt atom. The remaining distances are in line with the isolated $[\text{Co}@\text{Ge}_9]^{5-}$ unit. It is of note that the short bond lengths are usually between the middle tetrel atom and the transition metals while the rest are elongated compared to that. The nickel filled cluster units represent the ideal symmetry of this unit – D_{2d} . This comes from the fact that in these cases the $\text{TM}-E-\text{TM}$ angle is 180° . When another transition metal is present in the cages the angle becomes more acute and the top unit is tilted in whole. This can be seen both in the examples of the tin clusters as well as in the example of the germanium cluster. The tilting of the cluster unit is always around 165° and slightly less when a second period transition metal is encapsulated. While no clear rule can be seen since the sample size is limited a trend can be observed where if the transition metal is neutral the angle is 180° resulting in a straight cluster condensate. If the transition metal is charged, as is the case with cobalt and rhodium, the angle shrinks linearly with the size of the incorporated element.

Table 27: Volume increase of [TM₂@Sn₁₇] (TM = Co, Rh, Ni) and [TM₂@Ge₁₇] (TM = Co, Ni) units when compared to the corresponding [E₉]⁴⁻ (E = Ge, Sn) unit. The values are mean values of the vertex combined [Sn₉] clusters present in the compounds.

	Clustervolume / Å ³	Volume change
[Ge ₉] ⁴⁻	22.1	
[Co ₂ @Ge ₁₇] ⁶⁻	26.7	20.8%
[Ni ₂ @Ge ₁₇] ^{4-a}	26.3	19.0%
[Sn ₉] ⁴⁻	32.9	
[Co ₂ @Sn ₁₇] ⁵⁻	36.4	10.6%
[Rh ₂ @Sn ₁₇] ⁶⁻	38.4	17.0%
[Ni ₂ @Sn ₁₇] ⁴⁻	36.5	10.9%

^a – the interstitial germanium atom in this case is split into two distinct atoms which makes definitive statements about bond lengths and angles problematic. For the volume analysis an ideal middle atom is used. This cluster is currently under investigation by Christoph Wallach, M. Sc., Chair of Inorganic Chemistry with Focus on Novel Materials.

With cobalt the angle is around 165 ° while with rhodium it is roughly 163 °. Further analysis is difficult again because of the limited sample size, no transition metal compounds featuring heavier incorporated or differently charged metals are known. Analyzing the volume of the cluster units it shows to be 26.7 Å³. This equates to a volumetric increase of 20.8% which is significantly higher than the tin congeners which are all around 13%. The reason for this is the same as for the “monomer” [Co@Ge₉]⁵⁻, because the [Ge₉] cage is stretched to the maximum when filled with a Co anion. A feature that all doublet clusters share is the presence of two [E₈] tubs. This structural unit was first reported by Fässler *et al.*^[183, 412] as a possible intermediate step during the formation of larger cluster from [E₉] units. This theory was then later further expanded upon by Dehnen *et al.*^[117-118] When taking this unit into consideration the cluster unit can be seen

as $[E_8]$ -[TM- E -TM]- $[E_8]$ where the two tubs encapsulate the transition metal and tetrel strand. In all cases of these $[E_{17}]$ units these tubs are not in line with one another, they are always rotated approximately 90° in relation to each other.

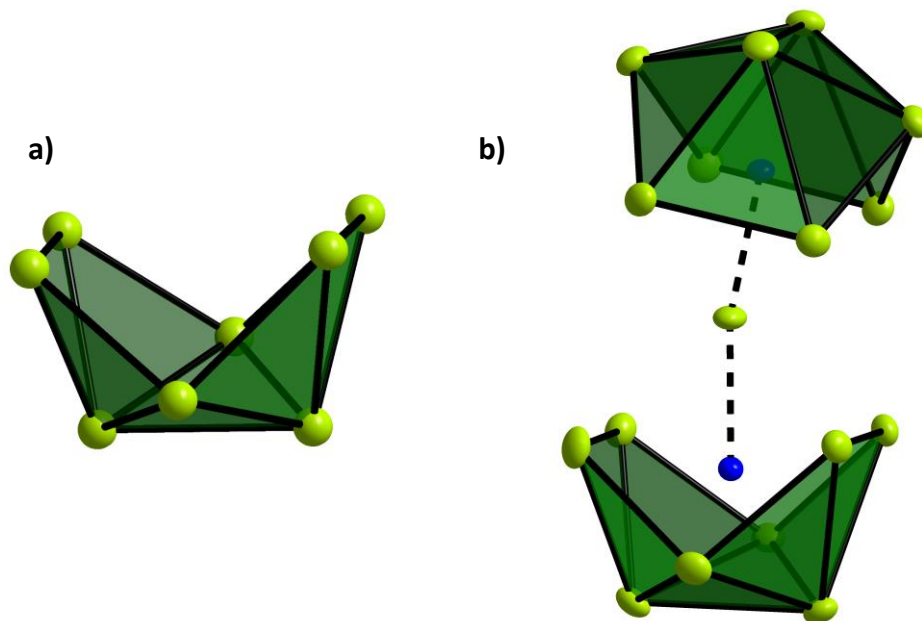


Figure 47: $[E_8]$ tub unit on its own a) and as it is in the $[TM_2@E_{17}]$ units – twisted by around 90° b).

4.3.6.2. Synthesis and characterization of compounds containing the endohedral $[Co@Ge_{10}]^{3-}$ cluster

The first of these known motifs is the $[Co@Ge_{10}]^{3-}$ cluster which first has been reported by Fässler *et al.*^[210] In this case the structure was obtained by dissolving a phase of the composition “ K_5CoGe_9 ” (Table 40) and $TiCl_2Cp(NH_3)_2$ in liquid ammonia with the intention of attaching a ligand to the filled cluster. Instead of an exo-bonded ligand on a filled $[E_9]$ unit a reaction took place forming the $[Co@Ge_{10}]^{3-}$ from $[Co@Ge_9]^{5-}$. Two compounds are characterized using single crystal diffraction - $[K(2.2.2-crypt)]_3[Co@Ge_{10}] \cdot 3 NH_3$ (Table 74) and $[K(2.2.2-crypt)]_3[Co@Ge_{10}] \cdot 9 NH_3$ (Table 75). Analyzing the transformation mechanism from the nine-atomic to the ten-atomic cluster is difficult since it all takes place in liquid ammonia and *in situ* studies are hard to conduct, thus no conclusive explanation for the formation of $[K(2.2.2-crypt)]_3[Co@Ge_{10}] \cdot 3 NH_3$ can be

given (Figure 48). Comparing the reported pentagonal prism to the newly characterized prism shows no significant distortions from an ideal prism. All bond lengths, Ge-Ge and Co-Ge, show nearly no difference to the reported cluster (Table 28).

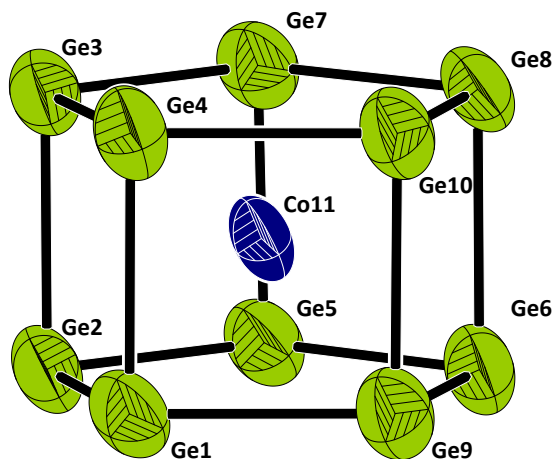


Figure 48: Pentagonal prism of $[\text{Co@Ge}_{10}]^{3-}$. Thermal ellipsoids shown at 50% probability level.

Table 28: Bond lengths of $[\text{Co@Ge}_{10}]^{3-}$ in $[\text{K}(\text{2.2.2-crypt})]_3[\text{Co@Ge}_{10}] \cdot 3 \text{ NH}_3$ in comparison between this work and the literature known structure.

Bond lengths / Å	$[\text{Co@Ge}_{10}]^{3-}$ (lit.) ^[210]	$[\text{Co@Ge}_{10}]^{3-}$
Co-Ge	2.4792(7) – 2.5247(7)	2.4774(16) – 2.532(5)
Ge-Ge (equatorial)	2.5015(6) – 2.5269(7)	2.500(4) – 2.541(4)
Ge-Ge (axial)	2.6003(6) – 2.6218(6)	2.585(5) – 2.631(5)

As before the pentagonal prism shows almost perfect D_{5h} symmetry which can be seen in the h/e ratio. The h in this case refers to the five heights of the prism while e are the ten edges present in the two planes. The h/e ratio in this case is 1.03 which is close to the ideal value, very similar to the reported cluster.

Compounds featuring this structural motif are found several times containing different amounts of liquid ammonia molecules. This can be explained by the time frame where the crystal were found, where the compound containing the increased amount of ammonia ($[\text{K}(\text{2.2.2-crypt})]_3[\text{Co@Ge}_{10}] \cdot 9 \text{ NH}_3$) is found several days after the one containing less ammonia ($[\text{K}(\text{2.2.2-crypt})]_3[\text{Co@Ge}_{10}] \cdot 3 \text{ NH}_3$). It is worth mentioning that both the compounds containing $[\text{Co@Ge}_{10}]$ and $[\text{Co}_2\text{@Ge}_{17}]$ are retrieved from the same experiment – a reaction of $\text{TiCp}_2(\text{NH}_3)_2\text{Cl}$ with “ K_5CoGe_9 ”. The conjoined cluster is found after the first time the ten vertex cluster was

discovered, opening the possibility that $[\text{Co}_2@\text{Ge}_{17}]$ cluster is formed by oxidation through air impurities. However the ability of titanium compounds to fragment $[E_9]$ clusters has been shown before^[183, 412] which makes this the more likely formation mechanism. The titanium complex reacts with the endohedral cluster to form these larger units. This can happen through combination of multiple endohedral clusters with one another or the incorporation of an empty $[\text{Ge}_9]$ unit which is also present in the “ K_5CoGe_9 ” phase. Again the exact mechanism is hard to determine in the case of reactions in liquid ammonia.

4.3.6.3. Synthesis and characterization of a compound containing the endohedral “ $[\text{Rh}@\text{Pb}_{12}]$ ” cluster

A compound containing the $[\text{Rh}@\text{Pb}_{12}]$ cluster was crystallized from liquid ammonia after dissolving “ K_5RhPb_9 ” (Table 39) alongside 18-crown-6 (Table 76). A single crystal was found and analyzed using single crystal diffraction (Table 76). Like with the compound containing $[\text{Rh}@\text{Sn}_9]$, the structural refinement is not yet complete. Probable causes are the crystal quality and the high absorption of lead. Because of this the sum formula as well as the structure refinement itself is not yet finalized. The lead cluster, which in literature has a charge of -3, will thus be referred to as $[\text{Rh}@\text{Pb}_{12}]$.

$[\text{Rh}@\text{Pb}_{12}]$ as a structure motif has been previously reported and isolated from en by Xu *et al.*^[236]. The dividing factor is that in this work, a precursor was synthesized using the elements and high temperatures instead of mixing K_4Pb_9 and $\text{Rh}(\text{PPh}_3)_3\text{Cl}$ in en. Preliminary Raman analysis of the precursor phase was not successful because $[\text{Pb}_9]^{4-}$ does not yield any observable signals. Since an endohedral cluster is found from solution the presence of some filled cluster in the solid state phase is highly likely. Both clusters feature almost identical Rh-Pb distances as well as Pb-Pb bond lengths (3.1512(26) – 3.1921(28) Å) (Table 29). The Rh-Pb distances also show close accordance with other filled $[\text{TM}@\text{Pb}_{12}]$ units like TM = Ni, Pd, Pt and Mn. The last one shows a larger range of distances because of the different symmetry the cluster presents itself in. All other instances show almost perfect I_h symmetry while $[\text{Mn}@\text{Pb}_{12}]^{3-}$ shows lower D_{2h} symmetry.

Table 29: Rh-Pb distances of $[\text{Rh@Pb}_{12}]^{3-}$ in comparison between this work and the literature known structure.

$d(\text{TM-E}) / \text{\AA}$	
$[\text{Rh@Pb}_{12}]^{3-}$ - this work	2.987(2) – 3.028(2)
$[\text{Rh@Pb}_{12}]^{3-}$ - lit. ^[236]	2.984(1) – 3.027(1)
$[\text{Mn@Pb}_{12}]^{3-}$ ^[233]	2.869(3) – 3.308(4)
$[\text{Ni@Pb}_{12}]^{2-}$ ^[226]	2.923(3) – 3.033(2)
$[\text{Pd@Pb}_{12}]^{2-}$ ^[226]	2.980(2) – 3.092(2)
$[\text{Pt@Pb}_{12}]^{2-}$ ^[226]	3.056(2) – 3.060(2)

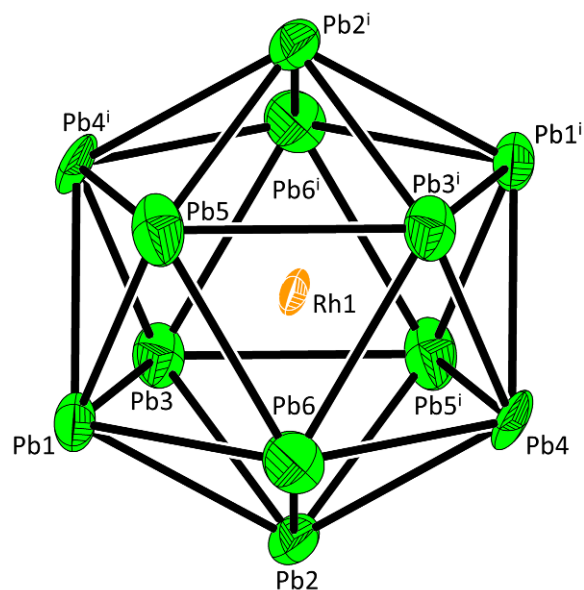


Figure 49: Endohedral cluster $[\text{Rh@Pb}_{12}]^{3-}$. Thermal ellipsoids are drawn at 50 % probability. Symmetry operations: (i) $-x, -y, (1-z)$.

Because of the close accord of the bond lengths and symmetry it can be assumed that the cluster is refined properly which would mean it has the charge -3. A better crystal will probably alleviate the problems and it would be possible to finalize the structure.

Unlike the previous compounds no pyramidal hydroxide unit is present. Both, this solution experiment and the one resulting in $[\text{Ru@Sn}_9]^{6-}$ were conducted in close proximity to one another. However, because of the relatively small charge of -3, the more common sequestering agents like 18-crown-6 crystallize alongside the cluster instead of the more highly charged pyramidal unit.

Additional Raman studies of solid state phases possibly containing endohedral cluster are conducted. All of these additional phases do not show any signs of the presence of filled species. Crystallization from solution subsequently did not yield any compounds containing endohedral

clusters. A list of all solid state phases, the contained species and solution experiments can be found in the experimental section 4.3.1.

4.3.7. Synthesis trails of ternary solid state phases containing filled cluster units featuring lighter tetrels and late transition metals

4.3.7.1. Synthesis trails of $[TM@E_9]$ units featuring light tetrel elements (TM = Co, Ni; E = Si, (Si/Ge))

To this day the lightest element cluster featuring a filled $[E_9]$ species is $[Ge_9]$ with Co and Ni at the center of the cluster. A large number of heavier filled cluster species is known and expanded in this work but no filled $[E_9]$ clusters made from silicon are known. Several experiments using nickel as the targeted central atom are conducted in this chapter. Experimental conditions are described in section 6.6.4.2 (Table 41).

Table 30: Raman shifts of the cluster contained in $K_{12}Si_{17}$ as well as the hypothetical cluster $[Ni@Si_9]^{4-}$.

	$“[Si_{17}]^{12-}“^{[48]}$	$[Si_4]^{4-}[173, 413]$	$[Si_9]^{4-}[173]$	$[Ni@Si_9]^{4-}$
Raman shifts / cm ⁻¹ (measd.)	283, 302, 355, 390, 485	287, 337, 364, 481	∅	∅
Raman shifts / cm ⁻¹ (calc.)	∅	305, 378, 499	286, 342, 395	188, 365, 409, 464

Nickel is chosen for the fact that it does not add any electrons to the cluster cage and thus will not change the electron count. In addition to this the experiments include usage of a mixture of Si/Ge in the ratio of 5/12. As described in the opening section the two elements form solid solutions, which in this case is achieved by ball milling. In order to use the same Raman analysis technique as used before a benchmark for the signal shift of the main signal and the area of the

characteristic signals needs to be determined. For this the hypothetical cluster $[\text{Ni@Si}_9]^{4-}$ is optimized and from this the Raman frequencies are calculated. Furthermore the signals of the pure $[\text{Si}_9]^{4-}$ cluster need to be determined which can be done the easiest by the exclusion principle.

In addition to this the calculated shifts of both $[\text{Si}_4]^{4-}$ and $[\text{Si}_9]^{4-}$ were recently published and show good accordance with all available measured samples. As with the heavier tetrel cluster, the main signal shifts by about 20 cm^{-1} towards higher energies, from 390 cm^{-1} to 409 cm^{-1} (Table 30). With the shifts of both, the unfilled as well as the hypothetical nickel filled cluster, the screening of the ternary phases can be performed preliminarily to the dissolution of the phases. All phases that were synthesized (section 6.6.4.2) show only Raman signals of the phases $\text{K}_{12}\text{Si}_{17}$ or K_4Si_4 which is corroborated by the X-ray powder diffraction analysis (Figure 50, Figure 125, Figure 126, Figure 127).

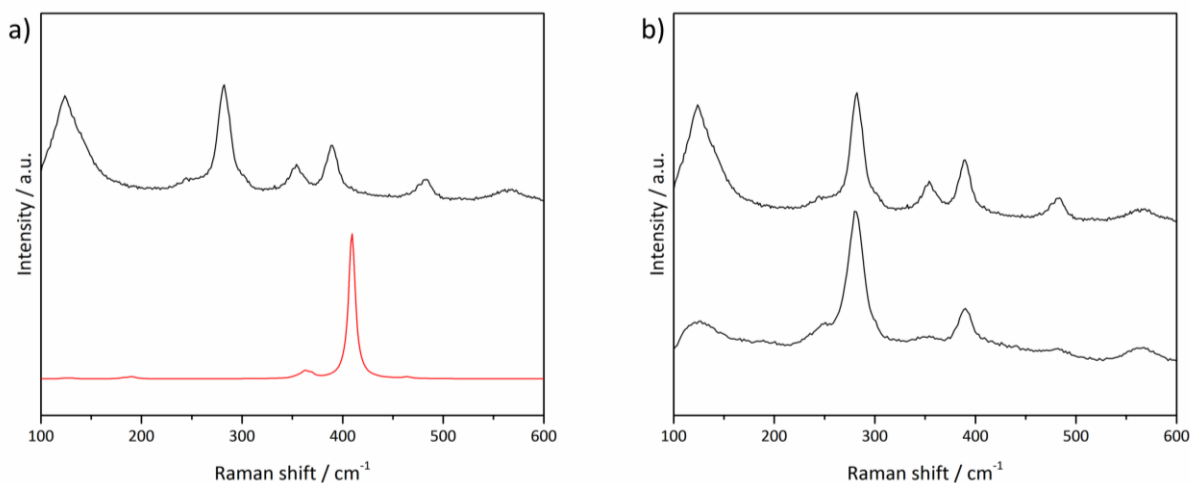


Figure 50: a) Comparison of a solid state phase with the composition "K₄NiSi₉" (black) and the calculated Raman spectrum of $[\text{Ni@Si}_9]^{4-}$. b) Comparison of a solid state phase with the composition "K₄NiSi₉" (black, top) and the experimental Raman spectrum of $\text{K}_{12}\text{Si}_{17}$ (black, bottom). All signals can be attributed to $\text{K}_{12}\text{Si}_{17}$ (Figure 72).^[48]

Filling a pure silicon cluster proved to be difficult. A filling trial of mixed precursors was done and instead of pure silicon a mixture of Si/Ge with a ratio of 5/12 is used. In this case cobalt and nickel were both tested as possible guest metals. For the synthesis of mixed tetrel clusters (Si/Ge) preground mixtures of the elements in the ratio $\text{Si/Ge} = 5/12$ are used. This ratio is calculated in a way that when used in the synthesis the overall molar ratio of tetrel elements comes out to $(\text{Si}_3/\text{Ge}_6) = E_9$. The preground mixture of elements is provided by Dr. Michael Giebel, Chair of Inorganic Chemistry with Focus on Novel Materials. Syntheses are described in section 6.6.4.2.

A phase with the nominal composition “ $\text{K}_5\text{CoSi}_3\text{Ge}_9$ ” shows closest approximation is with $[\text{Si}_{1.2}/\text{Ge}_{2.8}]^{4-}$ - a mixed tetrel cluster contained in the phase “ $\text{K}_{12}\text{Si}_5\text{Ge}_{12}$ ” (Figure 128). Mixed tetrel clusters and phases are more closely examined by Dr. Michael Giebel, Chair of Inorganic Chemistry with Focus on Novel Materials. Analysis of the syntheses using mixed Si/Ge solid state phases shows the absence of filled clusters. In the case of the synthesis using nickel, yielding a phase with the nominal composition “ $\text{K}_4\text{NiSi}_3\text{Ge}_9$ ”, the Raman analysis shows good agreement with $\text{K}_{12}\text{Ge}_{17}$ (Figure 129).

These results do not disprove the possibility that filled silicon clusters can be realized someday. For this a different approach needs to be taken since the same synthesis path yielding the filled $[E_9]$ ($E = \text{Ge}, \text{Sn}$) does not yet work in this system. The most probable explanation why the filling of the $[\text{Si}_9]^{4-}$ unit is so far unsuccessful is the size of the cluster itself. With a volume of only 18.9 \AA^3 ^[91] the cluster is significantly smaller than its heavier homologues. With even germanium clusters being 22.1 \AA^3 the size difference is 15.5% which seems to be enough that transition metal elements do not fit in the cavity anymore. Further supporting the idea that the $[\text{Si}_9]^{4-}$ cluster is simply too small to host a central atom is the fact that any atom, except for protons, in a crystal structure needs about 18 \AA^3 of space.^[414] This data is found through empirical considerations and is not a definitive rule but is often found to be true in crystal structures. With the cluster only having an internal volume of 18.9 \AA^3 it is unlikely to be able to host any atoms. The larger $[E_9]$ units with their increased volume however prove to be able to do so.

4.3.7.2. Synthesis trails of $[\text{Cu}@E_9]$ cluster units ($E = \text{Ge}, \text{Sn}$)

Synthesis of ternary phases with the element combination K-Cu- E ($E = \text{Ge}, \text{Sn}$) were unsuccessful in yielding the phases containing the desired $[\text{Cu}@E_9]^{3-}$ and $[\text{Cu}@Sn_9]^{3-}$. This can be seen by the absence of signals in the range of 240 cm^{-1} and $350 - 370\text{ cm}^{-1}$, in the case of germanium, and 170 cm^{-1} and $240 - 260\text{ cm}^{-1}$, in the case of tin. These signals are indicators of presence of endohedral clusters (section 4.3.2.2). Only signals attributable to K_4E_4 and K_4E_9 ($E = \text{Ge}, \text{Sn}$), or mixtures thereof, can be seen in PXRD and Raman analyses (Figure 130 - Figure 135). Synthesis details can be found in section 6.6.4.3 (Table 42).

4.3.8. DFT calculations on the clusters $[\text{Co}@Ge_9]^{5-}$ and $[\text{Ru}@Sn_9]^{6-}$

Since $[\text{Co}@Ge_9]^{5-}$ and $[\text{Ru}@Sn_9]^{6-}$ share crystallographic and structural similarities, MO calculations are conducted in order to determine the orbital situation and possible transition metal-cluster interactions.

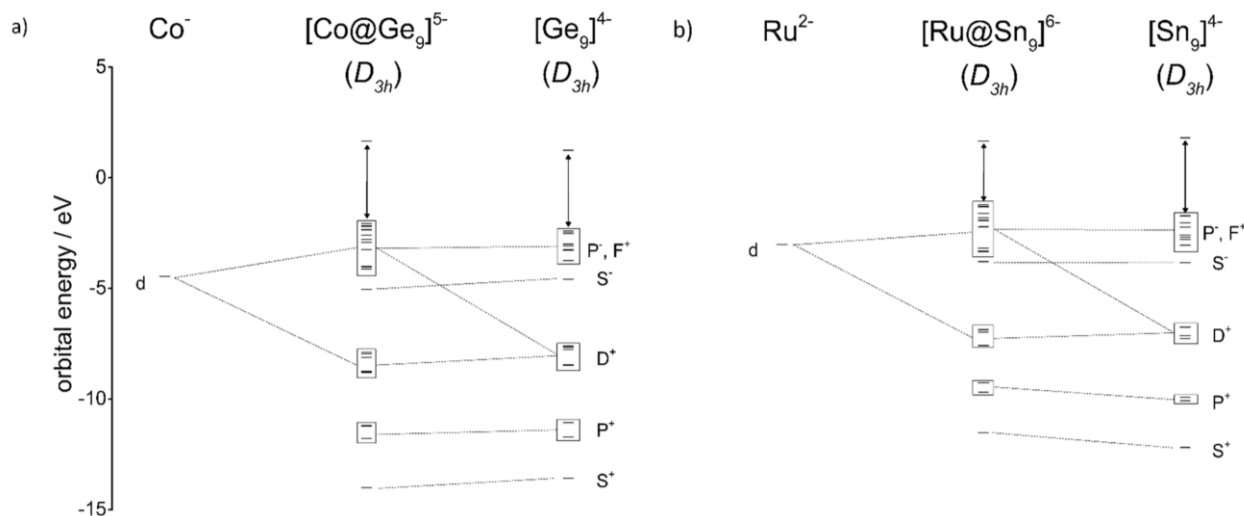


Figure 51: Molecular orbital interaction diagram of $[\text{Co}@Ge_9]^{5-}$ (a) in fragments of Co^- and $[\text{Ge}_9]^{4-}$ (D_{3h} symmetry) and of $[\text{Ru}@Sn_9]^{6-}$ (b) in fragments of Ru^{2-} and $[\text{Sn}_9]^{4-}$ (D_{3h} symmetry). Important contributions are indicated by dashed lines of both molecular orbital interaction diagrams.

These calculations are done by Jasmin Dums, M. Sc., Chair of Inorganic Chemistry with Focus on Novel Materials, and the author would like to extend his gratitude for the extensive help Ms. Dums provided with these calculations as well as the calculations of Raman spectra.

DFT calculations have been performed for $[\text{Co@Ge}_9]^{5-}$ and $[\text{Ru@Sn}_9]^{6-}$ as well as for the empty $[\text{Ge}_9]^{4-}$ and $[\text{Sn}_9]^{4-}$ ions using a polarized continuum model (PCM) solvate field based on water for negative charge compensation. In accordance to experimental findings the structure optimization leads to a D_{3h} symmetry for $[\text{Co@Ge}_9]^{5-}$ and $[\text{Ru@Sn}_9]^{6-}$ and to C_{4v} symmetry for the empty clusters (Table 31).

Table 31: Point group and HOMO-LUMO gap for each calculated structure.

	$[\text{Co@Ge}_9]^{5-}$	$[\text{Ge}_9]^{4-}$	$[\text{Ge}_9]^{4-}$	$[\text{Ru@Sn}_9]^{6-}$	$[\text{Sn}_9]^{4-}$	$[\text{Sn}_9]^{4-}$
Point group	D_{3h}	D_{3h}	C_{4v}	D_{3h}	D_{3h}	C_{4v}
Gap / eV	3.73	3.66	4.35	2.89	2.98	3.53

Single point calculations for the empty clusters $[\text{Ge}_9]^{4-}$ and $[\text{Sn}_9]^{4-}$ are performed in D_{3h} symmetry to derive an orbital interaction diagram, resulting in slightly different HOMO-LUMO gaps of 3.66 eV and 2.98 eV, respectively. The geometry is taken from the optimized structure of the filled clusters. The calculated interatomic distances of the optimized structures agree well with the experimental data showing deviations of less than 0.06 Å or below 2 % for all Ge-Ge/Sn-Sn and Ge-Co/Sn-Ru distances for both endohedral clusters, which reassures the optimized structure.

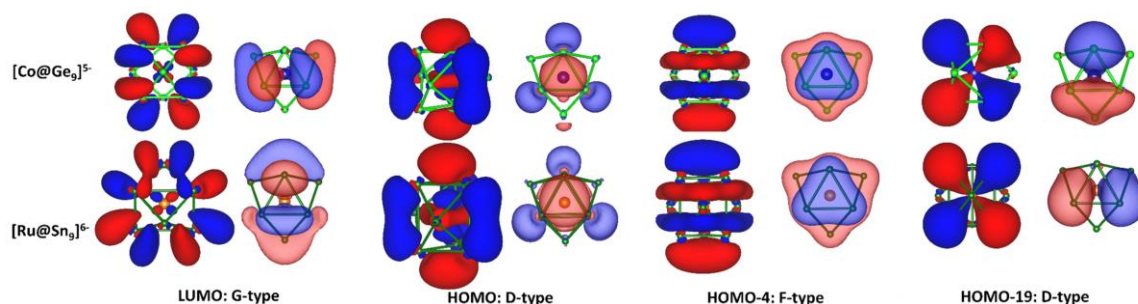


Figure 52: Molecular orbitals of $[\text{Co}@\text{Ge}_9]^{5-}$. $[\text{Ru}@\text{Sn}_9]^{6-}$ exhibits the same molecular orbitals with a small distortion. Each orbital shows a specific shape of orbital (S , P , D) according to the superatom model. The p type orbital is described by the interaction of p_y ($\text{Co}^-/\text{Ru}^{2-}$) and P_y of the empty cluster, whereas the d_{yz} of the $\text{Co}^-/\text{Ru}^{2-}$ interacts with the D_{yz} in case of the d type orbital. Additionally, HOMO and LUMO orbitals are illustrated.

Charge distribution based on population analyses according to Hirshfeld and natural population analyses are carried out, and all charges are given in the supporting information (Table S10). Both methods account for negative charges for the endohedral TM atoms which can formally be considered as $\text{Co}(-\text{I})$ in $[\text{Co}@\text{Ge}_9]^{5-}$ and $\text{Ru}(-\text{II})$ $[\text{Ru}@\text{Sn}_9]^{6-}$ and an s^2d^8 configuration. The almost perfectly spherical shapes of the filled clusters, the molecular orbitals shown in Figure 51 allow for a classification according to the tensor surface harmonic theory in S , P , D , F and G orbitals.^[415-417] The $1S^21P^61D^{10}2S^21F^{14}2P^6$ electronic configuration with an empty $1G$ orbital as LUMO perfectly fits the superatom model of the 40 electron clusters $[\text{E}_9]^{4-}$. The d orbitals of the $\text{Co}^-/\text{Ru}^{2-}$ interact with a D set of the cluster representing delocalized bonds, whereas the F and G type orbitals are mainly unaffected. The alternative analysis by Intrinsic Bond Orbitals^[418] shows that all interactions between TM and cluster atoms are multi-center bonds. Most intriguing is the formation of such clusters which leads to the anticipation of several mechanisms on a theoretical level, however, experimental data is scarcely reported.^[113, 183, 186, 419] The structures are optimized, and the characters of the stationary points were investigated by frequency calculations. $[\text{Ru}@\text{Sn}_9]^{6-}$ reveals a minor imaginary frequency ($17.8i \text{ cm}^{-1}$). The imaginary frequency of the highly charged clusters probably arise from the fact that the missing crystal surroundings are

replaced by a solvation model. Hirshfeld and natural charges are calculated for $[\text{Co}@\text{Ge}_9]^{5-}$ and $[\text{Ru}@\text{Sn}_9]^{6-}$.^[420-421] For a molecular orbital diagram single point calculations of $[\text{Ge}_9]^{4-}$ and $[\text{Sn}_9]^{4-}$ in D_{3h} symmetry are carried out. For Co^- and Ru^{2-} idealized orbitals are taken to construct the MO-scheme.

4.3.9. Synthesis trails with the goal of exo-bonded ligands on endohedral clusters

Several species of substituted endohedral clusters are known in literature but their syntheses are often not targeted using binary precursors and specific agents.^[180-181, 214, 228-230] Sun *et al.* showed that a targeted substitution of endohedral clusters is readily possible with numerous of different transition metal complexes.^[220] However a real covalent bond between a endohedral cluster and a main group element has not been reported yet. In this chapter reactions between main group reactants, transition metal complexes and solid state precursors containing endohedral clusters are discussed.

4.3.9.1. Reactions with main group reactants

The reaction of K_4Ge_9 and $[\text{Si}(\text{SiMe}_3)_3]\text{Cl}$ showed that cluster can be easily substituted in a heterogenic reactions under standard conditions with almost quantitative yields.^[141] With the similarity of the $[\text{Ge}_9]^{4-}$ and $[\text{Co}@\text{Ge}_9]^{5-}$ clusters as well as their solid state precursors the transfer of the reaction stands to reason. Experimental conditions are described in section 6.6.5.

However, with all the similarities the reactions proved to be vastly different with no reactivity overserved when the reaction is done the same way as with the empty cluster.^[141] During the reported reaction, using the phases containing the empty cluster like K_4Ge_9 , the solution turns red almost immediately and is completed within hours whereas with the endohedral precursor no such coloration can be observed. Even after elongated reaction times no reaction is observed. After the reactions following the reported synthesis method did not yield any of the desired results, i.e. an endohedral cluster with exo bonded silyl ligands, another synthesis route was

tested. This route was first reported by Sevov *et al.*^[110] and recently reused in a publication by the Fässler *et al.*^[173] The technique involves the extraction of the solid state precursor using liquid ammonia before the actual reaction takes place. This method was refined by Dr. Lorenz Schiegerl, Chair of Inorganic Chemistry with Focus on Novel Materials.

As mentioned before the first step is the extraction of the solid state precursor using liquid ammonia and in some cases sequestering agents like 18-crown-6 or 2.2.2-crypt. After this the ammonia is removed and the extraction product is dissolved in an appropriate solvent, like thf or pyr, and reaction at 0 °C.

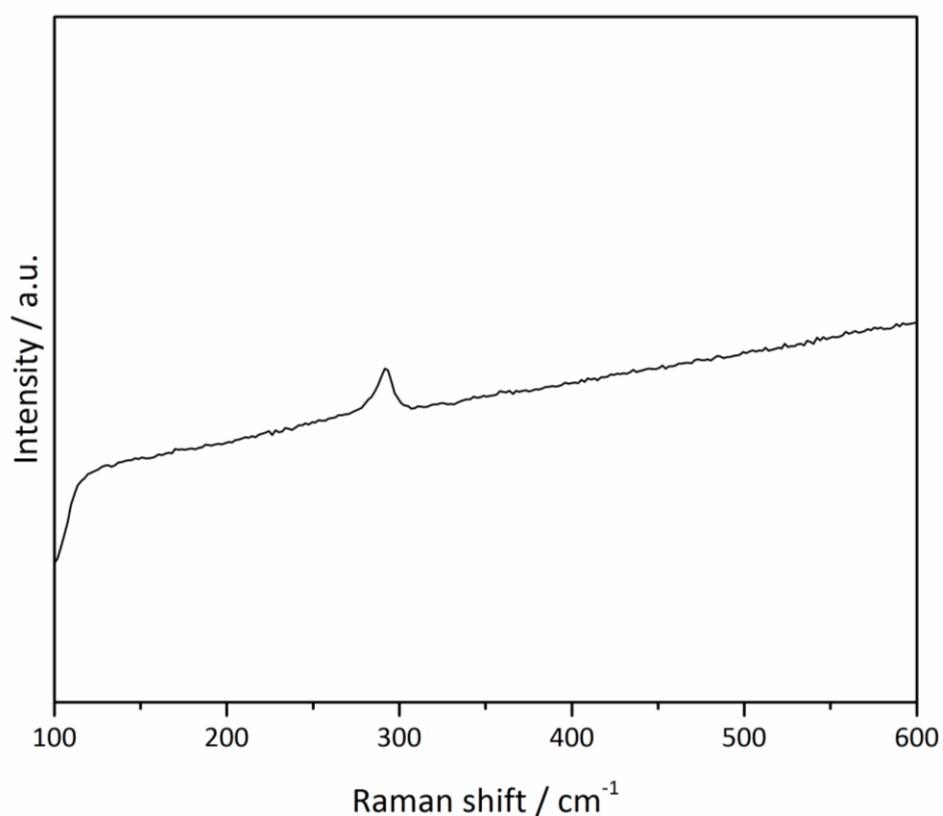


Figure 53: Exemplary Raman spectrum of the product of reactions including phases containing $[\text{Co@Ge}_9]^{5-}$ and with $\text{ClSi}(\text{SiMe}_3)_3$. One signal (292 cm^{-1}) attributable to germanium can be seen.

After the reaction the residue is washed with hex and finally analyzed. Using this technique with the endohedral solid state precursor of $[\text{Co@Ge}_9]^{5-}$ again like before no endohedral cluster with silyl ligands is found. Instead the bissilylated species $[\text{Ge}_9[\text{Si}(\text{SiMe}_3)_3]_2]^{2-}$ of the $[\text{Ge}_9]^{4-}$ can be clearly detected using ^1H -, ^{13}C - and ^{29}Si -NMR (Figure 68, Figure 69, Figure 70). Raman analysis of

these reactions also shows that a part of the reactant phase decomposes to elemental germanium (Figure 53).

All trails trying to synthesize endohedral clusters featuring ligands do not yield any of the desired results. Additional syntheses are done by Christoph Wallach, M. Sc., Chair of Inorganic Chemistry with Focus on Novel Materials.

4.3.9.2. Reactions with transition metal complexes

Sun *et al.* showed that reactions of endohedral clusters and transition metal complexes in solution are possible and lead to many different conformations.^[220] Reactions between phases with the nominal compositions “ K_5CoE_9 ” ($E = Ge, Sn$) yielded no single crystals which could be analyzed using single crystal diffraction or Raman spectroscopy. Experimental details can be found in section 6.6.5. Table 43 shows reactions between the phases containing endohedral clusters with a plethora of transition metal complexes while the experiments listed in Table 44 focus on the coordination of Cu-NHC complexes and phosphine ligands to endohedral clusters.^[137, 197]

5. Conclusion

In order to handle the rising greenhouse gas emissions new materials for the generation of renewable energy as well as storage materials need to be researched. Tetrel elements, especially silicon and germanium, are already established in these sectors but are still researched for more effective and efficient systems. One of these research topics are nanostructured materials which can be found as *Zintl* phases. These phases with compositions like K_4E_4 , K_4E_9 and $K_{12}E_{17}$ ($E = \text{Si, Ge, Sn}$) made from the elements using high temperature syntheses, feature complex structures and properties and can be used in a plethora of applications.

First the stability of the phases of $K_{12}\text{Si}_{17}$ and $K_4\text{Ge}_9$ against liquid ammonia are examined. Dissolution, filtration and removal of the solvent do not lead to decomposition of the phases. Decomposition of $K_{12}\text{Si}_{17}$ occurs during heating to 1000 °C in the DSC analysis. Undissolved residue of $K_4\text{Ge}_9$ shows previously undetected signals which indicate the presence of $[\text{Ge}_4]^{4-}$ clusters.

Using existing phases with the mentioned compositions the introduction of light alkali metals like Li and Na is the focus of the first main part of this thesis. The goal is to find new allotropes of the elements in question, namely Si and Ge. This is realized using the ion exchange resin Amberlyst 15 using the appropriate solvents, e.g. liquid ammonia, acn, dmf. First a repeatable system is established in regard to proper solvents, resin equivalents and exchange times using ICP-OES as means of analyzing the lithium ion/potassium ion ratio for a determination of complete ion exchange. Then using this system the mentioned phases are subjected to exchange experiments. Silicide phases are too volatile and react with the exchange resin while germanide phases decompose to elemental germanium. The exchange is successful with the substituted cluster $\text{K}[\text{Ge}_9[\text{Si}(\text{SiMe}_3)_3]_3]$ with the new compounds $\text{Li}[\text{Ge}_9[\text{Si}(\text{SiMe}_3)_3]_3]$ and $[\text{Li}(\text{B12crown4})_2][\text{Ge}_9[\text{Si}(\text{SiMe}_3)_3]_3]$. The only successful exchange of potassium for lithium ions in the context of a bare cluster is K_4Sn_9 which results in the compound $\text{Li}_4\text{Sn}_9 \cdot 17 \text{NH}_3$ which has been reported before using a different synthesis method.

Further experiments to stabilize the bare clusters, using polymers or oxidizing agents, failed and result in elemental germanium. Several reactions yielded germanium nanoparticles which could be analyzed using DLS and TEM which show dependence of what cation is loaded onto the

exchange resin. The size of these particles ranges between 10 and 100 nm which is a range of great interest. However the yield of these particles is so low that the syntheses were not pursued further.

The second main part of the thesis is the analysis of solid state precursors and crystallization of new endohedral *Zintl* clusters. Using Raman spectroscopy as a means to analyze bulk precursors and single crystal diffraction new information about endohedral clusters and the behavior in solution have been found.

Using preexisting empty $[E_9]$ ($E = \text{Ge, Sn}$) clusters the merit of determining Raman modes using DFT calculations is established. Transferring this technique to previously reported endohedral cluster units $[\text{TM}@\text{Sn}_9]^{n-}$ ($\text{TM} = \text{Co, Ni, Cu}$; $n = 5, 4, 3$) and $[\text{Ni}@\text{Ge}_9]^{4-}$ shows that endohedral clusters exhibit characteristic behavior when examined using Raman spectroscopy. The main signal, the “breathing” mode, is shifted to higher energies and new unique signals appear which are caused by the presence of an atom in the cluster center. Using this technique ternary solid state phases can be examined and the presence of endohedral clusters can be determined.

A plethora of new phases are synthesized with compositions $[\text{TM}@E_9]$ ($\text{TM} = \text{Fe – Os, Co – Ir, Ni – Pt, Cu, Ag, E} = \text{Si, Ge, Sn, Pb}$) and analyzed using the new technique of DFT enhanced Raman spectroscopy. Promising candidates are dissolved in liquid ammonia and crystallized. Three new compounds are crystallized each containing a new filled $[E_9]$ unit including $[\text{Co}@\text{Ge}_9]^{5-}$, $[\text{Ru}@\text{Sn}_9]^{6-}$ and $[\text{Rh}@\text{Sn}_9]$. Further solid state phases are found containing filled clusters $[\text{Ni}@\text{Ge}_9]^{4-}$ and $[\text{Pd}@\text{Sn}_9]^{4-}$ but no crystallization is realized. Fragmentation of $[\text{Co}@\text{Ge}_9]^{5-}$ by means of a titanium complex in liquid ammonia leads to $[\text{Co}_2@\text{Ge}_{17}]^{6-}$. This doublet cluster exhibits the same structural motif as other filled $[E_{17}]$ clusters before and expands the group of these clusters. In addition, the previously reported clusters $[\text{Co}@\text{Ge}_{10}]^{3-}$ and $[\text{Rh}@\text{Pb}_{12}]^{3-}$ could be isolated from liquid ammonia instead of en and using the solid state precursor instead of a binary phase and a transition metal complex.

DFT calculations of $[\text{Co}@\text{Ge}_9]$ and $[\text{Ru}@\text{Sn}_9]$ provide insight into the electronic and orbital structure of said clusters. Additional syntheses with the goal of yielding phases with filled $[\text{Si}_9]$, $[(\text{Si/Ge})_9]$ units as well as $[\text{Cu}@E_9]$ ($E = \text{Ge, Sn}$) clusters did not yield the desired result.

Reactions of phases with the nominal compositions “ K_5CoE_9 ” ($E = Ge, Sn$) with main-group reactants were carried out using silylizing agents as well as phosphines resulted in no substantial new compounds. The main result is the already reported tri- and bis-silylated $[Ge_9]$ clusters $[Ge_9(Si(SiMe_3)_3)_3]^-$ and $[Ge_9(Si(SiMe_3)_3)_3]^{2-}$. Reactions of transition metal complexes and phases containing filled $[E_9]$ ($E = Ge, Sn$) units did also not yield the desired endohedral clusters featuring exo-bonded ligands.

In conclusion it can be said that the method of using ion exchange resin to introduce lighter alkali metals to preexisting solid state *Zintl* phases is possible. A system of test reactions and well defined exchange parameters for several solvents was determined. However, while the exchange itself is possible, the desired preexisting structure of the phases is not retained and thus it is not possible to continue the reactions towards new tetrel allotropes. All efforts undertaken to stabilize the isolated cluster towards lithium ions were in vain. Several reactions show the development of germanium nanoparticles in an interesting size range but in such low yields that the viability of these reactions needs to be questioned.

A systematic approach on the bulk analysis of ternary phases containing endohedral clusters is established and used to generate new filled cluster species. DFT and Raman spectroscopy are introduced as potent tools to analyze solid state precursors for the presence of endohedral clusters. Using the phases with proven endohedral content several new compounds with new cluster compounds could be isolated. Further preexisting cluster motifs were isolated from a different solvent.

The field of ion exchange on *Zintl* phases shows questionable further promise, if any, while the established route of solid state analytics and crystallization from solvent of new endohedral clusters show promise for future application to new tetrel elements and transition metals.

6. Experimental Section

6.1. General Techniques

Most of the precursors and all products are highly sensitive towards air and moisture. Therefore, all reactions are carried out under argon atmosphere using standard glove box and Schlenk techniques. The glove boxes (*MBraun*, $\text{H}_2\text{O} < 1.0 \text{ ppm}$; $\text{O}_2 < 1.0 \text{ ppm}$) are operated with argon 4.8 (*Westfalen*, purity: 99.998 Vol.-%), which is permanently recycled via circulation over a copper catalyst and mole sieve. Frequent regeneration of the copper catalyst, using Ar/W5 (*Westphalen*, 95% argon, 5% hydrogen), ensures a stable inert gas atmosphere. Gloveboxes that operate with solvents inside are additionally equipped with an activated carbon filter. Reactions performed in solution are conducted in Schlenk conditions using argon 4.8 (*Westfalen*, purity: 99.998 Vol.-%), which is further purified prior to use (BTS catalyst, mole sieve 3 Å, Silica Gel Orange 2 - 5 mm and P_4O_{10}).

Standard Schlenk tubes (10 mL - 25 mL), after cleaning in a base bath (KOH/isopropanol) followed by an acid bath (1.0 M HCl_{aq}), are used as reaction vessels. The tubes are stored in a dry oven at 120 °C. Before use the tubes are heated to 650 °C under dynamic vacuum (pressure approx. $8 \cdot 10^{-3}$) and flooded with argon three consecutive times. The vacuum is achieved using a rotary vane pump (VACUUBRAND GmbH & Co. KG) and measured with a Pirani sensor (TPR 281, *Pfeiffer Vakuum*). Ground joints are lubricated with Lithelen high vacuum grease (*Leypold Vakuum*).

Unless stated otherwise weighing and filtrating is done in a glovebox. Unless stated otherwise filtrations are done using Whatman filters (*GE healthcare & life sciences*).

6.2. Solid state precursor syntheses

6.2.1. Reaction vessel preparation

Binary *Zintl* phases K_4E_9 ($E = \text{Ge, Sn}$) are synthesized using a stainless steel autoclave (dimensions: inner tube: 7.0 x 1.5 cm; outer tube: 9.0 x 2.5 cm) in a corundum tube under argon atmosphere. The autoclave is washed with deionized water and dried at 120 °C overnight before usage. The stainless steel tubes are filled inside a glovebox and deposited in a corundum tube, which is evacuated and flooded with argon three times prior to and after the autoclave is deposited. The reaction is conducted under argon pressure to ensure an oxygen and moisture free environment.

Other *Zintl* phases are prepared in small Ta cylinders (length: 6 cm), which were manually cut from adequate Ta tubes (diameter: 10 mm, 12.7 mm; wall thickness: 0.5 mm). The cylinders are furnished with a lid at one side, filled with reactants and subsequently arc melted shut using another lid and an arc furnace MAM 1 (*Edmund Bühler*). If required corundum ampoules can be placed into the tantalum ampoules. The corundum ampoules (*Friatec* AL23 R-Tiegel; outer diameter – 8 mm; inner diameter - ~ 4 mm) are rounded on the bottom and open on the top and are cut to a length of 5 cm.

The arc furnace system itself is installed inside a glovebox and features a movable tungsten electrode and a water-cooled copper block, which is enclosed inside a small chamber, connected to a vacuum pump. The ampoules are held in a removable copper block which is held in place by two clamps and cooled inside the copper block. Prior to use the ampoules are cleaned by sonication in acetone, acetic acid and acetone and dried inside a drying oven at 120 °C. The ampoules are then placed in a silica glass tube which is sealed by a removable lid and Lithilen vacuum grease, evacuated and flooded with argon three times before being placed in a tube furnace under vacuum.



Figure 54: Steel autoclave and tantalum ampoules used in solid state syntheses.

6.2.2. Tube furnace

The silica or corundum tubes are placed inside the tube furnace Loba 1200-40-600 (*HTM Reetz GmbH*) under static vacuum. The oven itself consisted of a steady heating zone, active cooling is not possible. Temperature control was carried out using special control units from the *Eurotherm Deutschland GmbH*.

6.3. Operating liquid ammonia

Zintl phases can be solvated, reacted or extracted using liquid ammonia. When in use, Ammonia 5.0 gas (*Westfalen*, purity: 99.999 Vol.-%) is condensed into a cooling trap filled with elemental sodium forming a blue solution; cooling is provided by a dry ice/isopropanol bath in a dewar. The condensation trap is linked to an inert gas system, in order to condense ammonia into reaction vessels. The Schlenk tubes are connected to the Schlenk line and cooled in the same manner as the cooling trap. In order to warm up, the trap is removed from the ammonia storage allowing it to condense into the connected Schlenk vessel. Storage of reactions in liquid ammonia is done in an ultra-cold fridge at $-40\text{ }^{\circ}\text{C}$ (*Elcold*).

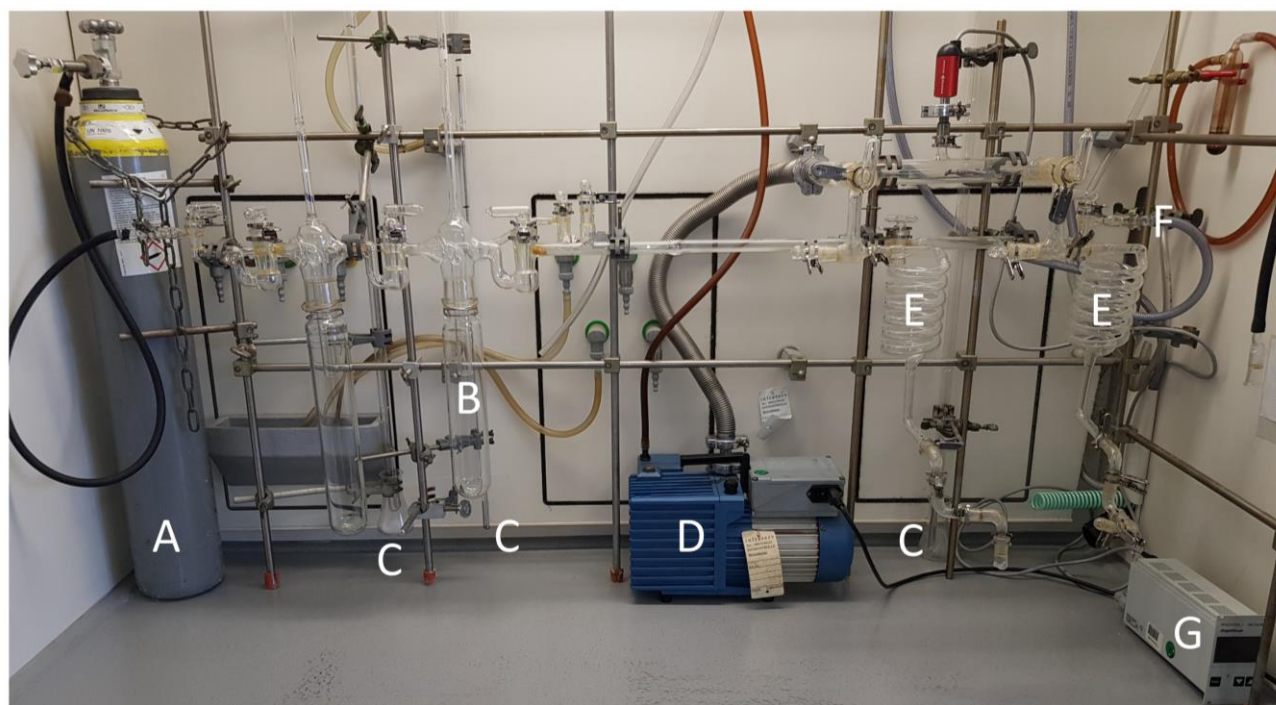


Figure 55: Liquid ammonia setup. (A) gas cylinder containing $\text{NH}_3(\text{g})$, (B) solvent trap containing elemental sodium, (C) mercury overpressure valves, (D) vacuum pump, (E) adapters for Schlenk flasks, (F) argon supply, (G) pressure gauge.

If desired samples can be filtered while dissolved in liquid ammonia. For this a special H-flask is used (Figure 57, Figure 58). Loading a H-flasks with reactant and liquid ammonia is done identically to normal flasks as described above, but only on one side. The liquid ammonia is

condensed (~ 10 mL) into both sides of the flask. Ammonia located on the side without reactant is then passed through the frit to the side loaded with reactant. For sufficient solvation of the reactant a minimum 12 hour period is given while stirring possible when using glass stir bars.

The filtration process is done while the flask is being connected to **E** (Figure 55) under static vacuum. The flask is taken out of cooling, which is why the filtration should be done with time in mind, tilted until the ammonia flows onto and through the frit. After the filtration is complete, the liquid ammonia is condensed back onto the remaining reactant in order to dissolve it again. This is done by cooling the side of the loaded reactant and leaving the side with the ammonia out of cooling. Depending on the substrate multiple cycles of filtration are needed for sufficient yield to analyze.

Experiments in liquid ammonia using ER are done using this technique, however they require additional equipment. Because of the inner surface area of the ER significant delayed boiling is triggered, even by miniscule temperature changes of the H-flask, e.g. transfer from a cooling box to isopropanol/dry ice bath. This delayed boiling is so intense that the solution is thrust up the H-flask resulting a deteriorated solution which is indicated by green or black color. To counteract this effect the ER is put in a glass bomb (Figure 57, a) & c). The bomb is a glass cylinder with two openings, one on the top and bottom, to allow liquid ammonia to flow through. This facilitates the exchange reaction. In order to load the bomb with ER it is closed one side using Whatman filters. The ER is placed on top of the filter and the bomb is “closed” on top of the ER again with filters (Figure 56, b). Using this method the delayed boiling is reduced to a point where the ammonia solution is prevented from jumping out of the cooled part of the H-flask, thus stabilizing the experiment. The bomb is placed on top of the desired reactant and the filtration is carried out as described above with the exception increased reaction times of at least 48 hours are employed to ensure complete exchange of ions within the dissolved reactant.

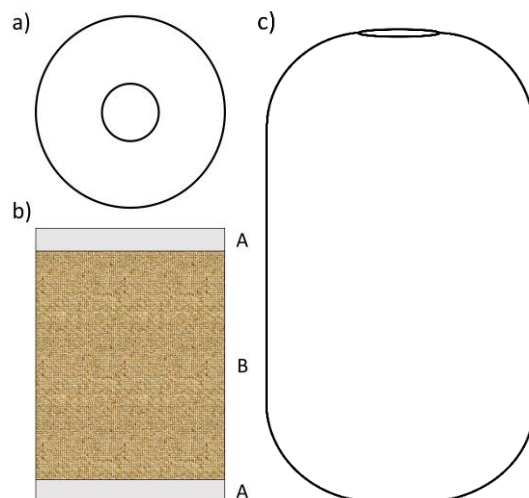


Figure 56: Schematic depiction of the ER bomb setup. a) Top view of ER glass bomb. b) Schematic depiction of layering inside the ER bomb: A – Whatman filters, B – ER. c) Front view of ER glass bomb (total width - ~1cm; total height - ~4 cm).

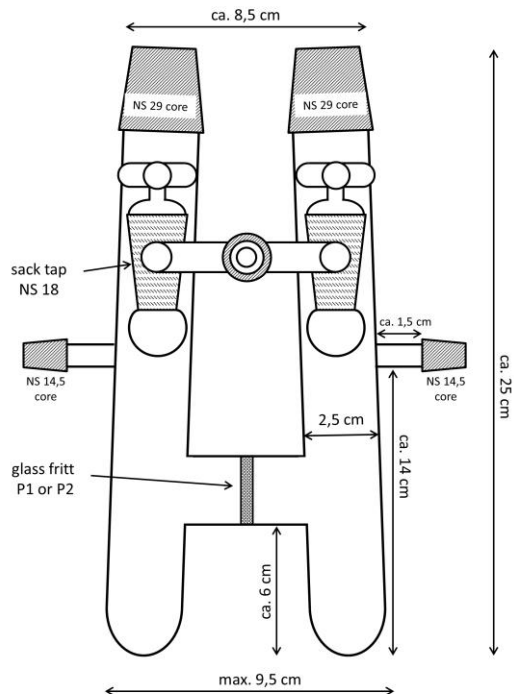


Figure 57: Schematic drawing (front view) of an H flask setup. Usage of depiction authorized by Dr. Wilhelm Klein, Chair of Inorganic Chemistry with Focus on Novel Materials.

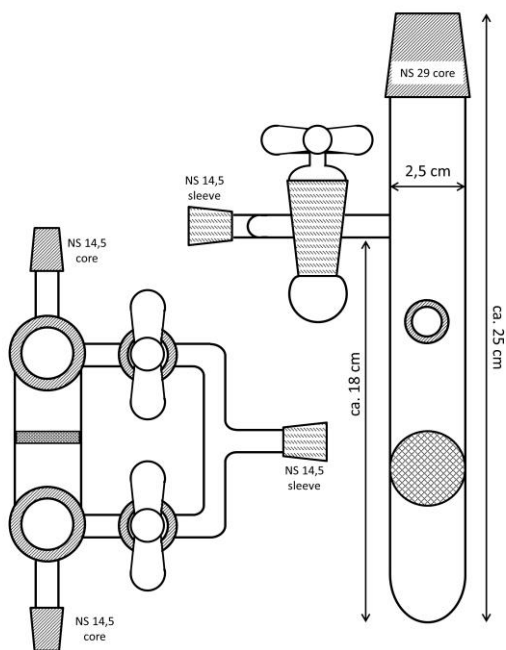


Figure 58: Schematic drawing (top and side view) of an H flask setup. Usage of depiction authorized by Dr. Wilhelm Klein, Chair of Inorganic Chemistry with Focus on Novel Materials.

6.4. Material list

A list of the materials used for synthesis can be found in Table. Solvents are either taken from a SPS station (MBraun) or dried over calcium hydride under reflux conditions and stored over molecular sieve (3 Å) and under Schlenk conditions or in a glovebox. The water content of ethylene diamine was monitored according to Fässler et al.^[422] Deuterated solvents for NMR studies are stored in a glovebox over molecular sieve (3 Å). Unless specified otherwise materials are used as delivered. 2.2.2-crypt and PEO is dried *in vacuo* for 8 hours, 18-crown-6 was sublimated under dynamic vacuum at a temperature of 80 °C and subsequently dried *in vacuo*.

Amberlyst 15 is washed with methanol, until the solvent runs clean and dried *in vacuo* at 100 °C for 48 h. If protons are the desired exchange species the resin is ready for usage under inert gas after this. If lithium or sodium ions are desired the polymer beads are suspended twice for one week in saturated LiOH · H₂O or NaOH solutions, respectively. The beads are washed until the pH of the washing solution is neutral and then dried again as described before.

Table 32: List of used chemicals.

Compound	Purity	Manufacturer	Morphology	Storage
18-crown-6	sublimated	Merck	Powder	GB
2.2.2-crypt	vacuo dried	Merck	Powder	GB
Acetonitrile	SPS	VWR	Liquid	Lab
Acetonitrile-d ₃ (99%)	Mol sieve	Deutero	Liquid	GB
Amberlyst 15	/	Sigma Aldrich	granules	GB
Ammonia	Na dried	Westfalen	Gas/liquid	Gas cylinder
Argon	99.998%	Westfalen AG	Gas	Gas cylinder
B12crown4	/	Merck	Solid	Lab

Calcium Hydrid	for synthesis	Merck	Solid	Lab
Chloroform-d (99.8%)	/	Deutero	Liquid	Lab
Chlorotris(trimethylsilyl)silane	>95%	TCI	solid	GB
Cobalt	99.8%	Alfa Aesar	Powder	GB
Copper	99.99%	Alfa Aesar	Wire	GB
Ethylendiamine	dried over CaH ₂	Merck	Liquid	Lab
Germanium	99.999%	ChemPur	Pieces	GB
Hypersilylchloride	>95.0%	TCI	Solid	GB
Iridium	99.9%	Chempur	Powder	GB
K ₄ Sn ₉	/	/	Powder	GB
K ₄ Ge ₉	/	/	Powder	GB
K ₄ Sn ₉	/	/	Powder	GB
K[Ge ₉ (Hyp) ₃]	/	Literature ^[141]	Powder	GB
Lead	99.95%	Chempur	Powder	GB
LiBr	99%	Alfa Aesar	Powder	GB
Lithiumhydroxide Monohydrate	For synthesis	Carl Roth	Powder	Lab
Nickel	99.98%	Alfa Aesar	Wire	GB
Osmium	99.9%	Venton	Powder	GB
Palladium	99.9+%	Chempur	Sponge	GB
PEO (~300 kDa)	>98%	Sigma Aldrich	Powder	GB
Platinum	99.9%	Sigma Aldrich	Powder	GB
Potassium	≥ 98%	Merck	Pieces	GB
Pyridin	max. 0,0075% H ₂ O	Merck	Liquid	GB

Rhodium	99.9%	Chempur	Powder	GB
Ruthenium	99.9%	Alfa Aesar	Powder	GB
Silicon	/	Wacker	Powder	GB
Silver	99.9%	Sigma Aldrich	Wire	GB
Sodium	99%	Merck	Pieces	GB
Sodium Hydroxide	For synthesis	/	Pellets	Lab
Tetrahydrofuran	SPS	Kraft	Liquid	GB
THF-d ₈ (99%)	Mol sieve	Deutero	Liquid	GB
Tin	99.999%	Chempur	Pieces	GB
TiCp ₂ Cl(NH ₃) ₂	/	Dr. Felix Geitner	powder	GB
Toluene	SPS	Brenntag	Liquid	Lab

6.5. Analytical Methods

6.5.1. Inductively coupled plasma optical emission spectroscopy (ICP-OES)

The concentrations of Li and K were measured by ICP-OES (iCAP 7600 Duo, *Thermo Fisher Scientific*, Waltham, MA, USA). Both elements were measured at a radial plasma observation. The emission lines at 670.784 nm (Li) and 766.490 nm (K) were used.

Samples are dissolved in *aqua reagens* and are diluted in ultrapure water, obtained from the Direct-Q® 5 UV water purification system (*Merck Millipore*, Darmstadt, Germany). For calibration, the ICP multi-element standard solution IV (*Merck Millipore*, Darmstadt, Germany) was used. The calibration solutions were prepared in diluted nitric acid (65% for analysis, *Merck*, Darmstadt, Germany, dilution in ultrapure water). Nitric acid was purified by sub-boiling distillation prior to use. All solutions were prepared in polypropylene centrifuge tubes.

6.5.2. Infrared Spectroscopy (IR)

FT-Infrared spectra are measured on an Alpha FT-IR spectroscope (*Bruker*). The spectroscope uses ATR geometry as well as a Diamond ATR unit (Roland Fischer group, TUM). The measurements are done under argon atmosphere inside a glovebox. IR spectra of solutions are collected by putting a droplet on the measurement window and letting the solvent evaporate. Kathrin Kratzl, M. Sc. (Roland Fischer group, TUM) supported the author with measurements.

6.5.3. Nuclear magnetic resonance (NMR)

Chemical shifts are given in δ values (ppm), the coupling constants J in Hz in relation to SiMe_4 (tetramethylsilane). The signals of ^1H and ^{13}C spectra are calibrated on the rest proton signal of the used deuterated solvents $\text{acn-}d_3$ or $\text{chloroform-}d$. Samples are prepared in the Glovebox and measured immediately to ensure minimal air exposure. Signal multiplicities are abbreviated as follows: s - singlet, d - doublet, t – triplet q – quartet and m – multiplet. The spectra were evaluated with MestrelNova (*Mestrelab Research*).^[423]

6.5.3.1. Solution based NMR

^1H , ^{13}C and ^{29}Si NMR spectra are recorded on a Bruker Avance Ultrashield 400 MHz (*Bruker Corp.*). ^7Li NMR Spectra are recorded on a Bruker DPX 400 MHz (*Bruker Corp.*) at 300 K but Dr. Maria Matthews.

6.5.3.2. Magic angle spinning solid state NMR (MAS NMR)

Static and magic-angle spinning (MAS) NMR ^7Li experiments were carried out with Bruker Avance 300 (*Bruker Crop.*) operating at 7 T by Dr. Gabriele Raudschl-Sieber (Chair of Inorganic Chemistry with Focus on Novel Materials, TUM, Germany). For the measurements the samples are packed in an air-tight 4 mm ZrO_2 MAS-NMR rotor. For ^7Li a resonance frequency of 116.5 MHz was applied while the rotor was cooled and rotated using nitrogen.

MAS-NMR is performed at 15 kHz and 1.0 M aq. LiCl is used as a reference. The spectra are collected with the TopSpin software.

6.5.4. Raman spectroscopy

Raman spectroscopy is performed using a *Renishaw* inVia Raman microscope equipped with a CCD detector and three different lasers ($\lambda = 532$ nm, 633 nm, and 785 nm) with a maximum power of 500 mW. For operating the device, the software WiRe 4.2 (build 5037, *Renishaw*, 2002) is used. Samples are dried *in vacuo*, ground in an agate mortar inside a glovebox, filled into glass capillaries (inner diameter 0.3 – 0.7 mm, wall thickness 0.01 mm, *Hilgenberg GmbH*) which are sealed using capillary wax (*Hampton Research*). Data is processed using Origin (*OriginLab Corp.*).^[424] Calculated Raman shifts are subject to change using appropriate scale factors of up to 5%.^[380] Values treated with scale factors will be marked as such.

6.5.5. X-ray diffraction

6.5.5.1. Single crystal diffraction

Single crystal X-ray diffraction data collection is performed on both an *Oxford-Diffraction* Xcalibur3 diffractometer and a *STOE* StadiVari diffractometer. Goniometers with kappa geometry and CCD (charge coupled device) detectors are used in the *Oxford-Diffraction* Xcalibur3 diffractometer while euler geometry is employed on the *STOE* StadiVari diffractometer. Both devices while Mo-radiation is generated by an X-ray tube. X-ray sources are monochromatized to $\text{MoK}\alpha$ ($\lambda = 0.71073 \text{ \AA}$) using a graphite monochromator. Single crystals are fixed on a glass fibre or loop with perfluorinated ether and positioned in a N_2 stream ranging in temperature between 120 K and 150 K. The structures were solved by Direct Methods and refined by full-matrix least-squares calculations against F^2 using SHELX-2014.^[425] If possible, non-hydrogen atoms were treated with anisotropic displacement parameters. A final check concerning space groups is done using Platon.^[426] Pictures of the crystal structures were created with the program Diamond.^[427] Any data on the crystallographic volume of clusters or similar structures is geometrically calculated using the program Vesta.^[428]

6.5.5.2. Preparation of crystals under inert gas

Single crystals grown under cooling are prepared on a cooling table similar to the setup of *Kottke* and *Stalke*.^[429] Crystals are removed from the vessel under a continuous stream of Ar and transferred into perfluorinated polyether (Galden®, *Solvay Solexis*) on a slide. The slide is cooled by a dewar filled with liquid nitrogen from below and by a cool laminar N_2 stream from the side. The nitrogen stream also provides the sample protection from moisture and oxygen. Single crystals are isolated using a microscope (*Leica Microsystems GmbH*) and fixed on a loop on top of a crystal cap (*Hampton Research*). Utilizing a metal clamp the crystals are transferred to the diffractometer in a liquid nitrogen bath (Figure 59).

Crystals grown at room temperature are transferred into perfluoropolyalkylether (*ABCR GmbH & Co. KG*) on a slide in a glovebox and separated using a microscope (*Leica Microsystems GmbH*). The crystals are fixed on glass spikes and transferred to the diffractometer using polymer stoppers and glass hoods.

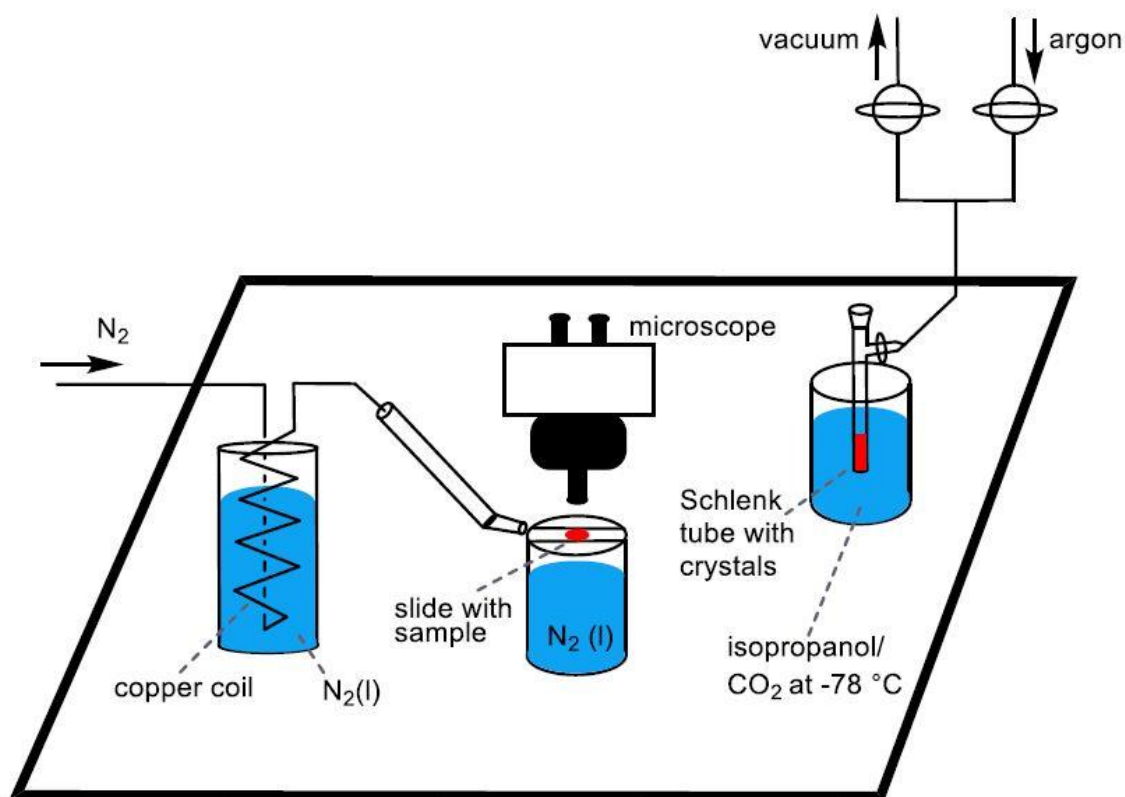


Figure 59: Cooling table setup for picking crystals out of liquid ammonia under inert gas. Usage of depiction authorized by Dr. Felix Geitner, Chair of Inorganic Chemistry with Focus on Novel Materials.

6.5.5.3. Powder X-ray diffraction (PXRD)

Phase analyses of solid bulk products are performed using a STADIP diffractometer (Ge(111) monochromator; CuK_{α} radiation; *STOE & Cie GmbH*) with a linear position-sensitive detector (Mythen1K, *DECTRIS Ltd.*). The compounds are ground inside a glovebox, sealed in glass capillaries

(inner diameter 0.3 – 0.7 mm, wall thickness 0.01 mm, Hilgenberg GmbH) and measured in Debye-Scherrer geometry. *STOE WinXPOW*^[430] software package is used for data analysis by direct comparison of measured diffractograms with calculated diffractograms obtained from single crystal analyses.

6.5.6. Dynamic scanning calorimetry (DSC)

Samples are weighed (approx. 20 – 50 mg) into niobium crucibles (Precision mechanical workshop TUM) which is welded shut. An empty niobium crucible serves as a reference. The crucibles are placed in the heating chamber of the machine (*Netzsch*, DSC 404 Pegasus) which is evacuated and flooded with Ar three times. The gas flow is constant at 75 mL/min during measurements. Control and evaluation of measurements is done using the *PROTEUS* thermal Analysis software.^[431]

6.5.7. Electron spray mass spectrometry (ESI-MS)

Compounds are dissolved in respective best solvent, filtered through a syringe filter (diameter 25 mm, pore size 0.2 µm) and are diluted to a concentration of approx. $2.0 \cdot 10^{-4}$ mmol/mL. Measurements are performed on a HCT instrument (*Bruker Corp.*). Analysis of the data was evaluated using the program *Bruker Compass Data Analysis 4.0 SP 5* (*Bruker Corp.*). The dry gas temperature is set at 125 °C and the injection speed at 240 µL/h. Data evaluation is done using *Origin* (*OriginLab Corp.*).^[424]

6.5.8. Dynamic light scattering (DLS) & Zeta potential measurements

In order to measure the size of germanium nanoparticles dynamic light scattering (DLS) is used. The Zeta potential is examined for particles suspended in water as well. The measurements are performed on a *Malvern ZEN 3600 Zetasizer*. The size determination was done using the parameters displayed in Table 33. DLS measurements are done by placing 0.5 mL of the dispersant in the cuvette and then adding 0.05 mL drops of the sample in the dispersant and mix until homogenous. The sample is added until a stable measurement is gained. Before each

measurement the sample is mixed and given an equilibrium time of 120 s. The measurements are done at an angle of 173 °.

The Zeta potential is measured using a DTS1070 cuvette by *Malvern*. The cuvette is cleaned prior to use with EtOH and deionized water and then loaded with the pure sample and the measurement is done using the Smolchulski setup.

Table 33: Measurement parameters of size determination and Zeta potential measurements using the *Malvern* ZEN 3600 Zetasizer.

Measurement	Dispersant	Refractive index	Viscosity / Ns/m ²	Dielectric constant / C/Vm
For Size	acn	1.34	3.340	37.5
For Zetapotential	H ₂ O	1.33	8.872	78.5

Material	Refractive index	Absorption
Germanium	4	0.03

For Size	A sum of 10 measurements is done. Each measurement consists of 5 runs where each run is ten seconds.
For Zetapotential	A sum of 5 measurements is done. Each measurement consists of 5 runs where each run is ten seconds.

6.5.9. Transmission electron microscopy (TEM)

Electrondiffraction, high resolution TEM (HR-TEM), dark field, EDX and scanning transmission electron microscopy and TEM measurements are done on an Tecnai F30 G² STwin (*FEI*) at 300 kV FEG. Sample preparation is done by dissolving the solid samples (about 1-2 mg) in *tert*-butanol as

then examined the suspension. The measurements are done by Dr.-Ing. Torben Dankwort, Synthesis and Real Structure Group at the CAU Kiel.

6.5.10. Quantum chemical Calculations

Computational analyses are performed using the Gaussian09 program package,^[432] with exchange correlation hybrid functional after Perdew, Burke and Ernzerhof (PBE0)^[433] and def2–TZVPP basis sets for all considered elements (Ru,^[434-435] Co,^[436] Rh,^[434-435] Ni,^[435] Pd,^[434-435] Si,^[435] Ge,^[437] Sn^[435, 438]). Structure parameters for single point calculations are taken from respective single crystal structures and the compensation of positive charges occurred using a solvation model (polarizable continuum model, PCM).^[436] For clusters where no structures are reported or discussed in this work, reported clusters are used and the elements switched. After this the cluster structures are optimized and Raman spectra are calculated. Jmol,^[439] VESTA 3^[428], IBOview^[440] and Origin 9.1^[424] are used for data processing and visualization. Calculated Raman shifts are subject to change using appropriate scale factors of up to 5%.^[380] Values treated with scale factors will be marked as such. Calculations are done by M. Sc. Jasmin Dums, Chair of Inorganic Chemistry with Focus on Novel Materials.

6.6. Syntheses

6.6.1. Binary *Zintl* phases

Binary *Zintl* phases are synthesized in Ta ampules, while K_4Ge_9 is synthesized in a steel autoclave for increased yield.

Compound	Heating rate / °C/min	Heating temperature / °C	Heating time / h	Cooling rate / °C/min	Molar ratio K/E
K_4Si_4	2	600	10	0.2	1/1
$K_{12}Si_{17}$	2	800	15	1	1/1.42
K_4Ge_4	2	600	10	0.2	1/1
K_4Ge_9	2	650	46	1	1/2.05
K_4Sn_4	2	550	46	1	1/1
K_4Sn_9	2	550	46	1	1/2.05

6.6.2. Stability of binary *Zintl* phases $K_{12}Si_{17}$ and K_4Ge_9 in liquid ammonia

K_4Ge_9 (0.5 g, 0.6172 mmol) or $K_{12}Si_{17}$ (0.5 g, 0.5282 mmol) is weighed into a H-flask and filtrated as described in section 6.3. The yield of filtrated K_4Ge_9 after 5 filtration cycles is about 50% while $K_{12}Si_{17}$ yields only about 10%. After filtration both the residue (undissolved *Zintl* phase) as well as the solid product gained from solvent evaporation of the filtrate are examined using Raman and PXRD. DSC analysis is performed after which again Raman and PXRD is used to examine the solid after heating.

6.6.3. Ion exchange experiments using Amberlyst 15 and Zintl phases

6.6.3.1. Determination of exchange parameters

Parameters – different solvents, amount of ER equivalents and exchange times – of ion exchange reactions are determined using ICP-OES as a quantitative analysis method (section 6.5.1). ICP-OES measurement data can be found in section 7.1. The values in the tables describe the amount of solid product dissolved in the given amount of *aqua reagens*.

Determining the viability of Cs^+ ions versus K^+ ions Cs_4Ge_9 (0.146 g, 0.1234 mmol) and K_4Ge_9 (0.1 g, 0.1234 mmol) and alongside 20 equivalents LiER are dissolved in ~10 mL liquid ammonia, left to exchange over night, filtrated, dried and analysed using ICP-OES.

In order to determine the viability of different solvents, the amount of lithium after the exchange reaction (24 hours) was determined using ICP-OES. K_4Ge_9 was dissolved in dmf (10 mL) (0.05 g, 0.06172 mmol) and liquid ammonia (~ 10 mL) (0.1 g, 0.1234 mmol) alongside 20 equivalents of LiER. $\text{K}[\text{Ge}_9[\text{Si}(\text{SiMe}_3)_3]_3]$ was dissolved in 10 mL acn (0.05 g, 0.0548 mmol) alongside 20 equivalents of LiER. After the exchange time, the solutions are filtrated, dried and analysed using ICP-OES.

Table 34: Weight and solution volume of solvent tests for lithium ion exchange reactions.

Sample	Weight of sample dissolved for ICP-OES / mg	Amount of <i>aqua reagens</i> used for solvation / mL
K_4Ge_9	2	10
Cs_4Ge_9	2	20
dmf solvent test	0.5	10
NH_3 solvent test	2	20
acn solvent test	13.4	10

The determination of the time frame was done by dissolving $\text{K}[\text{Ge}_9[\text{Si}(\text{SiMe}_3)_3]_3]$ (0.05 g, 0.0548 mmol) in 5 mL of acn alongside 20 equivalents of LiER and letting the exchange reaction go for several different times. Times tested were: 1 h, 2 h, 4 h, 8 h, 24 h and 48 h. The exchange was stopped by separating the solution and LiER.

Table 35: Weight and solution volume of time trials for lithium ion exchange reactions.

Exchange times / h	Weight of sample dissolved for ICP-OES / mg	Amount of <i>aqua reagens</i> used for solvation / mL
1 h	1.3	10
2 h	12.9	10
4 h	13.4	10
8 h	12.3	10
24 h	13.4	10
48 h	16.9	20

The determination of the proper amount of LiER equivalents was done by dissolving $\text{K}[\text{Ge}_9[\text{Si}(\text{SiMe}_3)_3]_3]$ (0.05 g, 0.0548 mmol) in 5 mL of acn alongside differing equivalents of LiER and letting the exchange reaction go for 24 hours. Equivalents tested were; 1, 2, 5, 10. The exchange was stopped by separating the solution and LiER.

Table 36: Weight and solution volume of equivalent trials for lithium ion exchange reactions.

Equivalents of LiER	Weight of sample dissolved for ICP-OES / mg	Amount of <i>aqua reaxis</i> used for solvation / mL
2	16.3	10
5	12.6	10
10	18.3	20

6.6.3.2. Lithium ion exchange experiments on bare *Zintl* phases

Table 37: Amount of *Zintl* phase and LiER in ion exchange experiments in liquid ammonia. *Zintl* phase/LiER ratio is to be interpreted as per alkali metal atom. About 10 mL of liquid ammonia are used in these experiments.

<i>Zintl</i> phase	m(<i>Zintl</i> phase) / g	<i>Zintl</i> phase/LiER ratio
K ₄ Si ₄	0.1	1/3
K ₁₂ Si ₁₇	0.05	1/20
K ₄ Ge ₄	0.1	1/5
K ₄ Ge ₉	0.15	1/20
K ₄ Sn ₉	0.1	1/5

These experiments are done in a H-flask under Schlenk conditions (section 6.3). No yield could be isolated in experiments including silicide clusters because of gas expulsion during the reaction. A pressure increase from $8.5 \cdot 10^{-4}$ to $6.5 \cdot 10^{-1}$ can be observed. An additional reaction was done

with $\text{K}_{12}\text{Si}_{17}$ and LiBr to determine if the presence of lithium ions has effects $[\text{Si}_9]^{4-}$ and $[\text{Si}_4]^{4-}$ clusters in dissolved in liquid ammonia. For this ~10 mL of liquid ammonia are condensed onto $\text{K}_{12}\text{Si}_{17}$ (0.075 g, 0.07923 mmol). $\text{K}_{12}\text{Si}_{17}$ is given several hours to dissolve and is then filtrated onto the LiBr (0.0826 g, 0.951 mmol). When the liquid ammonia touches the LiBr gas expulsion can be seen. This expulsion increases the pressure to 1.1 mbar. The amount of gas expulsion diminishes after each filtration but is still noticeable. Before analysis the samples were exposed to small quantities of air, which does not seem to have been detrimental to the analyses. Samples after extraction are always extremely amorphous even without miniscule air exposure and the fact that gas expulsion took place is unchanged.

Experiments using germanides showed a yield of about 20% after 5 extraction cycles. Stannide exchange reactions showed only crystals in a yield of about 20%.

$\text{Li}_4\text{Sn}_9 \cdot 17 \text{NH}_3$ is isolated by placing K_4Sn_9 (0.1 g, 0.0816 mmol) and LiER (0.346 g, 1.63 mmol) in a H-flask and about 10 mL liquid ammonia is condensed into the flask. The red solution is extracted ten times every 48 hours. Long black crystals are obtained after eight weeks of storage at -40 °C (yield ~20%).

6.6.3.3. Lithium ion exchange experiments on *Zintl* clusters featuring ligands

$\text{K}[\text{Ge}_9[\text{Si}(\text{SiMe}_3)_3]_3]$ is synthesized using a modified method from Sevov *et al.*^[141] K_4Ge_9 (0.9 g; 1.11 mmol) is weighed into a Schlenk tube. Chlorotris(trimethylsilyl)silane (0.942 g; 3.33 mmol) is dissolved in 35 mL of acn and added to K_4Ge_9 . The mixture is stirred overnight, filtered and the acetonitrile is removed *in vacuo*.

^1H NMR (400 MHz, 298 K, $\text{acn}-d_3$): δ [ppm] = 0.22 (s, SiMe_3)

^{29}Si -INEPT NMR (79 MHz, 298 K, $\text{acn}-d_3$): δ [ppm] = -9.82 (s, SiMe_3), -108.19 ppm (s, Si_{Ge_9})

$\text{Li}[\text{Ge}_9[\text{Si}(\text{SiMe}_3)_3]_3]$ is isolated by dissolution of $\text{K}[\text{Ge}_9[\text{Si}(\text{SiMe}_3)_3]_3]$ (0.05 g, 0.0358 mmol) in 5 mL acetonitrile, filtration onto LiER (0.34 g, 1.564 mmol) and exchange for 5 days. The solution is

separated from the LiER, the solvent is removed and the product is dried *in vacuo*. For the iCP-OES analysis 16.9 mg are weighed out and analyzed as described in section 6.6.3.1.

^1H NMR: (400 MHz, 298 K, $\text{acn-}d_3$): δ [ppm] = 0.22 (s, 81 H, SiMe_3)

^7Li -NMR: (155 MHz, 298 K, $\text{acn-}d_3$): δ [ppm] = -2.72 (s, Li)

^{29}Si -INEPT NMR: (79 MHz, 298 K, $\text{acn-}d_3$): δ [ppm] = -9.48 (s, SiMe_3), -107.93 (s, Si_{Ge9})

ICP-OES: Li/K [mol-%] = 98.4/1.6

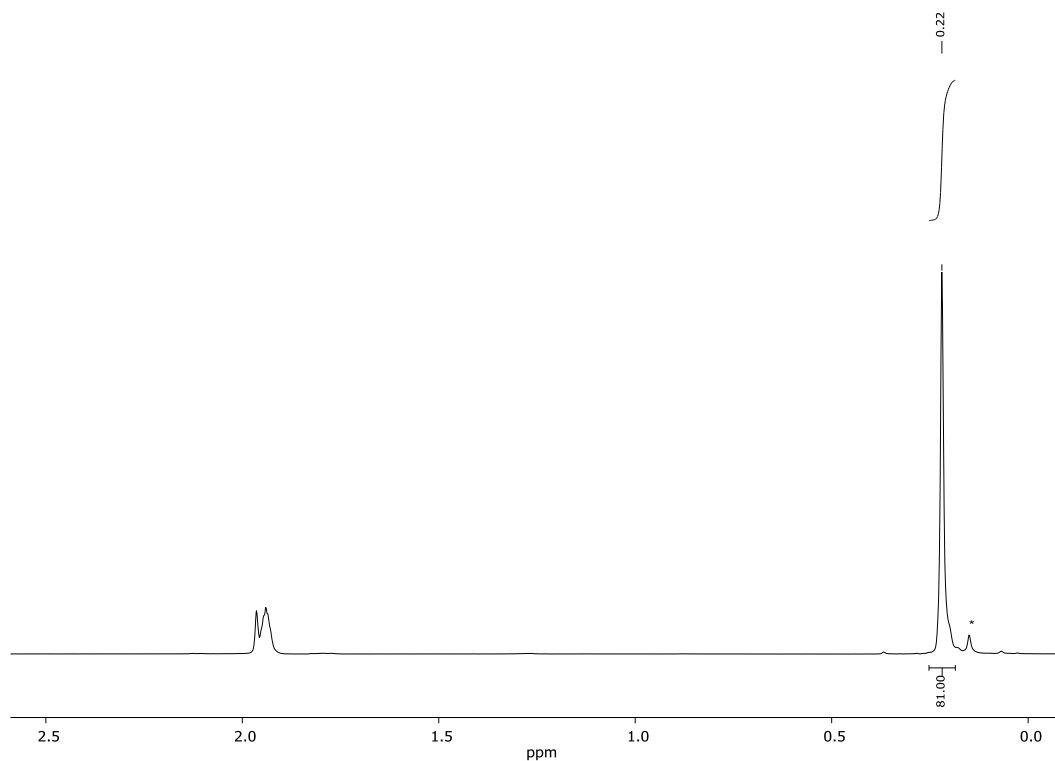


Figure 60: ^1H -NMR spectrum of $\text{Li}[\text{Ge}_9(\text{Si}(\text{SiMe}_3)_3)_3]$. Broad signal at 1.95 ppm is residual acn.

^1H NMR (400 MHz, 298 K, $\text{acn-}d_3$): δ [ppm] = 0.22 (s, SiMe_3)

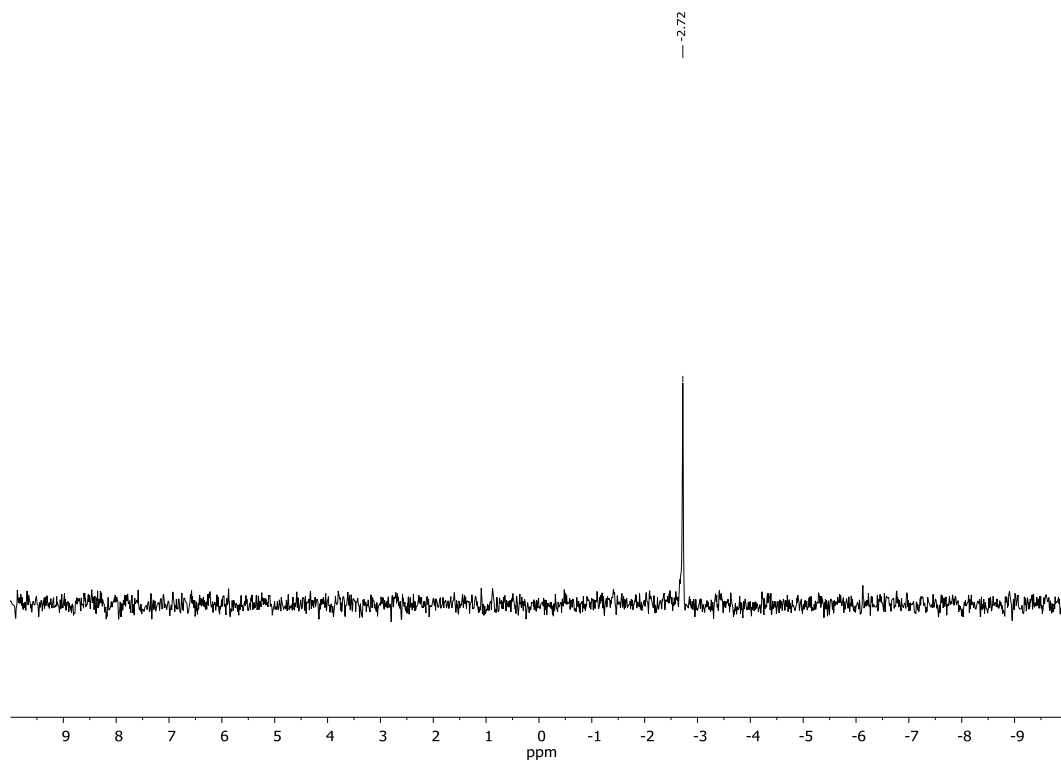


Figure 61: ^7Li -NMR spectrum of $\text{Li}[\text{Ge}_9(\text{Si}(\text{SiMe}_3)_3)_3]$.

^7Li NMR (400 MHz, 298 K, $\text{acn}-d_3$): δ [ppm] = -2.72 (s, SiMe₃)

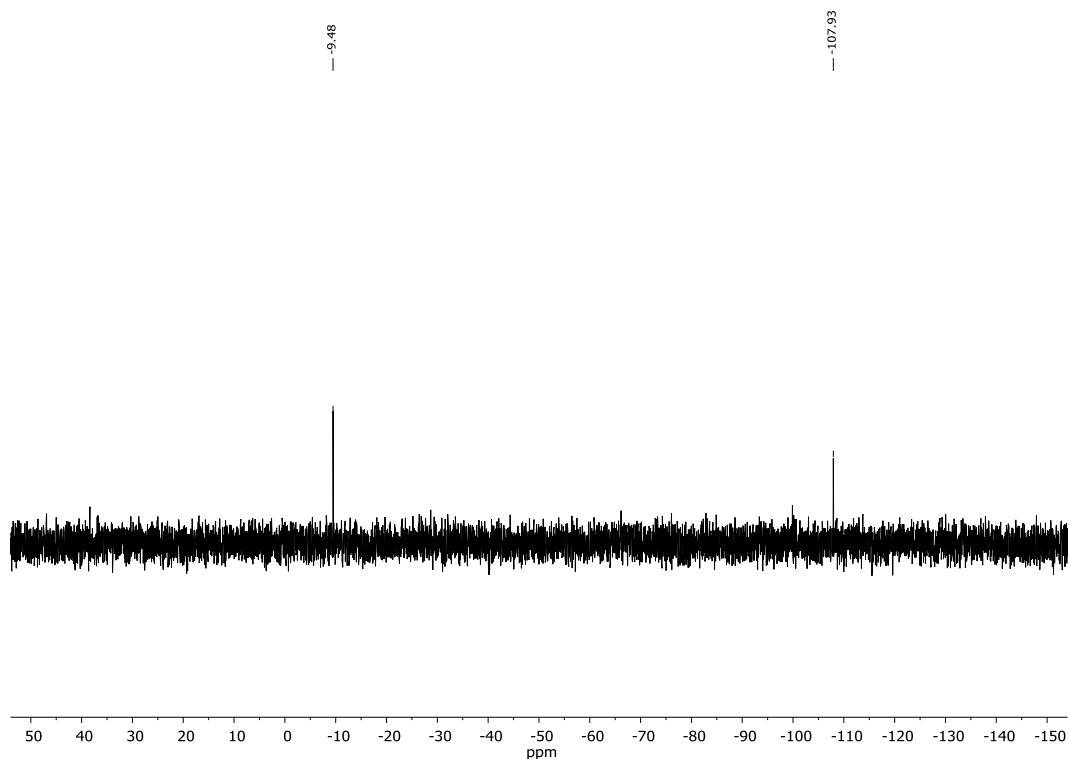


Figure 62: ^{29}Si -INEPT-NMR spectrum of $\text{Li}[\text{Ge}_9(\text{Si}(\text{SiMe}_3)_3)_3]$.

^{29}Si -INEPT NMR (79 MHz, 298 K, $\text{acn}-d_3$): δ [ppm] = -9.48 (s, SiMe_3), -107.93 ppm (s, Si_{Ge_9})

$[\text{Li}(\text{B12crown4})_2][\text{Ge}_9(\text{Si}(\text{SiMe}_3)_3)_3]$ is isolated by dissolution of $\text{K}[\text{Ge}_9(\text{Si}(\text{SiMe}_3)_3)_3]$ (0.05 g, 0.0358 mmol) in 5 mL acetonitrile. The solution is filtrated onto LiER (0.34 g, 1.564 mmol) and left to exchange for 5 days. The solution was then filtrated onto B12C4 (0.008 g, 0.0358 mmol) and stored at $-32\text{ }^\circ\text{C}$. Large red crystals were obtained after three weeks (yield $\sim 80\%$).

6.6.3.4. Stabilization of lithium ions towards *Zintl* clusters using PEO

$\text{Li}[\text{Ge}_9(\text{Si}(\text{SiMe}_3)_3)_3]$ is synthesized as described in section 6.6.3.3. $\text{Li}[\text{Ge}_9(\text{Si}(\text{SiMe}_3)_3)_3]$ is dissolved in 5 mL acn along with n eq ($n = 1, 3, 6, 12$) PEO. acn is removed *in vacuo* and the resulting foil is analysed using Raman spectroscopy and NMR spectrometry.

K_4Ge_9 (0.1 g, 0.124 mmol) is dissolved in 8 mL dmf and allowed to react with LiER (2.1 g, 2.48 mmol) over the course of 24 hours. The red solution is filtered through a syringe filter and n eq ($n = 1, 3, 6, 12$) PEO are added to the solution. dmf is removed *in vacuo* and the resulting foil is analysed using Raman spectroscopy.

K_4Ge_9 (0.1 g, 0.124 mmol) is dissolved in ~10 mL liquid ammonia and allowed to react with LiER (1.056 g, 1.24 mmol) over the course of 24 hours. The red solution is filtered multiple times through a frit onto PEO (0.049 g, 1.12 mmol). Liquid ammonia is removed *in vacuo* and the resulting solid is analysed using Raman spectroscopy.

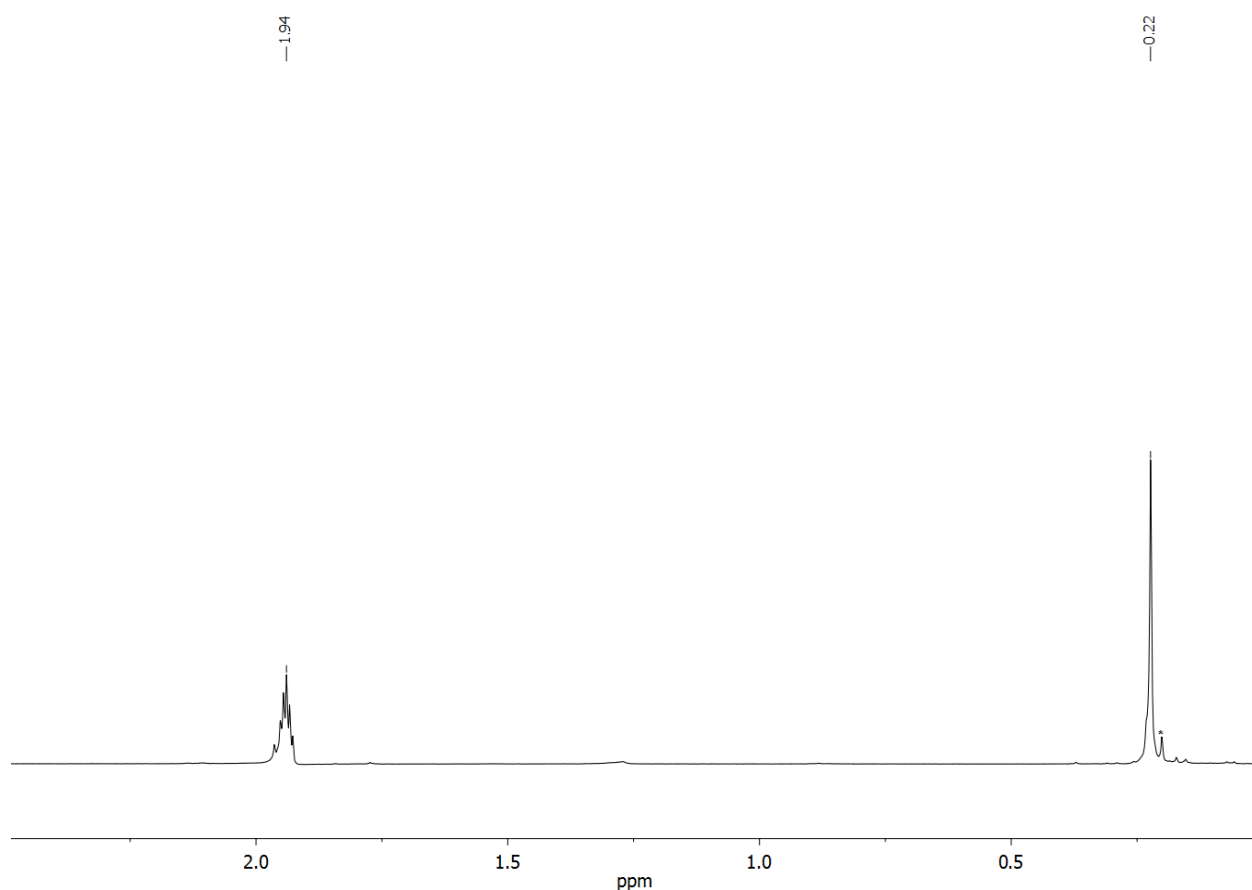


Figure 63: ^1H -NMR spectrum of $\text{Li}[\text{Ge}_9(\text{Si}(\text{SiMe}_3)_3)_3]$ and 3 equivalents of PEO reacted in 5 mL of can.

6.6.3.5. Crystallization experiments of lithiated *Zintl* phases

In order to crystallize compounds which include *Zintl* clusters and lithium ions several experiments are conducted with oxidizing agents to reduce the charge of the *Zintl* clusters. For this the *Zintl* phase and the sequestering agent are dissolved in liquid ammonia (~10 mL) and stirred for 30 min. After this Me₃SnCl is added and the solution is stirred for another 10 min. Ammonia is evaporated and 5 mL of the crystallization solvent is added and the solution is filtrated onto the LiER after which the solution is left to exchange for 7 days. After the exchange the solution is filtered onto two equivalents B12crown4 and left to crystallize at –32 °C. Unless stated otherwise the solutions in liquid ammonia were red and opaque.

Table 38: Reaction parameters of oxidizing reactions aimed at reducing the overall charge of *Zintl* phases in order to increase the stability towards lithium ions.

<i>Zintl</i> phase	<i>Zintl</i> phase mass / g	Eq of Me ₃ SnCl	Sequestering agent / eq	Crystallization solvent
K ₄ Si ₄ ^a	0.05	1	2.5 eq 18-crown-6	acn
K ₁₂ Si ₁₇ ^a	0.1	1; 2; 2.1	1.8; 3.05 eq 18-crown-6	acn
K ₄ Ge ₄	0.05	1; 2	1.8; 2.5; 3 eq 18-crown-6	thf; acn; pyr
K ₄ Ge ₉	0.1	1; 2	3.05 eq 18-crown-6	acn
K ₁₂ Ge ₁₇	0.1	1	1.8 eq 18-crown-6	pyr; acn
K ₄ Sn ₄	0.05	1	1.8 eq 18-crown-6	pyr; acn
K ₄ Sn ₉	0.05/0.1	1	1.8 eq 18-crown-6	pyr; acn

a – solutions of silicide phases yield red solutions which are clear.

6.6.3.6. Syntheses of Ge nanoparticles using K_4Ge_9 and Amberlyst 15

K_4Ge_9 (0.1 g; 0.1234 mmol) and Amberlyst 15, loaded with the desired ions, (1.056 g; 4.93 mmol) are weighed into the reaction flask and 10 mL of acn are added. The reaction mixture is left standing for 24 hours with occasional agitation. The red suspension is then filtrated and analyzed by TEM and DLS. DLS analysis parameters can be found in section 6.5.8. Analysis parameters of the TEM measurements can be found in section 6.5.9. For the TEM the samples are dried *in vacuo* and then suspended in *tert*-butanol.

For Zeta-Potential measurements the nanoparticles are suspended in water. This is done by removing the acn from a nanoparticle suspension and then suspend the particles in 10 mL water. For this the suspension is sonicated and immediately examined for the Zeta-Potential.

6.6.4. Ternary *Zintl* Phases

Ternary *Zintl* phases are synthesized exclusively in tantalum ampoules. This is done to ensure no side reactions take place. Some phases however show the possibility of side reactions with the tantalum ampoule material. If this is the case an extra corundum tube can be placed in the tantalum ampoule to inhibit these unwanted side reactions. Some syntheses of ternary, endohedral *Zintl* phases are done by Dr. Marina Boyko, Chair of Inorganic Chemistry with Focus on Novel Materials, and given for further investigation and dissolving.

Phases marked “*” feature an additional synthesis step of arc melting the tetrel and transition metal together before the reaction with the alkali metal. The melting is done three times between each melting step the alloy is flipped 180 ° to ensure a complete melt. Arc furnace intensities are noted in each table description. If the one of the two elements which are to be arc melted is a powder they are pressed together (Hydraulic press by *Specac*; pressing is done with a steel cylinder with an inner diameter of 6 mm) with 2 t for 20 min before arc melting.

Table 39: Syntheses parameters of ternary phases. The phases with the nominal compositions listed in this table are synthesized by Dr. Marina Boyko, Chair of Inorganic Chemistry with Focus on Novel Materials. For more detailed information on the synthesis of these phases refer to Dr. Marina Boykos dissertation.^[385]

Phase Composition	Ampoule material	Temperature profile	Identified clusters contained in compounds according to Raman analysis
"K ₅ Fe _{1.5} Ge ₉ "	Ta	IX	[Ge ₄] ⁴⁻ , [Ge ₉] ⁴⁻
"K ₅ Ru _{1.5} Ge ₉ "	Ta	IX	[Ge ₄] ⁴⁻ , [Ge ₉] ⁴⁻
"K ₄ Ru ₃ Sn ₇ "	Ta	I	[Ru@Sn ₉] ⁶⁻
"K ₅ Pd _{1.5} Ge _{14.7} "	Ta	IX	[Ge ₉] ⁴⁻
"Cs ₄ Ag _{1.5} Ge ₉ "	Ta	X	[Ge ₄] ⁴⁻ , [Ge ₉] ⁴⁻
"K ₄ OsSn ₉ "	Ta	V	[Sn ₉] ⁴⁻
"Na ₄ RhSn ₄ "	Ta	I	∅
"Na ₁₃ RhSn ₁₇ "	Nb	IV	[Rh@Sn ₉] ⁵⁻
"K ₅ RhSn ₉ "	Ta	III	[Rh@Sn ₉] ^{5-a}
"K ₄ Ni ₃ Sn ₉ "	Ta	V	β-tin, [Ni@Sn ₉] ⁴⁻
"K ₅ PdSn ₉ "	Ta	III	[Sn ₄] ⁴⁻ , [Sn ₉] ⁴⁻
"K ₅ PtSn ₉ "	Ta	III	∅
"Cs ₁₃ Cu _{1.5} Sn ₁₇ "	Ta	XI	[Sn ₄] ⁴⁻ , [Sn ₉] ⁴⁻
"Na ₁₂ Pd ₂ Sn ₁₇ "	Ta	V	[Pd@Sn ₉] ⁴⁻
"K ₂ PdSn ₄ "	Ta	I	[Sn ₄] ⁴⁻ , [Sn ₉] ⁴⁻
"K ₅ RhPb ₉ "	Ta	II	∅
"K ₅ IrPb ₉ "	Ta	III	∅
"K ₅ PdPb ₉ "	Ta	III	∅

^a – the presence of this cluster in the solid state is not proven by Raman analysis but the crystallization of a compound containing the [Rh@Sn₉] cluster from liquid ammonia after solvation of “K₅RhSn₉”. It can be postulated that this phase, as well as the phase “Na₁₃RhSn₁₇”, both contain the filled tin cluster.

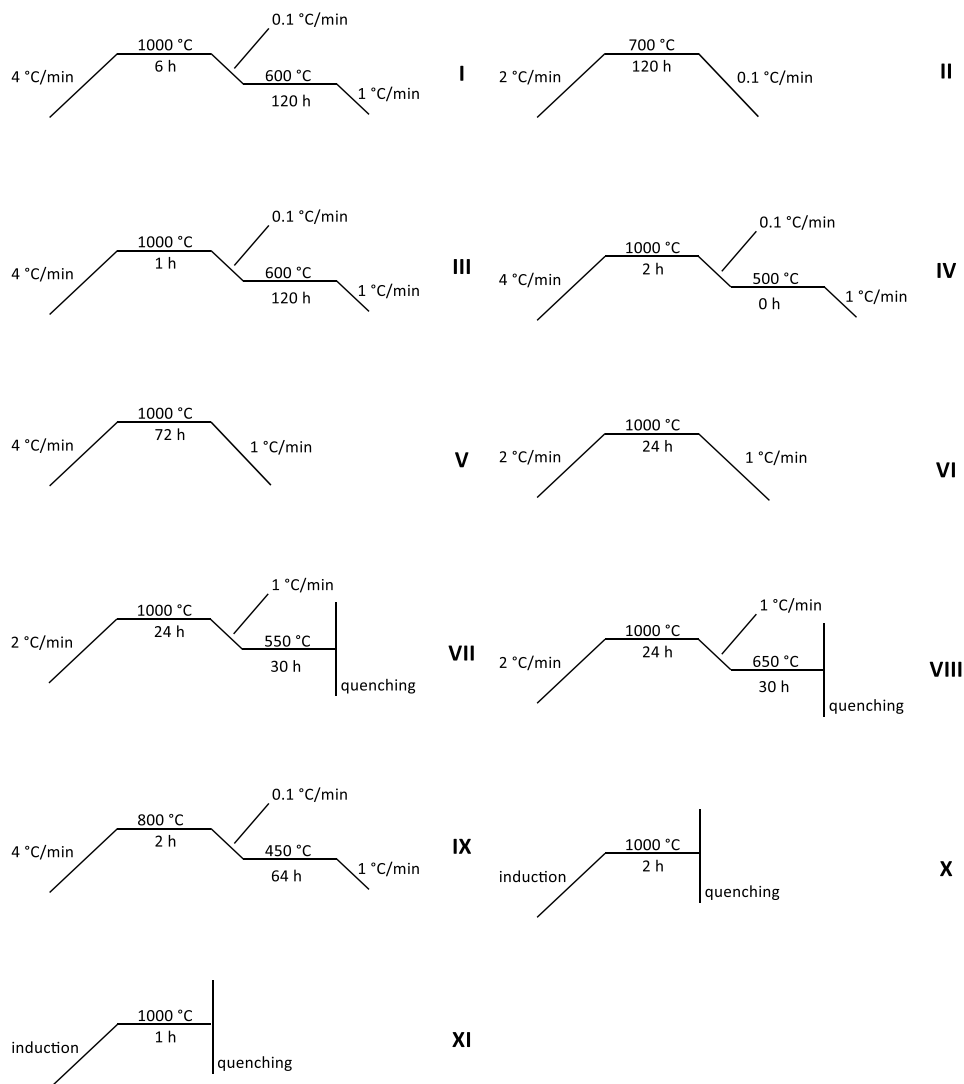


Figure 64: Collection of temperature profiles used for syntheses of solid state phases described in Table 39.

All phases marked with “NH₃(l)” in the last column of Table 39 are dissolved separately with 1.8 equivalents of 18-crown-6 and 2.2.2-crypt in ~5 mL of liquid ammonia. Phases marked with “∅” either do not yield any Raman signals, as is the case with all samples containing lead, or could not be investigated because all sample material was used for solution experiments. All results of X-

ray powder diffraction experiments and Raman spectroscopy of the ternary phases can be found in the appendix (section 7.3.5). All phases yielded opaque, red solutions upon dissolving in liquid ammonia with the sequestering agents used, unless stated otherwise.

$\text{K}_7[\text{Ru}@\text{Sn}_9](\text{OH}) \cdot 10 \text{ NH}_3$ was isolated by dissolving “ $\text{K}_4\text{Ru}_3\text{Sn}_7$ ” (0.075 g, 0.058 mmol) and 18-crown-6 (0.027 g, 0.105 mmol) in approx. 5 mL of liquid ammonia and storage at -42°C . After two months black crystals could be isolated with a yield of 25 %.

$\text{C}_{100}\text{H}_{200}\text{K}_8\text{N}_{10}\text{O}_{20}\text{Rh}_4\text{Sn}_{36}$ was isolated by dissolving “ K_5RhSn_9 ” (0.075 g, 0.0549 mmol) and 18-crown-6 (0.026 g, 0.0988 mmol) in approx. 5 mL of liquid ammonia and storage at -42°C . After two months a few black crystals could be isolated.

$\text{K}_3[\text{Rh}@\text{Pb}_{12}]$ was isolated by dissolving “ K_5RhPb_9 ” (0.075, 0.03467 mmol) and 2.2.2-crypt (0.0235 g, 0.06241 mmol) are dissolved in approx. 5 mL of liquid ammonia and storage at -42°C . After two months several black crystals could be isolated.

$[\text{Cs}(18\text{-crown-6})][\text{Ge}_9[\text{Si}(\text{SiMe}_3)_3]_3][\text{ClSi}(\text{SiMe}_3)_3]_2$ was isolated by dissolving $\text{Cl}(\text{Si}(\text{SiMe}_3)_3)$ (0.140 g, 0.1671 mmol) in 10 mL acn, filtrating unto “ $\text{Cs}_4\text{Ag}_{1.5}\text{Ge}_9$ ” (0.075 g, 0.0557) and is stirring overnight. The brown solution is filtered onto 18-crown-6 (0.026 g, 0.100 mmol). The solvent volume is reduced and the solution is stored at -32°C . After several months crystals could be isolated.

$[\text{K}_5(\text{OH})]\text{Ge}_9 \cdot 8 \text{ NH}_3$ was isolated by dissolving “ $\text{K}_5\text{Fe}_{1.5}\text{Ge}_9$ ” (0.075 g, 0.0804 mmol) and 2.2.2-crypt (0.054 g, 0.1448 mmol) in approx. 5 mL of liquid ammonia and storing at -42°C . After a few months black several crystals could be isolated.

$[\text{K}(18\text{-crown-6})]_3\text{Ge}_9$ was isolated by dissolving “ $\text{K}_5\text{Pd}_{1.5}\text{Ge}_{14.7}$ ” (0.075 g, 0.0527 mmol) and 18-crown-6 (0.0251 g, 0.0949 mmol) in approx. 5 mL of liquid ammonia and storage at -42°C . After four months a few black crystals could be isolated.

$\text{K}_2[\text{K}(2.2.2\text{-crypt})]_4[\text{Ge}_9\text{-Ge}_9] \cdot 13 \text{ NH}_3$ was isolated by dissolving “ $\text{K}_5\text{Pd}_{1.5}\text{Ge}_{14.7}$ ” (0.075 g, 0.0527 mmol) and 2.2.2-crypt (0.0357 g, 0.0949 mmol) in approx. 5 mL of liquid ammonia and storing at -42°C . After a few months some black crystals could be isolated.

6.6.4.1. Syntheses in the ternary system of K-Co-*E* (*E* = Ge, Sn)

Table 40: Syntheses parameters of ternary phases containing K-Co-*E* (*E* = Ge, Sn). Arc melt intensities for all experiments are as follows: 2.5, 3, 3.5.

Phase Composition	Ampoule material	Temperature profile	Identified clusters contained in compounds according to Raman analysis
"K ₅ Co _{1.2} Ge ₉ "*	Ta	I	[Ge ₄] ⁴⁻ , [Ge ₉] ⁴⁻ , [Co@Ge ₉] ⁵⁻
"K ₅ CoGe ₉ "*	Ta	II	[Ge ₄] ⁴⁻ , [Ge ₉] ⁴⁻ , [Co@Ge ₉] ⁵⁻
"K ₅ Co ₃ Sn ₉ "	Ta	III	[Sn ₄] ⁴⁻ , [Sn ₉] ⁴⁻ , [Co@Sn ₉] ⁵⁻

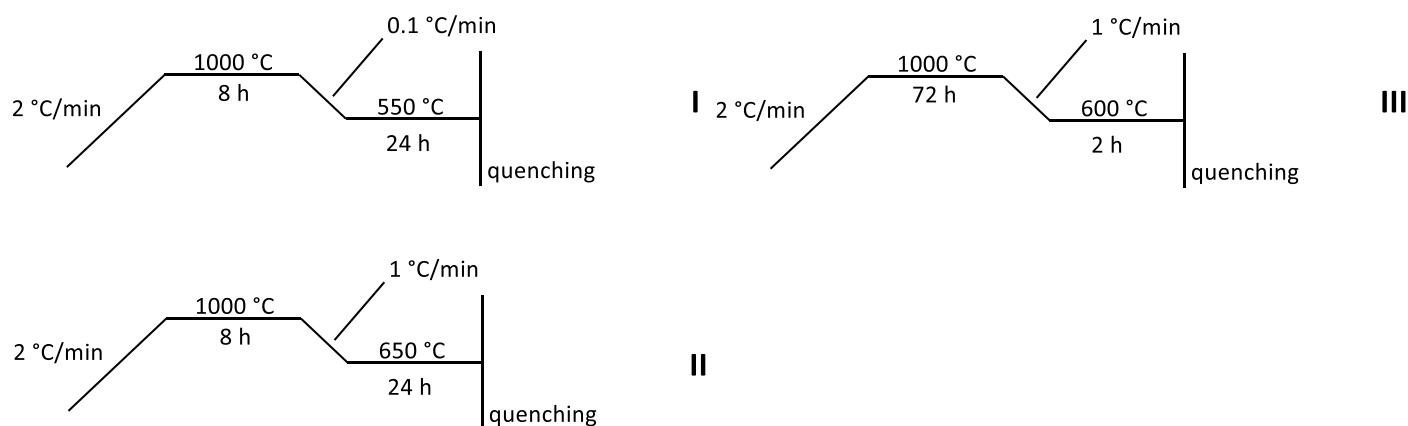


Figure 65: Collection of temperature profiles used for syntheses of solid state phases containing K-Co-*E* (*E* = Ge, Sn).

K₆[Co@Ge₉](OH) · 16 NH₃ was isolated by dissolving "K₅Co_{1.2}Ge₉" (0.1 g, 0.11 mmol) and 2.2.2–crypt (0.0745 g, 0.198 mmol) in approx. 5 mL liquid ammonia. The resulting dark red solution is stored at -42 °C. After six months black crystals were isolated with a yield of only a few crystals.

$[\text{K}(2.2.2\text{-crypt})]_2\text{K}_4[\text{Co}_2@\text{Ge}_{17}]$ was isolated by dissolving “ K_5CoGe_9 ” (0.1 g, 0.1133 mmol), 2.2.2-crypt (0.0768 g, 0.204 mmol) and $\text{TiCp}_2\text{Cl}(\text{NH}_3)$ (0.02803 g, 0.1133 mmol) in approx. 5 mL of liquid ammonia and stored at $-42\text{ }^\circ\text{C}$. After four months only a few black crystals could be isolated.

$[\text{K}(2.2.2\text{-crypt})]_3[\text{Co}@\text{Ge}_{10}] \cdot 3\text{ NH}_3$ was isolated by dissolving “ K_5CoGe_9 ” (0.1 g, 0.1133 mmol), 2.2.2-crypt (0.0768 g, 0.204 mmol) and $\text{TiCp}_2\text{Cl}(\text{NH}_3)_2$ (0.02803 g, 0.1133 mmol) in approx. 5 mL of liquid ammonia and stored at $-42\text{ }^\circ\text{C}$. After four months several black crystals could be isolated.

$[\text{K}(2.2.2\text{-crypt})]_3[\text{Co}@\text{Ge}_{10}] \cdot 9\text{ NH}_3$ was isolated by dissolving “ K_5CoGe_9 ” (0.1 g, 0.1133 mmol), 2.2.2-crypt (0.0768 g, 0.204 mmol) and $\text{TiCp}_2\text{Cl}(\text{NH}_3)_2$ (0.02803 g, 0.1133 mmol) in approx. 5 mL of liquid ammonia and stored at $-42\text{ }^\circ\text{C}$. After four months only one black crystal could be isolated.

$\text{K}_6[\text{OH}][\text{Co}@\text{Sn}_9] \cdot 17\text{ NH}_3$ was isolated by dissolving “ $\text{K}_5\text{Co}_3\text{Sn}_9$ ” (0.075 g, 0.0521 mmol), 18-crown-6 (0.0247 g, 0.0937 mmol) and CuDippCl (0.0248 g, 0.0521 mmol) in approx. 5 mL of liquid ammonia and storing at $-42\text{ }^\circ\text{C}$. After four months several black crystals could be isolated.

6.6.4.2. Syntheses in the ternary system of K-TM-E (TM = Co, Ni; E = Si, Ge)

Table 41: Syntheses parameters of ternary phases containing K-TM-E (TM = Co, Ni; E = Si, Ge). Arc melt intensities for germanium experiments are 2.5, 3, 3.5. For experiments involving silicon the intensities are: 3, 3.5, 4.

For the synthesis of mixed tetrel clusters (Si/Ge) preground mixtures of the elements in the ratio Ge/Si = 12/5 are used. This ratio is calculated in a way that when used in the synthesis the overall molar ratio of tetrel elements comes out to $(\text{Ge}_6/\text{Si}_3) = E_9$. The preground mixture of elements is provided by Dr. Michael Giebel, Chair of Inorganic Chemistry with Focus on Novel Materials.

Phase Composition	Ampoule material	Temperature profile	Definable clusters contained in compounds according to Raman analysis
"K ₄ NiSi ₉ "*	Corundum in Ta	II	[Si ₄] ⁴⁻ , [Si ₉] ⁴⁻
"K ₄ Ni ₂ Si ₉ "*	Corundum in Ta	II	[Si ₄] ⁴⁻ , [Si ₉] ⁴⁻
"K ₄ Ni ₃ Si ₉ "*	Corundum in Ta	VIII	[Si ₄] ⁴⁻
"K ₄ NiGe ₆ Si ₃ "*	Corundum in Ta	IX	[Ge ₄] ⁴⁻ , [Ge ₉] ⁴⁻
"K ₅ CoGe ₆ Si ₃ "*	Ta	IX	[Si _{1.2} /Ge _{2.8}] ^{4-a}
"K ₄ NiGe ₉ "*	Corundum in Ta	I	[Ge ₄] ⁴⁻ , [Ge ₉] ⁴⁻
		II	[Ge ₉] ⁴⁻
		III	a-Ge
		IV	[Ge ₄] ⁴⁻ , [Ge ₉] ⁴⁻
"K ₄ Ni ₂ Ge ₉ "*	Corundum in Ta	II	[Ge ₉] ⁴⁻
"K ₄ Ni ₃ Ge ₉ "*	Corundum in Ta	I	[Ge ₉] ⁴⁻ , [Ni@Ge ₉] ⁴⁻
		V	[Ge ₉] ⁴⁻
		VI	[Ge ₄] ⁴⁻ , [Ge ₉] ⁴⁻
		VII	[Ge ₉] ⁴⁻
"K ₄ Ni ₃ Ge ₇ "*	Corundum in Ta	II	[Ge ₄] ⁴⁻ , [Ge ₉] ⁴⁻ , a-Ge
"K ₅ Ni ₃ Ge ₇ "*	Corundum in Ta	II	[Ge ₄] ⁴⁻ , [Ge ₉] ⁴⁻

^a – The closest approximation is with [Si_{1.2}/Ge_{2.8}]⁴⁻ – a mixed tetrel cluster contained in the phase "K₁₂Ge₁₂Si₅". Mixed tetrel clusters and phases are more closely examined by Dr. Michael Giebel, Chair of Inorganic Chemistry with Focus on Novel Materials.

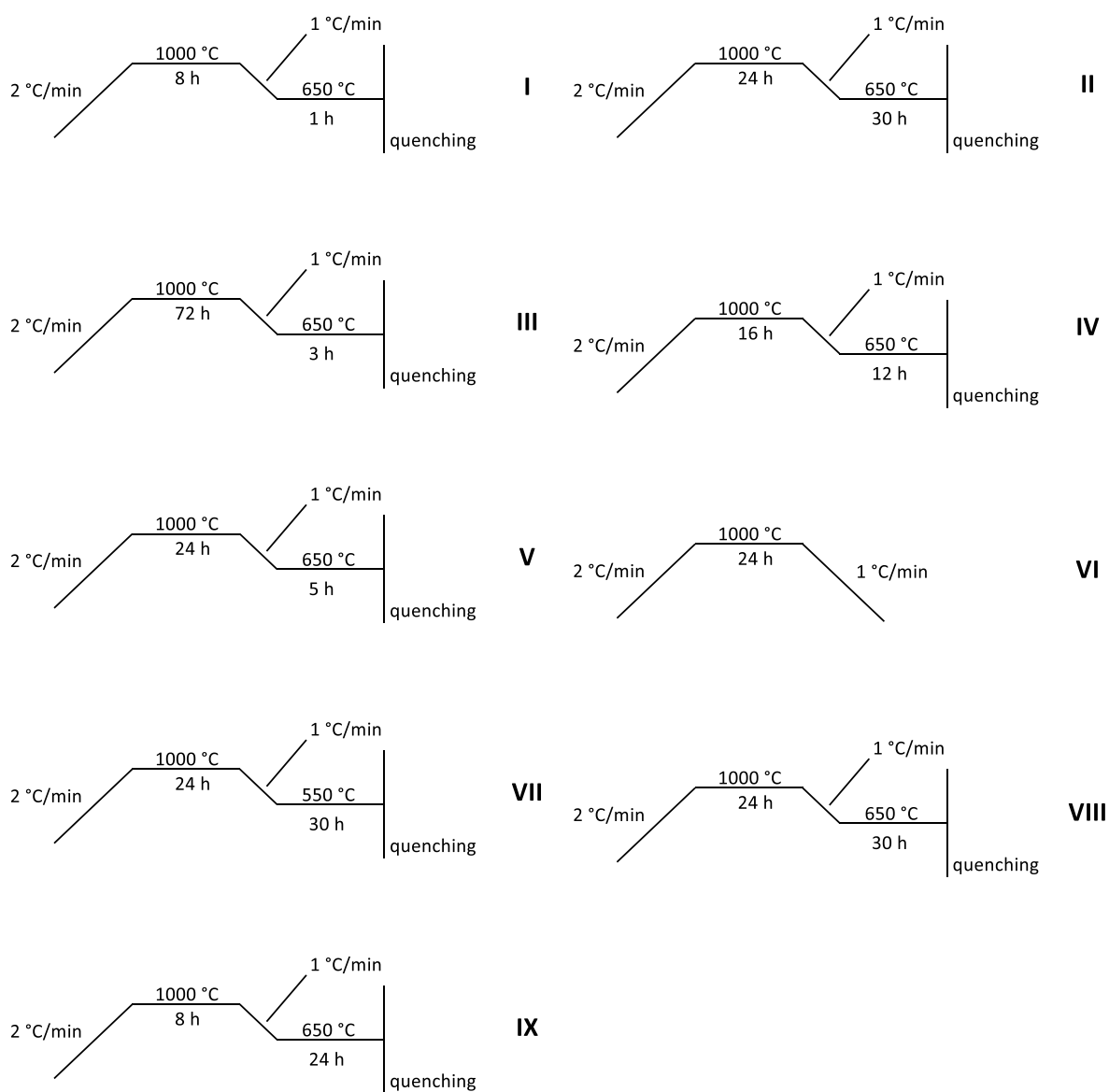


Figure 66: Collection of temperature profiles used for syntheses of solid state phases containing K-Ni-E (E = Si, Ge).

6.6.4.3. Syntheses in the ternary system of K-Cu-*E* (*E* = Ge, Sn)

Table 42: Syntheses parameters of ternary phases containing K-Cu-*E* (*E* = Ge, Sn). Arc melt intensities for all experiments are as follows: 2.5, 3, 3.5.

Phase Composition	Ampoule material	Temperature profile	Definable clusters contained in compounds according to Raman analysis
"K ₃ CuGe ₉ "*	Corundum in Ta	II	[Ge ₉] ⁴⁻
"K ₃ Cu ₂ Ge ₉ "*	Corundum in Ta	I	[Ge ₉] ⁴⁻
"K ₃ Cu ₃ Ge ₉ "*	Corundum in Ta	I	[Ge ₄] ⁴⁻ , [Ge ₉] ⁴⁻
"K ₃ CuSn ₉ "*	Ta	II	[Sn ₄] ⁴⁻ , [Sn ₉] ⁴⁻
"K ₃ Cu ₂ Sn ₉ "*	Ta	II	[Sn ₄] ⁴⁻ , [Sn ₉] ⁴⁻
"K ₃ Cu ₃ Sn ₉ "*	Ta	II	[Sn ₄] ⁴⁻ , [Sn ₉] ⁴⁻

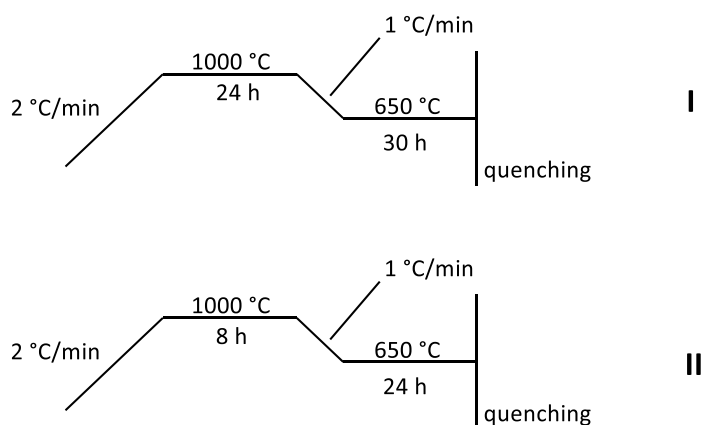


Figure 67: Collection of temperature profiles used for syntheses of solid state phases containing K-Cu-*E* (*E* = Ge, Sn).

K₄[Sn₉] · 9 dmf was isolated by dissolving K₄Sn₉ (0.1837 g, 0.150 mmol), 2.2.2-crypt (0.056 g, 0.270 mmol) and MesCu (0.0274 g, 0.150 mmol) in 2 mL of dmf and stirring for two hours. The

solution is filtered and overlayed with 1 mL of tol and stored at -32 °C. After one month several crystals could be isolated.

6.6.5. Reactions of endohedral clusters with transition metal or main group ligands

Several reactions are conducted using different substitution agents and solid state phase which contain endohedral cluster units in order to yield new substituted cluster species.

Table 43: Substitution reactions of endohedral phases “K₅CoE₉” (E = Ge, Sn) with transition metal complexes. Molar ratio of reactants is: “K₅CoE₉”/2.2.2-crypt/TM-complex = 1/1.8/1. The reactions are done in dried en, which is layered with 1.5 mL of toluene and stored at RT to crystallize.

“K ₅ CoGe ₉ ”	“K ₅ Co ₃ Sn ₉ ”
RT	
Cp*FeCp(CO)Me	
(PPh ₃) ₃ Co-Me	
(COD)Co(C ₈ H ₁₃)	
Zn(Cp*) ₂	
ZnCl ₂ (PPh ₃)	
Ni(COD) ₂	
RuCl ₃ (PCyHex ₃) ₃	

Table 44: Experiments using different Cu-NHCs and Cu-phosphine in order to yield substituted endohedral species. 2.2.2-crypt and 18-crown-6 are used as 1.8 equivalents unless stated otherwise. The numbers in the fields indicate the number of equivalents of the respective reactants used in the trial.

		"K ₅ Co _{1.2} Ge ₉ "		"K ₅ Co ₃ Sn ₉ "	
		2.2.2-crypt	18crown6	2.2.2-crypt	18crown6
I	DippNHC-Cu-Cl	1;2	1;2	1;2	1;2
II	DippNHC-Cu-Cl	1;2	∅	∅	∅
III	((iPr ₂)N) ₂ P-Cl	∅	2;3		
IV	((iPr ₂)N) ₂ P-Cl	∅	2;3		

The following reactions are done similarly to the substitution of bare [Sn₉]⁴⁻^[137] and substituted [Ge₉(Si(SiMe₃)₃)₃]⁻^[200] clusters by Fässler *et al.* All amounts of weighed materials are noted in Table 44. NHC- and phosphine-complexes were kindly supplied by (This chemical is kindly provided by Dr. Felix Geitner, Chair of Inorganic Chemistry with Focus on Novel Materials).^[441]

I: Endohedral reactant (0.075 g), sequestering agent and DippNHC-Cu-Cl are weighed into a flask and ~5 mL of liquid ammonia are condensed onto the solid. The vessel is stored at -40 °C for crystallization.

II: Endohedral reactant (0.075 g) and sequestering agent are weighed into a flask and ~5 mL of liquid ammonia are condensed onto the solid. The mixture is stirred for 1.5 hours and the solvent is evaporated. The yellow residue is dissolved in 8 mL acn and 3 equivalents of ((iPr₂)N)₂P-Cl are added. The mixture is filtrated and DippNHC-Cu-Cl, dissolved in a minimal amount of acn, is added and the solvent is evaporated. The residue is dissolved in 9 mL of toluene, filtrated, stinted and stored at -40 °C for crystallization.

III: Endohedral reactant and sequestering agent are weighed into a flask and ~5 mL of liquid ammonia are condensed onto the solid. The mixture is stirred for 1.5 hours and the solvent is

evaporated. The yellow residue is dissolved in 5 mL acn and filtrated. $((iPr_2)N)_2P-Cl$ is added, the solution is filtrated and acn is evaporated and the residue is dissolved in toluene. The vessel is stored at $-40\text{ }^{\circ}C$ for crystallization.

IV: Endohedral reactant and sequestering agent are weighed into a flask and dissolved in 5 mL of en. The mixture is stirred for 1.5 hours, filtrated and the solvent is evaporated. The yellow residue is dissolved in 5 mL acn and filtrated. $((iPr_2)N)_2P-Cl$ is added, the solution is filtrated and acn is evaporated and the residue is dissolved in toluene. The vessel is stored at $-40\text{ }^{\circ}C$ for crystallization.

The phase " K_5CoGe_9 " was also used in a synthesis method first reported by Sevov et al.^[141] and further refined by Dr. Lorenz Schiegerl, Chair of Inorganic Chemistry with Focus Novel Materials.

The first step is the extraction of the solid state precursor " K_5CoGe_9 " (0.075 g, 0.0826 mmol) using liquid ammonia. Additional sequestering agents like 1.8 equivalents 18-crown-6 or 2.2.2-crypt are added. After this the ammonia is removed and the extraction product is dissolved in an appropriate solvent, like thf or pyr (5 mL). Three equivalents of $Cl[Si(SiMe_3)_3]$, dissolved in the appropriate solvent, are added at $0\text{ }^{\circ}C$ and reacted over night. After the reaction, the solution is filtrated, the solvent removed. The oily residue is washed with hex and finally analyzed.

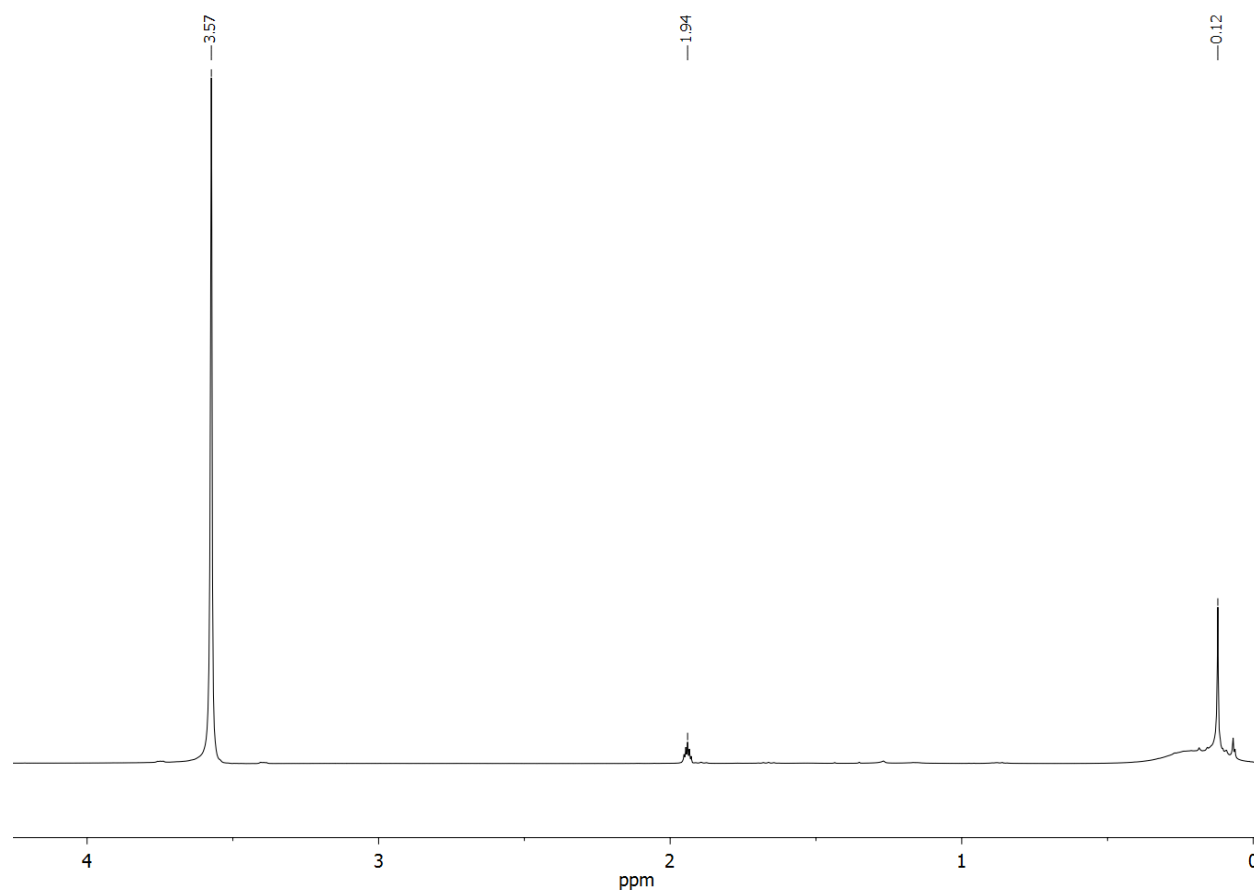


Figure 68: ^1H -NMR spectrum of " K_5CoGe_9 " after reaction with $\text{ClSi}(\text{SiMe}_3)_3$.

^1H NMR (400 MHz, 298 K, $\text{acn-}d_3$): δ [ppm] = 0.12 (s, SiMe_3)

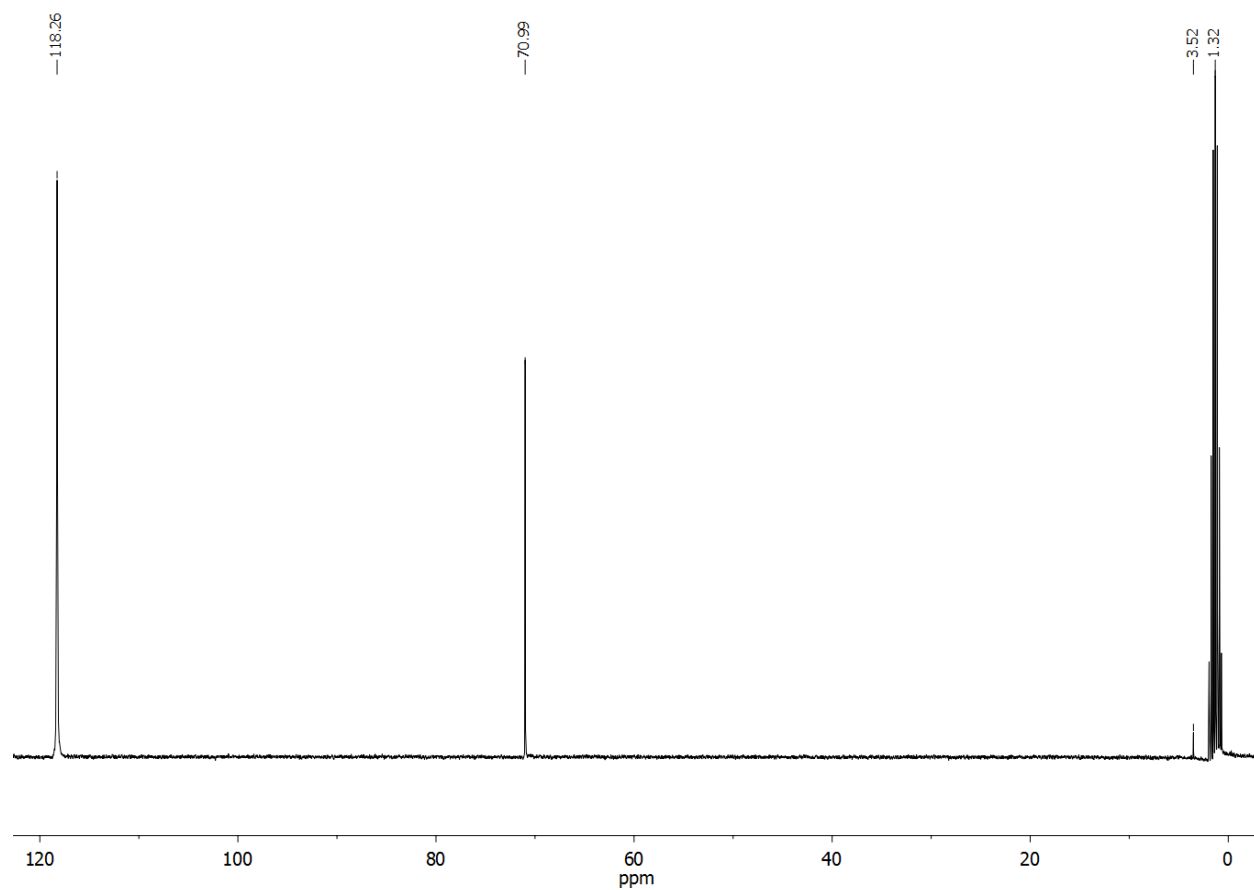


Figure 69: ^{13}C -NMR spectrum of “ K_5CoGe_9 ” after reaction with $\text{ClSi}(\text{SiMe}_3)_3$.

^{13}C NMR (400 MHz, 298 K, $\text{acn-}d_3$): δ [ppm] = 3.52 (s, CH_3)

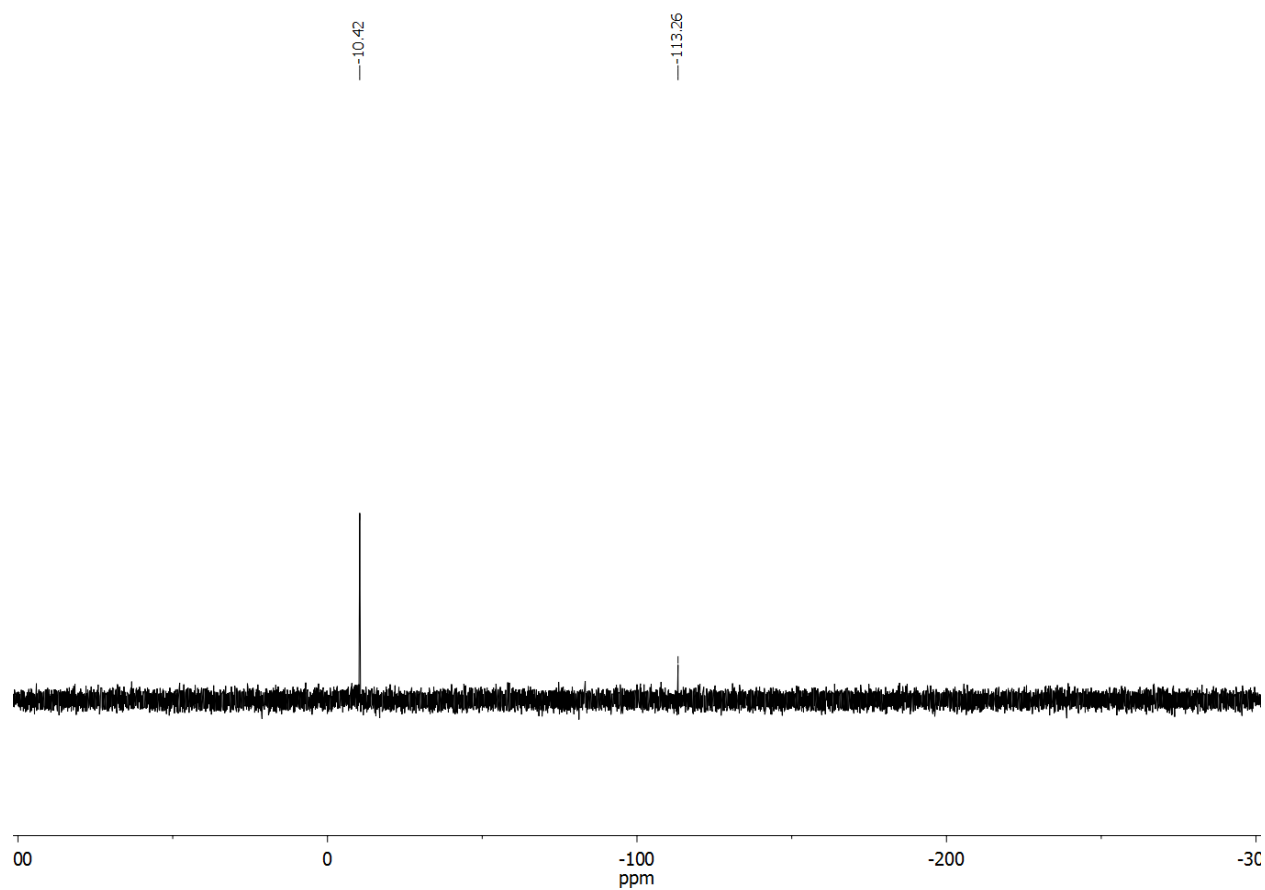


Figure 70: ^{29}Si -INEPT-NMR spectrum of " K_5CoGe_9 " after reaction with $\text{ClSi}(\text{SiMe}_3)_3$.

^{29}Si -INEPT NMR (79 MHz, 298 K, $\text{acn-}d_3$): δ [ppm] = -10.42 (s, SiMe_3), -113.26 ppm (s, Si_{Ge_9}).

7. Appendix

7.1. ICP-OES data

Table 45: Moles of lithium and potassium contained in different samples of lithium ion exchange trails. Sample weights and dissolutions can be found in section 6.6.3.1.

Sample	n(Li) in sample / μmol	n(K) in sample / μmol
Solvent trials		
dmf – K_4Ge_9	3.082 ± 0.0806	1.24 ± 0.0259
NH_3 – K_4Ge_9	15.2 ± 0.167	0.821 ± 0.0753
NH_3 – Cs_4Ge_9	35.4 ± 1.67	0.342 ± 0.0589
acn – $\text{K}[\text{Ge}_9[\text{Si}(\text{SiMe}_3)_3]_3]$	76.5 ± 3.43	3.18 ± 0.103
Time trials		
1 h	1.93 ± 0.0183	1.81 ± 0.0872
2 h	53.7 ± 0.721	22.6 ± 0.593
4 h	8.66 ± 0.235	1.72 ± 0.0989
8 h	63.3 ± 1.43	2.40 ± 0.177
24 h	76.5 ± 3.43	3.18 ± 0.103
48 h	50.5 ± 2.23	0.835 ± 0.0573
LiER equivalent trials		
2	48.03 ± 0.332	48.6 ± 0.325
5	52.6 ± 0.900	14.2 ± 0.292
10	43.3 ± 0.612	9.85 ± 0.250

7.2. Calculated Raman shifts and intensities

Calculated Raman shifts are subject to change using appropriate scale factors of up to 5%.^[380]

Values treated with scale factors will be marked as such.

Table 46: Raman modes of the $[\text{Si}_9]^{4-}$ cluster measured (by principle of exclusion using Raman spectra of $\text{K}_{12}\text{Si}_{17}$ and K_4Si_4) and calculated. The experimental main mode is marked with “**M**”.

$[\text{Si}_9]^{4-}$ (exp. lit.) ^[48, 173, 413]		$[\text{Si}_9]^{4-}$ (calc.)
Raman shift / cm^{-1}	Raman shift / cm^{-1}	Raman intensity / a. u.
	62.6091	28.7808
	153.818	0.1368
	172.5801	0.9108
	234.3144	5.3293
	242.413	3.6091
	258.6785	26.9175
	270.7115	0.2773
	272.5311	1.0412
	275.5324	38.1021
	275.924	39.1221
	295.1747	0.6695
302	298.3212	0.4748
	320.5895	55.0011
	337.4181	19.4107
	343.4476	21.0138
	362.8461	64.2872
	380.5414	49.1116
390 - M	393.2594	1688.3869
	401.0377	0.3504
	404.8657	0.4019
	429.1349	9.6674

Table 47: Raman modes of the $[\text{Ge}_9]^{4-}$ cluster measured and calculated. The experimental main mode is marked with “**M**”.

$[\text{Ge}_9]^{4-}(\text{exp. lit.})^{[43]}$		$[\text{Ge}_9]^{4-}(\text{calc.})$
Raman shift / cm^{-1}	Raman shift / cm^{-1}	Raman intensity / a. u.
	10,4352	4E^{-4}
	84,2251	3,5896
104	84,5099	3,5402
125	132,2154	0,1771
	133,4766	44,928
	142,8463	38,2905
147	149,7479	14,5326
	149,9169	14,7862
	153,7852	18,4116
	157,9789	18,0637
	161,6941	27,4144
164	161,8127	27,2713
	177,2363	20,0727
188	194,0926	0,0484
	194,2546	0,0438
	197,7929	0,3964
	217,9758	2,5868
220 - M	225,3544	677,4837
	228,4357	4,3902
	228,4916	4,3939
241	241,4949	16,2125

Table 48: Raman modes of the $[\text{Sn}_9]^{4-}$ cluster measured and calculated. The experimental main mode is marked with “**M**”.

[Sn_9] $^{4-}$ (exp. lit.) ^[43]	[Sn_9] $^{4-}$ (calc.)	
	Raman shift / cm^{-1}	Raman intensity / a. u.
99	9,5752	2,8503
	56,0156	6,751
	56,0578	6,7194
	84,4421	14,2045
	89,1948	10,9156
	92,1377	14,6307
	94,0746	6,8812
	99,5294	26,0614
	99,5879	26,1779
	105,8489	42,9438
	108,4646	0,825
	108,4839	0,7785
	118,897	36,3929
	130,3429	3,6693
	130,5298	2,1009
	130,5616	2,1696
146 - M	145,6974	0,3491
	148,6258	1961,4644
	153,71	13,1649
	153,7661	12,9086
	164,0781	28,0904

Table 49: Calculated Raman shifts and intensities of literature known endohedral [Sn₉] units.

[Co@Sn ₉] ⁵⁻		[Ni@Sn ₉] ⁴⁻		[Cu@Sn ₉] ³⁻	
Raman shift / cm ⁻¹	Intensity / a.u.	Raman shift / cm ⁻¹	Intensity / a.u.	Raman shift / cm ⁻¹	Intensity / a.u.
-16,1694	3,216	13,0052	0,7437	8,51	2,9362
31,3004	11,8279	41,7532	8,6174	21,6348	1,2911
44,4353	12,5574	43,802	8,6322	65,3452	4,4929
75,5152	2,8183	78,9021	0,2478	69,0751	5,4326
76,5135	12,8617	82,588	9,4478	85,2418	15,0217
88,6982	11,8091	92,2643	9,833	88,1082	0,2265
93,4799	23,5853	94,3395	26,4298	89,1217	0,2087
94,3042	1,4126	97,6074	2,445	95,1654	0,4164
99,4185	0,3908	97,9838	2,7936	97,0531	0,1527
105,5052	18,6734	105,4224	17,725	99,1682	0,3037
106,4491	4,0318	108,9233	1,6618	103,6394	1,3504
109,0469	17,0491	109,1862	9,2112	105,0597	2,4864
113,0416	36,086	109,4155	10,556	107,4622	10,0259
127,6235	38,7152	123,4656	13,9004	110,4532	10,0655
130,414	31,6753	123,8871	13,4526	118,4095	0,0763
134,9194	23,4226	136,5829	15,7342	133,71	58,0489
145,6051	93,8361	142,9657	68,4219	134,8829	47,9531
146,1306	67,9521	143,2149	70,0907	135,9826	39,3893
147,6815	105,2598	144,1155	82,6268	141,019	84,4135
151,8073	176,9181	149,4983	77,8124	142,3417	73,2838
169,8604	3018,502	167,0913	2428,2578	160,492	2233,5618
245,0683	83,9973	223,7348	57,3494	220,9735	9,7979
278,4907	11,168	259,2244	5,5898	225,2918	6,8943
284,989	7,2277	260,0377	5,2901	252,128	0,1544

Table 50: Calculated Raman shifts and intensities of new endohedral [Si₉] units.

[Ni@Si ₉] ⁴⁻	
Raman shift / cm ⁻¹	Intensity / a.u.
61,0707	6,0613
74,8299	4,9581
123,6665	11,7055
131,1134	9,9092
162,1999	0,8491
181,2529	11,4359
185,2822	8,2207
189,2924	5,1646
189,7174	11,2869
190,8952	9,35
191,728	2,5323
194,797	7,3342
225,6309	0,1913
234,1682	0,0853
236,7884	0,3851
351,9667	13,4609
355,744	16,7714
360,6104	47,8034
363,5974	69,465
369,0326	61,3829
409,2344	2500,5675
462,8913	15,2739
465,4722	11,7082
502,7602	0,2862

Table 51: Calculated Raman shifts and intensities of new endohedral [Ge₉] units.

[Co@Ge ₉] ⁵⁻		[Ni@Ge ₉] ⁴⁻	
Raman shift / cm ⁻¹	Intensity / a.u.	Raman shift / cm ⁻¹	Intensity / a.u.
-9,0048	3,5774	11,337	2,769
47,9379	4,1159	42,9589	3,4036
68,3644	6,6259	78,2618	5,7853
72,5473	5,6084	79,6329	4,6898
104,8867	0,3208	104,3165	0,1826
109,4522	14,1006	113,4909	0,3573
110,4715	0,8715	116,2633	14,6756
120,5719	0,7297	119,7284	0,0082
123,9841	2,0082	123,843	0,3889
124,1366	0,0556	124,2222	0,1594
127,3815	1,3927	124,9234	0,0683
129,1968	1,542	127,3491	0,7191
158,964	8,5861	150,9345	3,2327
159,3896	8,5508	151,5832	3,864
167,6892	0,0466	158,2937	0,0153
198,9968	29,0217	200,2332	29,9242
200,8552	32,3147	201,7538	31,9899
203,4279	15,1089	203,5729	28,8333
207,0603	97,262	208,1352	68,1637
207,6378	94,9739	208,2554	65,0588
244,902	1057,8968	239,7259	998,6389
358,4778	23,2263	330,361	11,41
361,9272	21,0236	334,7761	8,9057
398,3911	0,0094	371,2657	0,0043

Table 52: Calculated Raman shifts and intensities of new endohedral [Sn₉] units.

[Ru@Sn ₉] ⁶⁻		[Rh@Sn ₉] ⁵⁻		[Pd@Sn ₉] ⁴⁻	
Raman shift / cm ⁻¹ 1	Intensity / a.u.	Raman shift / cm ⁻¹	Intensity / a.u.	Raman shift / cm ⁻¹	Intensity / a.u.
-18,1671	3,5914	26,9	6,4664	-26,8077	5,9413
4,9177	1,5605	41,8451	3,8603	10,036	7,5131
51,7352	7,9598	57,1943	16,2878	54,3361	12,3041
59,7848	6,6546	62,2066	14,4646	58,0734	11,0016
62,2146	20,2362	76,7914	23,4798	71,7821	15,5464
81,517	2,03	80,7264	0,466	76,5133	0,1768
83,1717	3,2801	83,5529	0,4649	78,7589	0,0353
84,8514	16,4034	89,6686	2,8991	84,186	1,5951
87,2652	20,6745	91,3273	5,0562	85,1062	1,3802
88,7587	18,6943	91,7349	11,2695	88,8454	0,3078
89,1754	14,7395	93,273	8,9541	88,9369	3,6061
91,3356	0,3915	96,6167	0,5275	90,637	3,0932
107,0218	25,6073	111,1612	11,3365	100,3656	4,2781
113,5953	22,6529	111,6096	8,2111	102,0654	3,0153
122,4432	1,1109	116,3911	1,13	106,1516	0,0607
139,3269	119,3927	139,955	55,3263	134,7269	61,2312
139,7299	103,8563	141,0916	48,5819	136,1146	52,4962
140,9487	330,4158	142,6039	61,0186	136,8549	58,2364
144,1402	79,6537	145,6492	181,9076	141,47	124,4874
147,3002	300,3879	146,4759	181,2828	141,8443	124,4818
174,5632	4370,5307	174,5058	3332,9054	166,8742	2837,3143
265,6251	109,0143	244,2653	35,9279	219,4814	21,1197
266,9495	104,1657	245,2156	35,6809	221,8346	14,4845
286,4102	0,067	268,4667	0,0114	244,9805	0,0482

7.3. Recorded spectra and diffractograms

7.3.1. Reactant phases

7.3.1.1. Binary *Zintl* phases

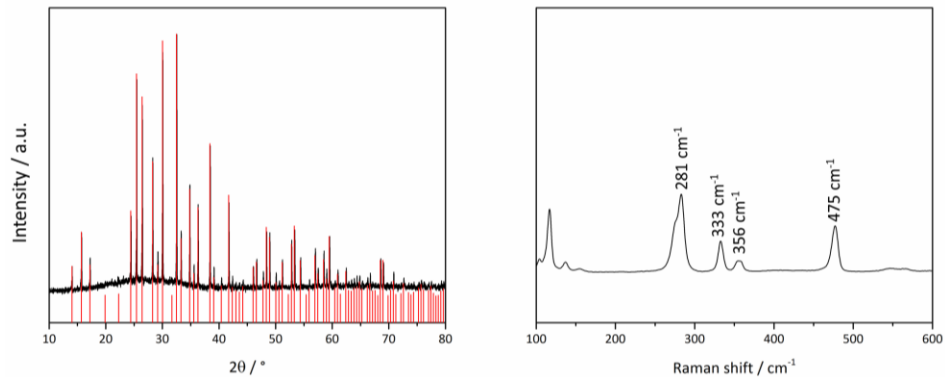


Figure 71: Left: X-ray powder diffractogram measured (black) and calculated (red) of K_4Si_4 . The calculated diffractogram is based on single crystal data.^[442] The diffractogram is measured using $\text{Cu-K}\alpha_1$ radiation Right: Raman spectrum of K_4Si_4 with all visible signals attributed to K_4Si_4 .^[413]

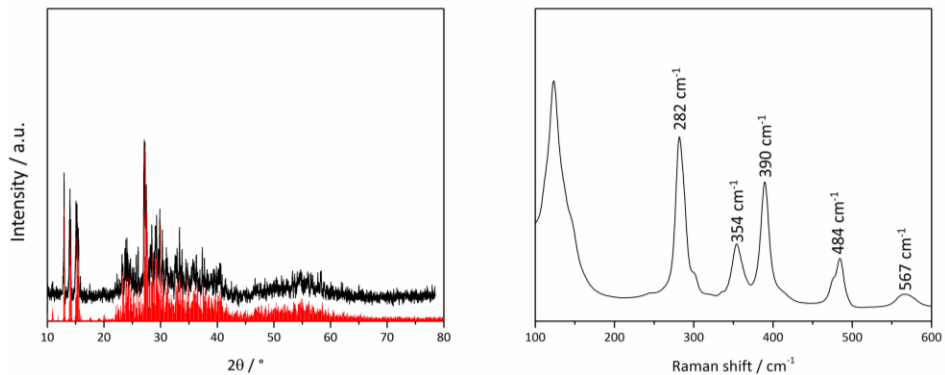


Figure 72: Left: X-ray powder diffractogram measured (black) and calculated (red) of $\text{K}_{12}\text{Si}_{17}$. The calculated diffractogram is based on single crystal data.^[48] The diffractogram is measured using $\text{Cu-K}\alpha_1$ radiation Right: Raman spectrum of $\text{K}_{12}\text{Si}_{17}$ with all visible signals attributed to $\text{K}_{12}\text{Si}_{17}$.^[48] The large signal at around 115 cm^{-1} can be attributed to the Raman spectrometer.

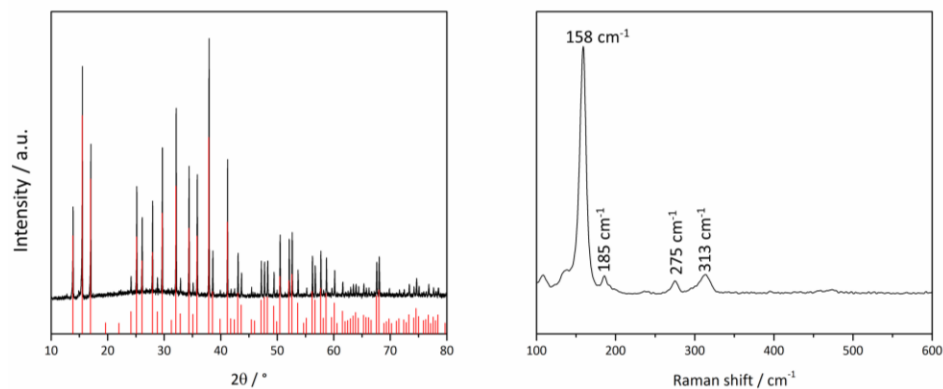


Figure 73: Left: X-ray powder diffractogram measured (black) and calculated (red) of K_4Ge_4 . The calculated diffractogram is based on single crystal data.^[442] The diffractogram is measured using $\text{Cu-K}\alpha_1$ radiation Right: Raman spectrum of K_4Ge_4 with all visible signals attributed to K_4Ge_4 .^[378]

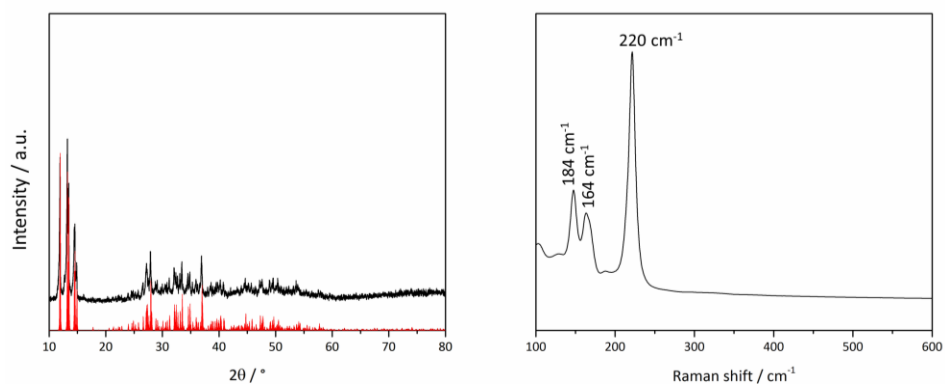


Figure 74: Left: X-ray powder diffractogram measured (black) and calculated (red) of K_4Ge_9 . The calculated diffractogram is based on single crystal data.^[44] The diffractogram is measured using $\text{Cu-K}\alpha_1$ radiation Right: Raman spectrum of K_4Ge_9 with all visible signals attributed to K_4Ge_9 .^[43]

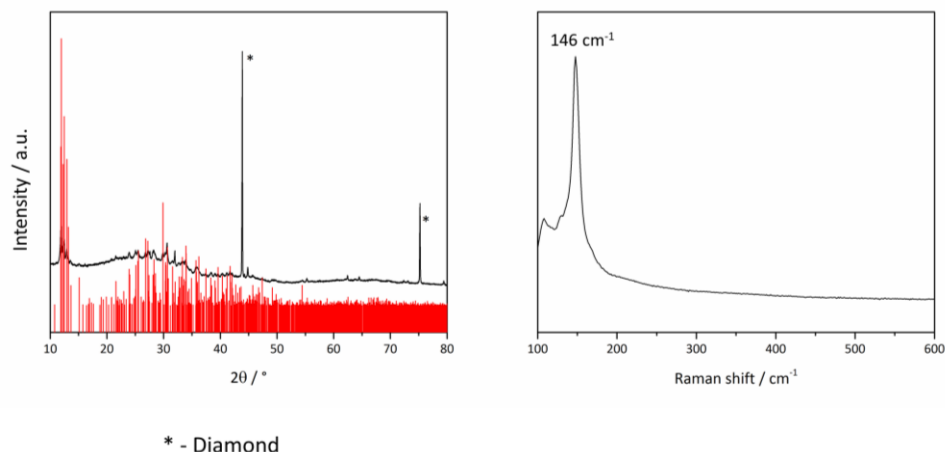


Figure 75: Left: X-ray powder diffractogram measured (black) and calculated (red) of K_4Sn_9 . The calculated diffractogram is based on single crystal data.^[46] The diffractogram is measured using $\text{Cu-K}\alpha_1$ radiation. Right: Raman spectrum of K_4Ge_9 with all visible signals attributed to K_4Sn_9 .^[43]

7.3.2. Stability of *Zintl* phases in liquid ammonia

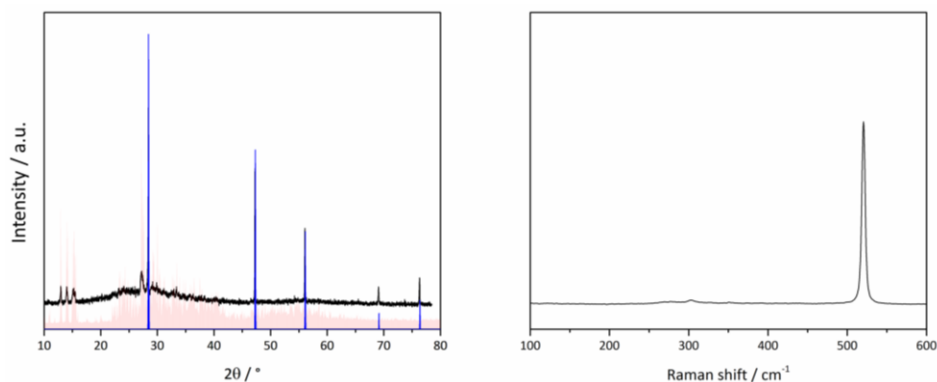


Figure 76: Left: X-ray powder diffractogram measured (black) of filtrated $\text{K}_{12}\text{Si}_{17}$ which is analyzed after using DSC, calculated (red) of $\text{K}_{12}\text{Si}_{17}$ and calculated (blue) of elemental silicon. The calculated diffractogram is based on single crystal data.^[48, 443] The diffractogram is measured using $\text{Cu-K}\alpha_1$ radiation. Right: Raman spectrum of filtrated $\text{K}_{12}\text{Si}_{17}$ with best agreement to elemental silicon.^[444]

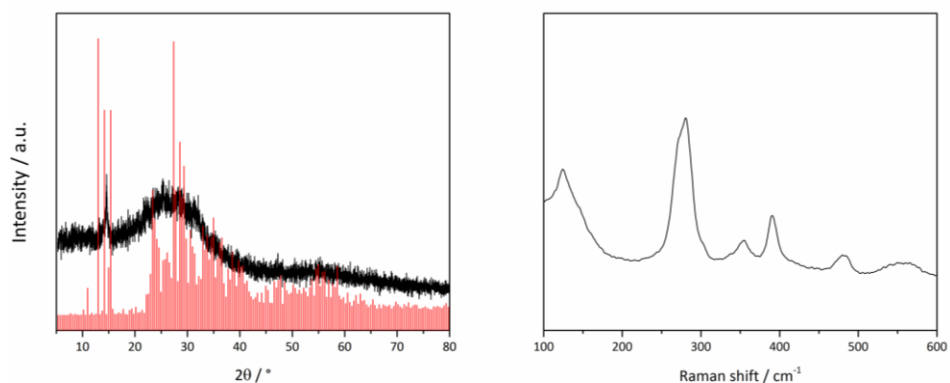


Figure 77: Left: X-ray powder diffractogram measured (black) of the residue of the $K_{12}Si_{17}$ filtration and calculated (red) of $K_{12}Si_{17}$. The calculated diffractogram is based on single crystal data.^[48, 443] The diffractogram is measured using Cu- $K\alpha_1$ radiation. Right: Raman spectrum of the residue of the $K_{12}Si_{17}$ filtration with best agreement to $K_{12}Si_{17}$.^[48]

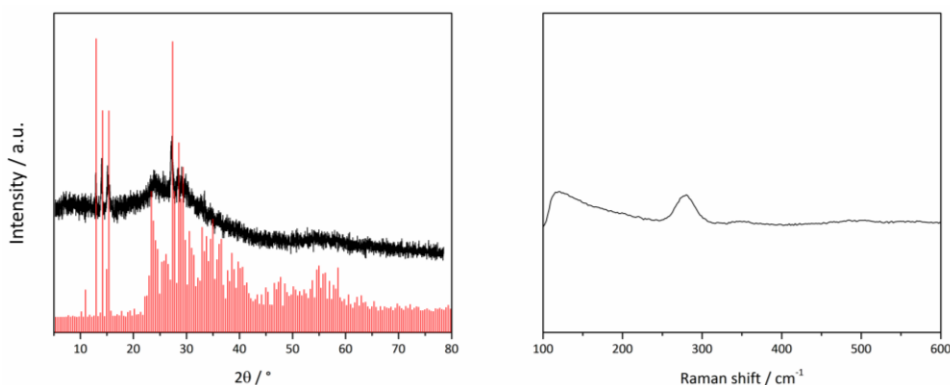


Figure 78: Left: X-ray powder diffractogram measured (black) of the residue of the $K_{12}Si_{17}$ filtration after DSC analysis and calculated (red) of $K_{12}Si_{17}$. The calculated diffractogram is based on single crystal data.^[48, 443] The diffractogram is measured using Cu- $K\alpha_1$ radiation. Right: Raman spectrum of the residue of the $K_{12}Si_{17}$ filtration after DSC analysis with best agreement to $K_{12}Si_{17}$.^[48]

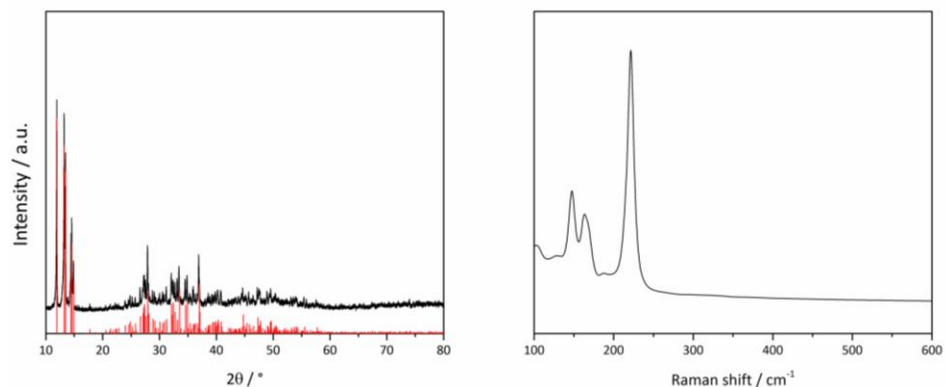


Figure 79: Left: X-ray powder diffractogram measured (black) of filtrated K_4Ge_9 which was analyzed after using DSC and calculated (red) of K_4Ge_9 . The calculated diffractogram is based on single crystal data.^[44] The diffractogram is measured using $\text{Cu-K}\alpha_1$ radiation. Right: Raman spectrum of filtrated K_4Ge_9 with best agreement to K_4Ge_9 .^[43]

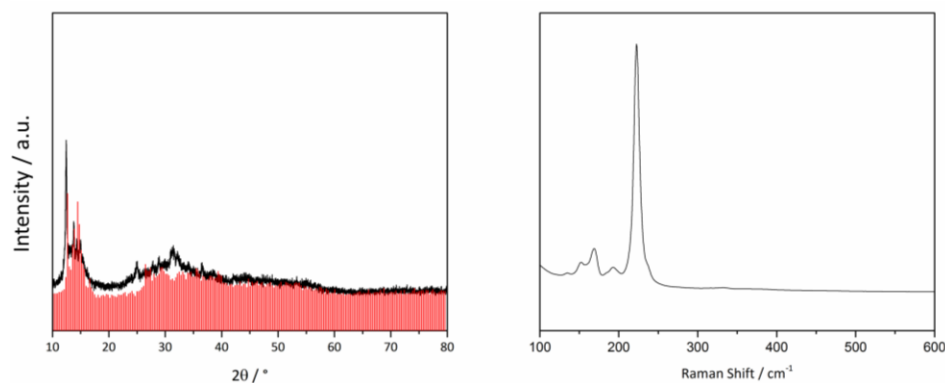


Figure 80: Left: X-ray powder diffractogram measured (black) of the residue of the K_4Ge_9 filtration and experimental (red) of $\text{K}_{12}\text{Ge}_{17}$. The diffractogram is measured using $\text{Cu-K}\alpha_1$ radiation. Raman spectrum of the residue of the K_4Ge_9 filtration with best agreement to K_4Ge_9 .^[43]

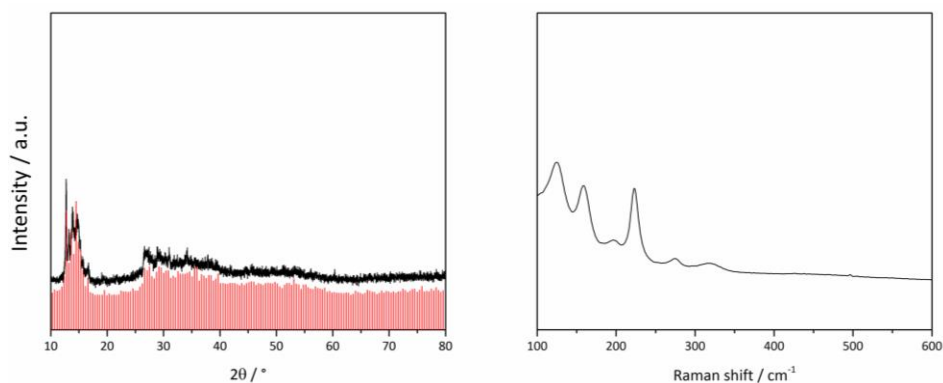


Figure 81: Left: X-ray powder diffractogram measured (black) of the residue of the K_4Ge_9 filtration after the DSC analysis and experimental (red) of $K_{12}Ge_{17}$. The diffractogram is measured using $Cu-K_{\alpha 1}$ radiation Right: Raman spectrum of the residue of the K_4Ge_9 filtration after DSC analysis with best agreement to $K_{12}Ge_{17}$.^[43]

7.3.3. Ion exchange experiments on *Zintl* phases

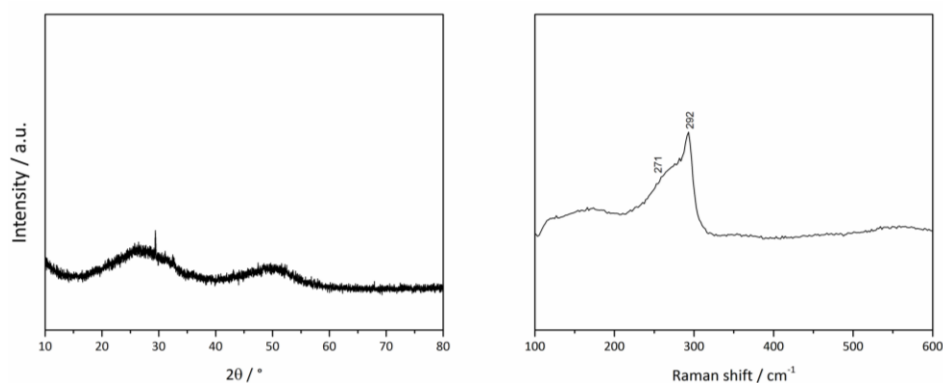


Figure 82: Left: X-ray powder measured diffractogram (black) of the $K_{12}Si_{17}$ sample after lithium ion exchange. The diffractogram is measured using $Cu-K_{\alpha 1}$ radiation. Right: Raman spectrum the $K_{12}Si_{17}$ sample after lithium ion exchange.

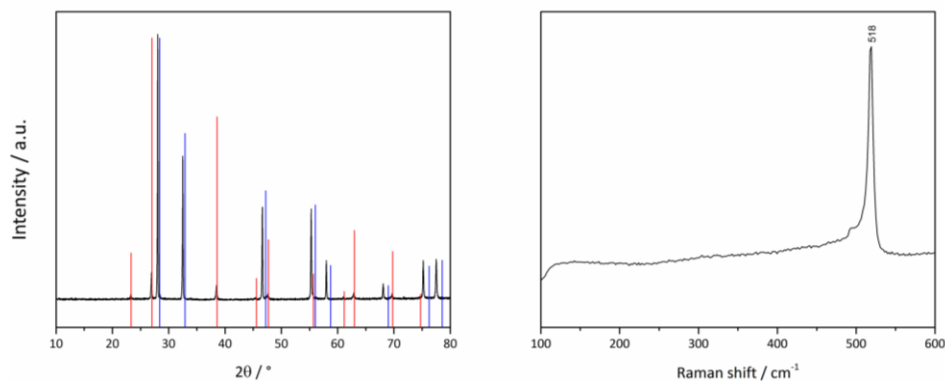


Figure 83: Left: X-ray powder measured diffractogram (black) of the $\text{K}_{12}\text{Si}_{17}$ sample after lithium ion exchange and calculated (red) KBr and (blue) of LiBr. The calculated diffractogram is based on single crystal data.^[445-446] The diffractogram is measured using $\text{Cu-K}\alpha_1$ radiation. Right: Raman spectrum of the $\text{K}_{12}\text{Si}_{17}$ sample, with one signal attributable to elemental silicon.^[444]

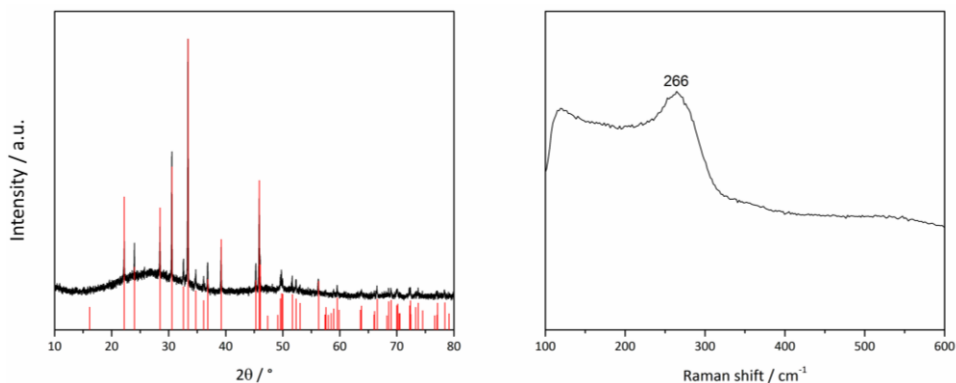


Figure 84: Left: X-ray powder measured diffractogram (black) of the K_4Ge_4 sample after lithium ion exchange and calculated (red) of $\text{KNH}_2 \cdot \text{NH}_3$. The calculated diffractogram is based on single crystal data.^[447] The diffractogram is measured using $\text{Cu-K}\alpha_1$ radiation. Right: Raman spectrum of the K_4Ge_4 sample, with one signal attributable to a-Ge.

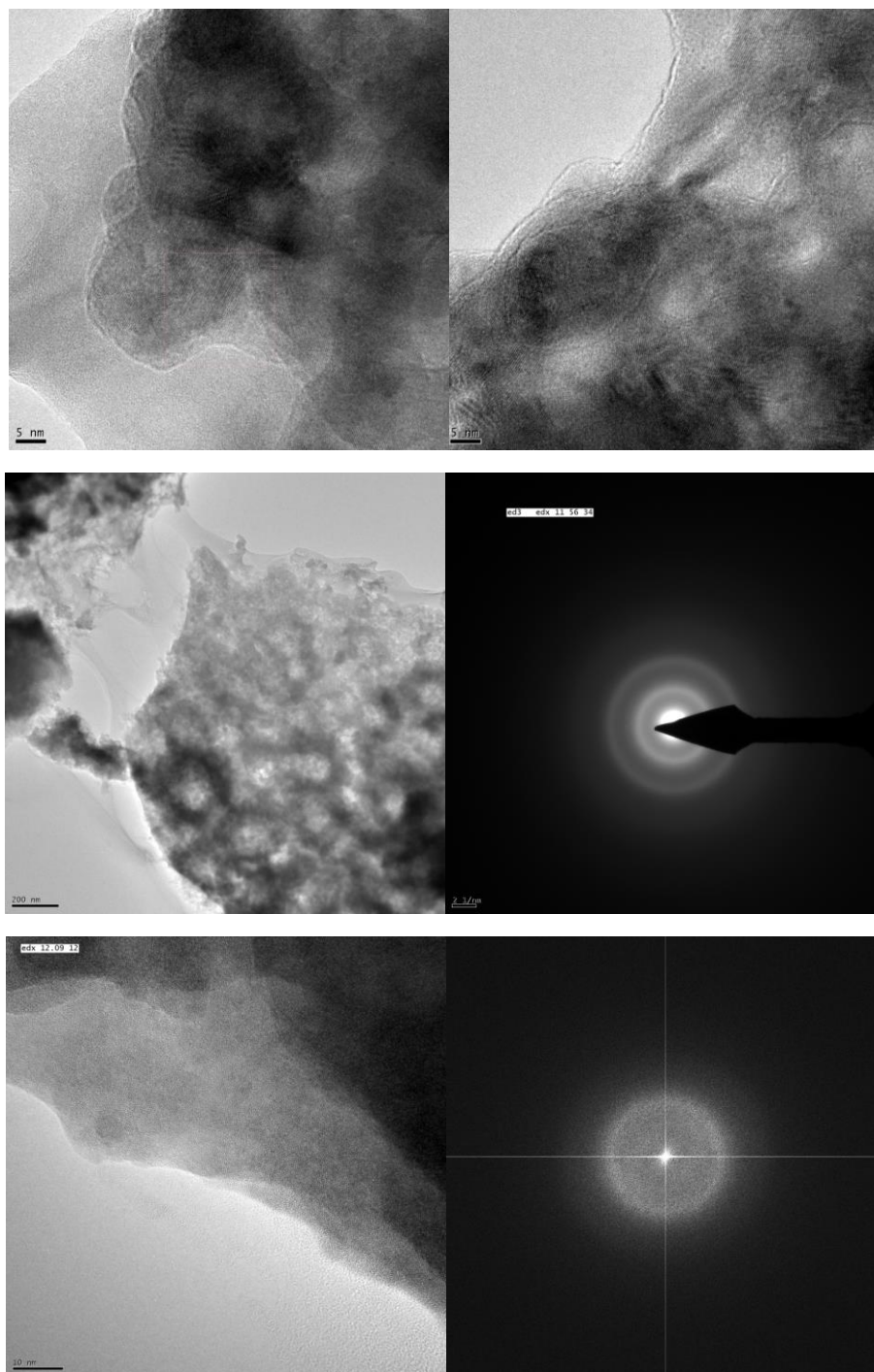
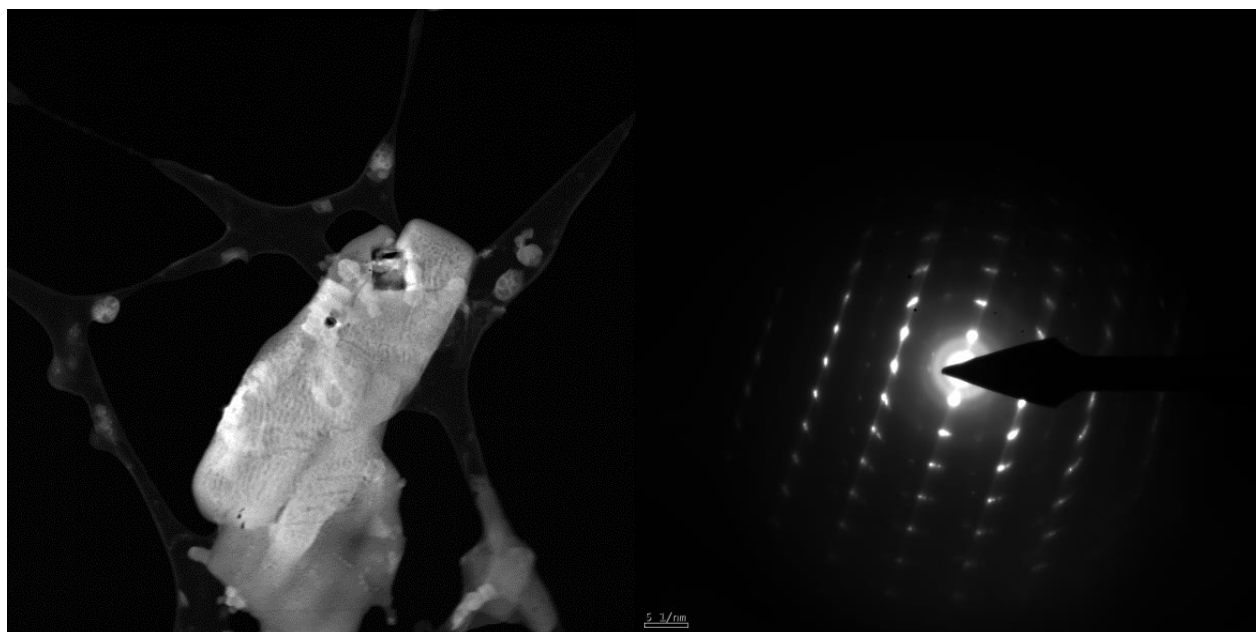
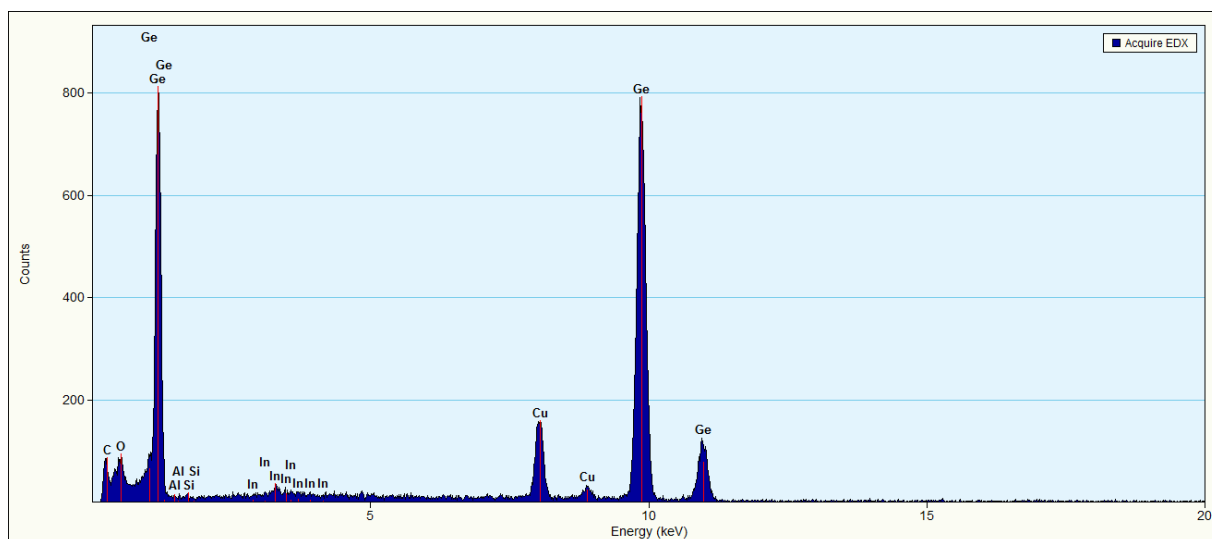


Figure 85: TEM images of the dried filtrate of the reaction of K_4Ge_9 and LiER in liquid ammonia. Top: Amorphous agglomerates of elemental germanium. Middle & bottom: Left pictures shows agglomerated germanium which proves to be amorphous by FFT diffraction (right). EDX analysis depicted in Figure 86 shows the presence of almost exclusively germanium.



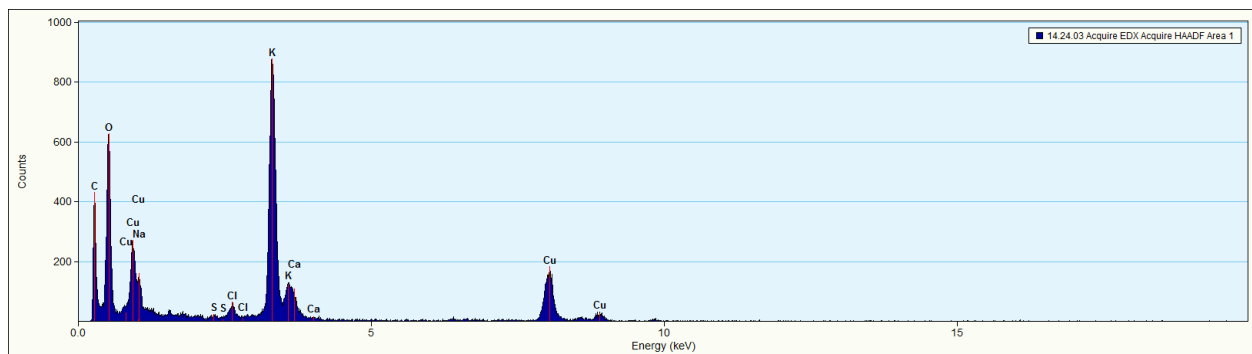


Figure 88: EDX analysis of the dried filtrate of the reaction of K_4Ge_4 and LiER in liquid ammonia. High amounts of potassium can be detected while germanium is almost absent.

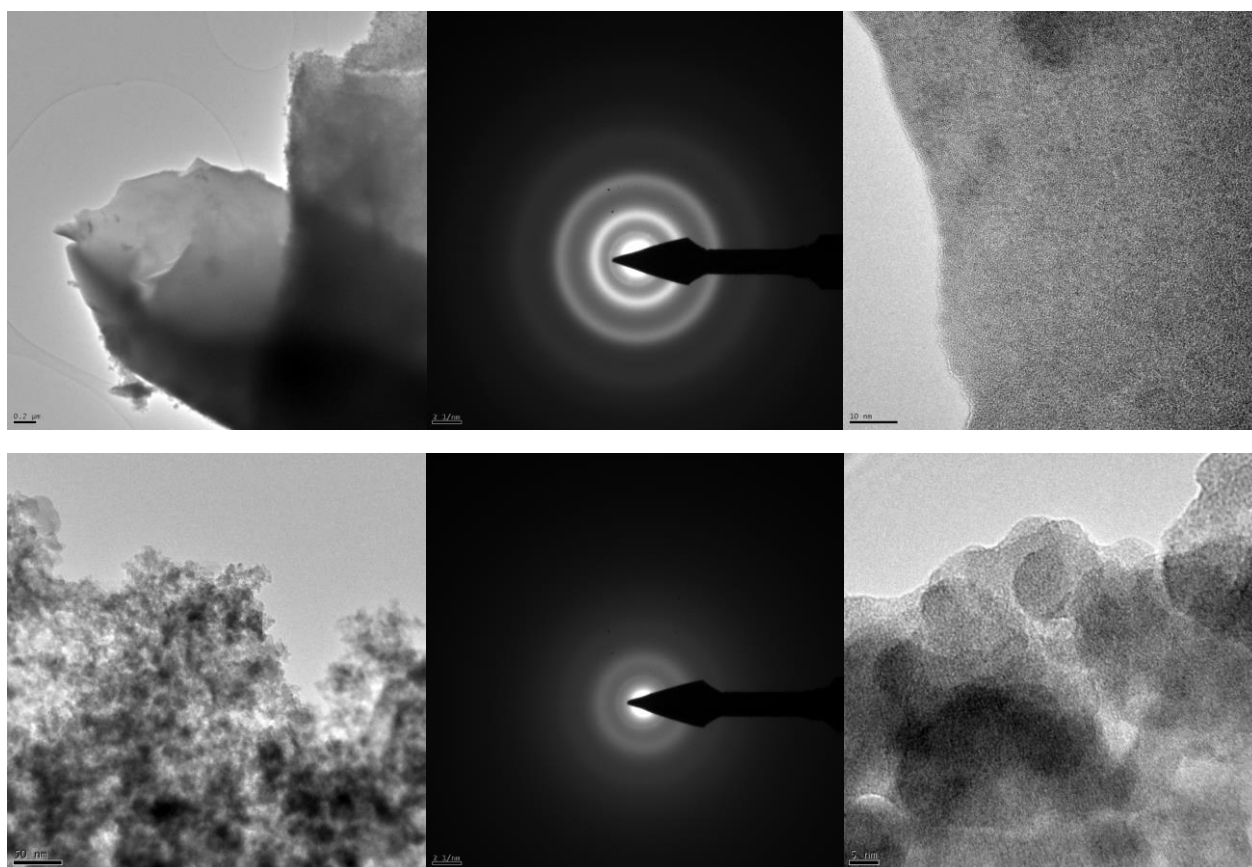


Figure 89: TEM analysis of K_4Ge_9 and HER in acn after the experiment and the removal of suspension medium. Top and bottom pictures show amorphous agglomerations of elemental germanium. This is addition to the crystalline nanoparticles in Figure 27 and Figure 90.

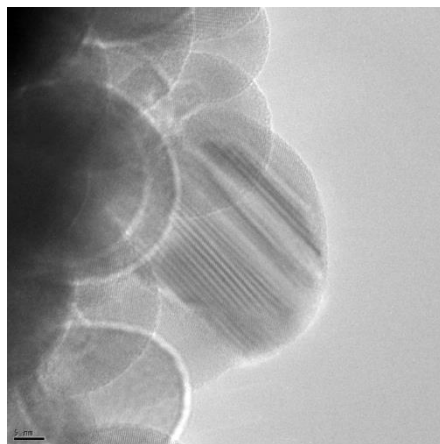


Figure 90: TEM analysis of K_4Ge_9 and HER in acn after the experiment and the removal of suspension medium. TEM analysis shows nanoparticles of crystalline, elemental germanium in the size range of 20-40 nm.

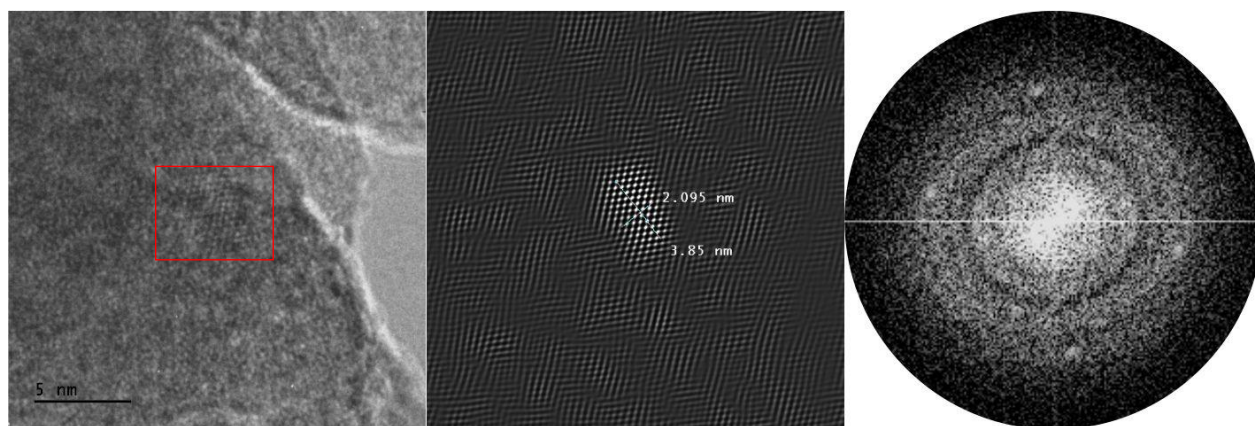


Figure 91: TEM analysis of K_4Ge_9 and LiER in acn after the experiment and the removal of suspension medium. Left: The red square shows a single nanoparticle embedded in an amorphous matrix. Middle: Inverse FFT of the area in the red square. Right: d-values fit elemental germanium.

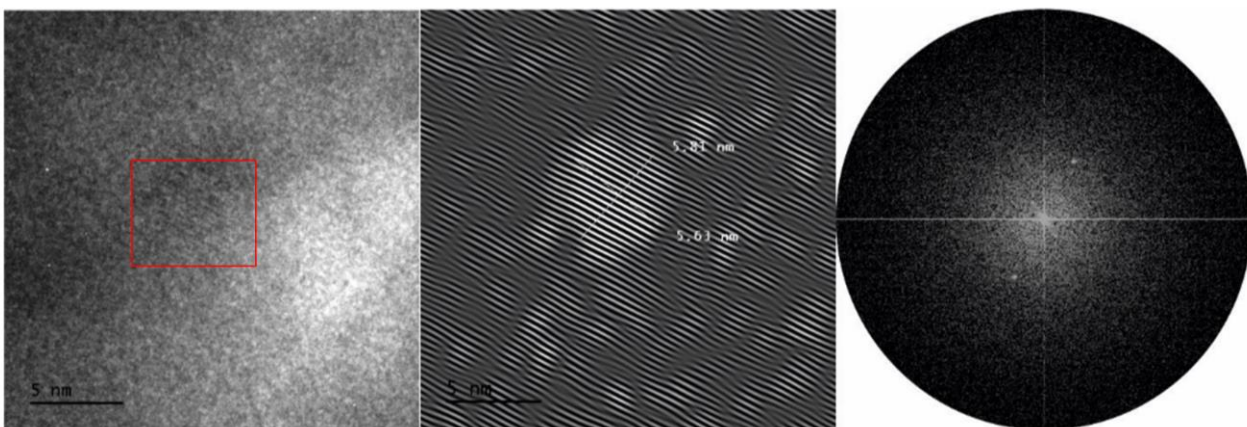


Figure 92: TEM analysis of K_4Ge_9 and NaER in acn after the experiment and the removal of suspension medium. Left: The red square shows a single nanoparticle embedded in an amorphous matrix. Middle: Inverse FFT of the area in the red square. Right: Absence of proper Diffraction pattern.

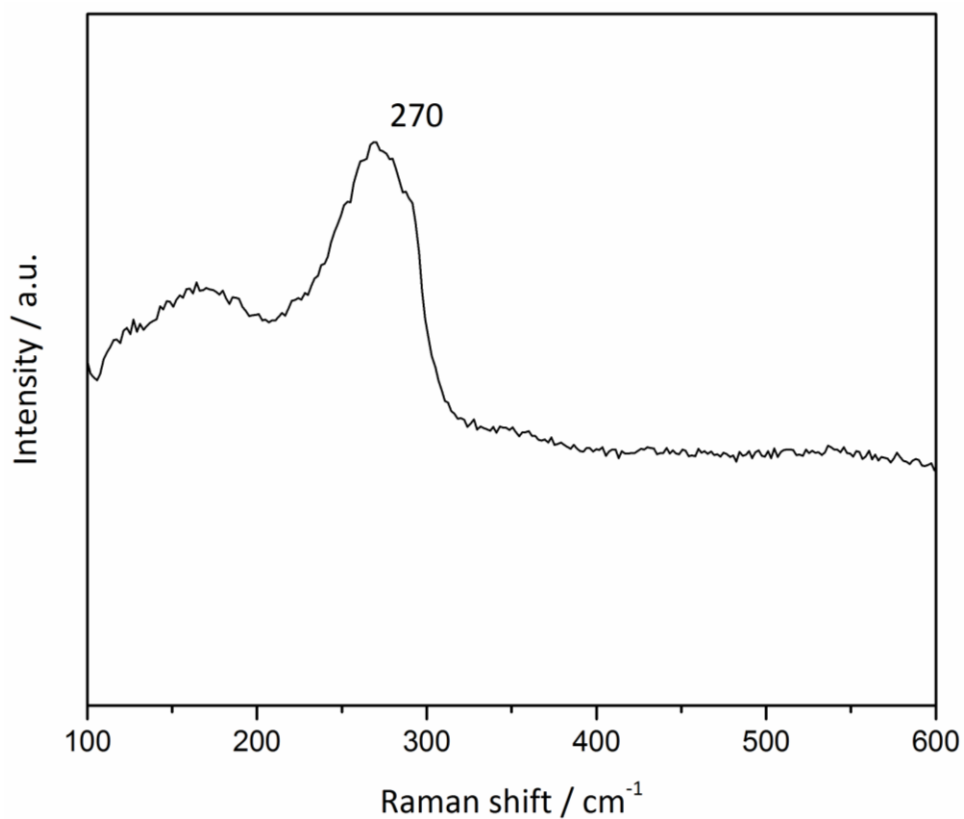


Figure 93: Raman spectrum of amorphous germanium. Product is yielded by reaction of K_4Ge_9 and LiER in liquid ammonia with subsequent filtration onto 9 equivalents of PEO.

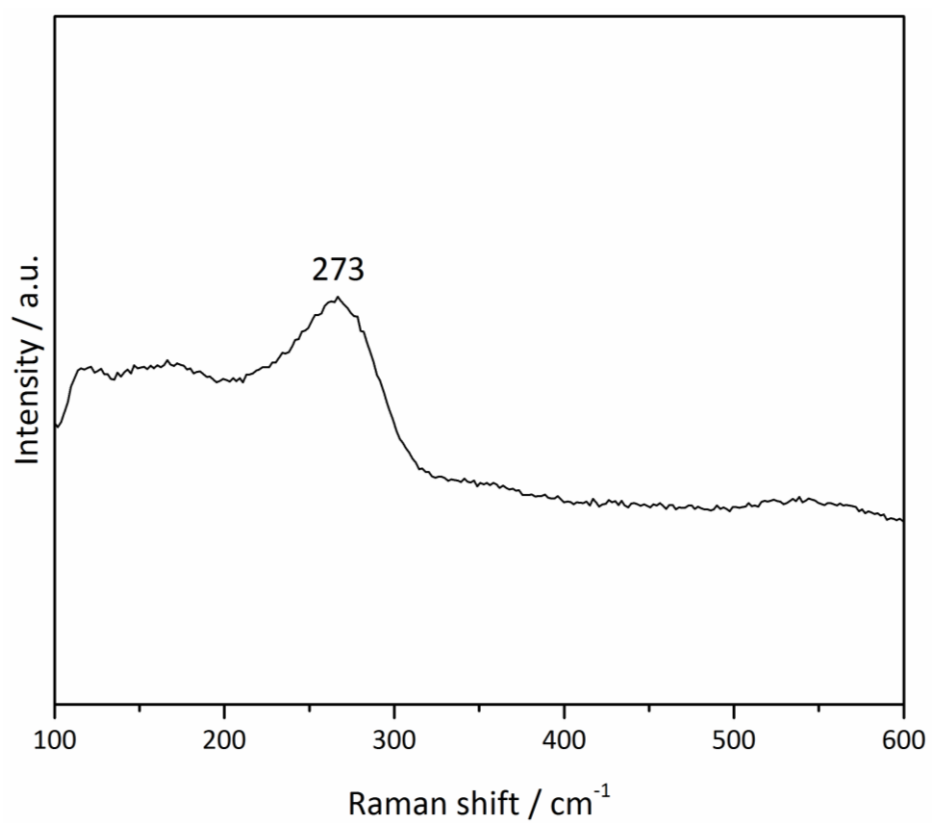


Figure 94: Exemplary Raman spectrum of amorphous germanium. Product is yielded by reaction of K_4Ge_9 and LiER in dmf with subsequent filtration onto 6 equivalents of PEO.

7.3.4. Germanium nanoparticles through reaction of K_4Ge_9 and Amberlyst 15

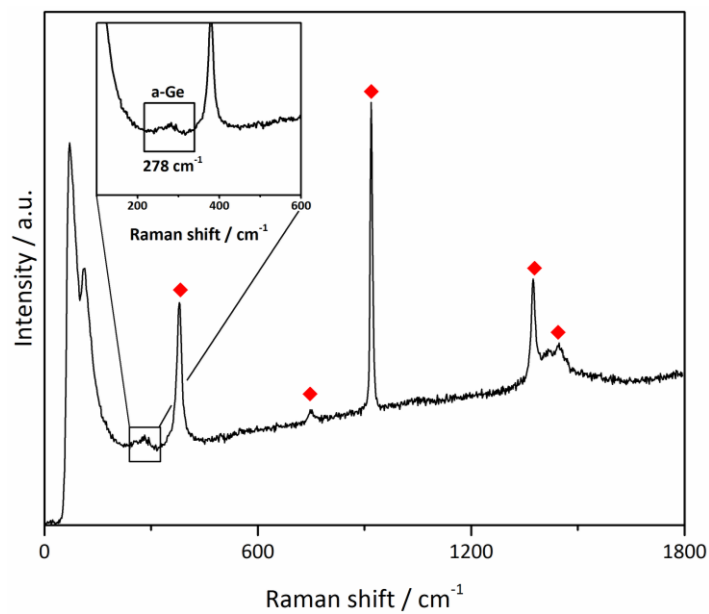


Figure 95: Raman spectrum of Ge nanoparticles in acn suspension yielded by reaction of K_4Ge_9 and proton loaded Amberlyst 15. Red diamonds indicate Raman shifts of acn. Enlarged section shows broad signal of amorphous germanium.

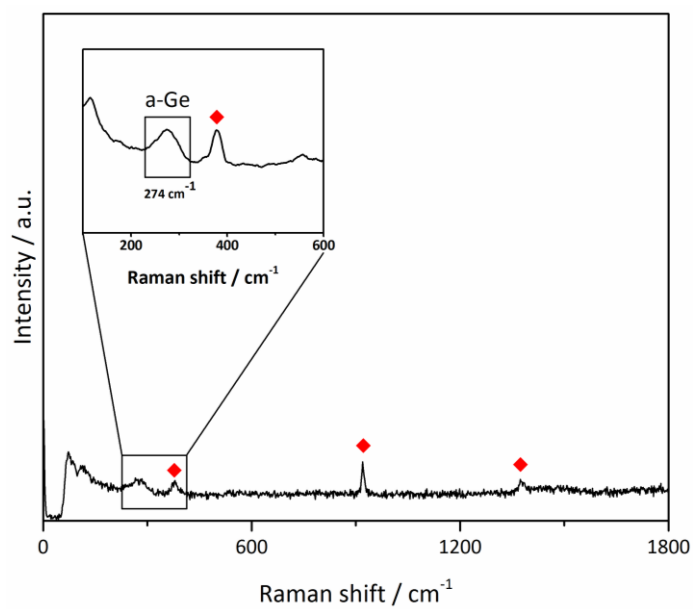


Figure 96: Raman spectrum of Ge nanoparticles in acn suspension yielded by reaction of K_4Ge_9 and lithium ion loaded Amberlyst 15. Red diamonds indicate Raman shifts of acn. Enlarged section shows broad signal of amorphous germanium.

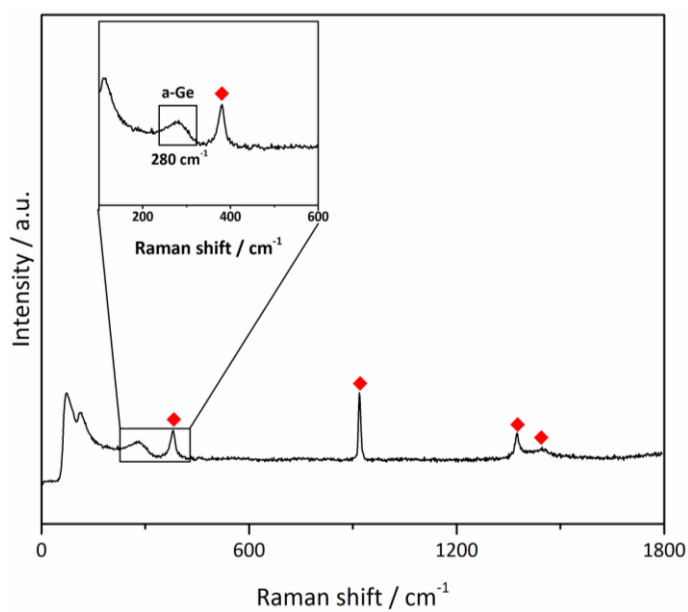


Figure 97: Raman spectrum of Ge nanoparticles in acn suspension yielded by reaction of K_4Ge_9 and sodium ion loaded Amberlyst 15. Red diamonds indicate Raman shifts of acn. Enlarged section shows broad signal of amorphous germanium.

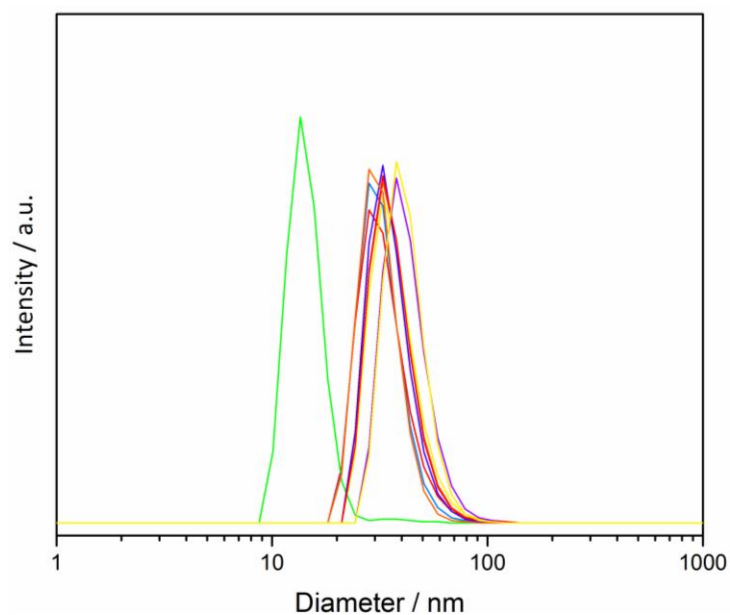


Figure 98: DLS measurement of size of germanium nanoparticles obtained from the reaction of K_4Ge_9 and HER in acn.

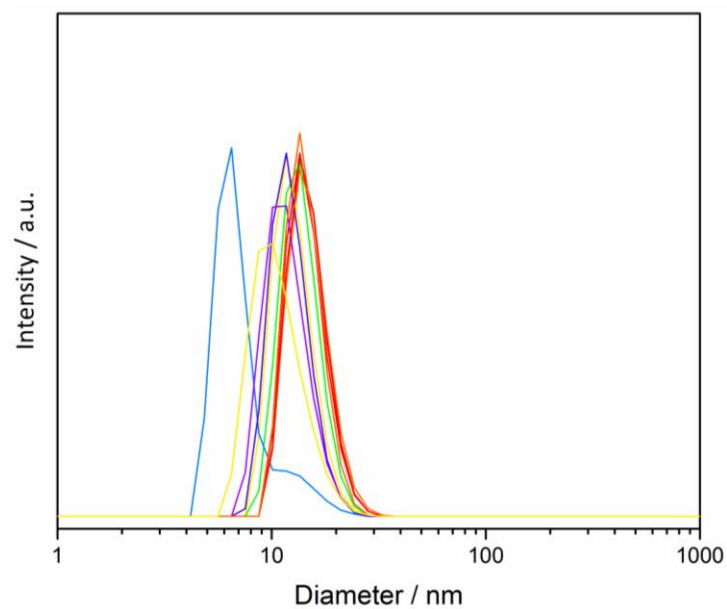


Figure 99: DLS measurement of size of germanium nanoparticles obtained from the reaction of K_4Ge_9 and NaER acn.

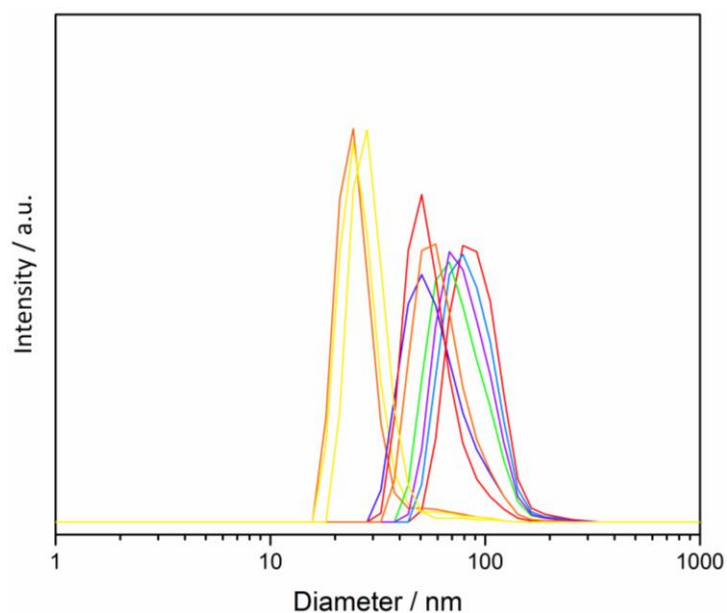


Figure 100: DLS measurement of size of germanium nanoparticles obtained from the reaction of K_4Ge_9 and LiER acn.

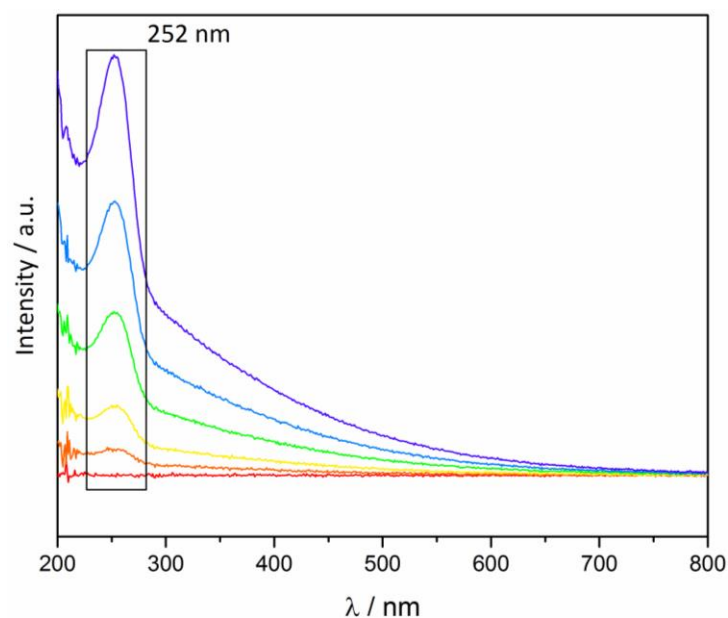


Figure 101: UV-VIS analysis of Ge nanoparticles in acn suspension yielded by reaction of K_4Ge_9 and sodium ion loaded Amberlyst 15. The particles show absorption at 255 nm but no emission. The increase in intensity is due to increase in reaction solution. The graph showing no intensity is pure acn.

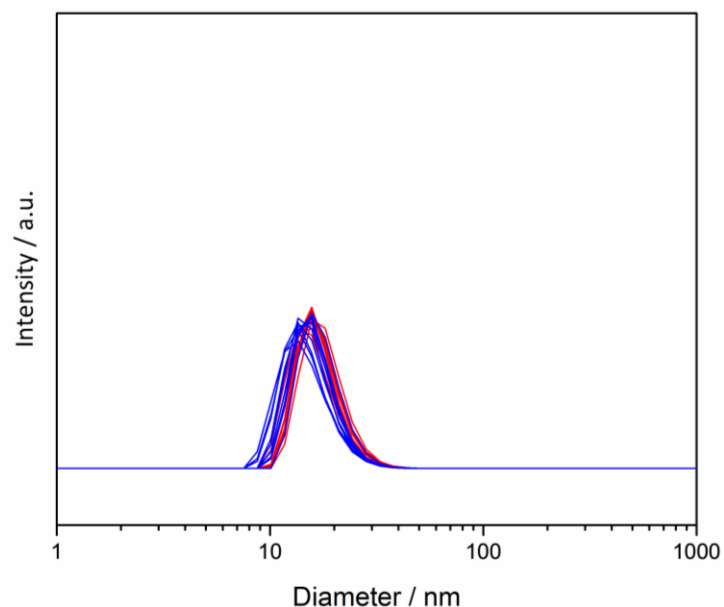


Figure 102: DLS analysis of a two month old sample (red) and a 24 hour old sample (blue) yielded by reaction of K_4Ge_9 , NaER in acn. This shows the stability of the Ge nanoparticles in suspension.

7.3.5. Ternary phases containing Endohedral cluster species

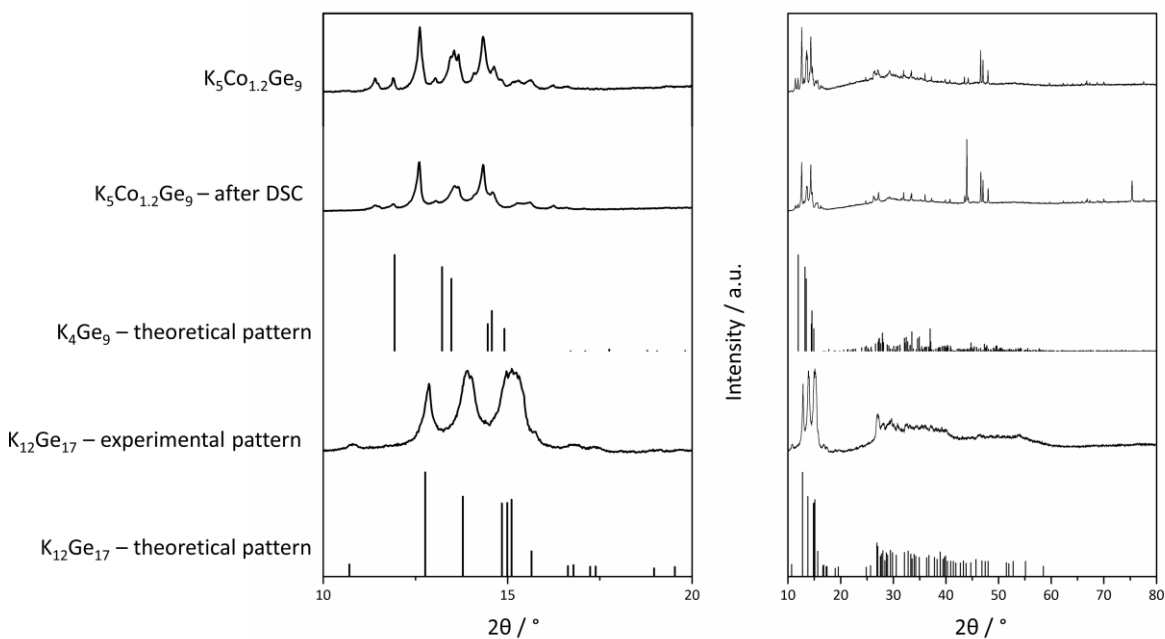


Figure 103: X-ray powder diffractogram measured of “ $\text{K}_5\text{Co}_{1.2}\text{Ge}_9$ ”, “ $\text{K}_5\text{Co}_{1.2}\text{Ge}_9$ ” after DSC analysis and $\text{K}_{12}\text{Ge}_{17}$ and calculated of K_4Ge_9 and experimental of $\text{K}_{12}\text{Ge}_{17}$. The calculated diffractograms

are based on single crystal data.^[44] The diffractogram is measured using Cu-K α_1 radiation. Left: close up on 10 to 20 2 θ . Right: Comparison of full diffractograms.

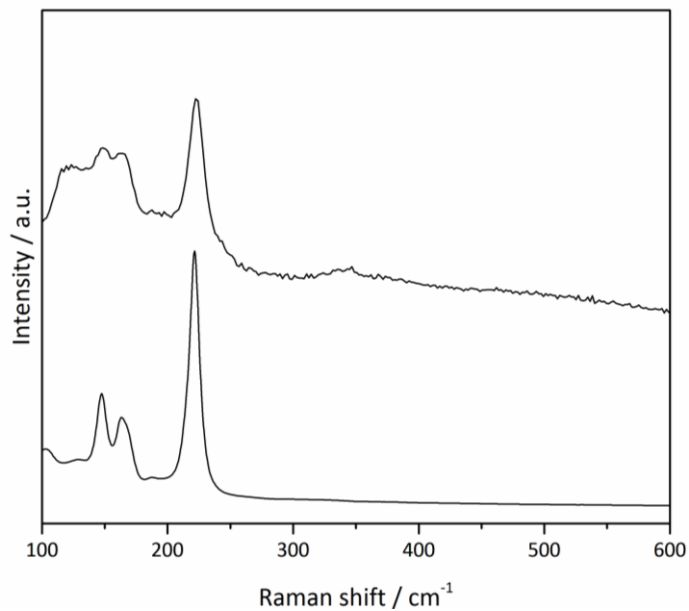


Figure 104: Raman spectrum of " $\text{K}_5\text{Co}_{1.2}\text{Ge}_9$ " after heating to 1000 °C (top) and K_4Ge_9 (bottom).

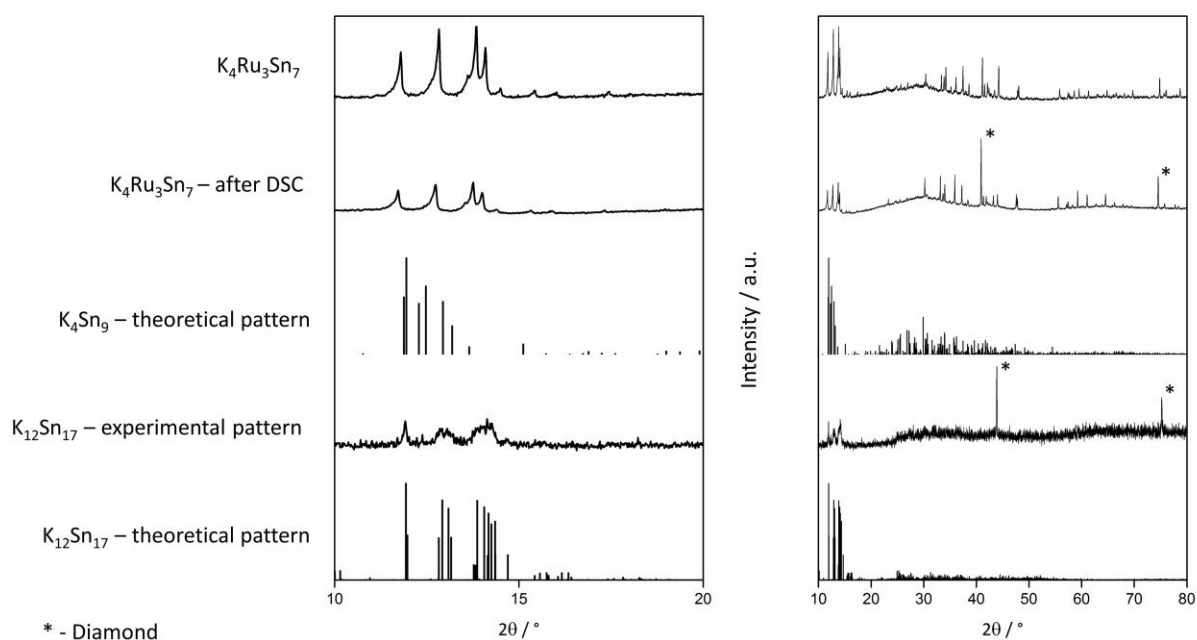


Figure 105: X-ray powder diffractogram measured of “ $K_4Ru_3Sn_7$ ”, “ $K_4Ru_3Sn_7$ ” after DSC analysis and $K_{12}Sn_{17}$ and calculated of K_4Sn_9 and $K_{12}Sn_{17}$. The calculated diffractograms is based on single crystal data.^[46] The diffractogram is measured using Cu- $K\alpha_1$ radiation. Left: close up on 10 to 20 2θ . Right: Comparison of full diffractograms.

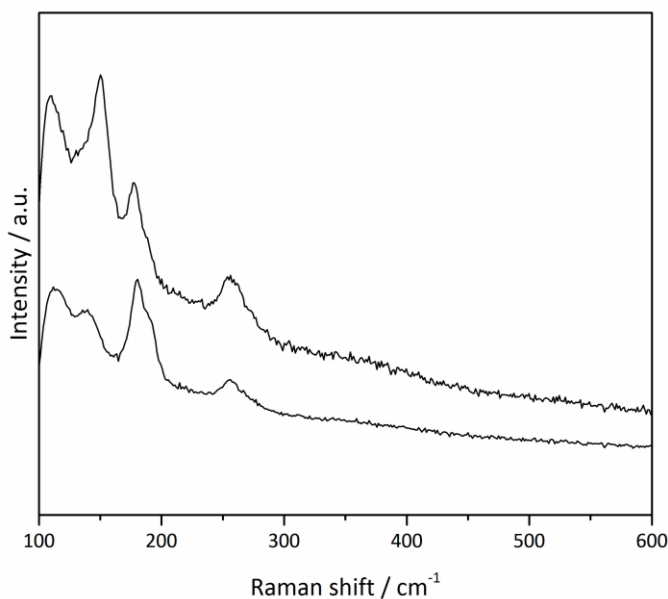


Figure 106: Raman spectrum of “ $K_4Ru_3Sn_7$ ” before heating to 1000 °C (top) and after (bottom).

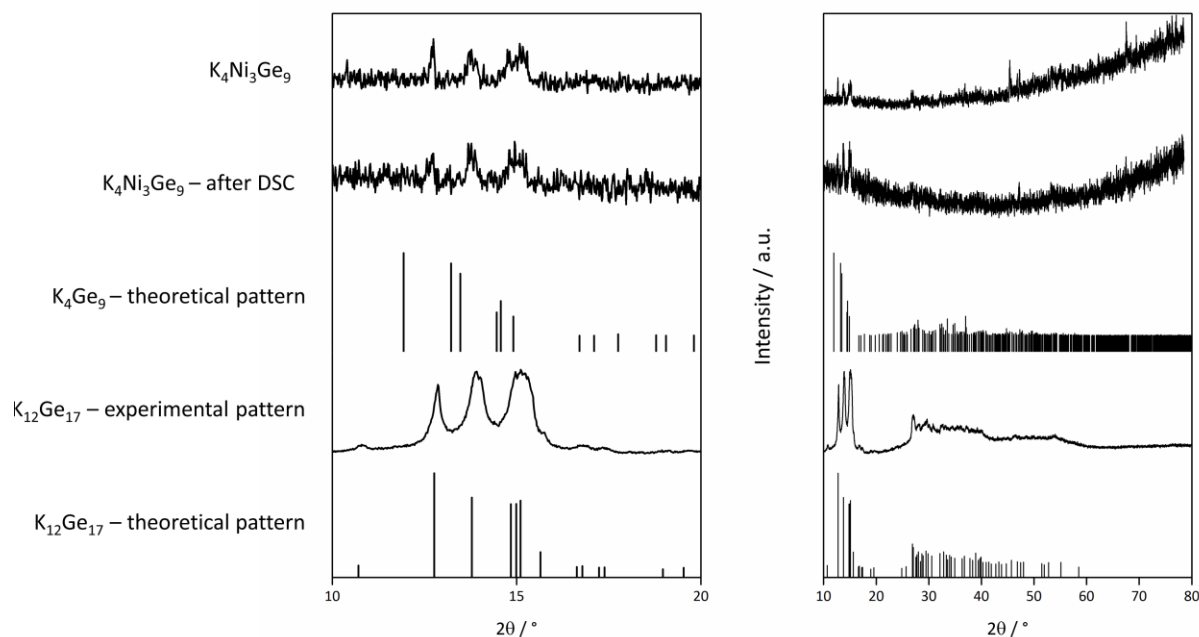


Figure 107: X-ray powder diffractogram measured of “ $K_4Ni_3Ge_9$ ”, “ $K_4Ni_3Ge_9$ ” after DSC analysis and $K_{12}Ge_{17}$ and calculated of K_4Ge_9 and experimental of $K_{12}Ge_{17}$. The calculated diffractograms are based on single crystal data.^[44] The diffractogram is measured using Cu- $K\alpha_1$ radiation. Left: close up on 10 to 20 2θ . Right: Comparison of full diffractograms.

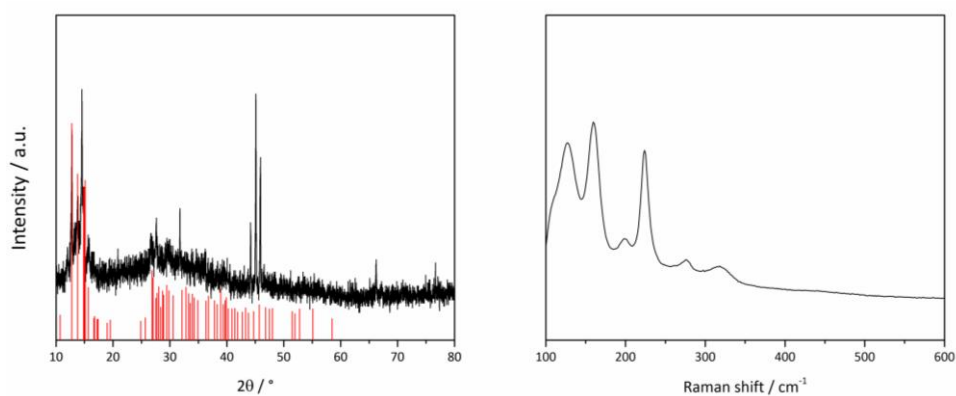


Figure 108: Left: X-ray powder diffractogram measured (black) of “ $K_5Fe_{1.5}Ge_9$ ” and calculated (red) of $K_{12}Ge_{17}$. The calculated diffractogram is based on single crystal data.^[448] The diffractogram is measured using Cu- $K\alpha_1$ radiation. Right: Raman spectrum of “ $K_5Fe_{1.5}Ge_9$ ” with best agreement to $K_{12}Ge_{17}$.^[43]

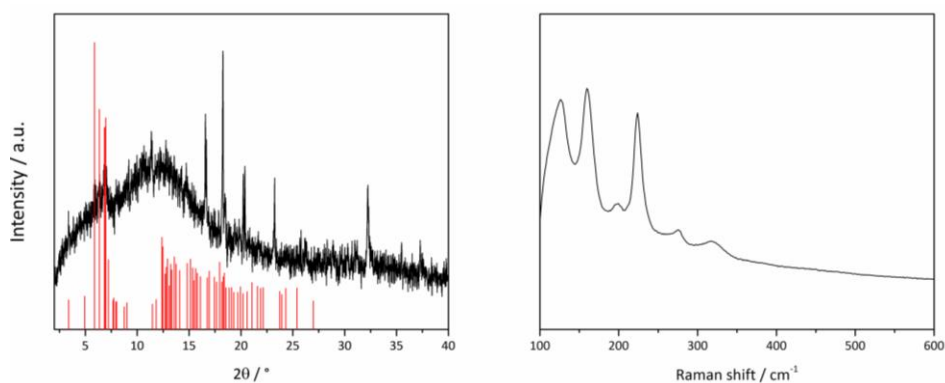


Figure 109: Left: X-ray powder diffractogram measured (black) of “ $K_5Ru_{1.5}Ge_9$ ” and calculated (red) of $K_{12}Ge_{17}$. The calculated diffractogram is based on single crystal data.^[448] The diffractogram is measured using Mo- $K_{\alpha 1}$ radiation Right: Raman spectrum of “ $K_5Ru_{1.5}Ge_9$ ” with best agreement to $K_{12}Ge_{17}$.^[43]

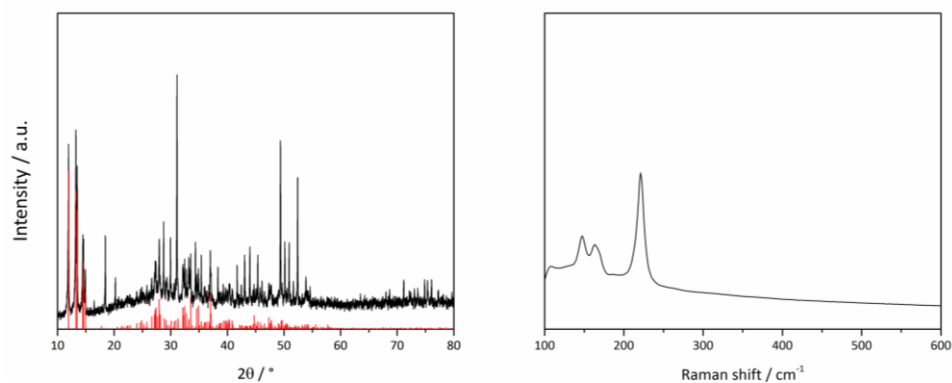


Figure 110: Left: X-ray powder diffractogram measured (black) of “ $K_5Pd_{1.5}Ge_{14.7}$ ” and calculated (red) of K_4Ge_9 . The calculated diffractogram is based on single crystal data.^[44] The diffractogram is measured using Cu- $K_{\alpha 1}$ radiation Right: Raman spectrum of “ $K_5Pd_{1.5}Ge_{14.7}$ ” with best agreement to K_4Ge_9 .^[43]

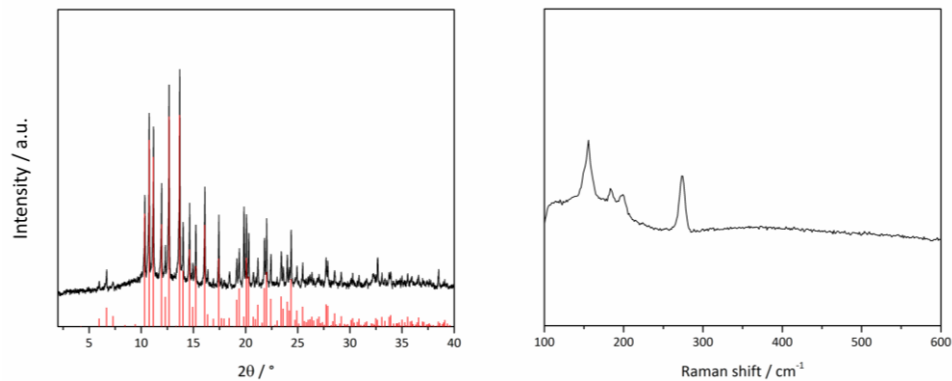


Figure 111: Left: X-ray powder diffractogram measured (black) of “ $\text{Cs}_{13}\text{Cu}_{1.5}\text{Ge}_{17}$ ” and calculated (red) of Cs_4Ge_4 . The calculated diffractogram is based on single crystal data.^[449] The diffractogram is measured using Mo- $\text{K}\alpha_1$ radiation. Right: Raman spectrum of “ $\text{Cs}_{13}\text{Cu}_{1.5}\text{Ge}_{17}$ ” with best agreement to K_4Ge_4 .^[43]

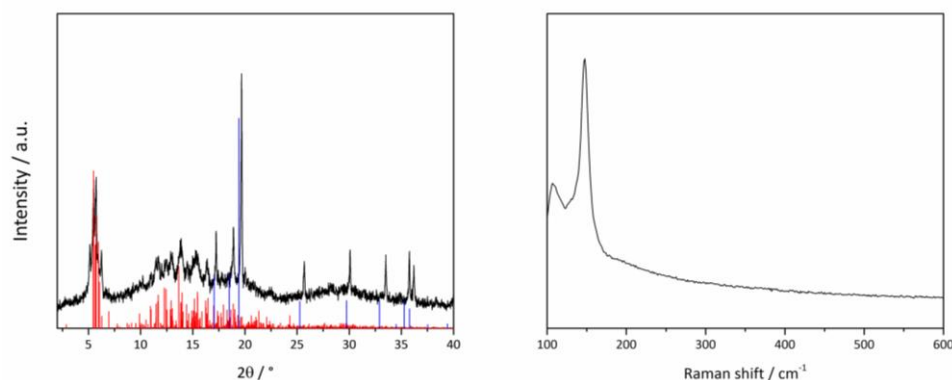


Figure 112: Left: X-ray powder diffractogram measured (black) of “ K_4OsSn_9 ” and calculated (red) of K_4Sn_9 and calculated (blue) of $\text{Ta}_{0.2}\text{Os}_{0.8}$. The calculated diffractogram is based on single crystal data.^[46, 450] The diffractogram is measured using Mo- $\text{K}\alpha_1$ radiation. Right: Raman spectrum of “ K_4OsSn_9 ” with best agreement to K_4Sn_9 .^[43]

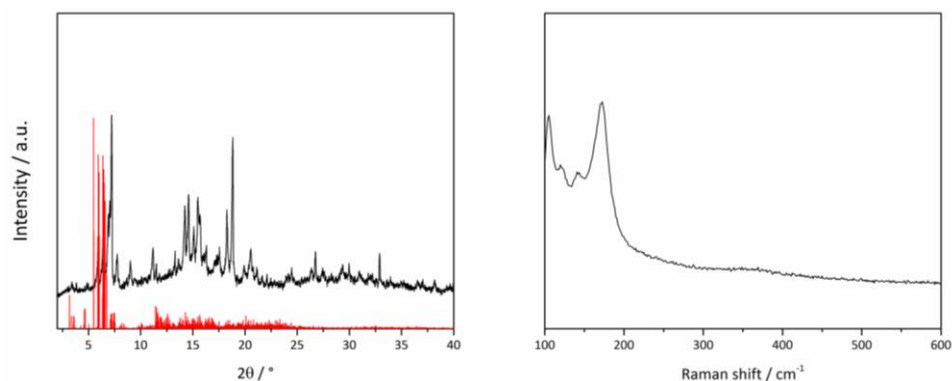


Figure 113: Left: X-ray powder diffractogram measured (black) of “ $Na_{13}RhSn_{17}$ ” and calculated (red) of $K_{12}Sn_{17}$. The calculated diffractogram is based on single crystal data.^[451] The diffractogram is measured using Mo- $K_{\alpha 1}$ radiation. Right: Raman spectrum of “ $Na_{13}RhSn_{17}$ ” with best agreement to the theoretical spectrum of $[Rh@Sn_9]^{5-}$.

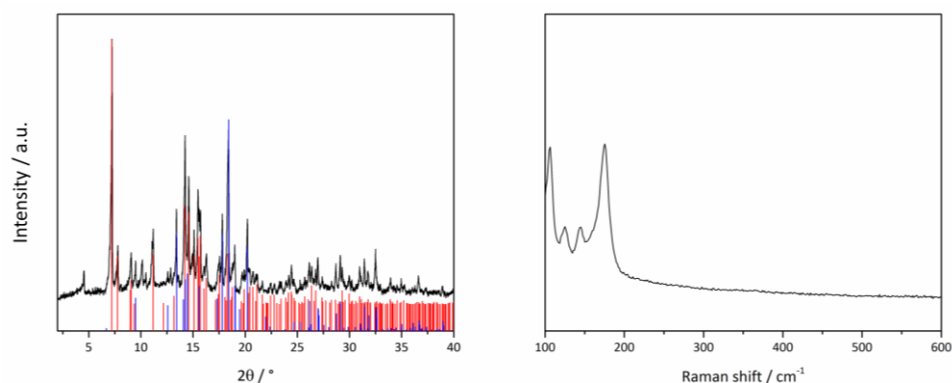


Figure 114: Left: X-ray powder diffractogram measured (black) of “ $Na_{12}Pd_2Sn_{17}$ ” and calculated (red) of Na_4Sn_4 and calculated (blue) of $Pd_{0.89}Sn_2$. The calculated diffractogram is based on single crystal data.^[452-453] The diffractogram is measured using Mo- $K_{\alpha 1}$ radiation. Right: Raman spectrum of “ $Na_{12}Pd_2Sn_{17}$ ” with best agreement to K_4Sn_4 .^[379]

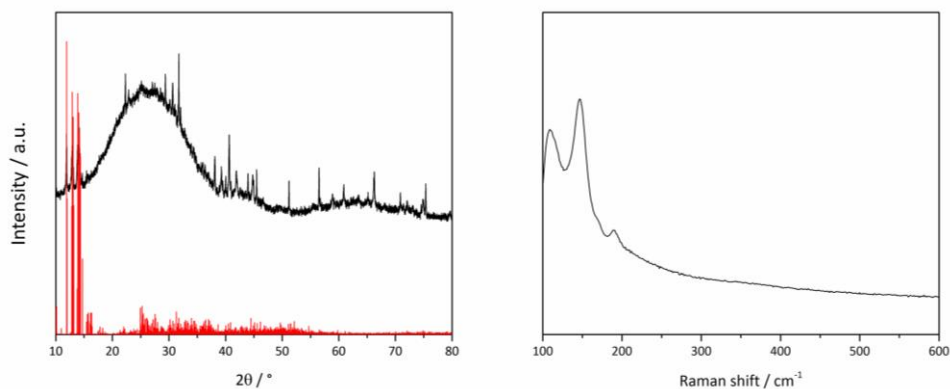


Figure 115: Left: X-ray powder diffractogram measured (black) of “ K_2PdSn_4 ” and calculated (red) of $K_{12}Sn_{17}$. The calculated diffractogram is based on single crystal data.^[451] The diffractogram is measured using Cu- $K_{\alpha 1}$ radiation. Right: Raman spectrum of “ K_2PdSn_4 ” with best agreement to $K_{12}Sn_{17}$.^[43]

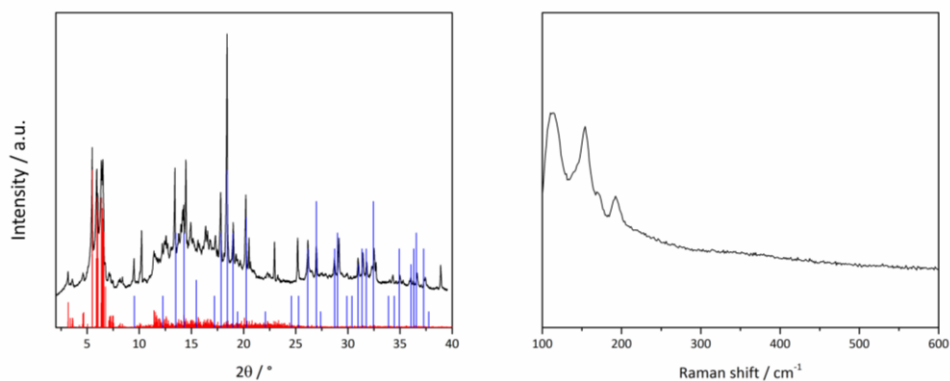


Figure 116: X-ray powder diffractogram measured (black) of “ K_5PdSn_9 ” and calculated (red) of $K_{12}Sn_{17}$ and calculated (blue) of $PdSn_2$. The calculated diffractogram is based on single crystal data.^[451, 454] The diffractogram is measured using Mo- $K_{\alpha 1}$ radiation. Right: Raman spectrum of “ K_5PdSn_9 ” with best agreement to theoretical spectrum of $[Pd@Sn_9]^{4-}$.

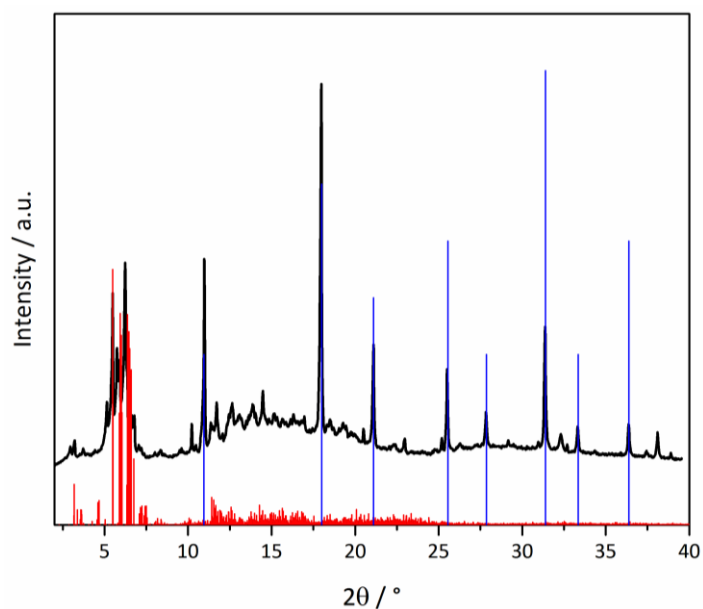


Figure 117: X-ray powder diffractogram measured (black) of “ K_5PtSn_9 ” and calculated (red) of $K_{12}Sn_{17}$ and calculated (blue) of $PtSn_2$. The calculated diffractogram is based on single crystal data.^[451, 455] The diffractogram is measured using Mo- $K_{\alpha 1}$ radiation.

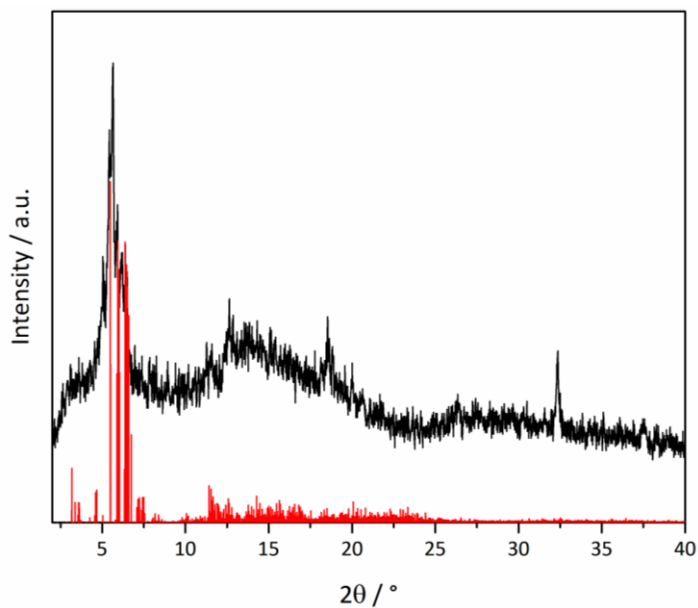


Figure 118: X-ray powder diffractogram measured (black) of “ K_5RhSn_9 ” and calculated (red) of $K_{12}Sn_{17}$. The calculated diffractogram is based on single crystal data.^[451] The diffractogram is measured using Mo- $K_{\alpha 1}$ radiation.

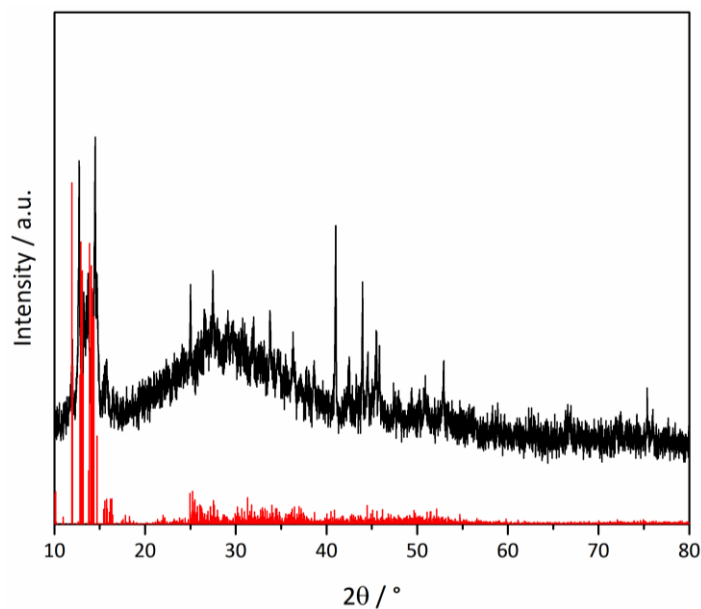


Figure 119: X-ray powder diffractogram measured (black) of “K₅RuSn₉” and calculated (red) of K₁₂Sn₁₇. The calculated diffractogram is based on single crystal data.^[451] The diffractogram is measured using Cu-K_{α1} radiation.

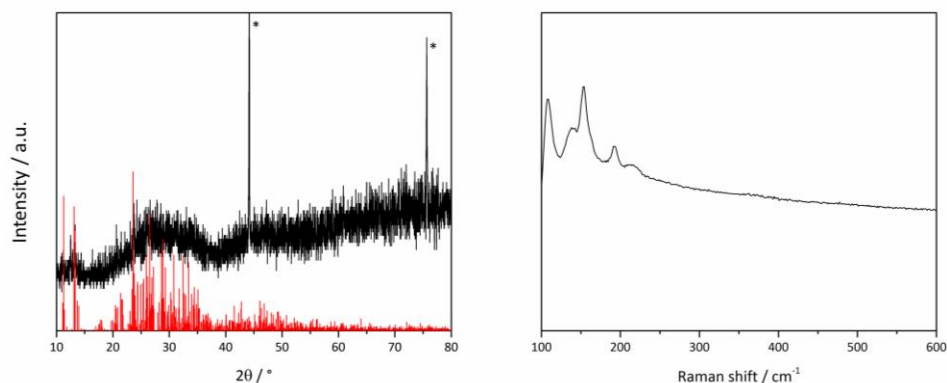


Figure 120: X-ray powder diffractogram measured (black) of “Cs₁₃Cu_{1.5}Sn₁₇” and calculated (red) of Cs₁₂Sn₁₇. The calculated diffractogram is based on single crystal data.^[48] The diffractogram is measured using Mo-K_{α1} radiation. Right: Raman spectrum of “Cs₁₃Cu_{1.5}Sn₁₇” with best agreement to K₁₂Sn₁₇.^[43]

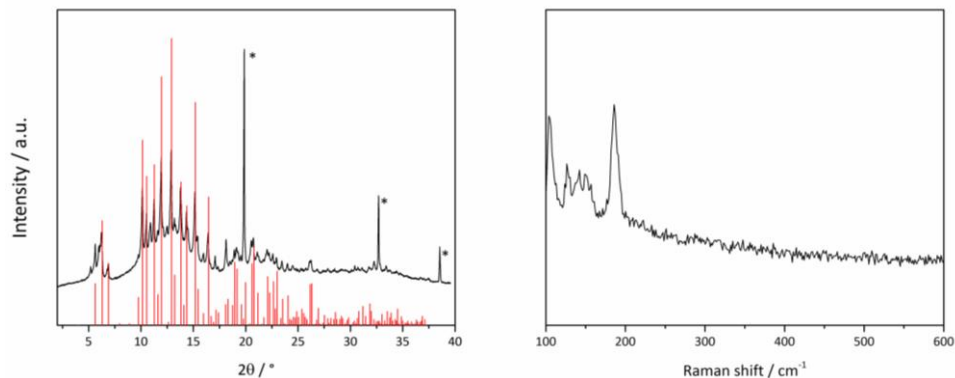


Figure 121: X-ray powder diffractogram measured (black) of “ $\text{Cs}_{13}\text{Ag}_{1.5}\text{Sn}_{17}$ ” and calculated (red) of Cs_8Sn_8 . The calculated diffractogram is based on single crystal data.^[456] The signals marked with * result from diamond.^[457] The diffractogram is measured using Mo- $\text{K}\alpha_1$ radiation. Right: Raman spectrum of “ $\text{Cs}_{13}\text{Ag}_{1.5}\text{Sn}_{17}$ ” with best agreement to $\text{K}_{12}\text{Sn}_{17}$.^[43]

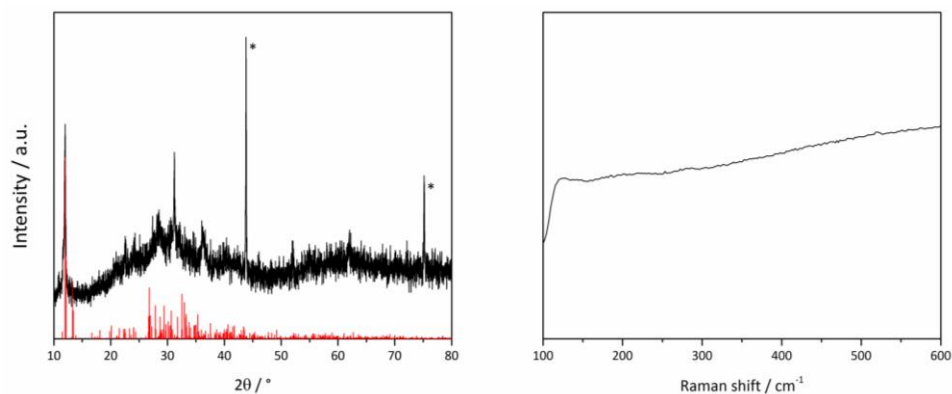


Figure 122: Left: X-ray powder diffractogram measured (black) of “ K_5RhPb_9 ” and calculated (red) of K_4Pb_9 . The signals marked with * result from diamond.^[457] The calculated diffractogram is based on single crystal data.^[458] The diffractogram is measured using Mo- $\text{K}\alpha_1$ radiation. Right: Raman spectrum of “ K_5RhPb_9 ”.

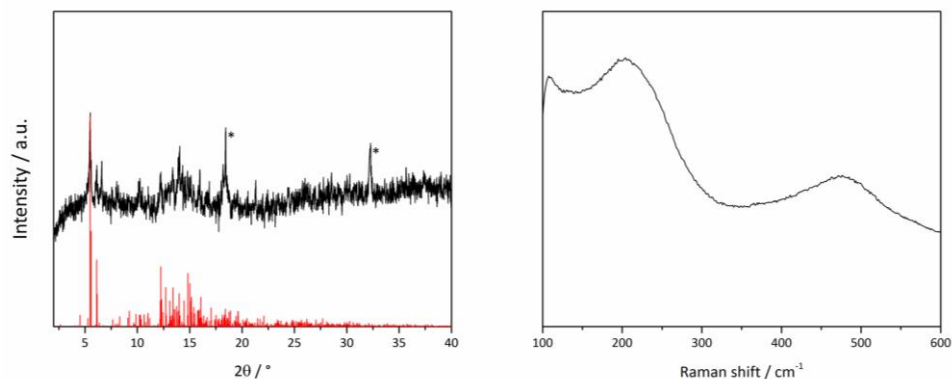


Figure 123: Left: X-ray powder diffractogram measured (black) of “ K_5IrPb_9 ” and calculated (red) of K_4Pb_9 . The signals marked with * result from diamond.^[457] The calculated diffractogram is based on single crystal data.^[458] The diffractogram is measured using Mo- $K_{\alpha 1}$ radiation. Right: Raman spectrum of “ K_5IrPb_9 ”.

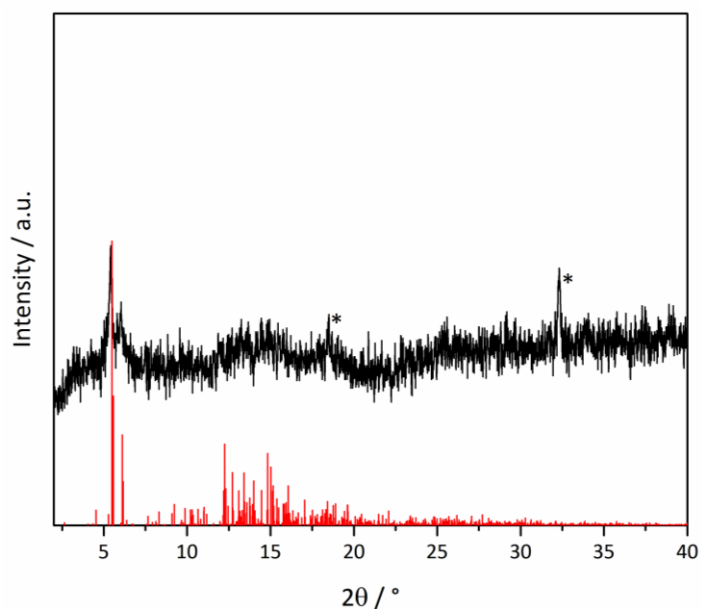


Figure 124: X-ray powder diffractogram measured (black) of “ K_5PdPb_9 ” and calculated (red) of K_4Pb_9 . The signals marked with * result from diamond.^[457] The calculated diffractogram is based on single crystal data.^[458] The diffractogram is measured using Mo- $K_{\alpha 1}$ radiation.

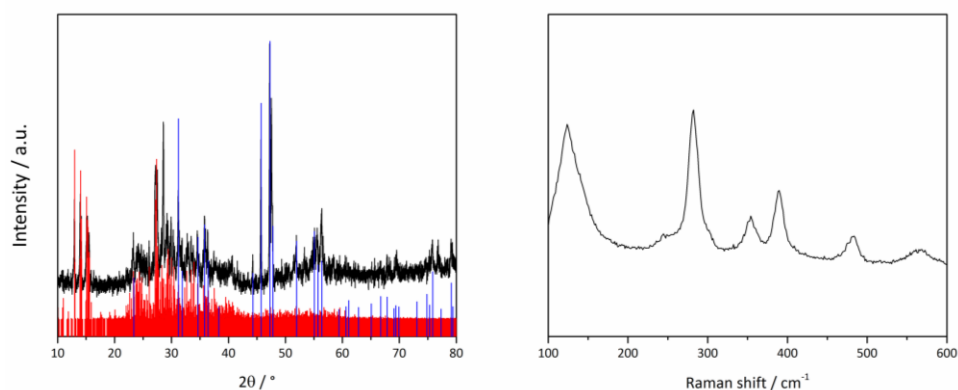


Figure 125: Left: X-ray powder diffractogram measured (black) of “ K_4NiSi_9 ” and calculated (red) of $K_{12}Si_{17}$ and (blue) of NiSi. The calculated diffractogram is based on single crystal data.^[48, 459] The diffractogram is measured using Cu- $K_{\alpha 1}$ radiation Right: Raman spectrum of “ K_4NiSi_9 ” with best agreement to $K_{12}Si_{17}$.^[48]

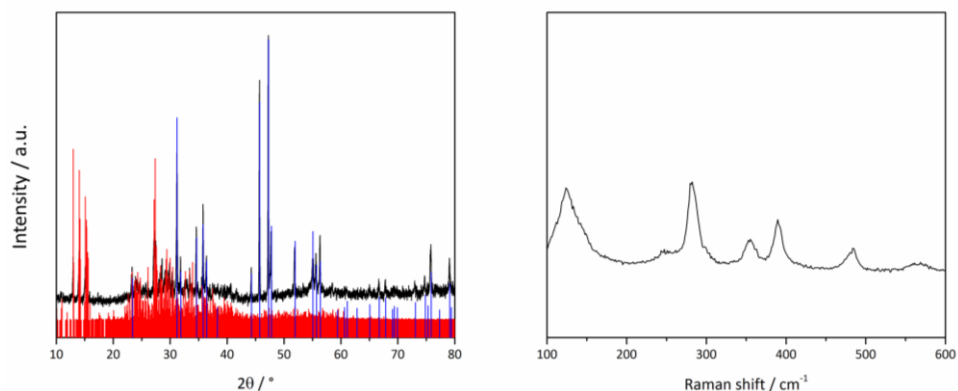


Figure 126: Left: X-ray powder diffractogram measured (black) of “ $K_4Ni_2Si_9$ ” and calculated (red) of $K_{12}Si_{17}$ and (blue) of NiSi. The calculated diffractogram is based on single crystal data.^[48, 459] The diffractogram is measured using Cu- $K_{\alpha 1}$ radiation Right: Raman spectrum of “ $K_4Ni_2Si_9$ ” with best agreement to $K_{12}Si_{17}$.^[48]

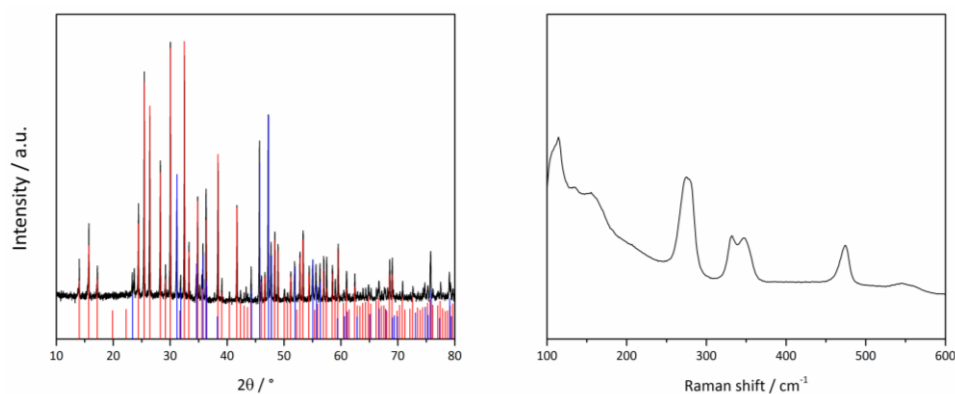


Figure 127: Left: X-ray powder diffractogram measured (black) of “ $K_4Ni_3Si_9$ ” and calculated (red) of K_4Si_4 and (blue) of $NiSi$. The calculated diffractogram is based on single crystal data.^[442, 459] The diffractogram is measured using $Cu-K\alpha_1$ radiation Right: Raman spectrum of “ $K_4Ni_3Si_9$ ” with best agreement to K_4Si_4 .^[413]

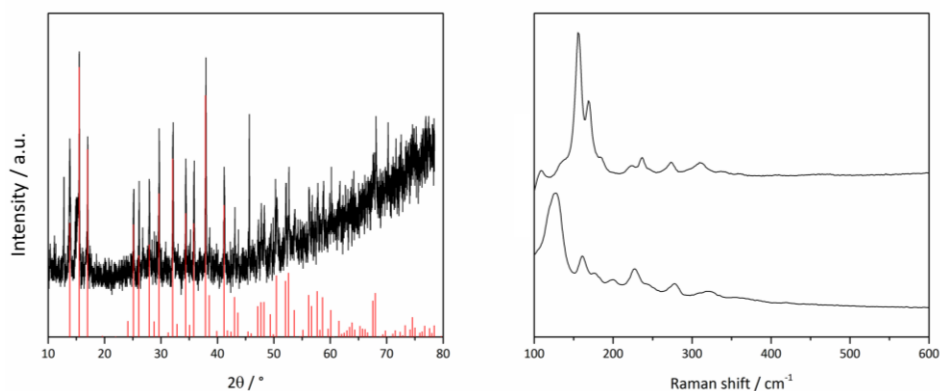


Figure 128: Left: X-ray powder diffractogram measured (black) of a phase with the nominal composition “ $K_5CoSi_3Ge_6$ ” and calculated (red) of K_4Ge_4 .^[442] The calculated diffractogram is based on single crystal data. The diffractogram is measured using $Cu-K\alpha_1$ radiation Right: Raman spectrum of a phase with the nominal composition “ $K_4CoSi_3Ge_6$ ”. The closest approximation is with $[Si_{1.2}/Ge_{2.8}]^{4-}$ - a mixed tetrel cluster contained in the phase “ $K_{12}Si_5Ge_{12}$ ”. Mixed tetrel clusters and phases are more closely examined by Michael Giebel, M. Sc, Chair of Inorganic Chemistry with Focus on Novel Materials.

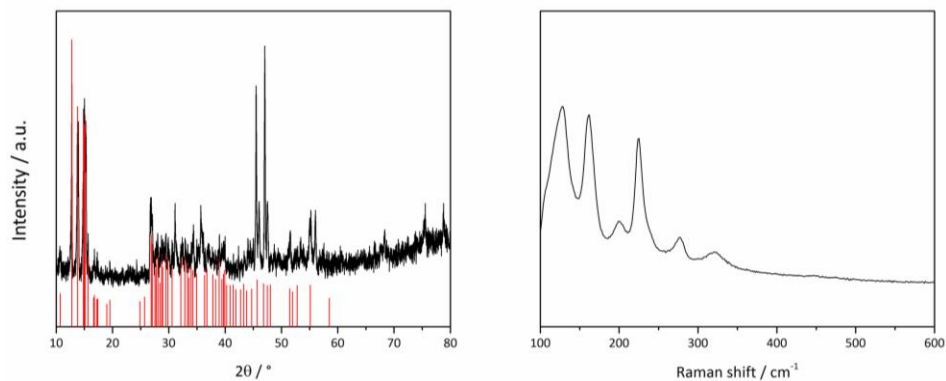


Figure 129: Left: X-ray powder diffractogram measured (black) of a phase with the nominal composition “ $K_4NiSi_3Ge_6$ ” and calculated (red) of $K_{12}Ge_{17}$.^[448] The calculated diffractogram is based on single crystal data. The diffractogram is measured using Cu- $K_{\alpha 1}$ radiation. Right Raman spectrum of a phase with the nominal composition “ $K_4NiSi_3Ge_6$ ” with best agreement to $K_{12}Ge_{17}$.^[43]

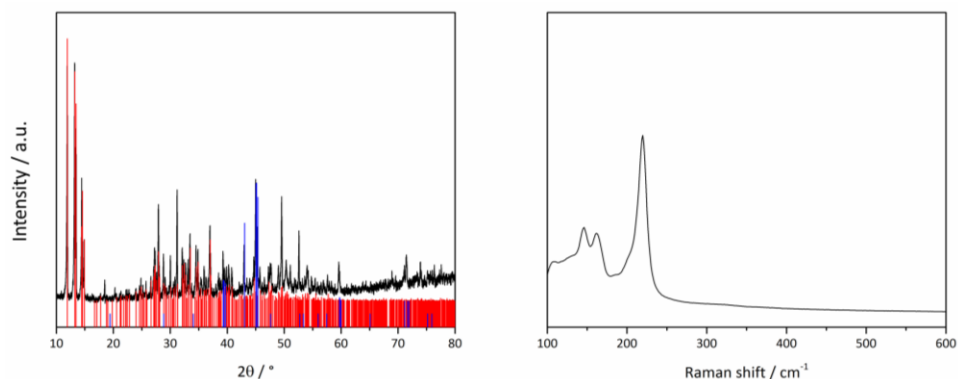


Figure 130: Left: X-ray powder diffractogram measured (black) “ K_3CuGe_9 ”, calculated (red) of K_4Ge_9 and (blue) of Cu_3Ge . The calculated diffractogram is based on single crystal data.^[44, 460] The diffractogram is measured using Cu- $K_{\alpha 1}$ radiation. Right: Raman spectrum of “ K_3CuGe_9 ” with best agreement to K_4Ge_9 .^[378]

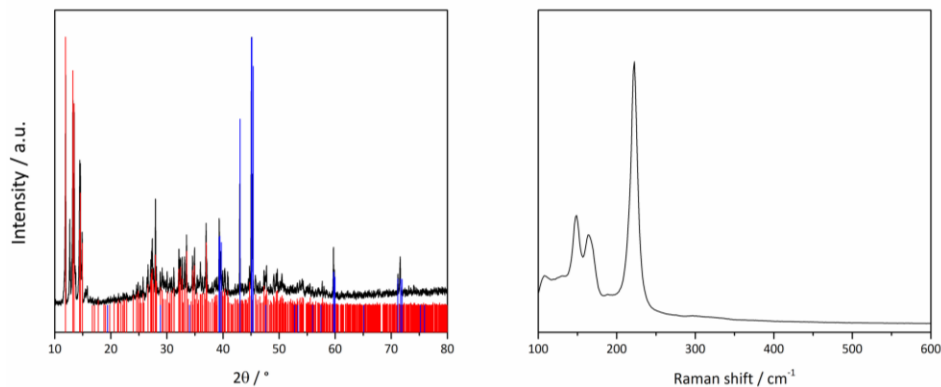


Figure 131: Left: X-ray powder diffractogram measured (black) “ $K_3Cu_2Ge_9$ ”, calculated (red) of K_4Ge_9 and (blue) of Cu_3Ge . The calculated diffractogram is based on single crystal data.^[44, 460] The diffractogram is measured using Cu- $K_{\alpha 1}$ radiation. Right: Raman spectrum of “ K_3CuGe_9 ” with best agreement to K_4Ge_9 .^[378]

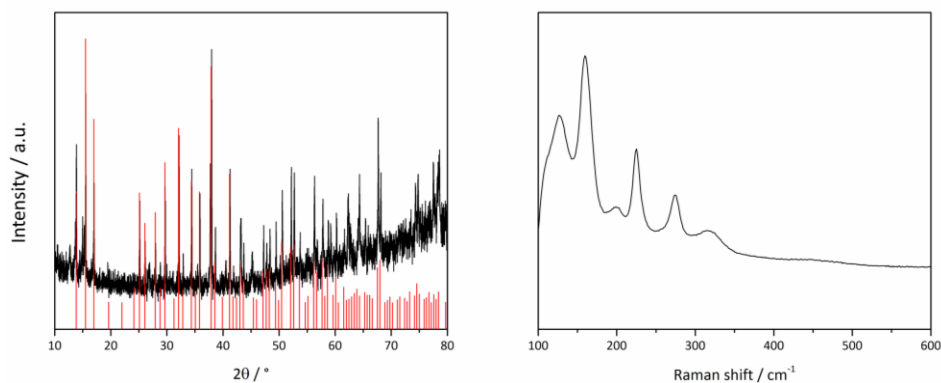


Figure 132: Left: X-ray powder diffractogram measured (black) “ $K_3Cu_3Ge_9$ ” and calculated (red) of K_4Ge_4 . The calculated diffractogram is based on single crystal data.^[442] The diffractogram is measured using Cu- $K_{\alpha 1}$ radiation. Right: Raman spectrum of “ $K_3Cu_3Ge_9$ ” with best agreement to $K_{12}Ge_{17}$.^[378]

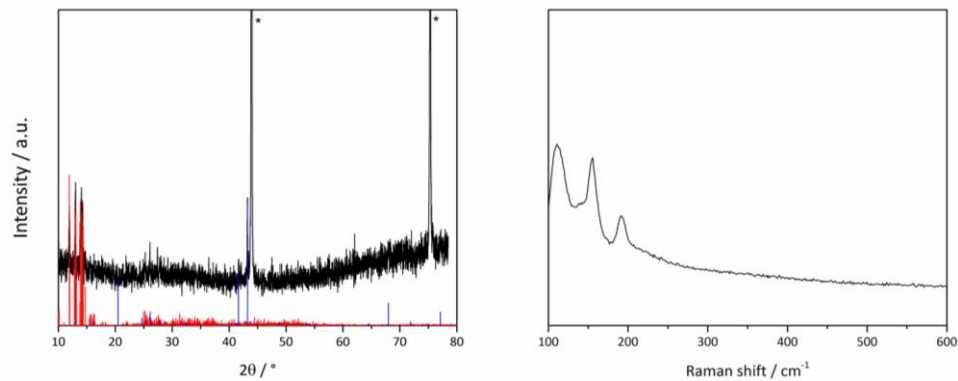


Figure 133: Left: X-ray powder diffractogram measured (black) “ K_3CuSn_9 ”, calculated (red) of $K_{12}Sn_{17}$ and calculated (blue) of Cu_3Sn . The calculated diffractogram is based on single crystal data.^[451, 461] The diffractogram is measured using Cu- $K_{\alpha 1}$ radiation. * - Diamond. Right: Raman spectrum of solid state phase with the nominal composition of “ K_3CuSn_9 ” with best agreement to $K_{12}Sn_{17}$.^[43]

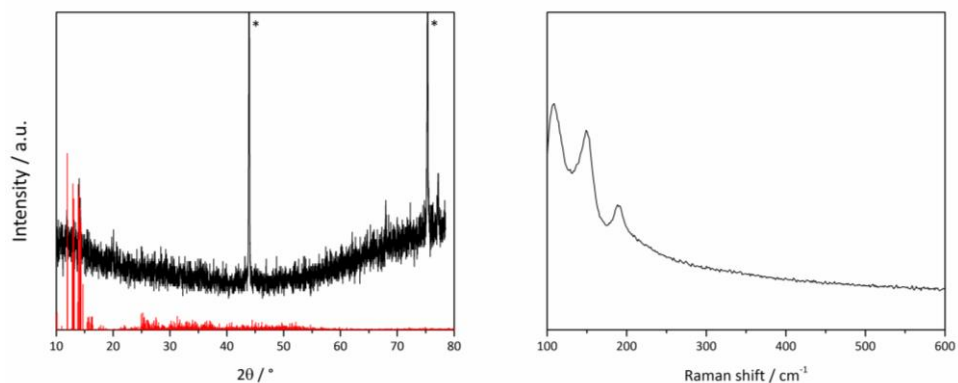


Figure 134: Left: X-ray powder diffractogram measured (black) “ $K_3Cu_2Sn_9$ ” and calculated (red) of $K_{12}Sn_{17}$. The calculated diffractogram is based on single crystal data.^[451] The diffractogram is measured using Cu- $K_{\alpha 1}$ radiation. * - Diamond. Right: Raman spectrum of solid state phase with the nominal composition of “ $K_3Cu_2Sn_9$ ” with best agreement to $K_{12}Sn_{17}$.^[43]

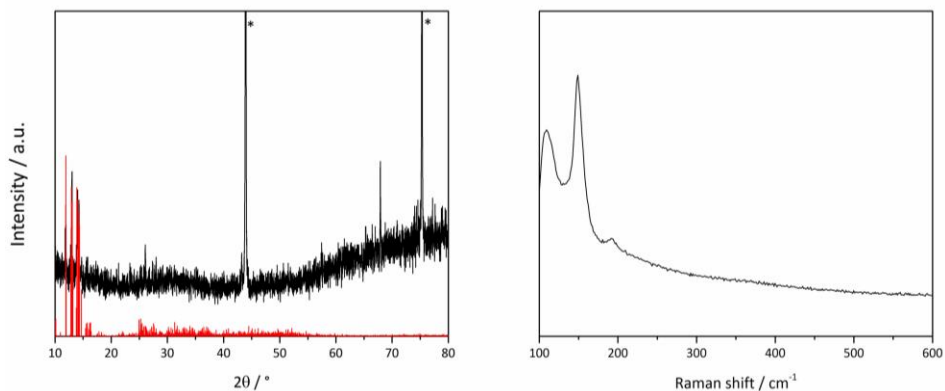


Figure 135: Left: X-ray powder diffractogram measured (black) “ $\text{K}_3\text{Cu}_3\text{Sn}_9$ ” and calculated (red) of $\text{K}_{12}\text{Sn}_{17}$. The calculated diffractogram is based on single crystal data.^[451] The diffractogram is measured using Cu- $\text{K}\alpha_1$ radiation. * - Diamond. Right: Raman spectrum of solid state phase with the nominal composition of “ $\text{K}_3\text{Cu}_3\text{Sn}_9$ ” with best agreement to $\text{K}_{12}\text{Sn}_{17}$.^[43]

7.3.6. ESI-MS spectra

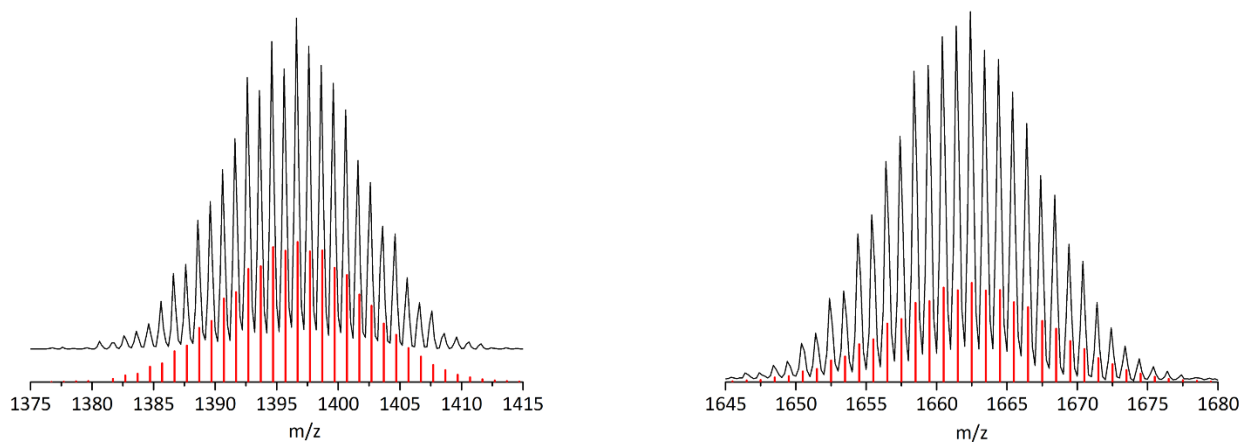


Figure 136: ESI-MS Analysis of the reaction between “ $\text{Cs}_4\text{Ag}_{1.5}\text{Ge}_9$ ” and $[\text{Si}(\text{SiMe}_3)_3]\text{Cl}$. Left: negative mass spectrum of $[\text{Ge}_9(\text{Si}(\text{SiMe}_3)_3)_3]^-$. Right: positive mass spectrum of $\text{Cs}_2[\text{Ge}_9(\text{Si}(\text{SiMe}_3)_3)_3]^+$.

7.3.7. Density functional theory calculations

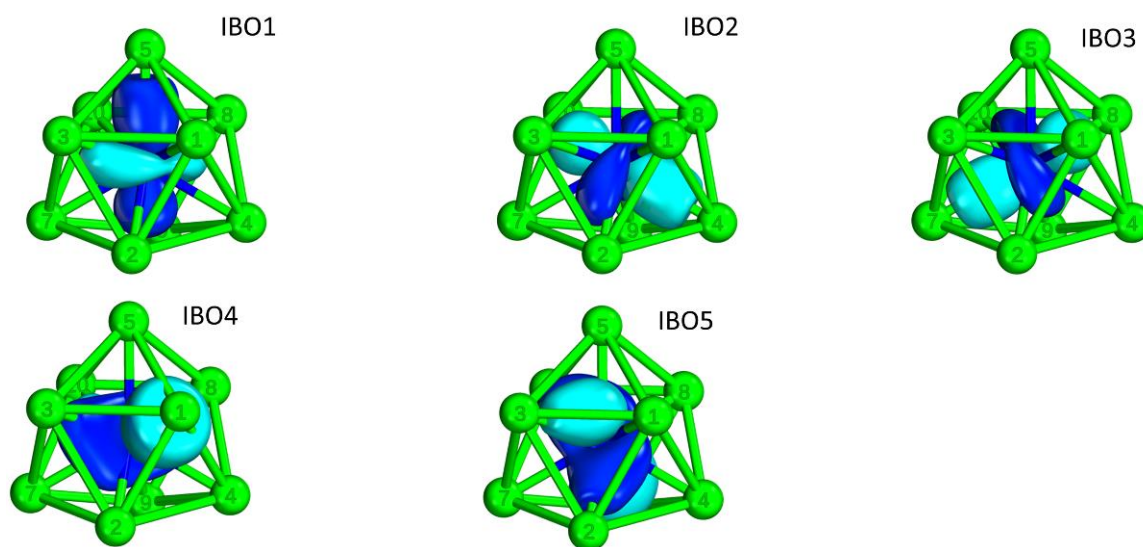


Figure 137: Intrinsic bond orbitals of the central Co^- of $[\text{Co}@\text{Ge}_9]^{5-}$. Co and Ge are shown in blue and light green, respectively.

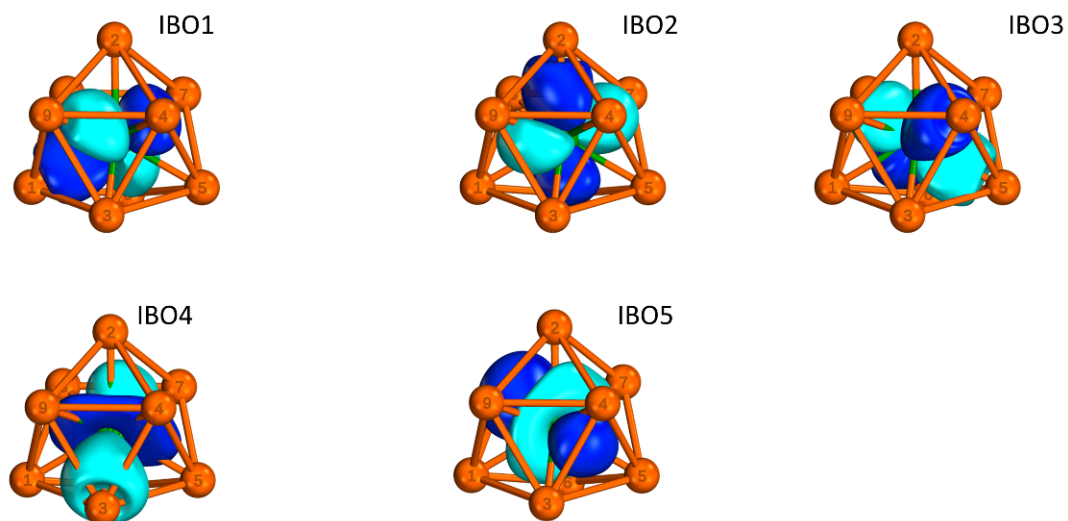


Figure 138: Intrinsic bond orbitals of the central Ru^- of $[\text{Ru}@\text{Sn}_9]^{6-}$. Ru and Sn are shown in dark green and orange, respectively.

7.3.8. Dynamic scanning calorimetry

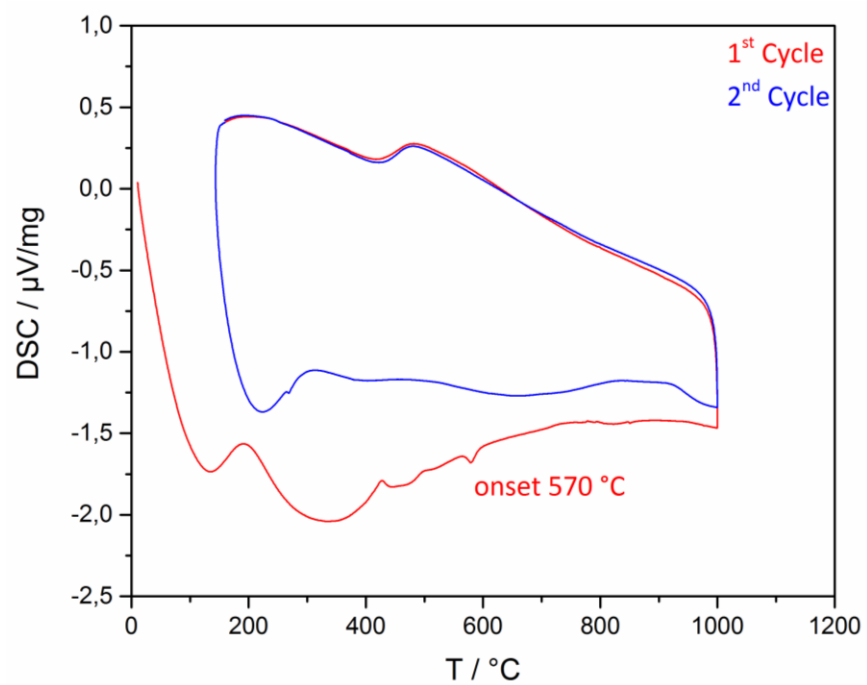


Figure 139: DSC analysis of filtrated $\text{K}_{12}\text{Si}_{17}$ between RT and 1000 $^{\circ}\text{C}$.

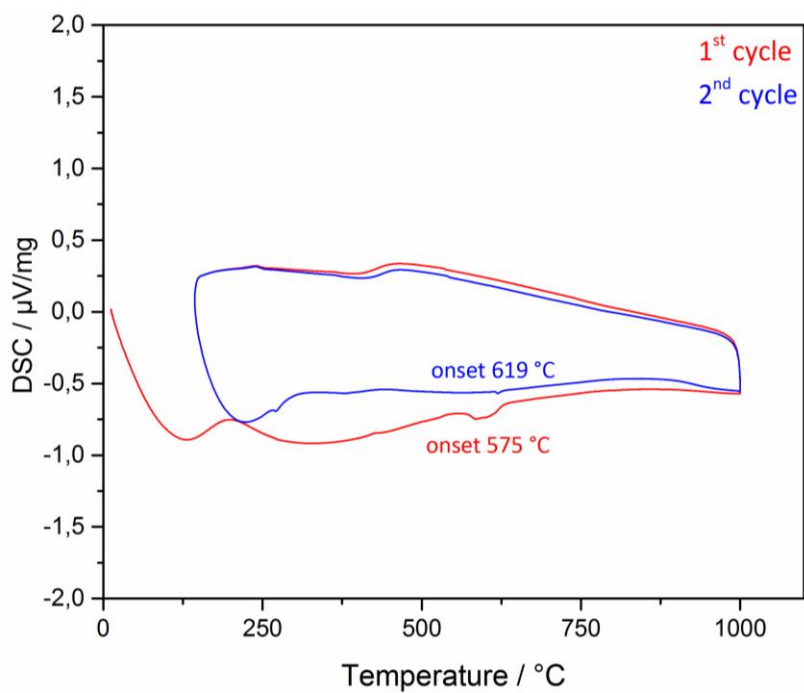


Figure 140: DSC analysis of the residue of the filtration of $\text{K}_{12}\text{Si}_{17}$ between RT and 1000 $^{\circ}\text{C}$.

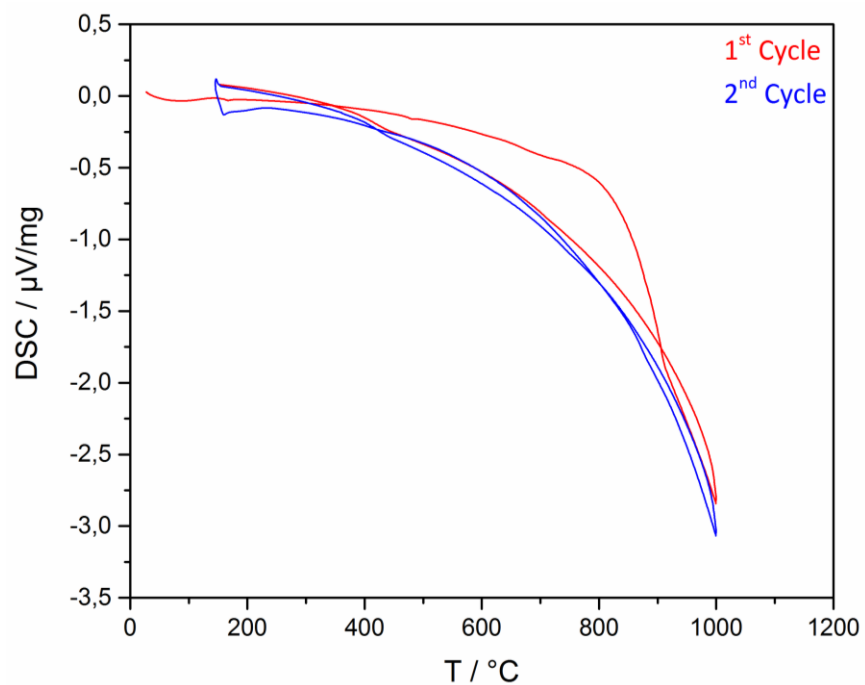


Figure 141: DSC analysis of filtrated K_4Ge_9 between RT and 1000 $^{\circ}\text{C}$.

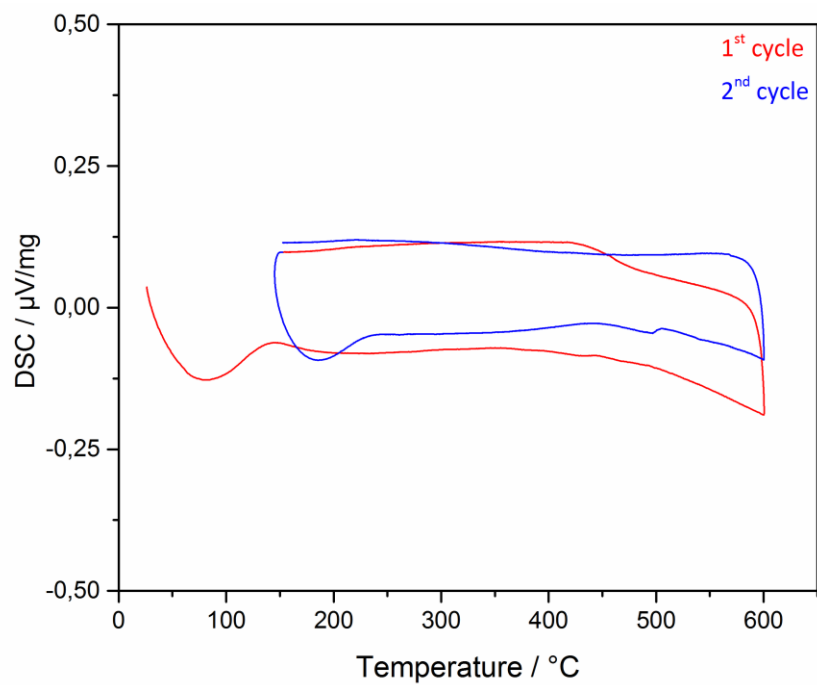


Figure 142: DSC analysis of the residue of the filtration of K_4Ge_9 between RT and 600 $^{\circ}\text{C}$.

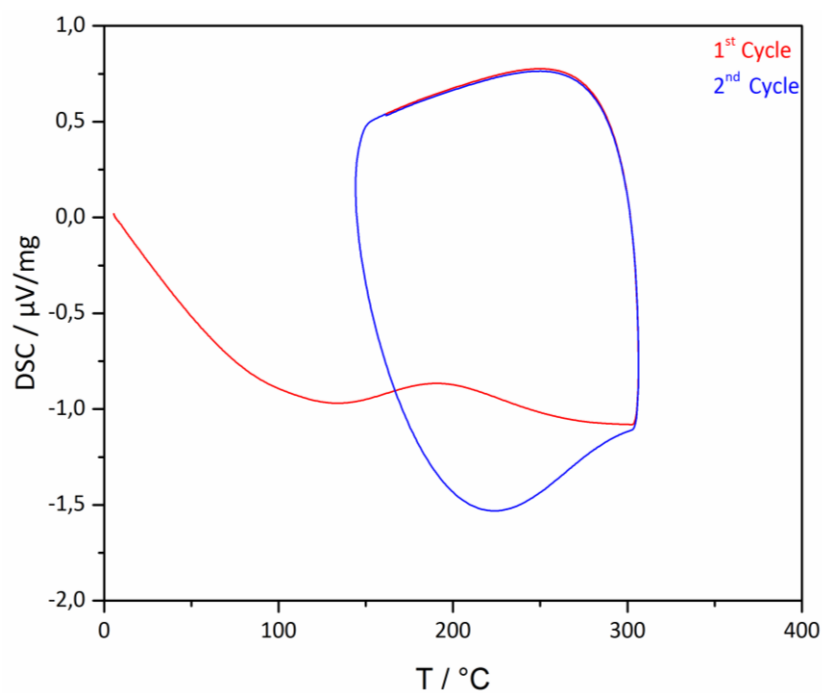


Figure 143: DSC analysis of lithiated $\text{K}_{12}\text{Si}_{17}$ from RT to 300 $^{\circ}\text{C}$.

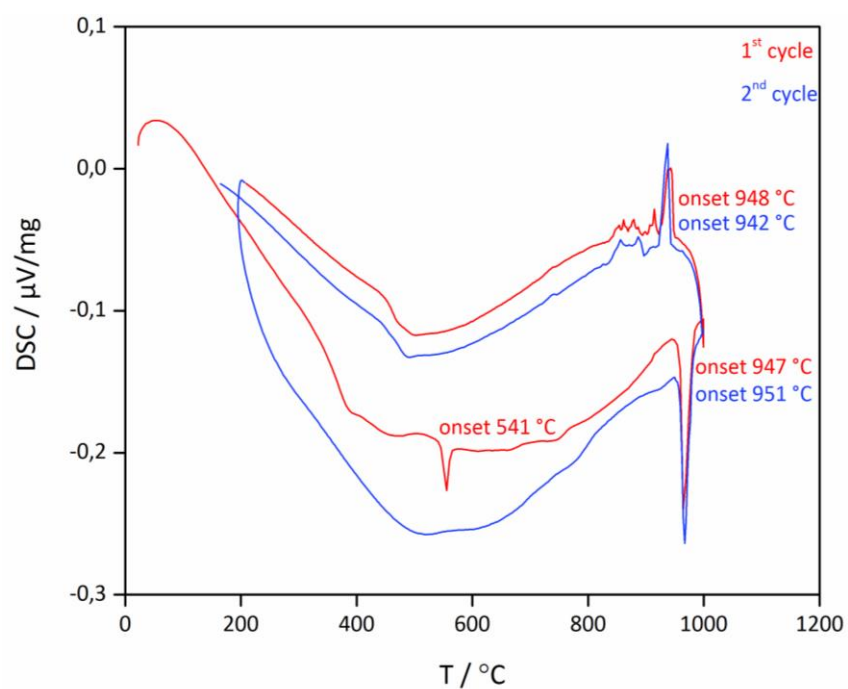


Figure 144: DSC analysis of “K₅Co_{1.2}Ge₉” between room temperature and 1000 °C.

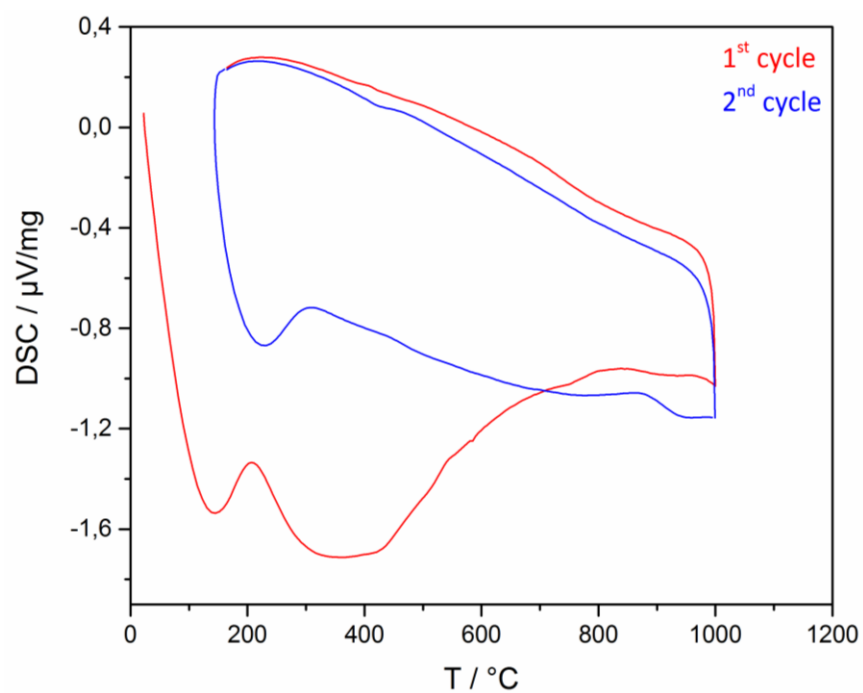


Figure 145: DSC analysis of “K₄Ru₃Sn₇” between room temperature and 1000 °C.

7.4. Crystallographic data and structure refinement of new compounds

The following section contains all crystallographic data and parameters of structural refinements of all new compounds. For compounds with a wR_2 value of below 30 additionally atomic coordinates, occupation where applicable and atomic displacement parameters data is given.

7.4.1. $[\text{Li}(\text{B12crown4})_2][\text{Ge}_9(\text{Si}(\text{SiMe}_3)_3)_3]$

Table 53: Crystallographic data and structure refinement of $(\text{Li}(\text{B12C4})_2)[\text{Ge}_9(\text{Si}(\text{SiMe}_3)_3)_3]$.

	$(\text{Li}(\text{B12C4})_2)[\text{Ge}_9(\text{Si}(\text{SiMe}_3)_3)_3]$
Sum formula	$\text{H}_{113}\text{LiC}_{51}\text{O}_8\text{Si}_{12}\text{Ge}_9$
Molecular weight [g/mol]	1851.74
Crystal system	triclinic
Space group	P-1
a [Å]	15.727(3)
b [Å]	16.960(3)
c [Å]	17.289(4)
α [°]	85.33(3)
β [°]	88.47(3)
γ [°]	65.50(3)
V [Å ³]	4182.2(14)
Z	2
T [K]	100(1)
μ [mm ⁻¹]	3.398
Measured reflections	69139
hkl ranges	-19 < h < 18 -20 < k < 20 -21 < l < 21
θ min. / max.	2.31 °; 26 °
Rint	0.0581
Independent reflections	16424
Reflections ($I > 2 \sigma$)	10900
Parameters	757
R_1 ($I > 2 \sigma$; all)	0.0441; 0.0774
wR_2 ($I > 2 \sigma$; all)	0.1010; 0.1165
GooF	0.956
max. / min. residual e- density [e/Å ³]	0.542; -0.539

Table 54: Fractional atomic coordinates and isotropic or equivalent isotropic displacement parameters of $(\text{Li}(\text{B}_{12}\text{C}_4)_2)[\text{Ge}_9(\text{Si}(\text{SiMe}_3)_3)_3]$.

	x	y	z	Uiso*/Ueq
Ge1	0.49192 (4)	0.86095 (4)	0.18158 (3)	0.05237 (14)
Si1	0.30468 (10)	0.75743 (9)	0.24190 (8)	0.0463 (3)
Ge2	0.48521 (4)	0.87623 (4)	0.33176 (4)	0.05281 (14)
Si2	0.18524 (10)	0.89728 (10)	0.25141 (10)	0.0569 (4)
Ge3	0.64379 (4)	0.85423 (4)	0.25478 (3)	0.05042 (14)
Si3	0.30928 (12)	0.72051 (11)	0.11351 (9)	0.0588 (4)
Ge4	0.45151 (4)	0.75703 (4)	0.27604 (4)	0.05097 (14)
Si4	0.27169 (10)	0.65474 (10)	0.32192 (9)	0.0505 (3)
Ge5	0.65315 (4)	0.74252 (4)	0.16194 (3)	0.04993 (14)
Si5	0.74809 (9)	0.74971 (9)	0.47920 (8)	0.0440 (3)
Ge9	0.73080 (4)	0.64672 (3)	0.28204 (3)	0.04725 (13)
Si9	0.74502 (10)	0.72423 (9)	0.04756 (8)	0.0466 (3)
Ge8	0.58151 (4)	0.64557 (3)	0.36237 (3)	0.04657 (13)
Si8	0.88807 (11)	0.75139 (11)	0.43020 (10)	0.0574 (4)
Ge7	0.58605 (4)	0.63613 (4)	0.21172 (3)	0.05089 (14)
Si7	0.78043 (10)	0.62068 (9)	0.55684 (9)	0.0513 (3)
Ge6	0.64334 (4)	0.75964 (3)	0.37762 (3)	0.04782 (13)
Si6	0.67730 (10)	0.86768 (9)	0.55553 (9)	0.0473 (3)
Si10	0.67781 (12)	0.85213 (10)	-0.03424 (9)	0.0548 (4)
Si11	0.89943 (11)	0.69811 (11)	0.07865 (10)	0.0581 (4)
Si12	0.73664 (12)	0.60648 (10)	-0.00876 (10)	0.0602 (4)

Table 55: Atomic displacement parameters of heavy elements of $(\text{Li}(\text{B12C4})_2)[\text{Ge}_9(\text{Si}(\text{SiMe}_3)_3)_3]$.

	U^{11}	U^{22}	U^{33}	U^{12}	U^{13}	U^{23}
Ge1	0.0439 (3)	0.0595 (3)	0.0512 (3)	-0.0200 (2)	-0.0022 (2)	0.0024 (3)
Si1	0.0409 (7)	0.0552 (8)	0.0461 (8)	-0.0232 (6)	-0.0003 (6)	-0.0035 (6)
Ge2	0.0437 (3)	0.0574 (3)	0.0566 (3)	-0.0186 (2)	0.0059 (2)	-0.0150 (3)
Si2	0.0421 (8)	0.0593 (9)	0.0664 (10)	-0.0191 (6)	-0.0008 (7)	0.0010 (7)
Ge3	0.0500 (3)	0.0536 (3)	0.0540 (3)	-0.0278 (2)	0.0022 (3)	-0.0047 (2)
Si3	0.0578 (9)	0.0777 (10)	0.0462 (9)	-0.0330 (8)	-0.0021 (7)	-0.0058 (7)
Ge4	0.0397 (3)	0.0519 (3)	0.0637 (4)	-0.0216 (2)	-0.0033 (2)	-0.0016 (3)
Si4	0.0498 (8)	0.0575 (8)	0.0510 (8)	-0.0290 (7)	-0.0013 (6)	-0.0028 (7)
Ge5	0.0514 (3)	0.0520 (3)	0.0446 (3)	-0.0199 (2)	0.0085 (2)	-0.0043 (2)
Si5	0.0397 (7)	0.0481 (7)	0.0470 (8)	-0.0200 (6)	0.0014 (6)	-0.0088 (6)
Ge9	0.0406 (3)	0.0525 (3)	0.0468 (3)	-0.0171 (2)	0.0007 (2)	-0.0069 (2)
Si9	0.0465 (8)	0.0500 (7)	0.0446 (8)	-0.0212 (6)	0.0060 (6)	-0.0058 (6)
Ge8	0.0464 (3)	0.0542 (3)	0.0430 (3)	-0.0249 (2)	0.0003 (2)	-0.0025 (2)
Si8	0.0433 (8)	0.0768 (10)	0.0585 (10)	-0.0294 (7)	0.0073 (7)	-0.0174 (8)
Ge7	0.0519 (3)	0.0618 (3)	0.0470 (3)	-0.0303 (3)	0.0037 (2)	-0.0120 (3)
Si7	0.0507 (8)	0.0479 (7)	0.0563 (9)	-0.0211 (6)	-0.0063 (7)	-0.0041 (6)
Ge6	0.0489 (3)	0.0505 (3)	0.0466 (3)	-0.0223 (2)	-0.0024 (2)	-0.0077 (2)
Si6	0.0471 (8)	0.0489 (7)	0.0484 (8)	-0.0216 (6)	0.0048 (6)	-0.0097 (6)
Si10	0.0672 (10)	0.0528 (8)	0.0441 (8)	-0.0248 (7)	0.0027 (7)	-0.0031 (6)
Si11	0.0459 (8)	0.0715 (10)	0.0582 (10)	-0.0251 (7)	0.0071 (7)	-0.0097 (8)
Si12	0.0693 (10)	0.0535 (8)	0.0610 (10)	-0.0272 (8)	0.0104 (8)	-0.0153 (7)

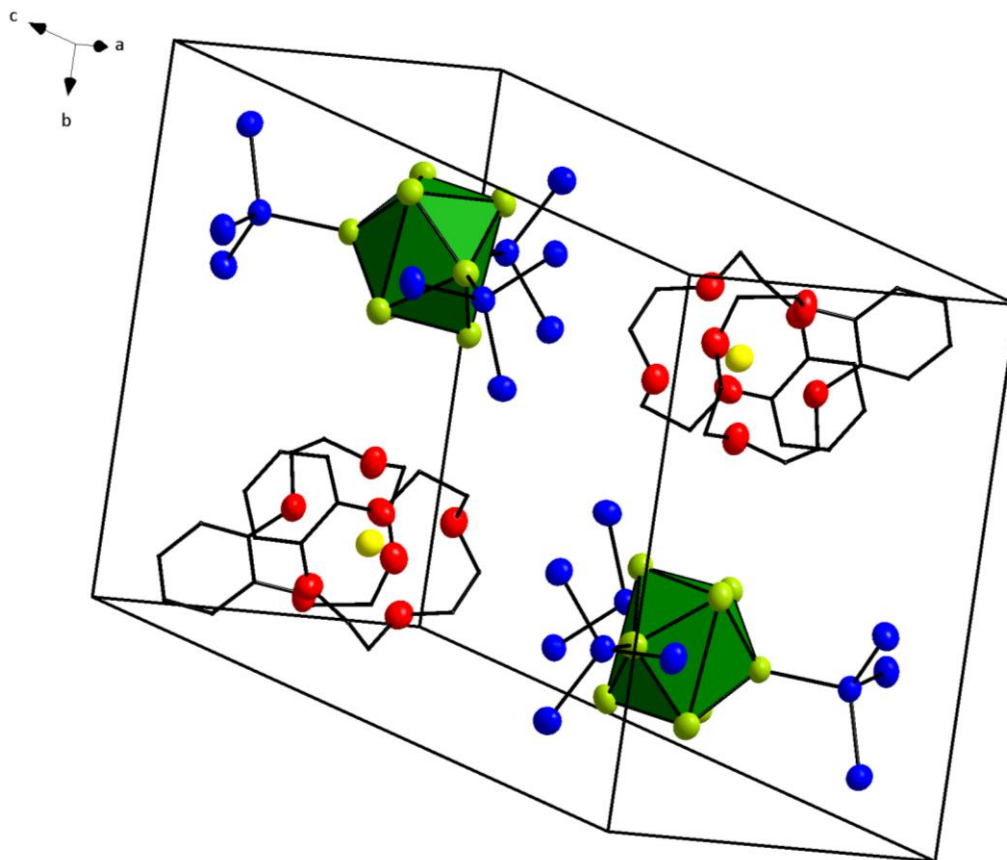


Figure 146: $[\text{Ge}_9(\text{Si}(\text{SiMe}_3)_3)_3]^-$ clusters (green polyhedra) and lithium ions in a sandwich configuration in $(\text{Li}(\text{B}_{12}\text{C}_4)_2)[\text{Ge}_9(\text{Si}(\text{SiMe}_3)_3)_3]$. Carbon is displayed as wire and sticks. Displacement ellipsoids are displayed with a 50 % probability. Methylgroups and H atoms are omitted for clarity. Green – germanium, light blue – silicon, red – oxygen, yellow – lithium.

7.4.2. $\text{Li}_4\text{Sn}_9 \cdot 17 \text{NH}_3$

Table 56: Crystallographic data and structure refinement of $\text{Li}_4\text{Sn}_9 \cdot 17 \text{NH}_3$.

	$\text{Li}_4\text{Sn}_9 \cdot 17 \text{NH}_3$
Sum formula	$\text{H}_{51}\text{Li}_4\text{N}_{17}\text{Sn}_9$
Molecular weight [g/mol]	1385.54
Crystal system	monoclinic
Space group	$P2_1/c$
a [Å]	10.5437(6)
b [Å]	17.6580(12)
c [Å]	21.2368(14)
α [°]	90
β [°]	98.921(6)
γ [°]	90
V [Å ³]	3906.1(4)
Z	4
T [K]	153(2)
μ [mm ⁻¹]	5.670
Measured reflections	74332
hkl ranges	-13 < h < 13 -21 < k < 21 -26 < l < 26
2 θ min. / max.	2.962 °; 25.997 °
Rint	0.1224
Independent reflections	7646
Reflections ($I > 2 \sigma$)	4850
Parameters	290
R_1 ($I > 2 \sigma$; all)	0.0335; 0.0766
wR_2 ($I > 2 \sigma$; all)	0.0667; 0.0729
GooF	0.862
max. / min. residual e- density	0.987; -1.097

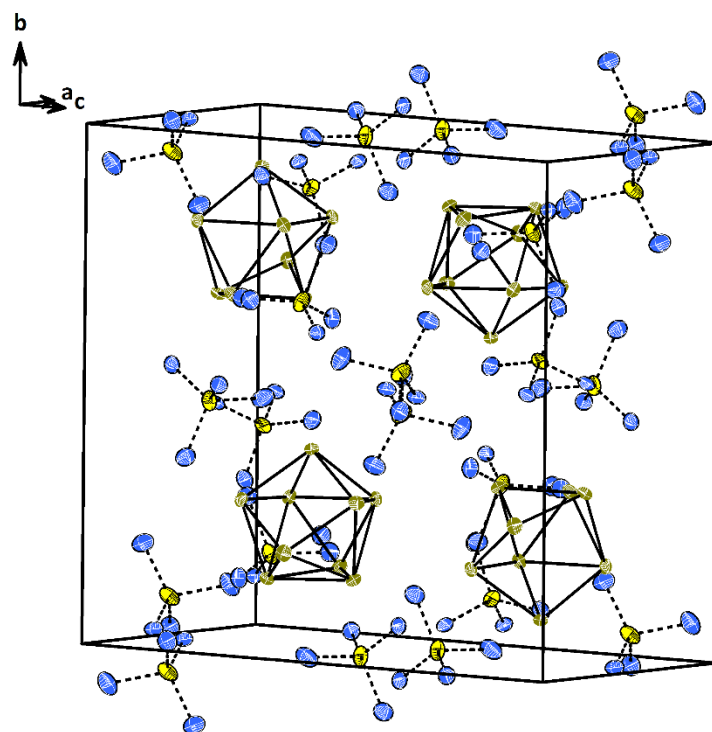


Figure 147: Extended unit cell of $\text{Li}_4\text{Sn}_9 \cdot 17 \text{NH}_3$. Displacement ellipsoids are displayed with a 50% probability. Protons are omitted for clarity. Green – tin, yellow – lithium, blue – nitrogen.

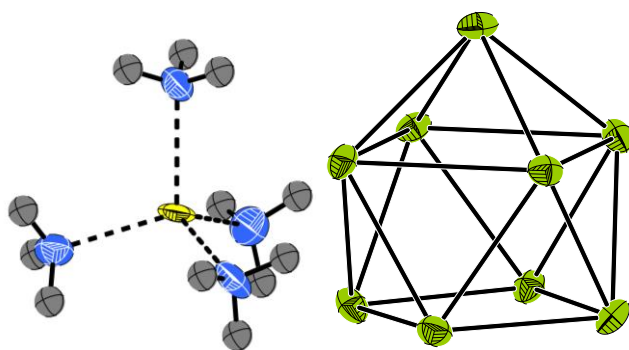


Figure 148: Structural units in $\text{Li}_4\text{Sn}_9 \cdot 17 \text{NH}_3$; left: $[\text{Sn}_9]^{4-}$ cluster; right: Li ion tetrahedrally coordinated by four ammonia molecules. Displacement ellipsoids are displayed with a 50% probability. Green – germanium, blue – nitrogen, grey – protons, yellow – lithium.

Table 57: Fractional atomic coordinates and isotropic or equivalent isotropic displacement parameters of $\text{Li}_4\text{Sn}_9 \cdot 17 \text{NH}_3$.

	x	y	z	Uiso*/Ueq
Sn1	0.44142 (5)	0.15930 (3)	0.39057 (3)	0.02951 (14)
Sn2	0.43772 (4)	0.29602 (3)	0.46946 (3)	0.02697 (13)
Sn3	0.33719 (4)	0.29353 (3)	0.32015 (2)	0.02547 (13)
Sn4	0.16781 (5)	0.14436 (3)	0.33702 (3)	0.02786 (13)
Sn5	0.26938 (5)	0.14780 (3)	0.48648 (2)	0.02560 (13)
Sn6	0.01336 (5)	0.20556 (3)	0.43130 (3)	0.03033 (14)
Sn7	0.19187 (5)	0.30126 (3)	0.51963 (3)	0.02805 (13)
Sn8	0.22873 (5)	0.39628 (3)	0.40856 (3)	0.02880 (13)
Sn9	0.05603 (4)	0.29856 (3)	0.32110 (3)	0.02643 (13)

Table 58: Atomic displacement parameters of heavy elements of $\text{Li}_4\text{Sn}_9 \cdot 17 \text{NH}_3$.

	U^{11}	U^{22}	U^{33}	U^{12}	U^{13}	U^{23}
Sn1	0.0256 (3)	0.0321 (3)	0.0323 (3)	0.0107 (2)	0.0091 (2)	0.0045 (3)
Sn2	0.0183 (2)	0.0319 (3)	0.0289 (3)	-0.0025 (2)	-0.0022 (2)	0.0003 (3)
Sn3	0.0210 (3)	0.0313 (3)	0.0249 (3)	0.0023 (2)	0.0060 (2)	0.0067 (3)
Sn4	0.0314 (3)	0.0223 (3)	0.0290 (3)	-0.0016 (2)	0.0018 (2)	-0.0041 (3)
Sn5	0.0289 (3)	0.0222 (3)	0.0265 (3)	0.0047 (2)	0.0069 (2)	0.0058 (2)
Sn6	0.0186 (3)	0.0390 (3)	0.0344 (3)	-0.0044 (2)	0.0073 (2)	0.0034 (3)
Sn7	0.0316 (3)	0.0264 (3)	0.0278 (3)	0.0021 (2)	0.0098 (2)	-0.0032 (3)
Sn8	0.0352 (3)	0.0188 (3)	0.0307 (3)	0.0025 (2)	-0.0002 (2)	0.0004 (3)
Sn9	0.0181 (2)	0.0286 (3)	0.0308 (3)	0.0013 (2)	-0.0017 (2)	0.0043 (3)

7.4.3. $\text{K}_6[\text{OH}][\text{Co}@\text{Ge}_9] \cdot 16 \text{NH}_3$

Table 59: Crystallographic data and structure refinement of $\text{K}_6[\text{OH}][\text{Co}@\text{Ge}_9] \cdot 16 \text{NH}_3$.

	$\text{K}_6[\text{OH}][\text{Co}@\text{Ge}_9] \cdot 16 \text{NH}_3$
Sum formula	$\text{CoGe}_9\text{H}_{49}\text{K}_6\text{N}_{16}\text{O}$
molecular weight [g/mol]	1236.39
crystal system	orthorhombic
space group	Pnma
a [Å]	25.463(2)
b [Å]	15.7469(12)
c [Å]	10.0509(11)
V [Å ³]	4030.1(6)
Z	4
T [K]	150(2)
μ [mm ⁻¹]	7.653
measured reflections	71159
hkl ranges	-31 < h < 31 -19 < k < 19 -12 < l < 12
2 θ range	4.36 - 52.0
R_{int}	0.1584
independent reflections	4111
reflections with $I > 2\sigma$	2992
parameters	170
R_1 ($I > 2\sigma$; all)	0.0425; 0.0675
wR_2 ($I > 2\sigma$; all)	0.0978; 0.1124
GooF	1.040
max. / min. residual electron density [e/Å ³]	1.13 / -1.11

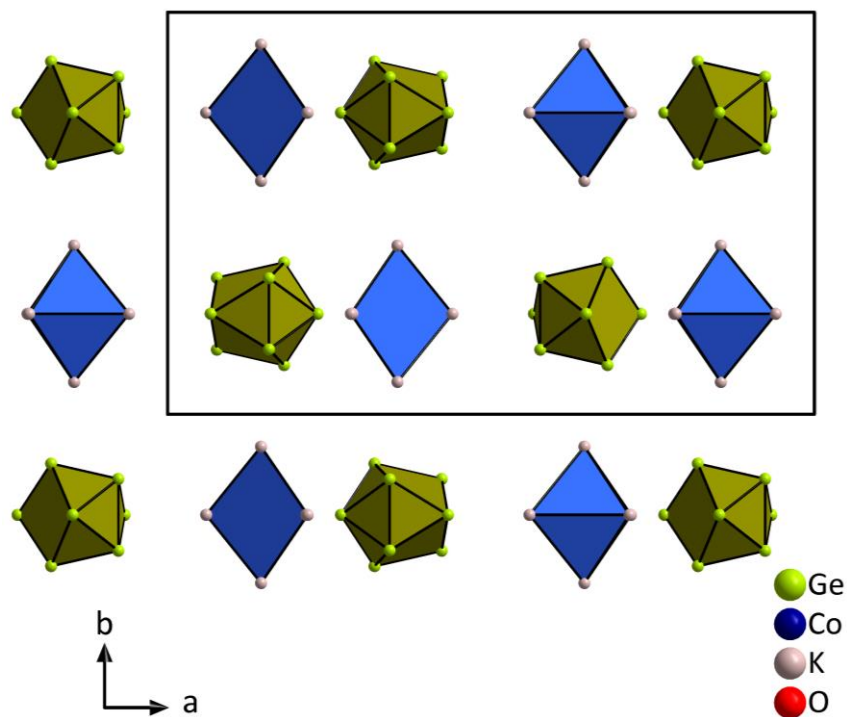


Figure 149: $[\text{K}_6(\text{OH})]^{5+}$ groups (blue pyramids) and $[\text{Co}@\text{Ge}_9]^{5-}$ clusters (green polyhedra) in $\text{K}_6(\text{OH})[\text{Co}@\text{Ge}_9] \cdot 16 \text{NH}_3$. N and H atoms are omitted for clarity.

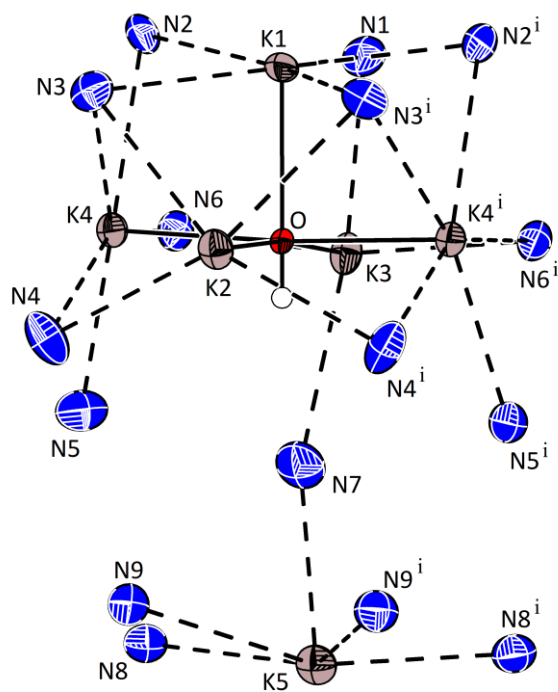


Figure 150: K atoms and ammonia molecules in $\text{K}_6(\text{OH})[\text{Co}@\text{Ge}_9] \cdot 16 \text{NH}_3$. Displacement ellipsoids are drawn at a 50 % probability level. H Atoms are omitted for clarity.

Table 60: Fractional atomic coordinates and isotropic or equivalent isotropic displacement parameters of $\text{K}_6[\text{OH}][\text{Co@Ge}_9] \cdot 16 \text{NH}_3$.

	x	y	z	Uiso*/Ueq
Ge1	0.23186 (4)	0.2500	0.62098 (8)	0.0239 (2)
Ge2	0.18006 (3)	0.12263 (4)	0.50183 (7)	0.03022 (19)
Ge3	0.14702 (4)	0.2500	0.33795 (8)	0.0292 (2)
Ge4	0.07624 (3)	0.16076 (4)	0.47947 (7)	0.03068 (19)
Ge5	0.15669 (3)	0.16156 (5)	0.75976 (6)	0.0308 (2)
Ge6	0.06657 (4)	0.2500	0.70690 (9)	0.0261 (2)
Co	0.14121 (4)	0.2500	0.57259 (9)	0.0123 (2)
K1	0.28586 (8)	0.2500	-0.07150 (18)	0.0280 (4)
K2	0.28349 (9)	0.2500	0.29438 (19)	0.0299 (5)
K3	0.44039 (8)	0.2500	-0.0545 (2)	0.0287 (4)
K4	0.35548 (5)	0.08041 (8)	0.10160 (13)	0.0244 (3)
K5	0.57682 (9)	0.2500	0.45043 (19)	0.0325 (5)

Table 61: Atomic displacement parameters of heavy elements of $\text{K}_6[\text{OH}][\text{Co@Ge}_9] \cdot 16 \text{NH}_3$.

	U^{11}	U^{22}	U^{33}	U^{12}	U^{13}	U^{23}
Ge1	0.0154 (5)	0.0362 (5)	0.0200 (4)	0.000	-0.0012 (3)	0.000
Ge2	0.0325 (4)	0.0149 (3)	0.0432 (4)	0.0039 (3)	0.0091 (3)	-0.0050 (3)
Ge3	0.0313 (6)	0.0437 (6)	0.0125 (4)	0.000	0.0009 (4)	0.000
Ge4	0.0233 (4)	0.0314 (4)	0.0374 (4)	-0.0103 (3)	0.0013 (3)	-0.0135 (3)
Ge5	0.0296 (4)	0.0385 (4)	0.0243 (3)	0.0046 (3)	0.0016 (3)	0.0176 (3)
Ge6	0.0170 (5)	0.0416 (6)	0.0196 (4)	0.000	0.0045 (4)	0.000
Co	0.0142 (6)	0.0116 (5)	0.0112 (4)	0.000	0.0001 (4)	0.000
K1	0.0371 (12)	0.0238 (9)	0.0231 (9)	0.000	-0.0102 (8)	0.000
K2	0.0383 (13)	0.0279 (10)	0.0235 (9)	0.000	0.0064 (8)	0.000
K3	0.0225 (11)	0.0222 (9)	0.0415 (11)	0.000	0.0075 (8)	0.000
K4	0.0266 (8)	0.0197 (6)	0.0267 (6)	0.0013 (5)	0.0005 (5)	-0.0001 (5)
K5	0.0346 (12)	0.0386 (11)	0.0244 (9)	0.000	0.0065 (8)	0.000

7.4.4. $\text{K}_7[\text{OH}][\text{Ru}@\text{Sn}_9] \cdot 11 \text{NH}_3$

Table 62: Crystallographic data and structure refinement of $\text{K}_7[\text{OH}][\text{Ru}@\text{Sn}_9] \cdot 11 \text{NH}_3$.

	$\text{K}_7[\text{OH}][\text{Ru}@\text{Sn}_9] \cdot 11 \text{NH}_3$
Sum formula	$\text{K}_{14}\text{O}_2\text{Ru}_2\text{Sn}_{18}\text{N}_{20}\text{H}_{62}$
molecular weight [g/mol]	3260.65
crystal system	orthorhombic
space group	Pnma
a [Å]	36.970(7)
b [Å]	19.700(4)
c [Å]	10.370(2)
V [Å ³]	7553(3)
Z	4
T [K]	150(2)
μ [mm ⁻¹]	7.015
measured reflections	197829
hkl ranges	-45 < h < 45 -24 < k < 24 -12 < l < 12
2θ range	4.08 - 52.0
R_{int}	0.1102
independent reflections	7653
reflections with $I > 2\sigma$	6025
parameters	277
R_1 ($I > 2\sigma$; all)	0.0323; 0.0484
wR_2 ($I > 2\sigma$; all)	0.0762; 0.0821
GooF	1.038
max. / min. residual electron density [e/Å ³]	4.23 / -2.11

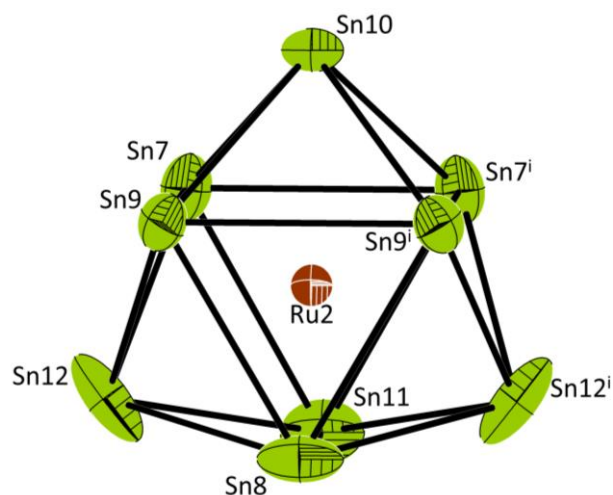


Figure 151: Endohedral cluster $[\text{Ru}@\text{Sn}_9]^{6-}$ (II). Displacement ellipsoids are drawn at 50 % probability level. Symmetry operations: (i) $x, 0.5-y, z$.

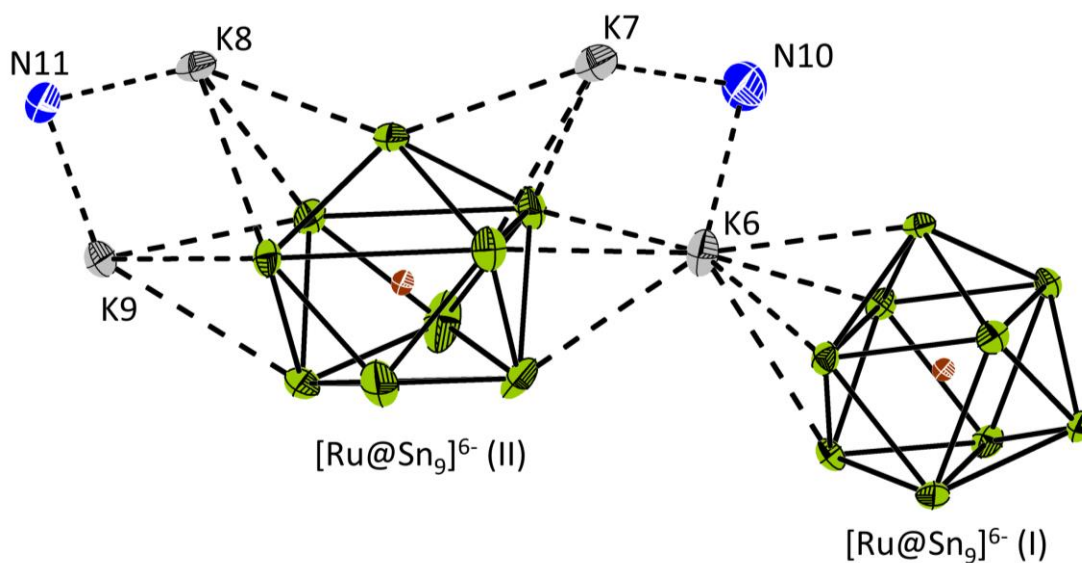


Figure 152: Partial coordination spheres of $[\text{Ru}@\text{Sn}_9]^{6-}$ (I) and $[\text{Ru}@\text{Sn}_9]^{6-}$ (II). Neighboring potassium atoms and ammonia molecules are displayed. Displacement ellipsoids are displayed with a 50 % probability. H atoms are omitted for clarity.

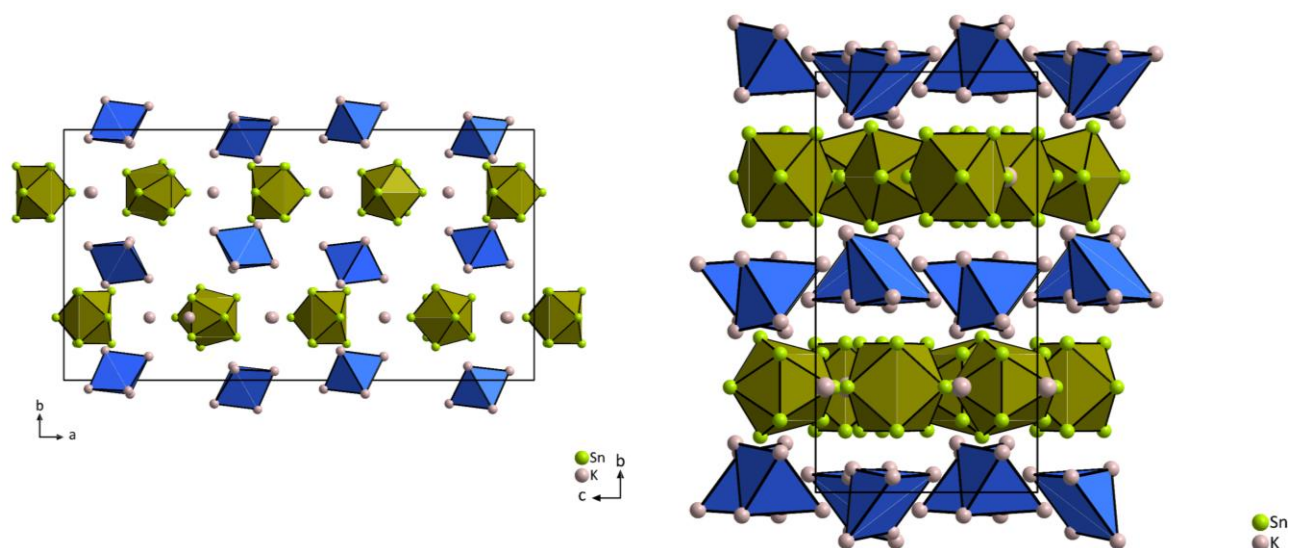


Figure 153: $[K_5(OH)]^{4+}$ groups (blue pyramids) and $[Ru@Sn_9]^{6-}$ clusters (green polyhedra) in $K_7(OH)[Ru@Sn_9] \cdot 10 NH_3$ with layered packing. K atoms which are not coordinated to the O atoms, are drawn as grey spheres. N and H atoms are omitted for clarity.

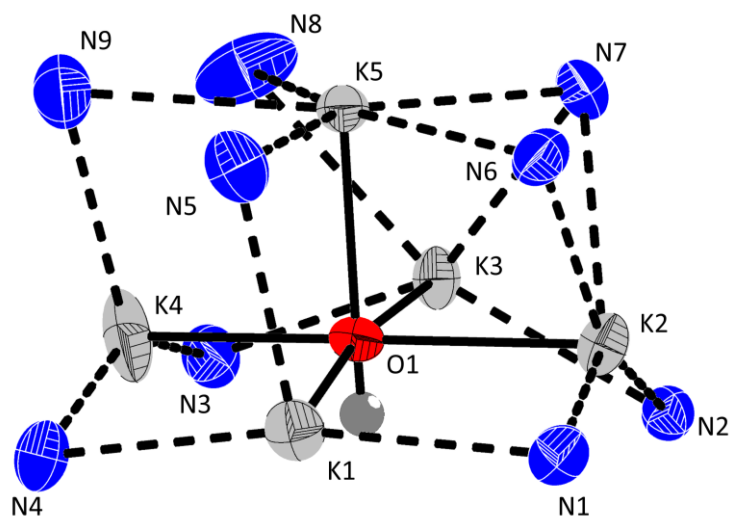


Figure 154: K atoms and ammonia molecules in $K_7(OH)[Ru@Sn_9] \cdot 11 NH_3$. Displacement ellipsoids are drawn at a 50 % probability level. H Atoms are omitted for clarity.

Table 63: Fractional atomic coordinates and isotropic or equivalent isotropic displacement parameters of $\text{K}_7[\text{OH}][\text{Ru}@\text{Sn}_9] \cdot 11 \text{NH}_3$.

	x	y	z	Uiso*/Ueq	Occ. (<1)
Sn1	0.02735 (2)	0.14766 (2)	0.49783 (4)	0.03438 (11)	
Sn2	0.03204 (2)	0.14670 (2)	0.80025 (4)	0.03418 (11)	
Sn3	0.10098 (2)	0.14553 (2)	0.63419 (4)	0.03266 (11)	
Sn4	0.08668 (2)	0.2500	0.41750 (6)	0.03495 (14)	
Sn5	-0.01673 (2)	0.2500	0.65977 (6)	0.03656 (15)	
Sn6	0.09286 (2)	0.2500	0.85791 (5)	0.03137 (13)	
Ru1	0.05379 (2)	0.2500	0.64487 (5)	0.01911 (12)	
Sn7	0.23790 (2)	0.2500	0.29456 (10)	0.0621 (3)	0.9391 (16)
Sn8	0.27161 (2)	0.17163 (2)	0.52802 (5)	0.04246 (16)	0.9391 (16)
Sn9	0.29040 (2)	0.13268 (4)	0.25036 (8)	0.0680 (3)	0.9391 (16)
Sn7B	0.2372 (4)	0.2500	0.4135 (19)	0.071 (4)	0.0609 (16)
Sn8B	0.2907 (3)	0.1325 (5)	0.4523 (13)	0.071 (4)	0.0609 (16)
Sn9B	0.2698 (5)	0.1682 (8)	0.1841 (12)	0.085 (4)	0.0609 (16)
Sn10	0.34115 (2)	0.2500	0.58220 (6)	0.04031 (16)	
Sn11	0.33191 (2)	0.2500	0.11488 (7)	0.0576 (2)	
Sn12	0.36654 (2)	0.17083 (2)	0.33885 (5)	0.03799 (11)	
Ru2	0.30759 (2)	0.2500	0.35743 (6)	0.02251 (13)	
K1	0.08820 (4)	0.38348 (8)	0.13821 (15)	0.0434 (3)	
K2	0.05256 (4)	0.53576 (8)	0.34720 (14)	0.0393 (3)	
K3	0.13650 (4)	0.54251 (7)	0.53074 (13)	0.0356 (3)	
K4	0.18034 (6)	0.40560 (11)	0.34151 (19)	0.0683 (6)	
K5	0.14083 (4)	0.55512 (6)	0.16705 (13)	0.0327 (3)	
K6	0.18226 (6)	0.2500	0.6416 (3)	0.0528 (6)	
K7	0.26607 (8)	0.2500	0.8629 (3)	0.0632 (7)	
K8	0.44060 (7)	0.2500	0.5416 (2)	0.0603 (7)	
K9	0.44452 (6)	0.2500	0.1556 (2)	0.0512 (6)	

Table 64: Atomic displacement parameters of heavy elements of $K_7[OH][Ru@Sn_9] \cdot 11 NH_3$.

	U^{11}	U^{22}	U^{33}	U^{12}	U^{13}	U^{23}
Sn1	0.0340 (2)	0.0328 (2)	0.0363 (2)	-0.00608 (17)	-0.00447 (17)	-0.01053 (17)
Sn2	0.0351 (2)	0.0339 (2)	0.0336 (2)	-0.00767 (17)	0.00218 (17)	0.01033 (17)
Sn3	0.0296 (2)	0.0284 (2)	0.0400 (2)	0.00857 (16)	0.00007 (17)	-0.00174 (17)
Sn4	0.0391 (3)	0.0403 (3)	0.0254 (3)	0.000	0.0093 (2)	0.000
Sn5	0.0195 (3)	0.0554 (4)	0.0348 (3)	0.000	0.0011 (2)	0.000
Sn6	0.0315 (3)	0.0366 (3)	0.0260 (3)	0.000	-0.0084 (2)	0.000
Ru1	0.0190 (3)	0.0183 (3)	0.0200 (3)	0.000	-0.0004 (2)	0.000
Sn7	0.0235 (4)	0.0907 (7)	0.0720 (6)	0.000	-0.0137 (4)	0.000
Sn8	0.0423 (3)	0.0322 (3)	0.0529 (3)	-0.0066 (2)	0.0129 (2)	0.0085 (2)
Sn9	0.0490 (4)	0.0662 (4)	0.0888 (5)	-0.0224 (3)	0.0167 (3)	-0.0525 (4)
Sn7B	0.059 (7)	0.063 (7)	0.092 (9)	0.000	0.028 (6)	0.000
Sn8B	0.053 (5)	0.058 (5)	0.100 (7)	-0.009 (4)	-0.011 (5)	0.047 (5)
Sn9B	0.102 (8)	0.089 (7)	0.063 (6)	-0.044 (6)	-0.003 (6)	-0.013 (5)
Sn10	0.0398 (3)	0.0527 (4)	0.0284 (3)	0.000	-0.0064 (3)	0.000
Sn11	0.0472 (4)	0.1012 (6)	0.0244 (3)	0.000	0.0024 (3)	0.000
Sn12	0.0337 (2)	0.0346 (2)	0.0456 (3)	0.01167 (17)	0.00387 (18)	-0.00044 (19)
Ru2	0.0194 (3)	0.0230 (3)	0.0251 (3)	0.000	0.0005 (2)	0.000
K1	0.0447 (8)	0.0408 (8)	0.0446 (8)	-0.0019 (6)	-0.0055 (6)	-0.0082 (6)
K2	0.0312 (7)	0.0505 (8)	0.0361 (7)	0.0002 (6)	0.0001 (5)	-0.0063 (6)
K3	0.0324 (7)	0.0400 (7)	0.0344 (7)	0.0068 (5)	-0.0045 (5)	-0.0059 (5)
K4	0.0741 (13)	0.0732 (12)	0.0576 (11)	0.0473 (10)	-0.0052 (9)	-0.0026 (9)
K5	0.0326 (6)	0.0306 (6)	0.0348 (7)	-0.0021 (5)	0.0007 (5)	0.0026 (5)
K6	0.0373 (11)	0.0466 (12)	0.0745 (16)	0.000	0.0102 (11)	0.000
K7	0.0545 (15)	0.0767 (18)	0.0583 (16)	0.000	-0.0126 (12)	0.000
K8	0.0449 (13)	0.096 (2)	0.0402 (12)	0.000	-0.0136 (10)	0.000
K9	0.0421 (12)	0.0754 (16)	0.0360 (11)	0.000	0.0083 (9)	0.000

7.4.5. $C_{100}H_{200}K_8N_{10}O_{20}Rh_4Sn_{36}$

Table 65: Crystallographic data and structure refinement of $C_{100}H_{200}K_8N_{10}O_{20}Rh_4Sn_{36}$.

Sum formula	$C_{100}H_{200}K_8N_{10}O_{20}Rh_4Sn_{36}$
molecular weight [g/mol]	6859.97
crystal system	Tetragonal
space group	I4/mmm
a [Å]	11.4328(8)
b [Å]	11.4328(8)
c [Å]	46.513(5)
α [°]	90
β [°]	90
γ [°]	90
V [Å ³]	6079.7(10)
Z	2
T [K]	120
μ [mm ⁻¹]	8.107
measured reflections	139774
	$-19 < h < 18$
hkl ranges	$-19 < k < 18$
	$-78 < l < 78$
2θ range	1.834 / 37.054
R_{int}	0.2721
independent reflections	4362
reflections with $I > 2\sigma$	1780
parameters	63
R_1 ($I > 2\sigma$; all)	0.1235; 0.2540
wR_2 ($I > 2\sigma$; all)	0.2849; 0.3311
GooF	1.496
max. / min. residual electron density [e/Å ³]	19.361/-5.676

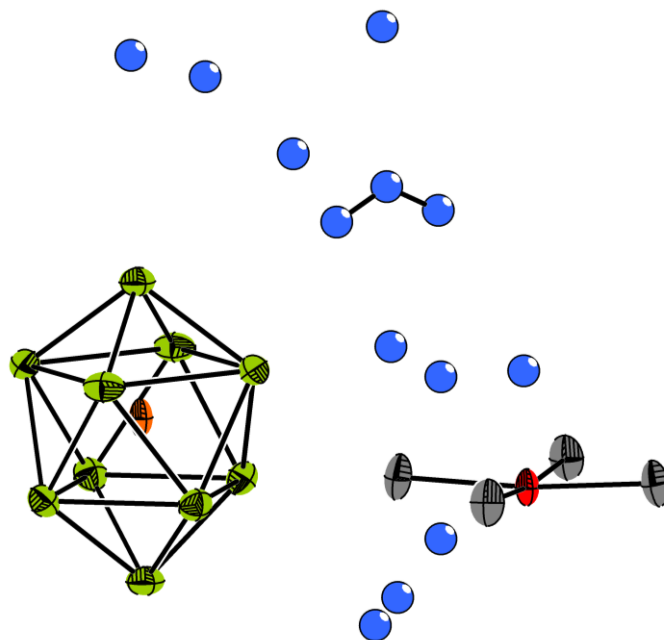


Figure 155: Asymmetric unit of $C_{100}H_{200}K_8N_{10}O_{20}Rh_4Sn_{36}$. Displacement ellipsoids are displayed with a 50 % probability. Ammonia molecules are displayed as Ball & Stick because of the unfinished nature of the refinement. Green – tin, red – oxygen, grey – potassium, blue – nitrogen, orange – rhodium.

Table 66: Fractional atomic coordinates and isotropic or equivalent isotropic displacement parameters of $C_{100}H_{200}K_8N_{10}O_{20}Rh_4Sn_{36}$.

	x	y	z	Uiso*/Ueq	Occ. (<1)
Rh	0.0000	0.0000	0.15854 (7)	0.0372 (6)	
Sn1	0.0000	0.0000	0.09897 (6)	0.0483 (6)	
Sn2	0.19712 (12)	0.0000	0.19017 (3)	0.0470 (3)	
Sn3	0.14901 (8)	0.14901 (8)	0.13650 (3)	0.0514 (4)	
Sn4	0.0000	0.0000	0.2301 (3)	0.054 (4)	0.234 (13)
K1	0.3329 (3)	0.3329 (3)	0.18169 (13)	0.0586 (12)	

Table 67: Atomic displacement parameters of heavy elements of $C_{100}H_{200}K_8N_{10}O_{20}Rh_4Sn_{36}$.

	U^{11}	U^{22}	U^{33}	U^{12}	U^{13}	U^{23}
Rh	0.0242 (6)	0.0242 (6)	0.0632 (17)	0.000	0.000	0.000
Sn1	0.0554 (10)	0.0554 (10)	0.0340 (12)	0.000	0.000	0.000
Sn2	0.0427 (7)	0.0517 (7)	0.0465 (7)	0.000	-0.0092 (5)	0.000
Sn3	0.0577 (6)	0.0577 (6)	0.0389 (6)	-0.0203 (6)	0.0015 (3)	0.0015 (3)
Sn4	0.064 (6)	0.064 (6)	0.034 (6)	0.000	0.000	0.000
K1	0.0420 (13)	0.0420 (13)	0.092 (4)	-0.0097 (17)	-0.0070 (14)	-0.0070 (14)

7.4.6. $\text{K}_6[\text{OH}][\text{Co}@\text{Sn}_9] \cdot 17 \text{NH}_3$

Table 68: Crystallographic data and structure refinement of $\text{K}_6[\text{OH}][\text{Co}@\text{Sn}_9] \cdot 17 \text{NH}_3$.

	$\text{K}_6[\text{OH}][\text{Co}@\text{Sn}_9] \cdot 17 \text{NH}_3$
Sum formula	$\text{K}_6\text{CoSn}_9\text{O}_1\text{N}_{17}\text{H}_{52}$
Molecular weight [g/mol]	1689.65
Crystal system	orthorhombic
Space group	$\text{P2}_1\text{2}_1\text{2}_1$
a [Å]	11.1941(2)
b [Å]	20.1908(2)
c [Å]	20.1870(3)
α [°]	90.00
β [°]	90.00
γ [°]	90.00
V [Å ³]	4562.62(12)
Z	4
T [K]	123
μ [mm ⁻¹]	5.744
Measured reflections	137398
<i>hkl</i> ranges	-13 < <i>h</i> < 13 -24 < <i>k</i> < 24 24 < <i>l</i> < 24
θ min. / max.	2.717 / 26.000
R_{int}	0.0307
Independent reflections	8964
Reflections ($I > 2 \sigma$)	8716
Parameters	315
R_1 ($I > 2 \sigma$; all)	0.0181; 0.0192
wR_2 ($I > 2 \sigma$; all)	0.0422; 0.0425
GooF	1.079
max. / min. residual e ⁻ density [e/Å ³]	0.880/-0.403

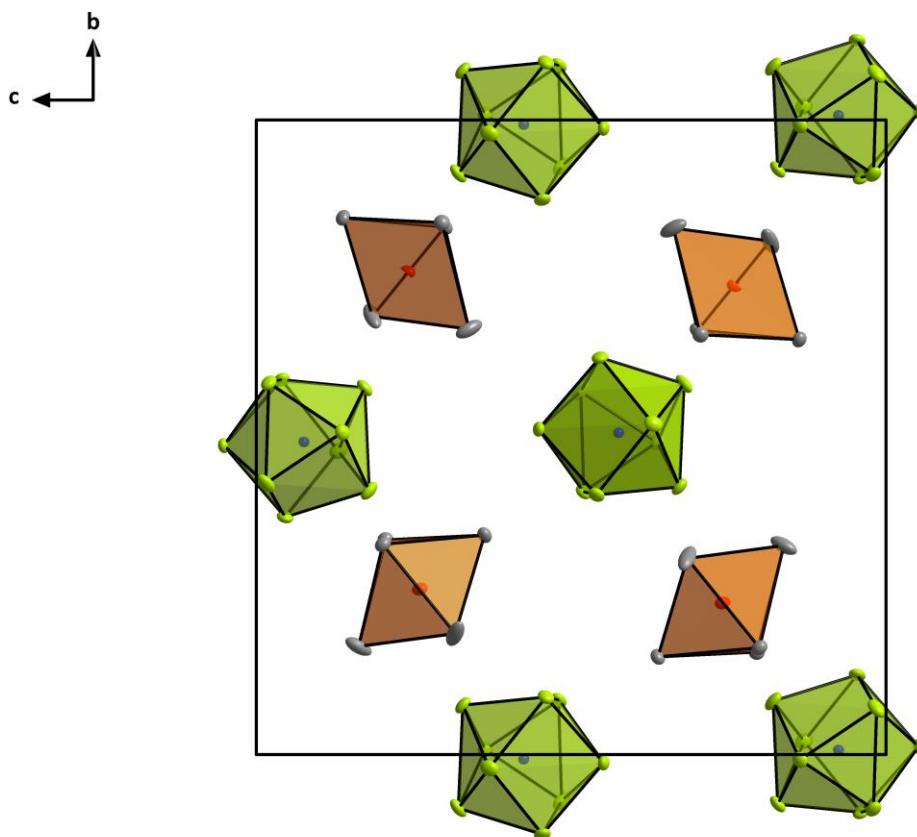


Figure 156: $[K_5(OH)]^{4+}$ groups (orange pyramids) and $[Co@Sn_9]^{5-}$ clusters (green polyhedra) in $K_6[OH][Co@Sn_9] \cdot 17 NH_3$ with layered packing. K atoms which are not coordinated to the O atoms, are omitted. N and H atoms are omitted for clarity.

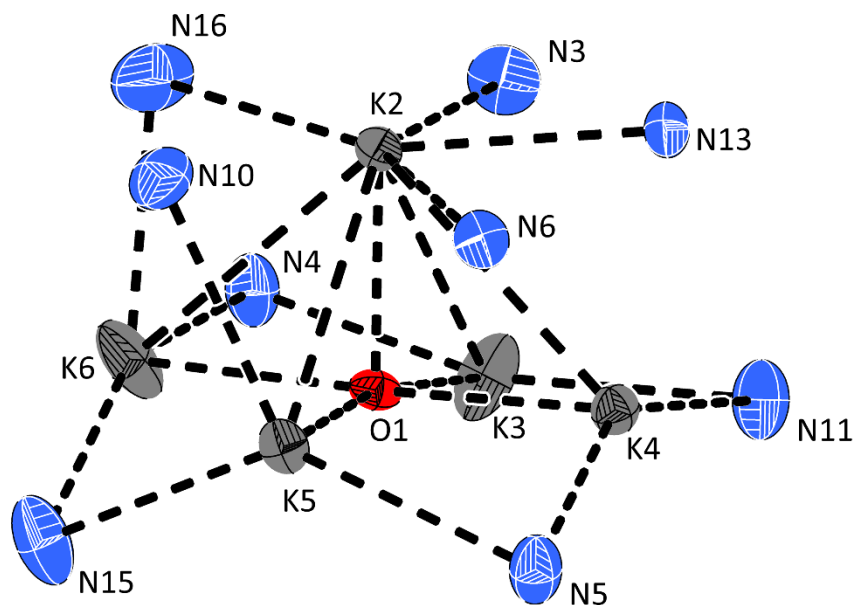


Figure 157: Hydroxide unit contained in $K_6[OH][Co@Sn_9] \cdot 17 NH_3$. Displacement ellipsoids are displayed with a 50 % probability. H atoms are omitted for clarity.

Table 69: Fractional atomic coordinates and isotropic or equivalent isotropic displacement parameters of $K_6[OH][Co@Sn_9] \cdot 17 NH_3$.

	x	y	z	Uiso*/Ueq
K1	0.65683 (14)	0.05203 (8)	-0.03422 (7)	0.0438 (4)
K2	0.67782 (12)	0.16857 (6)	0.20089 (6)	0.0261 (2)
K3	0.99017 (16)	0.17050 (8)	-0.16232 (9)	0.0523 (4)
K4	1.35069 (12)	0.16171 (6)	0.20528 (6)	0.0274 (3)
K5	0.98441 (12)	-0.15409 (6)	-0.13767 (6)	0.0283 (3)
Sn1	1.23500 (3)	-0.00811 (2)	0.13666 (2)	0.02322 (8)
Sn2	1.19613 (4)	0.07279 (2)	0.01496 (2)	0.03149 (10)
Sn3	1.15142 (4)	-0.08575 (2)	0.01983 (2)	0.02581 (8)
Sn4	1.00819 (4)	-0.07786 (2)	0.17192 (2)	0.02687 (9)
Sn5	1.04111 (4)	0.08420 (2)	0.17917 (2)	0.03146 (10)
Sn6	0.94729 (4)	0.12560 (2)	0.04575 (2)	0.03072 (10)
Sn7	0.98426 (4)	0.01295 (2)	-0.05163 (2)	0.02345 (8)
Sn8	0.88390 (4)	-0.09064 (2)	0.04004 (2)	0.02618 (9)
Sn9	0.81732 (3)	0.02147 (2)	0.13021 (2)	0.02718 (9)

Co	1.02698 (6)	0.00727 (3)	0.07543 (3)	0.01338 (12)
K6	0.79438 (19)	-0.30917 (9)	-0.18424 (8)	0.0611 (6)
O	0.9765 (4)	-0.23912 (17)	-0.24045 (18)	0.0239 (8)

Table 70: Atomic displacement parameters of heavy elements of $K_6[OH][Co@Sn_9] \cdot 17 NH_3$.

	U^{11}	U^{22}	U^{33}	U^{12}	U^{13}	U^{23}
K1	0.0335 (8)	0.0556 (9)	0.0423 (8)	0.0079 (7)	-0.0093 (6)	-0.0125 (6)
K2	0.0259 (6)	0.0246 (6)	0.0278 (6)	0.0019 (5)	0.0001 (5)	-0.0052 (4)
K3	0.0431 (9)	0.0378 (8)	0.0761 (11)	0.0085 (7)	0.0194 (8)	0.0293 (7)
K4	0.0264 (6)	0.0267 (6)	0.0291 (6)	-0.0032 (5)	-0.0002 (5)	-0.0001 (5)
K5	0.0344 (7)	0.0270 (5)	0.0234 (5)	-0.0066 (5)	-0.0007 (5)	-0.0041 (4)
Sn1	0.01801 (19)	0.02752 (18)	0.02413 (16)	0.00054 (14)	-0.00631 (14)	0.00298 (15)
Sn2	0.0238 (2)	0.0353 (2)	0.0353 (2)	-0.01142 (17)	-0.00381 (16)	0.01645 (17)
Sn3	0.0269 (2)	0.02347 (18)	0.02706 (17)	0.01025 (16)	-0.00170 (15)	-0.00692 (15)
Sn4	0.0258 (2)	0.02875 (19)	0.02602 (17)	-0.00077 (16)	-0.00001 (15)	0.01402 (15)
Sn5	0.0295 (2)	0.0349 (2)	0.02991 (19)	0.00493 (17)	-0.00836 (16)	-0.01753 (17)
Sn6	0.0447 (3)	0.01636 (17)	0.03113 (19)	0.01008 (16)	0.00065 (18)	0.00352 (15)
Sn7	0.0301 (2)	0.02505 (17)	0.01520 (14)	0.00083 (15)	-0.00463 (14)	0.00108 (13)
Sn8	0.0283 (2)	0.02074 (17)	0.02952 (19)	-0.00899 (15)	0.00025 (16)	-0.00527 (15)
Sn9	0.01670 (19)	0.02874 (19)	0.03610 (19)	0.00287 (15)	0.00535 (16)	-0.00536 (16)
Co	0.0142 (3)	0.0123 (3)	0.0136 (3)	0.0004 (2)	-0.0005 (2)	0.0003 (2)
K6	0.0799 (14)	0.0658 (11)	0.0376 (8)	-0.0526 (10)	-0.0194 (8)	0.0197 (7)
O	0.027 (2)	0.0179 (16)	0.0267 (19)	-0.0015 (16)	-0.0072 (17)	0.0025 (14)

7.4.7. $[\text{K}(2.2.2\text{-crypt})]_2\text{K}_4[\text{Co}_2@\text{Ge}_{17}] \cdot 13 \text{ NH}_3$

Table 71: Crystallographic data and structure refinement of $[\text{K}(2.2.2\text{-crypt})]_2\text{K}_4[\text{Co}_2@\text{Ge}_{17}] \cdot 13 \text{ NH}_3$.

	$[\text{K}(2.2.2\text{-crypt})]_2\text{K}_4[\text{Co}_2@\text{Ge}_{17}] \cdot 13 \text{ NH}_3$
Sum formula	$\text{Co}_2\text{Ge}_{17}\text{K}_6\text{N}_{17}\text{O}_{12}\text{C}_{36}\text{H}_{111}$
Molecular weight [g/mol]	2449.27
Crystal system	monoclinic
Space group	$P2_1/c$
a [Å]	19.680(4)
b [Å]	32.140(6)
c [Å]	15.400(3)
β [°]	110.60(3)
V [Å ³]	9118(3)
Z	4
T [K]	150
μ [mm ⁻¹]	6.182
Measured reflections	277863
	$-24 < h < 24$
<i>hkl</i> ranges	$-39 < k < 39$
	$-18 < l < 18$
ϑ min. / max.	2.72; 26.00
R_{int}	0.0555
Independent reflections	17909
Reflections ($I > 2\sigma$)	13813
Parameters	850
R_1 ($I > 2\sigma$; all)	0.0475; 0.0685
wR_2 ($I > 2\sigma$; all)	0.1202; 0.1339
GooF	0.874
max. / min. residual e ⁻ density	1.44, -1.53

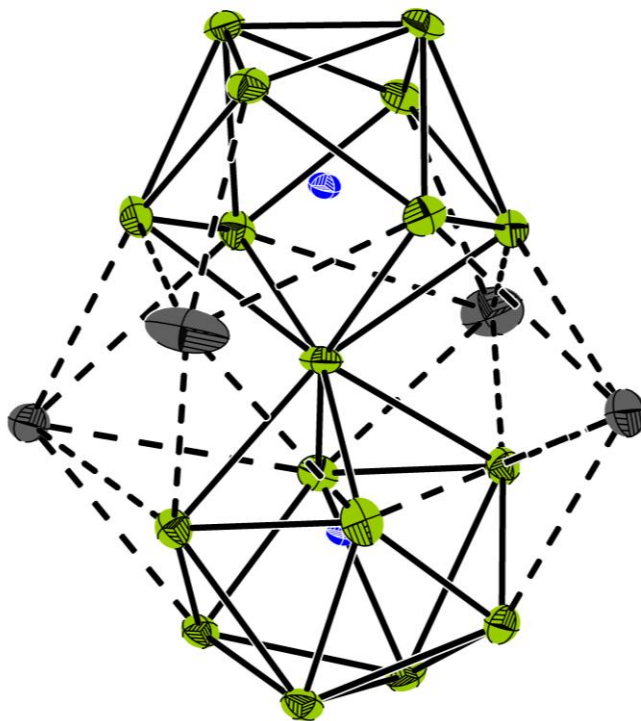


Figure 158: $[\text{Co}_2@\text{Ge}_{17}]^{6-}$ Cluster unit of $[\text{K}(2.2.2\text{-crypt})]_2\text{K}_4[\text{Co}_2@\text{Ge}_{17}] \cdot 13 \text{ NH}_3$. Displacement ellipsoids are displayed with a 50 % probability. Green – germanium, blue – cobalt, grey – potassium.

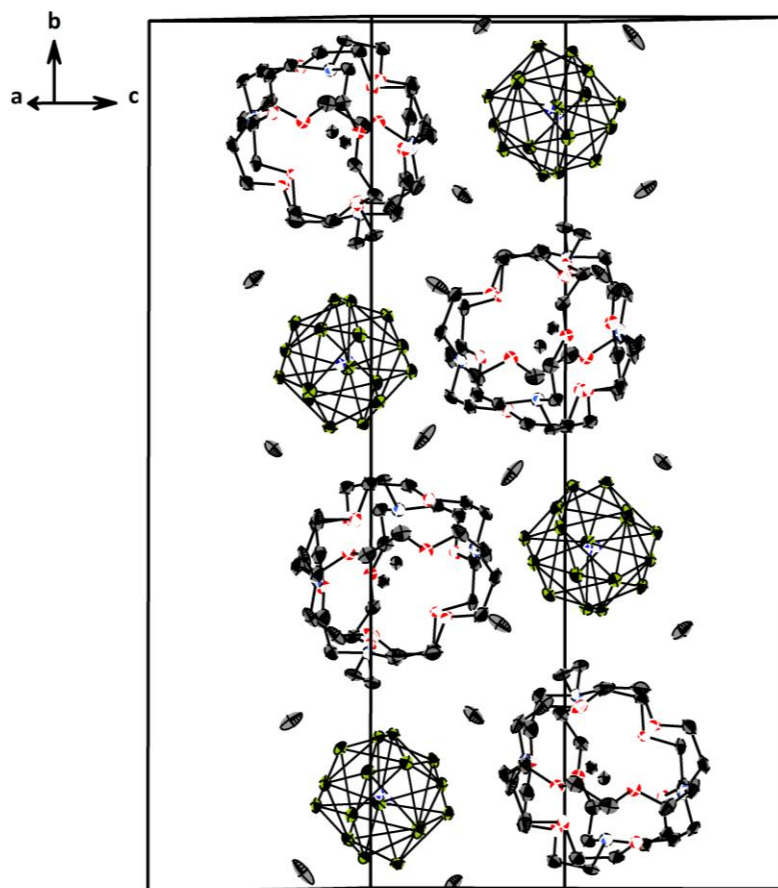


Figure 159: Unit cell of $[\text{K}(\text{2.2.2-crypt})]_2\text{K}_4[\text{Co}_2@\text{Ge}_{17}] \cdot 13 \text{NH}_3$. NH_3 molecules and H atoms are omitted for clarity; displacement ellipsoids are displayed with a 50 % probability. Dark blue – Co, green – germanium, light blue – nitrogen, red – oxygen, dark grey – potassium, light grey – carbon.

Table 72: Fractional atomic coordinates and isotropic or equivalent isotropic displacement parameters of $[K(2.2.2\text{-crypt})]_2K_4[Co_2@Ge_{17}] \cdot 13 NH_3$.

	x	y	z	Uiso*/Ueq
Ge1	0.23089 (4)	0.08473 (2)	0.07760 (5)	0.02479 (15)
Ge2	0.26086 (4)	0.06599 (2)	0.25604 (5)	0.02211 (15)
Ge3	0.23320 (4)	0.14491 (2)	0.21076 (5)	0.02368 (15)
Ge4	0.28729 (4)	0.16138 (2)	0.08128 (5)	0.02543 (16)
Ge5	0.34843 (4)	0.03653 (2)	0.17121 (5)	0.02477 (15)
Ge6	0.36640 (4)	0.09631 (2)	0.06510 (5)	0.02857 (17)
Ge7	0.37932 (4)	0.17871 (2)	0.25630 (5)	0.02232 (15)
Ge8	0.36088 (4)	0.12051 (2)	0.36404 (4)	0.02205 (15)
Ge9	0.45773 (3)	0.10040 (2)	0.26543 (5)	0.02359 (15)
Ge10	0.55173 (4)	0.03119 (2)	0.35931 (5)	0.02609 (16)
Ge11	0.52575 (4)	0.08874 (2)	0.46687 (5)	0.02349 (15)
Ge12	0.54620 (4)	0.17609 (2)	0.30934 (5)	0.02373 (15)
Ge13	0.57229 (4)	0.12331 (2)	0.19651 (5)	0.02602 (16)
Ge14	0.65540 (4)	0.05965 (2)	0.29699 (5)	0.02561 (16)
Ge15	0.67482 (4)	0.07287 (2)	0.47444 (5)	0.02554 (16)
Ge16	0.69003 (4)	0.13634 (2)	0.36262 (5)	0.02504 (15)
Ge17	0.62023 (4)	0.14991 (2)	0.48085 (5)	0.02491 (15)
Co1	0.34008 (4)	0.10958 (2)	0.20291 (5)	0.01492 (16)
Co2	0.57445 (4)	0.10366 (2)	0.34736 (5)	0.01572 (17)
K1	0.44601 (11)	0.19408 (6)	0.04710 (15)	0.0522 (5)
K2	0.50298 (10)	0.02062 (8)	0.10699 (17)	0.0629 (7)
K3	0.39434 (9)	0.00763 (5)	0.41076 (11)	0.0356 (4)
K4	0.46002 (11)	0.20089 (7)	0.49354 (13)	0.0507 (5)
K5	0.09017 (7)	0.12699 (4)	0.60872 (9)	0.0212 (3)
K6	0.84440 (7)	0.14357 (4)	0.98076 (9)	0.0207 (3)

Table 73: Atomic displacement parameters of heavy elements of [K(2.2.2-crypt)]₂K₄[Co₂@Ge₁₇] · 13 NH₃.

	U^{11}	U^{22}	U^{33}	U^{12}	U^{13}	U^{23}
Ge1	0.0196 (3)	0.0322 (4)	0.0184 (3)	-0.0056 (3)	0.0014 (3)	0.0000 (3)
Ge2	0.0179 (3)	0.0273 (4)	0.0229 (3)	-0.0032 (3)	0.0094 (3)	0.0032 (3)
Ge3	0.0170 (3)	0.0284 (4)	0.0267 (3)	0.0065 (3)	0.0090 (3)	0.0031 (3)
Ge4	0.0263 (4)	0.0268 (4)	0.0217 (3)	0.0012 (3)	0.0065 (3)	0.0078 (3)
Ge5	0.0264 (4)	0.0224 (3)	0.0280 (3)	-0.0015 (3)	0.0126 (3)	-0.0030 (3)
Ge6	0.0378 (4)	0.0313 (4)	0.0239 (3)	-0.0031 (3)	0.0199 (3)	-0.0024 (3)
Ge7	0.0248 (3)	0.0178 (3)	0.0230 (3)	-0.0016 (3)	0.0068 (3)	-0.0019 (3)
Ge8	0.0226 (3)	0.0285 (4)	0.0158 (3)	-0.0025 (3)	0.0078 (3)	-0.0019 (3)
Ge9	0.0121 (3)	0.0290 (4)	0.0273 (3)	-0.0002 (3)	0.0039 (3)	-0.0038 (3)
Ge10	0.0288 (4)	0.0188 (3)	0.0331 (4)	-0.0033 (3)	0.0139 (3)	0.0002 (3)
Ge11	0.0255 (4)	0.0261 (4)	0.0227 (3)	-0.0017 (3)	0.0132 (3)	0.0027 (3)
Ge12	0.0246 (3)	0.0201 (3)	0.0256 (3)	-0.0011 (3)	0.0077 (3)	0.0020 (3)
Ge13	0.0267 (4)	0.0343 (4)	0.0199 (3)	0.0030 (3)	0.0116 (3)	0.0033 (3)
Ge14	0.0203 (3)	0.0284 (4)	0.0306 (4)	0.0044 (3)	0.0120 (3)	-0.0022 (3)
Ge15	0.0169 (3)	0.0309 (4)	0.0256 (3)	0.0028 (3)	0.0035 (3)	0.0066 (3)
Ge16	0.0158 (3)	0.0320 (4)	0.0288 (4)	-0.0068 (3)	0.0097 (3)	-0.0010 (3)
Ge17	0.0223 (3)	0.0306 (4)	0.0203 (3)	-0.0048 (3)	0.0056 (3)	-0.0057 (3)
Co1	0.0128 (4)	0.0180 (4)	0.0142 (4)	-0.0010 (3)	0.0051 (3)	-0.0007 (3)
Co2	0.0114 (4)	0.0186 (4)	0.0174 (4)	-0.0012 (3)	0.0053 (3)	0.0004 (3)
K1	0.0389 (10)	0.0467 (11)	0.0637 (12)	-0.0086 (8)	0.0090 (9)	0.0280 (9)
K2	0.0318 (10)	0.0886 (16)	0.0703 (14)	-0.0048 (10)	0.0206 (9)	-0.0549 (13)
K3	0.0263 (8)	0.0394 (9)	0.0357 (8)	-0.0039 (7)	0.0044 (7)	0.0156 (7)
K4	0.0472 (11)	0.0515 (11)	0.0417 (10)	0.0054 (9)	0.0008 (8)	-0.0241 (9)
K5	0.0214 (6)	0.0239 (7)	0.0190 (6)	0.0006 (5)	0.0081 (5)	0.0005 (5)
K6	0.0203 (6)	0.0219 (7)	0.0214 (6)	-0.0011 (5)	0.0091 (5)	-0.0016 (5)

7.4.8. $[\text{K}(2.2.2\text{-crypt})]_3[\text{Co@Ge}_{10}] \cdot 3 \text{NH}_3$

Table 74: Crystallographic data and structure refinement of $[\text{K}(2.2.2\text{-crypt})]_3[\text{Co@Ge}_{10}] \cdot 3 \text{NH}_3$.

	$[\text{K}(2.2.2\text{-crypt})]_3[\text{Co@Ge}_{10}] \cdot 3 \text{NH}_3$
Sum formula	$\text{K}_3\text{C}_{54}\text{H}_{104}\text{CoN}_{10}\text{O}_{17}$
Molecular weight [g/mol]	2067.60
Crystal system	triclinic
Space group	P-1
a [Å]	12.410(3)
b [Å]	16.000(3)
c [Å]	23.220(5)
α [°]	76.70(3)
β [°]	88.10(3)
γ [°]	70.70(3)
V [Å ³]	4230.1(16)
Z	2
T [K]	150
μ [mm ⁻¹]	3.896
Measured reflections	34890
<i>hkl</i> ranges	-16 < <i>h</i> < 16 -20 < <i>k</i> < 20 -30 < <i>l</i> < 30
θ min. / max.	2.71 / 28.18
R _{int}	0.6471
Independent reflections	17151
Reflections (<i>I</i> > 2 σ)	2782
Parameters	801
<i>R</i> ₁ (<i>I</i> > 2 σ ; all)	0.1237; 0.3915
<i>wR</i> ₂ (<i>I</i> > 2 σ ; all)	0.2654; 0.3828
GooF	0.800
max. / min. residual e ⁻ density [e/Å ³]	1.80 / -1.22

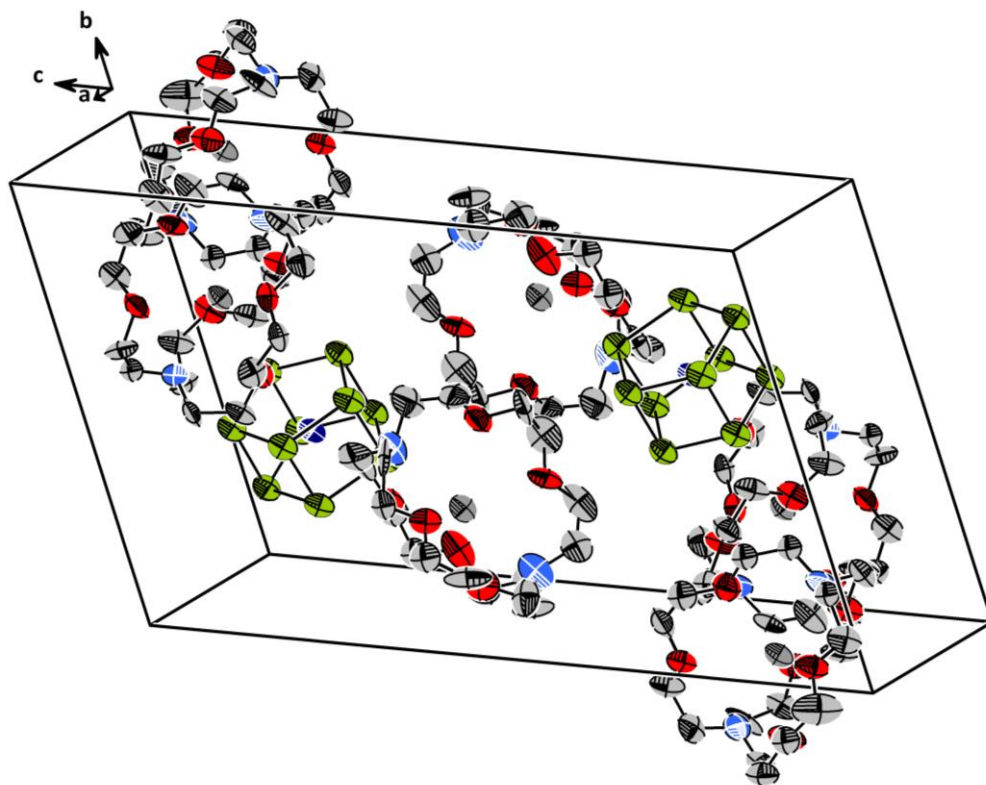


Figure 160: Extended unit cell of $[\text{K}(2.2.2\text{-crypt})]_3[\text{Co@Ge}_{10}] \cdot 3 \text{NH}_3$. Displacement ellipsoids are displayed with a 50 % probability. Ammonia molecules are omitted for clarity. Dark blue – Co, green – germanium, light blue – nitrogen, red – oxygen, dark grey – potassium, light grey – carbon.

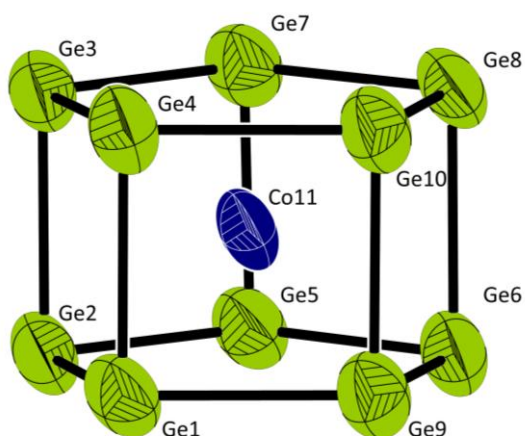


Figure 161: $[\text{Co@Ge}_{10}]^{3-}$ cluster unit contained in $[\text{K}(2.2.2\text{-crypt})]_3[\text{Co@Ge}_{10}] \cdot 3 \text{NH}_3$. Displacement ellipsoids are displayed with a 50 % probability.

7.4.9. $[\text{K}(2.2.2\text{-crypt})]_3[\text{Co@Ge}_{10}] \cdot 9 \text{NH}_3$

Table 75: Crystallographic data and structure refinement of $[\text{K}(2.2.2\text{-crypt})]_3[\text{Co@Ge}_{10}] \cdot 9 \text{NH}_3$.

	$[\text{K}(2.2.2\text{-crypt})]_3[\text{Co@Ge}_{10}] \cdot 9 \text{NH}_3$
Sum formula	$\text{C}_{54}\text{H}_{134}\text{CoGe}_{10}\text{K}_3\text{N}_{15}\text{O}_{18}$
Molecular weight [g/mol]	2183.89
Crystal system	triclinic
Space group	P-1
a [Å]	12.420(3)
b [Å]	16.160(3)
c [Å]	25.240(5)
α [°]	73.00(3)
β [°]	89.80(3)
γ [°]	70.40(3)
V [Å ³]	4538.6(16)
Z	2
T [K]	150
μ [mm ⁻¹]	3.637
Measured reflections	137996
<i>hkl</i> ranges	-16 < <i>h</i> < 16 -21 < <i>k</i> < 21 -32 < <i>l</i> < 32
ϑ min. / max.	2.60, 28.24
R _{int}	0.2864
Independent reflections	21132
Reflections (<i>I</i> > 2 σ)	9390
Parameters	895
R_1 (<i>I</i> > 2 σ ; all)	0.1413; 0.2038
wR_2 (<i>I</i> > 2 σ ; all)	0.3083, 0.3641
GooF	1.121
max. / min. residual e ⁻ density	2.64, -2.63

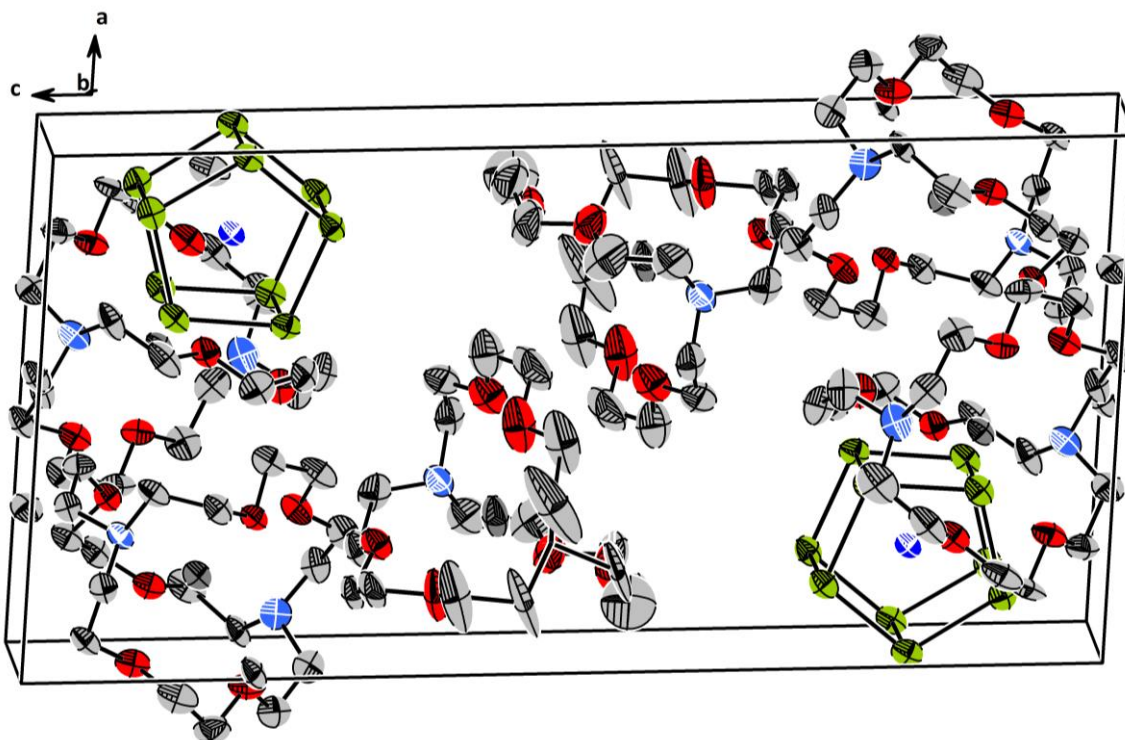


Figure 162: Extended unit cell of $[K(2.2.2\text{-crypt})]_3[Co@Ge_{10}] \cdot 9 NH_3$; Displacement ellipsoids are displayed with a 50 % probability. Ammonia molecules are omitted for clarity. Dark blue – Co, green – germanium, light blue – nitrogen, red – oxygen, dark grey – potassium, light grey – carbon.

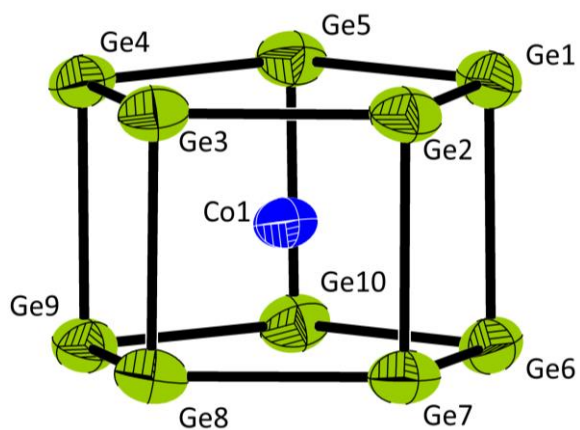


Figure 163: $[Co@Ge_{10}]^{3-}$ cluster unit contained in $[K(2.2.2\text{-crypt})]_3[Co@Ge_{10}] \cdot 9 NH_3$. Displacement ellipsoids are displayed with a 50 % probability.

7.4.10. C₇₂K₆O₃₆Pb₂₃Rh₃Table 76: Crystallographic data and structure refinement of C₇₂K₆O₃₆Pb₂₃Rh₃.

Sum formula	C ₇₂ K ₆ O ₃₆ Pb ₂₃ Rh ₃
Molecular weight [g/mol]	6917.54
Crystal system	triclinic
Space group	P-1
a [Å]	14.980(3)
b [Å]	15.150(3)
c [Å]	20.110(4)
α [°]	91.90(3)
β [°]	105.20(3)
γ [°]	97.50(3)
V [Å ³]	4355.7(15)
Z	1
T [K]	150
μ [mm ⁻¹]	22.596
Measured reflections	188510
<i>hkl</i> ranges	-25 < <i>h</i> < 25 -25 < <i>k</i> < 25 -32 < <i>l</i> < 33
θ min. / max.	2.76; 37.40
R _{int}	0.6579
Independent reflections	41830
Reflections (<i>I</i> > 2 σ)	8781
Parameters	60
<i>R</i> ₁ (<i>I</i> > 2 σ; all)	0.1750; 0.4183
<i>wR</i> ₂ (<i>I</i> > 2 σ; all)	0.3831; 0.5265
GooF	0.916
max. / min. residual e ⁻ density [e/Å ³]	6.35; -9.25

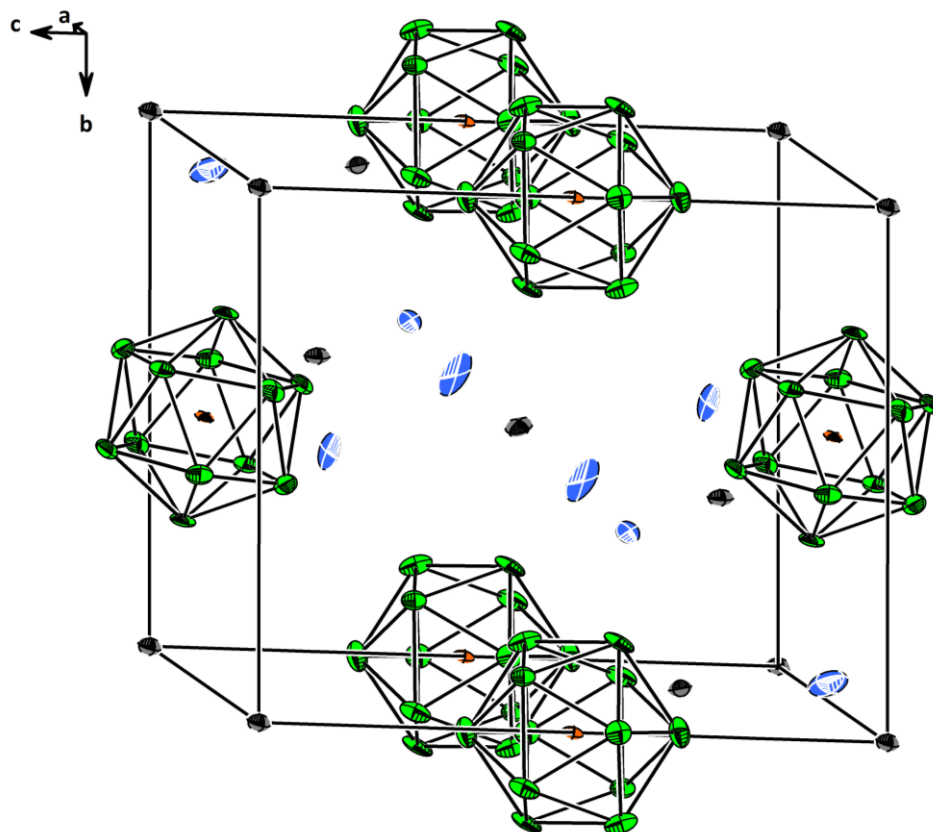


Figure 164: Extended unit cell of $C_{72}K_6O_{36}Pb_{23}Rh_3$. Displacement ellipsoids are displayed with a 50 % probability. A depiction of a unit cell is difficult due to the fact that the structure refinement is not finished. Orange – rhodium; Green – lead, light blue – nitrogen, dark grey – potassium.

7.4.11. [Cs(18-crown-6)][Ge₉[Si(SiMe₃)₃]₃][ClSi(SiMe₃)₃]₂

Table 77: Crystallographic data and structure refinement of [Cs(18-crown-6)][Ge₉[Si(SiMe₃)₃]₃][ClSi(SiMe₃)₃]₂.

	[Cs(18-crown-6)][Ge ₉ [Si(SiMe ₃) ₃] ₃][ClSi(SiMe ₃) ₃] ₂
Sum formula	C ₁₃₈ H ₃₄₉ Cl ₂ Cs ₂ Ge ₁₈ O ₂₄ Si ₄₀
Molecular weight [g/mol]	5160.11
Crystal system	P2 ₁
Space group	monoclinic
a [Å]	23.630(5)
b [Å]	23.650(5)
c [Å]	23.650(5)
α [°]	90
β [°]	90.10(3)
γ [°]	90
V [Å ³]	13217(5)
Z	2
T [K]	150
μ [mm ⁻¹]	2.529
Measured reflections	270440
<i>hkl</i> ranges	-29 < <i>h</i> < 29 -29 < <i>k</i> < 29 -29 < <i>l</i> < 29
θ min. / max.	2.58 / 26.00
R _{int}	0.0896
Independent reflections	51949
Reflections (<i>I</i> > 2 σ)	35976
Parameters	2159
R ₁ (<i>I</i> > 2 σ; all)	0.0575; 0.1004
wR ₂ (<i>I</i> > 2 σ; all)	0.1332; 0.1558
GooF	1.278
max. / min. residual e ⁻ density [e/Å ³]	2.51 / -1.70

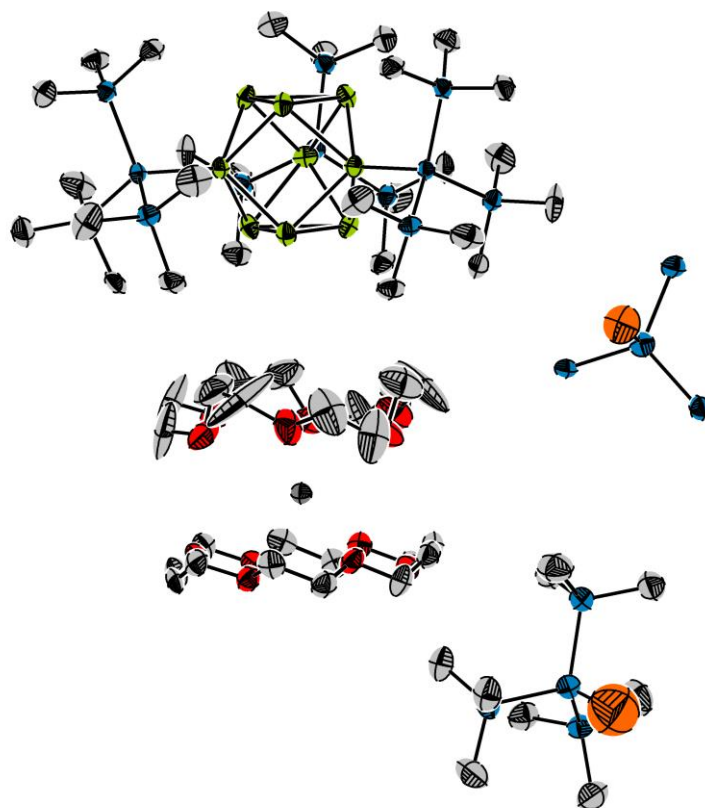


Figure 165: Asymmetric unit in $[\text{Cs}(18\text{-crown-6})][\text{Ge}_9[\text{Si}(\text{SiMe}_3)_3]_3][\text{ClSi}(\text{SiMe}_3)_3]_2$. Displacement ellipsoids are displayed with a 50 % probability. Methylatoms of the second $\text{ClSi}(\text{SiMe}_3)_3$ group are omitted because of a split position. H atoms are omitted for clarity. A depiction of a unit cell is difficult due to the fact that the cell is crowded and no good orientation is found where a good viewing point is given. Green – germanium, light blue – silicon, red – oxygen, orange – chlorine, dark grey – cesium, light grey – carbon.

7.4.12. $K_4[Sn_9] \cdot 9 \text{ dmf}$ Table 78: Crystallographic data and structure refinement of $K_4[Sn_9] \cdot 9 \text{ dmf}$.

	$K_4[Sn_9] \cdot 9 \text{ dmf}$
Sum formula	$K_4Sn_9C_{27}N_9O_9H_{63}$
Molecular weight [g/mol]	1882.63
Crystal system	monoclinic
Space group	$I2/c$
a [Å]	24.030(5)
b [Å]	13.220(3)
c [Å]	46.736(27)
α [°]	90
β [°]	97.73(3)
γ [°]	90
V [Å ³]	14712(7)
Z	8
T [K]	293
μ [mm ⁻¹]	3.223
Measured reflections	249069
<i>hkl</i> ranges	-31 < <i>h</i> < 31 -17 < <i>k</i> < 17 -61 < <i>l</i> < 60
θ min. / max.	2.61; 27.93
R_{int}	0.0654
Independent reflections	17266
Reflections ($I > 2 \sigma$)	10071
Parameters	541
R_1 ($I > 2 \sigma$; all)	0.0592; 0.1193
wR_2 ($I > 2 \sigma$; all)	0.1633; 0.1898
GooF	1.016
max. / min. residual e ⁻ density	2.92; -1.54

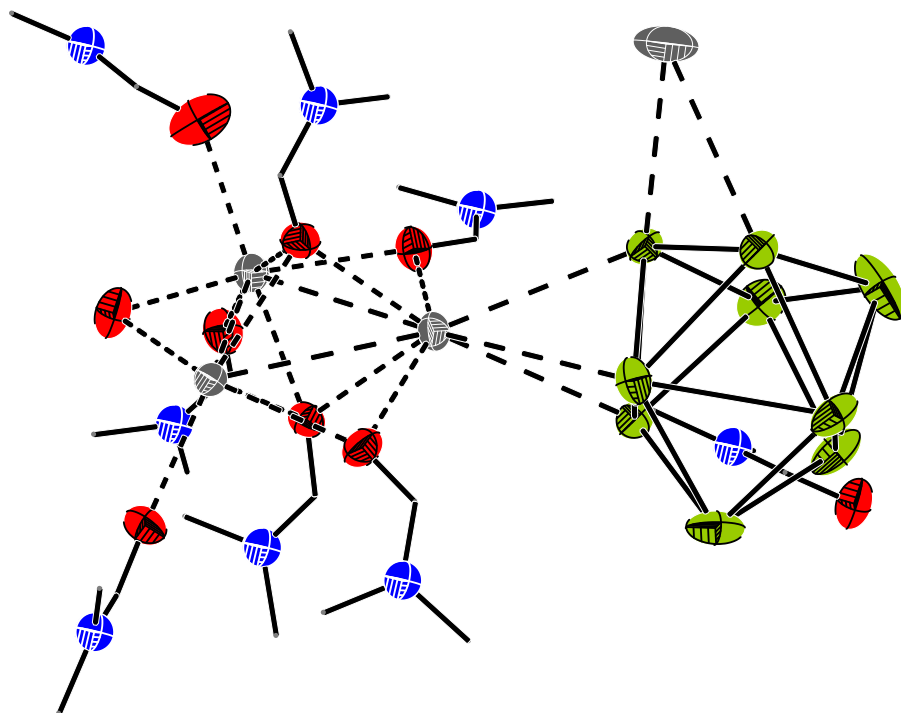


Figure 166: Asymmetric unit in $\text{K}_4[\text{Sn}_9] \cdot 9 \text{ dmf}$. Carbon atoms displayed as wire and sticks. Displacement ellipsoids are displayed with a 50 % probability. H atoms are omitted for clarity. Green – germanium, light blue – nitrogen, red – oxygen, grey – potassium.

Table 79: Fractional atomic coordinates and isotropic or equivalent isotropic displacement parameters of $\text{K}_4[\text{Sn}_9] \cdot 9 \text{ dmf}$.

	x	y	z	Uiso*/Ueq
Sn1	0.45001 (3)	0.77270 (8)	0.050325 (17)	0.0605 (2)
Sn2	0.48225 (3)	0.61064 (5)	0.092566 (17)	0.04465 (18)
Sn3	0.53687 (3)	0.83984 (6)	0.096702 (18)	0.0522 (2)
Sn4	0.41603 (3)	0.93260 (6)	0.08812 (2)	0.0578 (2)
Sn5	0.36040 (2)	0.70375 (5)	0.083225 (15)	0.04132 (17)
Sn6	0.41526 (2)	0.63825 (5)	0.141789 (14)	0.03749 (16)
Sn7	0.53371 (3)	0.70562 (5)	0.146718 (16)	0.04567 (18)
Sn8	0.48024 (4)	0.90692 (8)	0.14646 (2)	0.0812 (3)
Sn9	0.36177 (3)	0.83781 (6)	0.134440 (19)	0.0547 (2)
K1	0.33777 (8)	0.16282 (14)	0.06033 (4)	0.0337 (4)
K2	0.22620 (8)	0.26583 (15)	0.10401 (5)	0.0387 (4)
K3	0.35340 (8)	0.42882 (15)	0.09606 (5)	0.0395 (4)
K7	0.0022 (2)	0.9418 (3)	0.21017 (6)	0.1138 (16)

Table 80: Atomic displacement parameters of heavy elements of $K_4[Sn_9] \cdot 9 \text{ dmf}$.

	U^{11}	U^{22}	U^{33}	U^{12}	U^{13}	U^{23}
Sn1	0.0490 (4)	0.0988 (7)	0.0351 (4)	0.0051 (4)	0.0107 (3)	0.0135 (4)
Sn2	0.0362 (3)	0.0387 (3)	0.0585 (5)	0.0050 (3)	0.0045 (3)	-0.0105 (3)
Sn3	0.0273 (3)	0.0625 (5)	0.0671 (5)	-0.0056 (3)	0.0078 (3)	0.0277 (4)
Sn4	0.0486 (4)	0.0476 (4)	0.0799 (6)	0.0176 (3)	0.0187 (4)	0.0319 (4)
Sn5	0.0288 (3)	0.0457 (4)	0.0462 (4)	-0.0063 (2)	-0.0071 (3)	0.0117 (3)
Sn6	0.0314 (3)	0.0410 (3)	0.0387 (3)	-0.0046 (2)	-0.0002 (2)	0.0102 (3)
Sn7	0.0325 (3)	0.0500 (4)	0.0499 (4)	-0.0098 (3)	-0.0113 (3)	0.0142 (3)
Sn8	0.0562 (5)	0.0828 (6)	0.0970 (8)	0.0185 (4)	-0.0170 (5)	-0.0525 (6)
Sn9	0.0506 (4)	0.0534 (4)	0.0651 (5)	0.0153 (3)	0.0264 (4)	0.0052 (4)
K1	0.0369 (9)	0.0313 (9)	0.0328 (10)	0.0004 (7)	0.0041 (8)	0.0006 (7)
K2	0.0355 (9)	0.0367 (10)	0.0436 (11)	-0.0017 (8)	0.0039 (8)	-0.0017 (8)
K3	0.0397 (10)	0.0376 (10)	0.0417 (11)	-0.0101 (8)	0.0070 (8)	-0.0058 (8)
K7	0.229 (5)	0.074 (2)	0.0357 (15)	-0.042 (3)	0.010 (2)	-0.0040 (14)

7.4.13. $[\text{K}_5(\text{OH})][\text{Ge}_9] \cdot 8 \text{NH}_3$

Table 81: Crystallographic data and structure refinement of $[\text{K}_5(\text{OH})][\text{Ge}_9] \cdot 8 \text{NH}_3$

	$[\text{K}_5(\text{OH})][\text{Ge}_9] \cdot 8 \text{NH}_3$
Sum formula	$\text{Ge}_{36}\text{K}_{20}\text{N}_{32}\text{O}_4\text{H}_{100}$
Molecular weight [g/mol]	4008.21
Crystal system	orthorhombic
Space group	Pnma
a [Å]	12.750(3)
b [Å]	15.470(3)
c [Å]	14.390(3)
α [°]	90
β [°]	90
γ [°]	90
V [Å ³]	2838.3(10)
Z	4
T [K]	150
μ [mm ⁻¹]	10.127
Measured reflections	64405
hkl ranges	-16 < h < 16
	-20 < k < 20
	-18 < l < 18
θ min. / max.	1.93; 28.15
Rint	0.0527
Independent reflections	3511
Reflections ($I > 2 \sigma$)	2518
Parameters	133
R_1 ($I > 2 \sigma$; all)	0.0521; 0.0828
wR_2 ($I > 2 \sigma$; all)	0.1123; 0.1265
GooF	1.022
max. / min. residual e- density [e/Å ³]	-2.38; 2.38

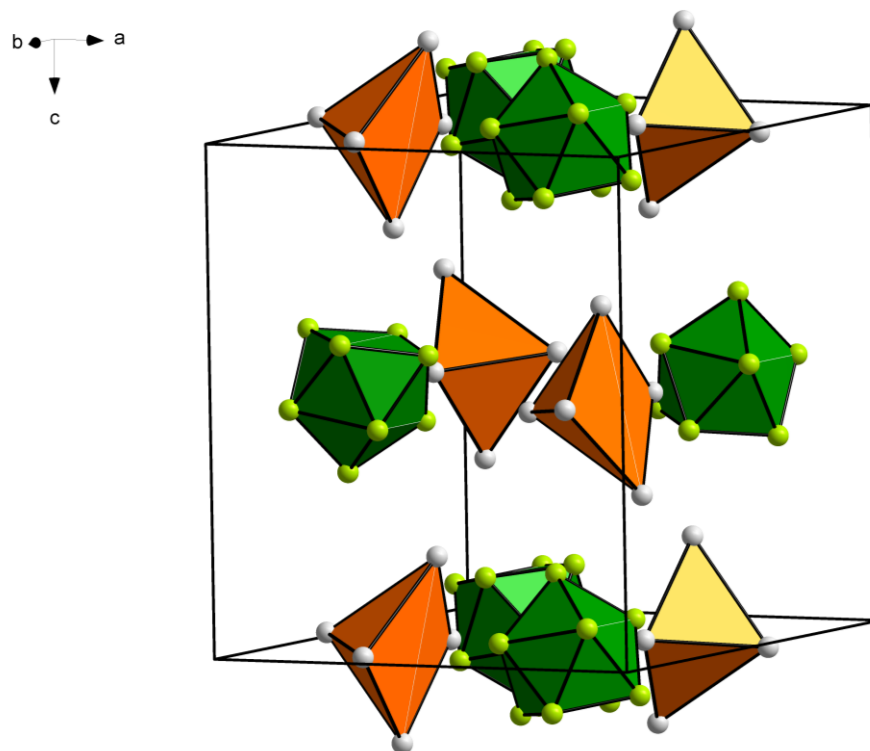


Figure 167: $[\text{Ge}_9]^{4-}$ clusters (green polyhedra) and pyramidal hydroxide units (orange polyhedral) in $[\text{K}_5(\text{OH})]\text{Ge}_9 \cdot 8 \text{NH}_3$. Displacement ellipsoids are displayed with a 50 % probability. ; H and N atoms are omitted for clarity.

Table 82: Fractional atomic coordinates and isotropic or equivalent isotropic displacement parameters of $[\text{K}_5(\text{OH})][\text{Ge}_9] \cdot 8 \text{NH}_3$.

	x	y	z	Uiso*/Ueq
Ge1	0.76729 (8)	0.13717 (6)	0.60069 (6)	0.0430 (3)
K1	0.18717 (13)	0.07740 (10)	0.49618 (11)	0.0311 (3)
Ge2	0.90439 (7)	0.15582 (6)	0.47035 (6)	0.0352 (2)
K2	0.38089 (16)	0.2500	0.47009 (17)	0.0313 (5)
Ge4	0.82245 (9)	0.2500	0.34197 (7)	0.0379 (3)
K4	0.20196 (17)	0.2500	0.68095 (14)	0.0278 (5)
Ge3	0.91352 (9)	0.2500	0.61825 (9)	0.0429 (3)
K3	0.11017 (17)	0.2500	0.31611 (14)	0.0275 (5)
Ge6	0.69118 (8)	0.34393 (9)	0.43616 (7)	0.0660 (4)
Ge5	0.62389 (8)	0.2500	0.57330 (9)	0.0468 (4)

Table 83: Atomic displacement parameters of heavy elements of $[K_5(OH)][Ge_9] \cdot 8 NH_3$.

	U^{11}	U^{22}	U^{33}	U^{12}	U^{13}	U^{23}
Ge1	0.0670 (6)	0.0233 (4)	0.0385 (5)	-0.0010 (4)	0.0261 (4)	0.0053 (4)
K1	0.0492 (9)	0.0180 (7)	0.0263 (7)	0.0002 (6)	0.0047 (7)	-0.0009 (6)
Ge2	0.0419 (5)	0.0272 (4)	0.0365 (4)	0.0139 (4)	0.0170 (3)	0.0027 (3)
K2	0.0188 (9)	0.0294 (12)	0.0456 (13)	0.000	0.0034 (9)	0.000
Ge4	0.0296 (6)	0.0681 (9)	0.0159 (5)	0.000	0.0006 (4)	0.000
K4	0.0352 (11)	0.0291 (11)	0.0190 (9)	0.000	-0.0003 (8)	0.000
Ge3	0.0275 (6)	0.0729 (10)	0.0285 (6)	0.000	-0.0107 (5)	0.000
K3	0.0347 (11)	0.0266 (11)	0.0211 (10)	0.000	-0.0003 (8)	0.000
Ge6	0.0536 (6)	0.1091 (10)	0.0353 (5)	0.0562 (6)	0.0092 (4)	0.0316 (6)
Ge5	0.0145 (5)	0.0905 (12)	0.0354 (7)	0.000	0.0059 (5)	0.000

7.4.14. [K(18-crown-6)]₃Ge₉Table 84: Crystallographic data and structure refinement of [K(18-crown-6)]₃Ge₉.

	[K(18-crown-6)] ₃ Ge ₉
Sum formula	C ₃₆ Ge ₉ K ₃ N ₄ O ₁₈ H ₈₄
Molecular weight [g/mol]	1631.68
Crystal system	monoclinic
Space group	P2 ₁ /c
a [Å]	15.110(3)
b [Å]	15.340(3)
c [Å]	26.980(3)
α [°]	90.00
β [°]	93.90(3)
γ [°]	90.00
V [Å ³]	6239(2)
Z	4
T [K]	150
μ [mm ⁻¹]	4.529
Measured reflections	140675
hkl ranges	-18 < h < 18
	-18 < k < 19
	-33 < l < 33
θ min. / max.	1.96; 26.34
R _{int}	0.0385
Independent reflections	12438
Reflections (I > 2 σ)	9560
Parameters	635
R ₁ (I > 2 σ; all)	0.0833; 0.1090
wR ₂ (I > 2 σ; all)	0.2099; 0.2341
GooF	0.974
max. / min. residual e- density [e/Å ³]	-4.36; 6.35

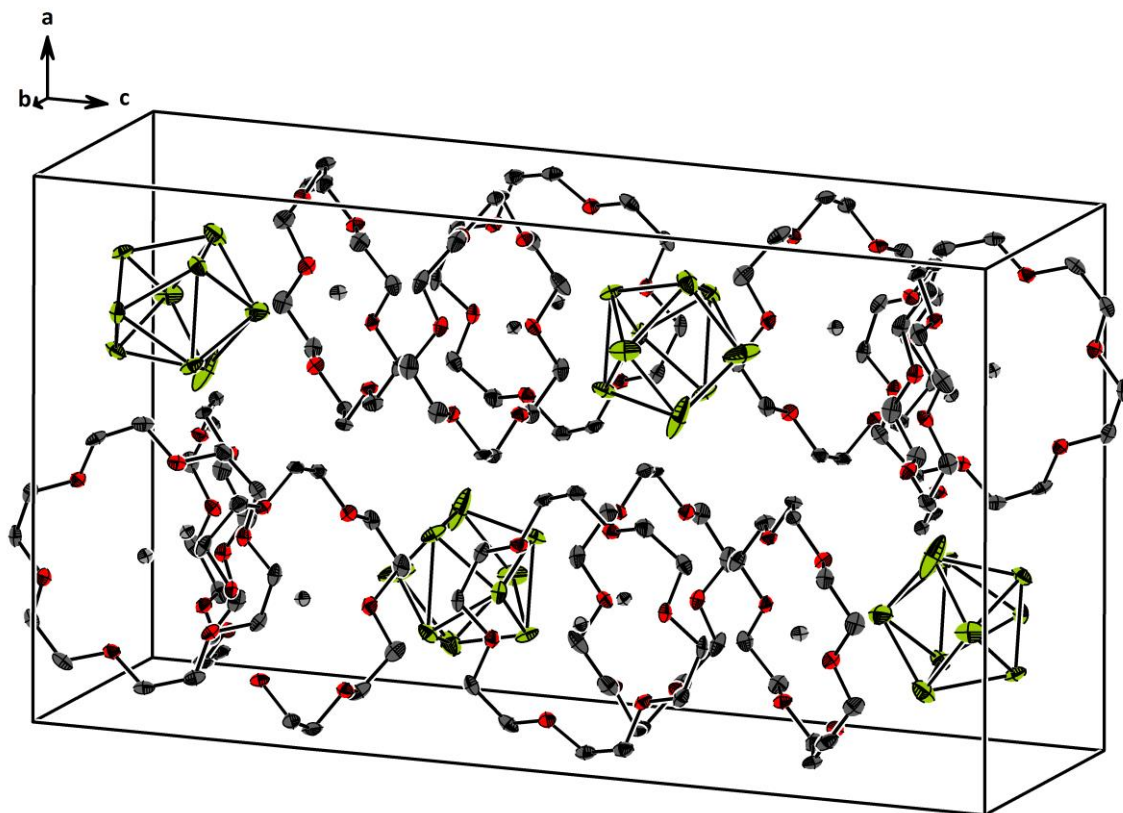


Figure 168: Extended unit cell in $[K(18\text{-crown-}6)]_3\text{Ge}_9$. Displacement ellipsoids are displayed with a 50 % probability. H atoms and ammonia molecules are omitted for clarity. Green – germanium, red – oxygen, grey – potassium, dark grey – carbon.

Table 85: Fractional atomic coordinates and isotropic or equivalent isotropic displacement parameters of [K(18-crown-6)]₃Ge₉.

	<i>x</i>	<i>y</i>	<i>z</i>	<i>U</i> _{iso} */ <i>U</i> _{eq}
Ge1	0.35978 (17)	0.23901 (11)	0.35249 (6)	0.0816 (7)
Ge2	0.23836 (8)	0.17098 (7)	0.40006 (6)	0.0413 (3)
Ge3	0.33212 (7)	0.30265 (7)	0.43827 (4)	0.0313 (3)
Ge4	0.11193 (9)	0.23723 (9)	0.34304 (5)	0.0436 (3)
Ge5	0.23858 (9)	0.28553 (14)	0.29212 (7)	0.0750 (6)
Ge6	0.33280 (7)	0.40363 (7)	0.34576 (4)	0.0308 (3)
Ge7	0.15123 (7)	0.30366 (7)	0.43130 (4)	0.0261 (2)
Ge8	0.24286 (7)	0.44370 (6)	0.41931 (4)	0.0236 (2)
Ge9	0.14983 (7)	0.40369 (7)	0.33992 (4)	0.0285 (3)
K2	0.74856 (12)	0.33992 (12)	0.23720 (7)	0.0179 (4)
K3	0.26554 (12)	0.58270 (12)	0.06513 (7)	0.0191 (4)
K5	0.24906 (12)	0.08841 (12)	0.04716 (7)	0.0165 (4)

Table 86: Atomic displacement parameters of heavy elements of [K(18-crown-6)]₃Ge₉.

	<i>U</i> ¹¹	<i>U</i> ²²	<i>U</i> ³³	<i>U</i> ¹²	<i>U</i> ¹³	<i>U</i> ²³
Ge1	0.158 (2)	0.0418 (8)	0.0531 (9)	0.0217 (10)	0.0624 (11)	0.0215 (7)
Ge2	0.0345 (6)	0.0134 (5)	0.0765 (9)	0.0017 (4)	0.0079 (6)	-0.0081 (5)
Ge3	0.0203 (5)	0.0317 (6)	0.0403 (6)	0.0066 (4)	-0.0095 (4)	-0.0149 (5)
Ge4	0.0411 (7)	0.0472 (8)	0.0405 (7)	-0.0177 (6)	-0.0124 (5)	0.0104 (6)
Ge5	0.0322 (7)	0.1163 (15)	0.0784 (11)	-0.0147 (8)	0.0177 (7)	-0.0733 (11)
Ge6	0.0278 (5)	0.0210 (5)	0.0461 (7)	-0.0067 (4)	0.0195 (5)	-0.0075 (5)
Ge7	0.0208 (5)	0.0200 (5)	0.0393 (6)	-0.0013 (4)	0.0145 (4)	-0.0053 (4)
Ge8	0.0382 (6)	0.0143 (4)	0.0185 (5)	-0.0037 (4)	0.0037 (4)	-0.0009 (4)
Ge9	0.0281 (5)	0.0246 (5)	0.0314 (5)	0.0075 (4)	-0.0071 (4)	-0.0028 (4)
K2	0.0175 (8)	0.0140 (8)	0.0225 (9)	-0.0004 (7)	0.0023 (7)	-0.0037 (7)
K3	0.0166 (9)	0.0220 (9)	0.0187 (9)	0.0004 (7)	0.0020 (7)	0.0021 (7)
K5	0.0161 (8)	0.0164 (9)	0.0174 (8)	0.0005 (7)	0.0033 (7)	-0.0007 (7)

7.4.15. $K_2[K(2.2.2\text{-crypt})]_4[Ge_9-Ge_9] \cdot 13 NH_3$

Table 87: Crystallographic data and structure refinement of $K_2[K(2.2.2\text{-crypt})]_4[Ge_9-Ge_9] \cdot 13 NH_3$.

	$K_2[K(2.2.2\text{-crypt})]_4[Ge_9-Ge_9] \cdot 13 NH_3$
Sum formula	$K_6C_{72}H_{183}O_{24}N_{21}Ge_{18}$
Molecular weight [g/mol]	3030.5
Crystal system	monoclinic
Space group	$P2_1/n$
a [Å]	13.860(3)
b [Å]	34.690(7)
c [Å]	29.590(6)
α [°]	90.0
β [°]	90.20(3)
γ [°]	90.0
V [Å ³]	14227(5)
Z	4
T [K]	150
μ [mm ⁻¹]	3.967
Measured reflections	405238
<i>hkl</i> ranges	-17 < <i>h</i> < 17 -43 < <i>k</i> < 43 -36 < <i>l</i> < 36
θ min. / max.	4.14/26.66
R_{int}	0.1483
Independent reflections	28477
Reflections ($I > 2 \sigma$)	11615
Parameters	1072
R_1 ($I > 2 \sigma$; all)	0.1148; 0.2256
wR_2 ($I > 2 \sigma$; all)	0.3355; 0.3922
GooF	1.057
max. / min. residual e ⁻ density [e/Å ³]	1.86; -1.00

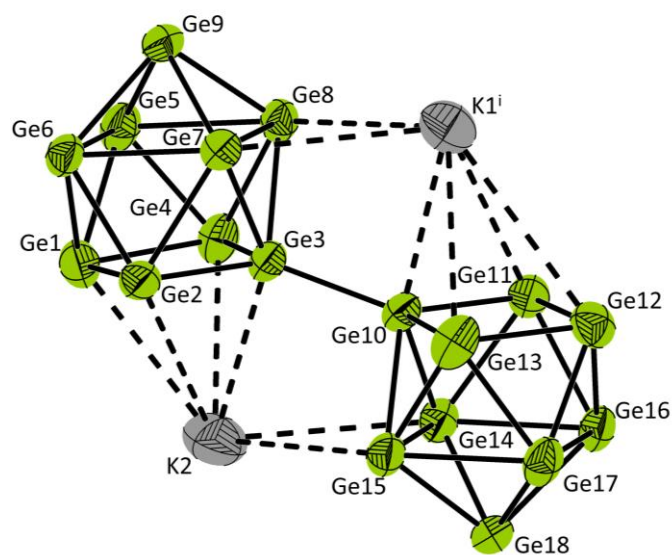


Figure 169: Cluster unit in $K_2[K([2.2.2]crypt)]_4[Ge_9-Ge_9] \cdot 13 NH_3$. Displacement ellipsoids are displayed with a 50 % probability. Green – germanium, grey – potassium.

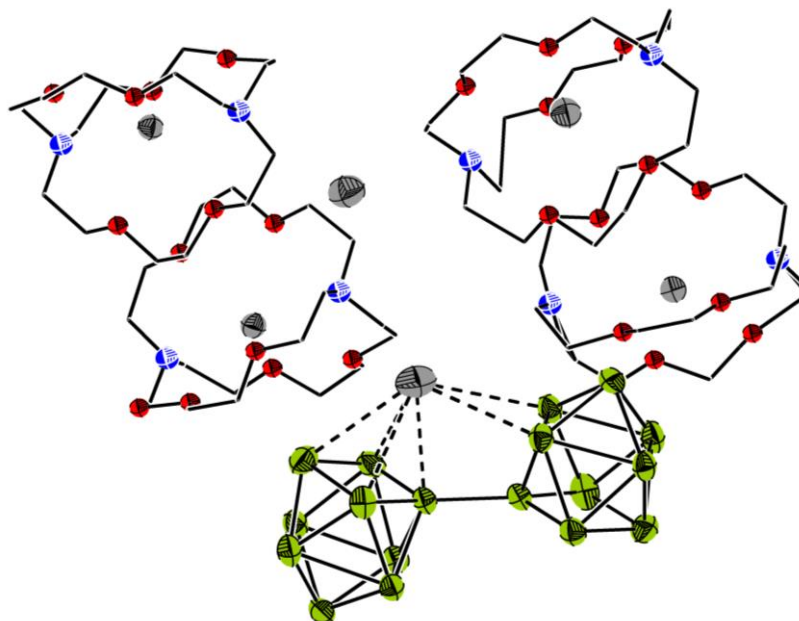


Figure 170: Asymmetric unit in $K_2[K([2.2.2]crypt)]_4[Ge_9-Ge_9] \cdot 13 NH_3$. Displacement ellipsoids are displayed with a 50 % probability. Carbon atoms are displayed as wire and sticks (Displacement ellipsoids of carbon atoms are quite large). Protons are omitted for clarity. Green – germanium, grey – potassium, blue- nitrogen.

8. References

1. *Key World Energy Statistics (2018)*, International Energy Agency, **2018**.
2. Lesch, H.; Kamphausen, K., *Die Menschheit schafft sich ab: Die Erde im Griff des Anthropozän*, Komplet-Media, **2016**.
3. Easterling, D. R.; Evans, J.; Groisman, P. Y.; Karl, T. R.; Kunkel, K. E.; Ambenje, P., *Bull. Am. Meteorol. Soc.* **2000**, 417.
4. Hansen, J.; Ruedy, R.; Sato, M.; Lo, K., *Reviews of Geophysics* **2010**, 48, 1.
5. P. Tans, K. R. N. E. a. S. I. o. O., retrieved from https://www.esrl.noaa.gov/gmd/webdata/ccgg/trends/co2_trend_mlo.png, **2020**.
6. Hollemann, A. F.; Wiberg, E.; Wiberg, N., *Lehrbuch der Anorganischen Chemie*, Vol. 102, Walter de Gruyter, Berlin, Germany, **2007**.
7. Housecroft, C. E.; Sharpe, A. G., *Inorganic Chemistry*, Vol. 2, Ashford Colour Press Ltd., Gosport, **2005**.
8. Papadopoulos, C., *Solid State Electronic Devices*, Springer, New York, U.S.A., **2014**.
9. Cho, E. C.; Park, S.; Hao, X.; Song, D.; Conibeer, G.; Park, S. C.; Green, M. A., *Nanotechnology* **2008**, 19, 245201.
10. Kanatzidis, M. G., *Adv. Mater.* **2007**, 19, 1165.
11. Ashuri, M.; He, Q.; Shaw, L. L., *Nanoscale* **2016**, 8, 74.
12. Graetz, J.; Ahn, C.; Yazami, R.; Fultz, B., *Electrochem. Solid-State Lett.* **2003**, 6, A194.
13. Chan, C. K.; Peng, H.; Liu, G.; McIlwrath, K.; Zhang, X. F.; Huggins, R. A.; Cui, Y., *Nat. Nanotechnol.* **2008**, 3, 31.
14. Chapin, D. M.; Fuller, C. S.; Pearson, G. L., *J. Appl. Phys.* **1954**, 25, 676.
15. Botti, S.; Flores-Livas, J. A.; Amsler, M.; Goedecker, S.; Marques, M. A. L., *Phys. Rev. B* **2012**, 86, 121204.
16. Fowler, A. B.; Howard, W. E.; Brock, G. E., *Phys. Rev.* **1962**, 128, 1664.
17. Fukata, N.; Sato, K.; Mitome, M.; Bando, Y.; Sekiguchi, T.; Kirkham, M.; Hong, J.-i.; Wang, Z. L.; Snyder, R. L., *ACS Nano* **2010**, 4, 3807.
18. Kasper, E.; Schuh, A.; Bauer, G.; Holländer, B.; Kibbel, H., *J. Cryst. Growth* **1995**, 157, 68.
19. Kasper, E., *J. Cryst. Growth* **1995**, 150, 921.
20. Stein, A., *Nature* **2006**, 441, 1055.
21. Pillarisetty, R., *Nature* **2011**, 479, 324.
22. Sevov, S. C.; Goicoechea, J. M., *Organometallics* **2006**, 25, 5678.
23. Höll, R.; Kling, M.; Schroll, E., *Ore Geol. Rev.* **2007**, 30, 145.
24. Claeys, C.; Simoen, E., 2011, Elsevier Science, Amsterdam,
25. Kasper, E.; Kittler, M.; Oehme, M.; Arguirov, T., *Photon. Res.* **2013**, 1, 69.
26. Geier, S.; Jung, R.; Peters, K.; Gasteiger, H. A.; Fattakhova-Rohlfing, D.; Fässler, T. F., *Sustain. Energ. Fuels* **2018**, 2, 85.
27. Bentlohner, M. M.; Waibel, M.; Zeller, P.; Sarkar, K.; Müller-Buschbaum, P.; Fattakhova-Rohlfing, D.; Fässler, T. F., *Angew. Chem. Int. Ed.* **2016**, 55, 2441.
28. Geier, S., Alloy-Based Anodes with Inverse Opal Structure for Lithium Ion Batteries, **2018**, *Chair of Inorganic Chemistry with Focus on Novel Materials*, Munich, Germany, TUM

29. von Schnering, H. G.; Llanos, J.; Chang, J. H.; Peters, K.; Peters, E. M.; Nesper, R., *Z. Kristallogr. - New Cryst. Struct.* **2005**, *220*, 324.
30. Busmann, E.; Lohmeyer, S., *Z. Anorg. Allg. Chem.* **1961**, *312*, 53.
31. Kiefer, F.; Karttunen, A. J.; Döblinger, M.; Fässler, T. F., *Chem. Mater.* **2011**, *23*, 4578.
32. Klemm, W., *Proc. Chem. Soc. London* **1959**, 329.
33. Zintl, E., *Angew. Chem.* **1939**, *52*, 1.
34. Busmann, E., *Z. Anorg. Allg. Chem.* **1961**, *313*, 90.
35. Wade, K., *Chem. Commun.* **1971**, 792.
36. Wade, K., *Adv. Inorg. Chem. Radiochem.* **1976**, *18*, 1.
37. Mingos, D. M. P., *Nat. Phys. Sci.* **1972**, *236*, 99.
38. Mingos, D. M. P., *Acc. Chem. Res.* **1984**, *17*, 311.
39. von Schnering, H. G.; Schwarzl, M.; Chang, J.-H.; Peters, K.; Peters, E.-M.; Nesper, R., *Z. Kristallogr. - New Cryst. Struct.* **2005**, *220*, 525.
40. Grin, Y.; Baitinger, M.; Knip, R.; von Schnering, H. G., *Z. Kristallogr. - New Cryst. Struct.* **1999**, *214*, 453.
41. Bobev, S.; Sevov, S. C., *Polyhedron* **2002**, *21*, 641.
42. Guloy, A. M.; Ramlau, R.; Tang, Z.; Schnelle, W.; Baitinger, M.; Grin, Y., *Nature* **2006**, *443*, 320.
43. Von Schnering, H. G.; Baitinger, M.; Bolle, U.; Carrillo-Cabrera, W.; Curda, J.; Grin, Y.; Heinemann, F.; Llanos, J.; Peters, K.; Schmeding, A.; Somer, M., *Z. Anorg. Allg. Chem.* **1997**, *623*, 1037.
44. Ponou, S.; Fässler, T. F., *Z. Anorg. Allg. Chem.* **2007**, *633*, 393.
45. Queneau, V.; Sevov, S. C., *Angew. Chem. Int. Ed.* **1997**, *36*, 1754.
46. Hoch, C.; Wendorff, M.; C, C. R., *Acta Crystallogr. Sect. C: Cryst. Struct. Commun.* **2002**, *58*, i45.
47. Queneau, V.; Sevov, S. C., *Inorg. Chem.* **1998**, *37*, 1358.
48. Hoch, C.; Wendorff, M.; Röhr, C., *J. Alloys Compd.* **2003**, *361*, 206.
49. Todorov, E.; Sevov, S. C., *Inorg. Chem.* **1998**, *37*, 3889.
50. Queneau, V.; Todorov, E.; Sevov, S. C., *J. Am. Chem. Soc.* **1998**, *120*, 3263.
51. Zintl, E.; Harder, A., *Z. Phys. Chem.* **1931**, *154*, 47.
52. Nienhaus, A.; Hauptmann, R.; Fässler, T. F., *Angew. Chem. Int. Ed.* **2002**, *41*, 3213.
53. Smyth, F. H., *J. Am. Chem. Soc.* **1917**, *39*, 1299.
54. Kummer, D.; Diehl, L., *Angew. Chem. Int. Ed.* **1970**, *9*, 895.
55. Fässler, T. F.; Scharfe, S., *Phil. Trans. R. Soc. A* **2010**, *368*, 1265.
56. Scharfe, S.; Kraus, F.; Stegmaier, S.; Schier, A.; Fässler, T. F., *Angew. Chem. Int. Ed.* **2011**, *50*, 3630.
57. Carrillo-Cabrera, W.; Cardoso Gil, R.; Somer, M.; Persil, Ö.; von Schnering, H. G., *Z. Anorg. Allg. Chem.* **2003**, *629*, 601.
58. Fässler, T. F., *Coord. Chem. Rev.* **2001**, *215*, 347.
59. Corbett, J. D., *Chem. Rev.* **1985**, *85*, 383.
60. Corbett, J. D., *Struct. Bond.* **1997**, *87*, 157.
61. Goicoechea, J. M.; Sevov, S. C., *J. Am. Chem. Soc.* **2004**, *126*, 6860.
62. Fässler, T. F.; Hunziker, M.; Spahr, M. E.; Lueken, H.; Schilder, H., *Z. Anorg. Allg. Chem.* **2000**, *626*, 692.

63. Critchlow, S. C.; Corbett, J. D., *J. Am. Chem. Soc.* **1983**, *105*, 5715.
64. Fässler, T. F.; Hunziker, M., *Inorg. Chem.* **1994**, *33*, 5380.
65. Fässler, T. F.; Schütz, U., *Inorg. Chem.* **1999**, *38*, 1866.
66. Fässler, T. F.; Hoffmann, R., *Angew. Chem. Int. Ed.* **1999**, *38*, 543.
67. Suchentrunk, C.; Korber, N., *Inorg. Chim. Acta* **2006**, *359*, 267.
68. von Schnering, H. G.; Somer, M.; Kaupp, M.; Carrillo-Cabrera, W.; Baitinger, M.; Schmeding, A.; Grin, Y., *Angew. Chem. Int. Ed.* **1998**, *37*, 2359.
69. Rosdahl, J.; Fässler, T. F.; Kloo, L., *Eur. J. Inorg. Chem.* **2005**, *2005*, 2888.
70. Gomez, S. J.; Cheikh, D.; Vo, T.; von Allmen, P.; Lee, K.; Wood, M.; Snyder, G. J.; Dunn, B. S.; Fleurial, J.-P.; Bux, S. K., *Chem. Mater.* **2019**, *31*, 4460.
71. Belin, C. H. E.; Corbett, J. D.; Cisar, A., *J. Am. Chem. Soc.* **1977**, *99*, 7163.
72. Campbell, J.; Schrobilgen, G. J., *Inorg. Chem.* **1997**, *36*, 4078.
73. Zhang, Q.; Armatas, G.; Kanatzidis, M. G., *Inorg. Chem.* **2009**, *48*, 8665.
74. Somer, M.; Carrillo-Cabrera, W.; Peters, E.-M.; Peters, K.; Kaupp, M.; von Schnering, H. G., *Z. Anorg. Allg. Chem.* **1999**, *625*, 37.
75. Hastreiter, F.; Lorenz, C.; Hioe, J.; Gärtner, S.; Nanjundappa, L.; Korber, N.; Gschwind, R. M., *Angew. Chem. Int. Ed.* **2019**, *58*, 3133.
76. Corbett, J. D.; Edwards, P. A., *J. Chem. Soc., Chem. Commun.* **1975**, 984.
77. Edwards, P. A.; Corbett, J. D., *Inorg. Chem.* **1977**, *16*, 903.
78. Gholiee, Y.; Salehzadeh, S.; Khodaveisi, S., *New J. Chem.* **2019**, *43*, 7797.
79. Liu, C.; Li, L.-J.; Pan, Q.-J.; Sun, Z.-M., *Chem. Commun.* **2017**, *53*, 6315.
80. Kircher, P.; Huttner, G.; Heinze, K.; Renner, G., *Angew. Chem. Int. Ed.* **1998**, *37*, 1664.
81. Peter, K.; Gottfried, H.; Laszlo, Z.; Alexander, D., *Angew. Chem. Int. Ed.* **1998**, *37*, 1666.
82. Spiekermann, A.; Hoffmann, S. D.; Fässler, T. F., *Angew. Chem. Int. Ed.* **2006**, *45*, 3459.
83. Ugrinov, A.; Sevov, S. C., *Chem. Eur. J.* **2004**, *10*, 3727.
84. Downie, C.; Mao, J.-G.; Parmar, H.; Guloy, A. M., *Inorg. Chem.* **2004**, *43*, 1992.
85. Lorenz, C.; Gärtner, S.; Korber, N., *Z. Anorg. Allg. Chem.* **2016**, *643*, 141.
86. Lorenz, C.; Gärtner, S.; Korber, N., *Crystals* **2018**, *8*, 276.
87. Wiesler, K.; Brandl, K.; Fleischmann, A.; Korber, N., *Z. Anorg. Allg. Chem.* **2009**, *635*, 508.
88. Waibel, M.; Fässler, T. F., *Z. Naturforsch., B: Chem. Sci.* **2013**, 732.
89. Joseph, S.; Suchentrunk, C.; Korber, N., *Z. Naturforsch., B: Chem. Sci.* **2010**, 1059.
90. Benda, C. B.; Henneberger, T.; Klein, W.; Fässler, T. F., *Z. Anorg. Allg. Chem.* **2016**, *643*, 146.
91. Joseph, S.; Suchentrunk, C.; Kraus, F.; Korber, N., *Eur. J. Inorg. Chem.* **2009**, *2009*, 4641.
92. Suchentrunk, C.; Daniels, J.; Somer, M.; Carrillo-Cabrera, W.; Korber, N., *Z. Naturforsch., B: Chem. Sci.* **2005**, *60b*, 277.
93. Downie, C.; Mao, J.-G.; Guloy, A. M., *Inorg. Chem.* **2001**, *40*, 4721.
94. Carrillo-Cabrera, W.; Aydemir, U.; Somer, M.; Kircali, A.; Fässler, T. F.; Hoffmann, S. D., *Z. Anorg. Allg. Chem.* **2007**, *633*, 1575.
95. Somer, M.; Carrillo-Cabrera, W.; Peters, E. M.; Peters, K.; von Schnering, H. G., *Z. Anorg. Allg. Chem.* **1998**, *624*, 1915.
96. Diehl, L.; Khodadadeh, K.; Kummer, D.; Strähle, J., *Z. Naturforsch., B: Anorg. Chem., Org. Chem.* **1976**, *31*, 522.

97. Diehl, L.; Khodadadeh, K.; Kummer, D.; Strähle, J., *Chem. Ber.* **1976**, *109*, 3404.
98. Corbett, J. D.; Edwards, P. A., *J. Am. Chem. Soc.* **1977**, *99*, 3313.
99. Hauptmann, R.; Hoffmann, R.; Fässler, T. F., *Z. Anorg. Allg. Chem.* **2001**, *627*, 2220.
100. Benda, C. B.; Waibel, M.; Köchner, T.; Fässler, T. F., *Chem. Eur. J.* **2014**, *20*, 16738.
101. Hauptmann, R.; Fässler, T. F., *Z. Anorg. Allg. Chem.* **2002**, *628*, 1500.
102. Yong, L.; Hoffmann, S. D.; Fässler, T. F., *Inorg. Chim. Acta* **2006**, *359*, 4774.
103. Fässler, T. F.; Hoffmann, R., *J. Chem. Soc., Dalton Trans.* **1999**, 3339.
104. Campbell, J.; Dixon, D. A.; Mercier, H. P. A.; Schrobilgen, G. J., *Inorg. Chem.* **1995**, *34*, 5798.
105. Angilella, V.; Belin, C., *Faraday Trans.* **1991**, *87*, 203.
106. Hauptmann, R.; Fässler, T. F., *Z. Kristallogr. - New Cryst. Struct.* **2003**, *218*, 461.
107. Fässler, T. F.; Hunziker, M., *Z. Anorg. Allg. Chem.* **1996**, *622*, 837.
108. Fässler, T. F.; Hoffmann, R., *Z. Kristallogr. - New Cryst. Struct.* **2000**, *215*, 139.
109. Yong, L.; Hoffmann, S. D.; Fässler, T. F., *Zeitschrift für Kristallographie - New Crystal Structures* **2005**, *49*, 220.
110. Goicoechea, J. M.; Sevov, S. C., *Inorg. Chem.* **2005**, *44*, 2654.
111. Åkerstedt, J.; Ponou, S.; Kloo, L.; Lidin, S., *Eur. J. Inorg. Chem.* **2011**, *2011*, 3999.
112. Fässler, T. F.; Hoffmann, S. D., *Angew. Chem. Int. Ed.* **2004**, *43*, 6242.
113. Mitzinger, S.; Broeckaert, L.; Massa, W.; Weigend, F.; Dehnen, S., *Nat. Commun.* **2016**, *7*, 10480.
114. Dehnen, S.; Weinert, B., *Struct. Bond.* **2017**, *174*, 99.
115. Liu, C.; Popov, I. A.; Chen, Z.; Boldyrev, A. I.; Sun, Z.-M., *Chem. Eur. J.* **2018**, *24*, 14583.
116. Mayer, K.; Weßing, J.; Fässler, T. F.; Fischer, R. A., *Angew. Chem. Int. Ed.* **2018**, *57*, 14372.
117. Weinert, B.; Mitzinger, S.; Dehnen, S., *Chem. Eur. J.* **2018**, *24*, 8470.
118. Wilson, R. J.; Weinert, B.; Dehnen, S., *Dalton Trans.* **2018**, *47*, 14861.
119. Liu, C.; Sun, Z.-M., *Coord. Chem. Rev.* **2019**, *382*, 32.
120. Wilson, R. J.; Lichtenberger, N.; Weinert, B.; Dehnen, S., *Chem. Rev.* **2019**, *119*, 8506.
121. Xu, L.; Sevov, S. C., *J. Am. Chem. Soc.* **1999**, *121*, 9245.
122. Hauptmann, R.; Fässler, T. F., *Z. Anorg. Allg. Chem.* **2003**, *629*, 2266.
123. Scharfe, S.; Fässler, T. F., *Z. Anorg. Allg. Chem.* **2011**, *637*, 901.
124. Benda, C. B.; He, H.; Klein, W.; Somer, M.; Fässler, T. F., *Z. Anorg. Allg. Chem.* **2015**, *641*, 1080.
125. Hansen, D. F.; Zhou, B.; Goicoechea, J. M., *J. Organomet. Chem.* **2012**, *721-722*, 53.
126. Ugrinov, A.; Sevov, S. C., *J. Am. Chem. Soc.* **2002**, *124*, 10990.
127. Yong, L.; Hoffmann, S. D.; Fässler, T. F., *Z. Anorg. Allg. Chem.* **2005**, *631*, 1149.
128. Ugrinov, A.; Sevov, S. C., *Inorg. Chem.* **2003**, *42*, 5789.
129. Yong, L.; Hoffmann, S. D.; Fässler, T. F., *Z. Anorg. Allg. Chem.* **2004**, *630*, 1977.
130. Downie, C.; Tang, Z.; Guloy, A. M., *Angew. Chem. Int. Ed.* **2000**, *39*, 337.
131. Benda, C. B.; Schäper, R.; Schulz, S.; Fässler, T. F., *Eur. J. Inorg. Chem.* **2013**, *2013*, 5964.
132. Mayer, K.; Jantke, L.-A.; Schulz, S.; Fässler, T. F., *Angew. Chem. Int. Ed.* **2017**, *56*, 2350.
133. Pancharatna, P. D.; Hoffmann, R., *Inorg. Chim. Acta* **2006**, *359*, 3776.
134. Karttunen, A. J.; Fässler, T. F.; Linnolahti, M.; Pakkanen, T. A., *ChemPhysChem* **2010**, *11*, 1944.

135. Jantke, L.-A.; Fässler, T. F., *Inorganics* **2018**, 6, 31.
136. Wang, J.-Q.; Wahl, B.; Fässler, T. F., *Angew. Chem. Int. Ed.* **2010**, 49, 6592.
137. Geitner, F. S.; Klein, W.; Fässler, T. F., *Dalton Trans.* **2017**, 46, 5796.
138. Ugrinov, A.; Sevov, S. C., *J. Am. Chem. Soc.* **2002**, 124, 2442.
139. Ugrinov, A.; Sevov, S. C., *J. Am. Chem. Soc.* **2003**, 125, 14059.
140. Schnepf, A., *Angew. Chem. Int. Ed.* **2003**, 42, 2624.
141. Li, F.; Sevov, S. C., *Inorg. Chem.* **2012**, 51, 2706.
142. Gillett-Kunnath, M. M.; Oliver, A. G.; Sevov, S. C., *J. Am. Chem. Soc.* **2011**, 133, 6560.
143. Kysliak, O.; Kunz, T.; Schnepf, A., *Eur. J. Inorg. Chem.* **2017**, 2017, 805.
144. Fässler, T. F.; Geitner, F.; Wallach, C., *Chem. Eur. J.* **2018**, 24, 4103.
145. Li, F.; Muñoz-Castro, A.; Sevov, S. C., *Angew. Chem. Int. Ed.* **2012**, 51, 8581.
146. Geitner, F. S.; Dums, J. V.; Fässler, T. F., *J. Am. Chem. Soc.* **2017**, 139, 11933.
147. Schrenk, C.; Neumaier, M.; Schnepf, A., *Inorg. Chem.* **2012**, 51, 3989.
148. Klinkhammer, K. W.; Xiong, Y.; Yao, S., *Angew. Chem. Int. Ed.* **2004**, 43, 6202.
149. Kysliak, O.; Schnepf, A., *Dalton Trans.* **2016**, 45, 2404.
150. Mayer, K.; Schiegerl, L. J.; Kratky, T.; Gunther, S.; Fässler, T. F., *Chem. Commun.* **2017**, 53, 11798.
151. Fässler, T. F.; Wallach, C.; Geitner, F.; Klein, W., *Chem. Eur. J.* **2019**, 25, 12349.
152. Muñoz-Castro, A.; Takahashi, K., *J. Phys. Chem. C* **2017**, 121, 1934.
153. Reddy, G. N.; Parida, R.; Giri, S., *Chem. Commun.* **2017**, 53, 13229.
154. Reddy, G. N.; Parida, R.; Chakraborty, A.; Giri, S., *Chem. Eur. J.* **2018**, 24, 13654.
155. Benda, C. B.; Wang, J.-Q.; Wahl, B.; Fässler, T. F., *Eur. J. Inorg. Chem.* **2011**, 2011, 4262.
156. Hull, M. W.; Sevov, S. C., *J. Am. Chem. Soc.* **2009**, 131, 9026.
157. Hull, M. W.; Sevov, S. C., *Angew. Chem. Int. Ed.* **2007**, 46, 6695.
158. Frischhut, S.; Klein, W.; Fässler, T. F., *Comptes Rendus Chimie* **2018**, 21, 932.
159. Bentlohner, M. M.; Klein, W.; Fard, Z. H.; Jantke, L.-A.; Fässler, T. F., *Angew. Chem. Int. Ed.* **2015**, 54, 3748.
160. Frischhut, S.; Bentlohner, M. M.; Klein, W.; Fässler, T. F., *Inorg. Chem.* **2017**, 56, 10691.
161. Frischhut, S.; Fässler, T. F., *Dalton Trans.* **2018**, 47, 3223.
162. Fässler, T. F.; Frischhut, S.; Klein, W.; Drees, M., *Chem. Eur. J.* **2018**, 24, 9009.
163. Hull, M. W.; Ugrinov, A.; Petrov, I.; Sevov, S. C., *Inorg. Chem.* **2007**, 46, 2704.
164. Gillett-Kunnath, M. M.; Petrov, I.; Sevov, S. C., *Inorg. Chem.* **2010**, 49, 721.
165. Chapman, D. J.; Sevov, S. C., *Inorg. Chem.* **2008**, 47, 6009.
166. Richards, A. F.; Eichler, B. E.; Brynda, M.; Olmstead, M. M.; Power, P. P., *Angew. Chem. Int. Ed.* **2005**, 44, 2546.
167. Kysliak, O.; Schrenk, C.; Schnepf, A., *Inorg. Chem.* **2017**, 56, 9693.
168. Hull, M. W.; Sevov, S. C., *Chem. Commun.* **2012**, 48, 7720.
169. Kocak, F. S.; Downing, D. O.; Zavalij, P.; Lam, Y.-F.; Vedernikov, A. N.; Eichhorn, B. W., *J. Am. Chem. Soc.* **2012**, 134, 9733.
170. Lorenz, C.; Korber, N., *Crystals* **2018**, 8, 374.
171. Henneberger, T.; Klein, W.; Fässler, T. F., *Z. Anorg. Allg. Chem.* **2018**, 644, 1018.
172. Lorenz, C.; Hastreiter, F.; Hioe, J.; Lokesh, N.; Gärtner, S.; Korber, N.; Gschwind, R. M., *Angew. Chem. Int. Ed.* **2018**, 57, 12956.

173. Schiegerl, L. J.; Karttunen, A. J.; Tillmann, J.; Geier, S.; Raudaschl-Sieber, G.; Waibel, M.; Fässler, T. F., *Angew. Chem. Int. Ed.* **2018**, *130*, 13132.
174. Henneberger, T.; Klein, W.; Dums, J.; Fässler, T. F., *Chem. Commun.* **2018**, *54*, 12381.
175. Goicoechea, J. M.; Sevov, S. C., *Organometallics* **2006**, *25*, 4530.
176. Gärtner, S.; Hamberger, M.; Korber, N., *Crystals* **2015**, *5*, 275.
177. Scharfe, S.; Fässler, T. F., *Eur. J. Inorg. Chem.* **2010**, *2010*, 1207.
178. Spiekermann, A.; Hoffmann, S. D.; Kraus, F.; Fässler, T. F., *Angew. Chem. Int. Ed.* **2007**, *46*, 1638.
179. Wang, L.; Wang, Y.; Li, Z.; Ruan, H.; Xu, L., *Dalton Trans.* **2017**, *46*, 6839.
180. Goicoechea, J. M.; Sevov, S. C., *J. Am. Chem. Soc.* **2006**, *128*, 4155.
181. Sun, Z.-M.; Zhao, Y.-F.; Li, J.; Wang, L.-S., *J. Cluster Sci.* **2009**, *20*, 601.
182. Zhou, B.; Goicoechea, J. M., *Chem. Eur. J.* **2010**, *16*, 11145.
183. Benda, C. B.; Waibel, M.; Fässler, T. F., *Angew. Chem. Int. Ed.* **2015**, *54*, 522.
184. Eichhorn, B. W.; Haushalter, R. C.; Pennington, W. T., *J. Am. Chem. Soc.* **1988**, *110*, 8704.
185. Campbell, J.; Mercier, H. P. A.; Franke, H.; Santry, D. P.; Dixon, D. A.; Schrobilgen, G. J., *Inorg. Chem.* **2002**, *41*, 86.
186. Wang, J.-Q.; Stegmaier, S.; Wahl, B.; Fässler, T. F., *Chem. Eur. J.* **2010**, *16*, 1793.
187. Waibel, M.; Kraus, F.; Scharfe, S.; Wahl, B.; Fässler, T. F., *Angew. Chem. Int. Ed.* **2010**, *49*, 6611.
188. Stegmaier, S.; Waibel, M.; Henze, A.; Jantke, L.-A.; Karttunen, A. J.; Fässler, T. F., *J. Am. Chem. Soc.* **2012**, *134*, 14450.
189. Waibel, M.; Raudaschl-Sieber, G.; Fässler, T. F., *Chem. Eur. J.* **2011**, *17*, 13391.
190. Waibel, M.; Pecher, O.; Mausolf, B.; Haarmann, F.; Fässler, T. F., *Eur. J. Inorg. Chem.* **2013**, *2013*, 5541.
191. Mitzinger, S.; Bandemehr, J.; Reiter, K.; Scott McIndoe, J.; Xie, X.; Weigend, F.; Corrigan, J. F.; Dehnen, S., *Chem. Commun.* **2018**, *54*, 1421.
192. Wiberg, N.; Hochmuth, W.; Nöth, H.; Appel, A.; Schmidt-Amelunxen, M., *Angew. Chem. Int. Ed.* **1996**, *35*, 1333.
193. Zachwieja, U.; Wlodarski, J., *Z. Anorg. Allg. Chem.* **2004**, *630*, 993.
194. Evgeny, T.; C., S. S., *Angew. Chem. Int. Ed.* **1999**, *38*, 1775.
195. Kysliak, O.; Schrenk, C.; Schnepf, A., *Chem. Eur. J.* **2016**, *22*, 18787.
196. Mayer, K.; Schiegerl, L. J.; Fässler, T. F., *Chem. Eur. J.* **2016**, *22*, 18794.
197. Geitner, F. S.; Giebel, M. A.; Pöthig, A.; Fässler, T. F., *Molecules* **2017**, *22*, 1204.
198. Schiegerl, L. J.; Geitner, F. S.; Fischer, C.; Klein, W.; Fässler, T. F., *Z. Anorg. Allg. Chem.* **2016**, *642*, 1419.
199. Geitner, F. S.; Klein, W.; Storchewa, O.; Tilley, T. D.; Fässler, T. F., *Inorg. Chem.* **2019**, *58*, 13293.
200. Geitner, F. S.; Fässler, T. F., *Eur. J. Inorg. Chem.* **2016**, *2016*, 2688.
201. Michenfelder, N. C.; Gienger, C.; Schnepf, A.; Unterreiner, A.-N., *Dalton Trans.* **2019**, *48*, 15577.
202. Li, F.; Sevov, S. C., *Inorg. Chem.* **2015**, *54*, 8121.
203. Schenk, C.; Henke, F.; Santiso-Quiñones, G.; Krossing, I.; Schnepf, A., *Dalton Trans.* **2008**, 4436.

204. Henke, F.; Schenk, C.; Schnepf, A., *Dalton Trans.* **2009**, 9141.
205. Kysliak, O.; Schnepf, A., *Z. Anorg. Allg. Chem.* **2019**, 645, 335.
206. Kysliak, O.; Nguyen, D. D.; Clayborne, A. Z.; Schnepf, A., *Inorg. Chem.* **2018**, 57, 12603.
207. Binder, M.; Schrenk, C.; Block, T.; Pöttgen, R.; Schnepf, A., *Chem. Commun.* **2017**, 53, 11314.
208. Kysliak, O.; Schrenk, C.; Schnepf, A., *Inorg. Chem.* **2015**, 54, 7083.
209. Scharfe, S.; Fässler, T. F.; Stegmaier, S.; Hoffmann, S. D.; Ruhland, K., *Chem. Eur. J.* **2008**, 14, 4479.
210. Wang, J.-Q.; Stegmaier, S.; Fässler, T. F., *Angew. Chem. Int. Ed.* **2009**, 48, 1998.
211. Sun, Z.-M.; Xiao, H.; Li, J.; Wang, L.-S., *J. Am. Chem. Soc.* **2007**, 129, 9560.
212. Stegmaier, S.; Fässler, T. F., *J. Am. Chem. Soc.* **2011**, 133, 19758.
213. Hlukhyy, V.; Stegmaier, S.; van Wüllen, L.; Fässler, T. F., *Chem. Eur. J.* **2014**, 20, 12157.
214. Rios, D.; Gillett-Kunnath, M. M.; Taylor, J. D.; Oliver, A. G.; Sevov, S. C., *Inorg. Chem.* **2011**, 50, 2373.
215. Goicoechea, J. M.; Sevov, S. C., *Angew. Chem. Int. Ed.* **2005**, 44, 4026.
216. He, H.; Klein, W.; Jantke, L.-A.; Fässler, T. F., *Z. Anorg. Allg. Chem.* **2014**, 640, 2864.
217. Hlukhyy, V.; He, H.; Jantke, L.-A.; Fässler, T. F., *Chem. Eur. J.* **2012**, 18, 12000.
218. Gillett-Kunnath, M. M.; Paik, J. I.; Jensen, S. M.; Taylor, J. D.; Sevov, S. C., *Inorg. Chem.* **2011**, 50, 11695.
219. Kesanli, B.; Halsig, J. E.; Zavalij, P.; Fettingner, J. C.; Lam, Y.-F.; Eichhorn, B. W., *J. Am. Chem. Soc.* **2007**, 129, 4567.
220. Liu, C.; Li, L.-J.; Jin, X.; McGrady, J. E.; Sun, Z.-M., *Inorg. Chem.* **2018**, 57, 3025.
221. Zhou, B.; Denning, M. S.; Kays, D. L.; Goicoechea, J. M., *J. Am. Chem. Soc.* **2009**, 131, 2802.
222. Kramer, T.; Duckworth, J. C. A.; Ingram, M. D.; Zhou, B.; McGrady, J. E.; Goicoechea, J. M., *Dalton Trans.* **2013**, 42, 12120.
223. Liu, C.; Jin, X.; Li, L.-J.; Xu, J.; McGrady, J. E.; Sun, Z.-M., *Chemical Science* **2019**, 10, 4394.
224. Sevov, S. C.; Corbett, J. D., *J. Am. Chem. Soc.* **1993**, 115, 9089.
225. Esenturk, E. N.; Fettingner, J.; Eichhorn, B. W., *Chem. Commun.* **2005**, 247.
226. Esenturk, E. N.; Fettingner, J.; Eichhorn, B. W., *J. Am. Chem. Soc.* **2006**, 128, 9178.
227. Cetin, A.; Esenturk, O.; Esenturk, E. N., *Eur. J. Inorg. Chem.* **2017**, 2017, 2413.
228. Eichhorn, B. W.; Fettingner, J.; Esenturk, E. N., *Polyhedron* **2006**, 25, 521.
229. Kocak, F. S.; Zavalij, P.; Eichhorn, B. W., *Chem. Eur. J.* **2011**, 17, 4858.
230. Kesanli, B.; Fettingner, J.; Gardner, D. R.; Eichhorn, B. W., *J. Am. Chem. Soc.* **2002**, 124, 4779.
231. Esenturk, E. N.; Fettingner, J.; Lam, Y.-F.; Eichhorn, B. W., *Angew. Chem. Int. Ed.* **2004**, 43, 2132.
232. Espinoza-Quintero, G.; Duckworth, J. C. A.; Myers, W. K.; McGrady, J. E.; Goicoechea, J. M., *J. Am. Chem. Soc.* **2014**, 136, 1210.
233. Zhou, B.; Krämer, T.; Thompson, A. L.; McGrady, J. E.; Goicoechea, J. M., *Inorg. Chem.* **2011**, 50, 8028.
234. Scherf, L. M.; Zeilinger, M.; Fässler, T. F., *Inorg. Chem.* **2014**, 53, 2096.
235. Bobev, S.; Sevov, S. C., *Inorg. Chem.* **2001**, 40, 5361.

236. Wang, Y.; Wang, L. L.; Ruan, H. P.; Luo, B. L.; Sang, R. L.; Xu, L., *Chin. J. Struc. Chem.* **2015**, *34*, 1253.
237. Kumar, V.; Kawazoe, Y., *Appl. Phys. Lett.* **2002**, *80*, 859.
238. Goicoechea, J. M.; McGrady, J. E., *Dalton Trans.* **2015**, *44*, 6755.
239. Hagelberg, F.; Xiao, C.; Lester, W. A., *Phys. Rev. B* **2003**, *67*, 035426-1.
240. Sekhar, P.; Ghosh, A.; Joshi, M.; Ghanty, T. K., *J. Phys. Chem. C* **2017**, *121*, 11932.
241. Joshi, M.; Chandrasekar, A.; Ghanty, T. K., *Phys. Chem. Chem. Phys.* **2018**, *10*, 15253.
242. Liu, C.; Popov, I. A.; Li, L.-J.; Li, N.; Boldyrev, A. I.; Sun, Z.-M., *Chem. Eur. J.* **2018**, *24*, 699.
243. Jin, X.; Espinoza-Quintero, G.; Below, B.; Arcisauskaite, V.; Goicoechea, J. M.; McGrady, J. E., *J. Organomet. Chem.* **2015**, *792*, 149.
244. Esenturk, E. N.; Fetting, J. C.; Eichhorn, B. W., *J. Am. Chem. Soc.* **2006**, *128*, 12.
245. Goicoechea, J. M.; Sevov, S. C., *J. Am. Chem. Soc.* **2005**, *127*, 7676.
246. Kocak, F. S.; Zavalij, P.; Lam, Y.-F.; Eichhorn, B. W., *Inorg. Chem.* **2008**, *47*, 3515.
247. Reis, C. L.; Pacheco, J. M., *J. Phys.: Condens. Matter* **2009**, *22*, 035501-1.
248. Iwasa, T.; Nakajima, A., *J. Phys. Chem. C* **2012**, *116*, 14071.
249. Zhang, C.; Morgan, H. W. T.; Wang, Z.; Liu, C.; Sun, Z.-M.; McGrady, J. E., *Dalton Trans.* **2019**, *48*, 15888.
250. Moses, M. J.; Fetting, J. C.; Eichhorn, B. W., *Science* **2003**, *300*, 778.
251. Li, Z.; Ruan, H.; Wang, L.; Liu, C.; Xu, L., *Dalton Trans.* **2017**, *46*, 3453.
252. Wang, Y.; Moses-DeBusk, M.; Stevens, L.; Hu, J.; Zavalij, P.; Bowen, K.; Dunlap, B. I.; Glaser, E. R.; Eichhorn, B. W., *J. Am. Chem. Soc.* **2017**, *139*, 619.
253. Bergmann, G.; Waugh, J. L. T.; Pauling, L., *Acta Cryst.* **1957**, *10*, 254.
254. Stegmaier, S.; Fässler, T. F., *Angew. Chem. Int. Ed.* **2012**, *51*, 2647.
255. Wilson, R. J.; Hastreiter, F.; Reiter, K.; Büschelberger, P.; Wolf, R.; Gschwind, R. M.; Weigend, F.; Dehnen, S., *Angew. Chem. Int. Ed.* **2018**, *57*, 15359.
256. Lips, F.; Clérac, R.; Dehnen, S., *Angew. Chem. Int. Ed.* **2011**, *50*, 960.
257. Lichtenberger, N.; Wilson, R. J.; Eulenstein, A. R.; Massa, W.; Clérac, R.; Weigend, F.; Dehnen, S., *J. Am. Chem. Soc.* **2016**, *138*, 9033.
258. Lips, F.; Clérac, R.; Dehnen, S., *J. Am. Chem. Soc.* **2011**, *133*, 14168.
259. Li, F.; Muñoz-Castro, A.; Sevov, S. C., *Angew. Chem. Int. Ed.* **2016**, *55*, 8630.
260. Perla, L. G.; Sevov, S. C., *J. Am. Chem. Soc.* **2016**, *138*, 9795.
261. Spiekermann, A.; Hoffmann, S. D.; Fässler, T. F.; Krossing, I.; Preiss, U., *Angew. Chem. Int. Ed.* **2007**, *46*, 5248.
262. Wang, Y.; Qin, Q.; Wang, J.; Sang, R.; Xu, L., *Chem. Commun.* **2014**, *50*, 4181.
263. Kysliak, O.; Schrenk, C.; Schnepf, A., *Angew. Chem. Int. Ed.* **2016**, *55*, 3216.
264. Perla, L. G.; Muñoz-Castro, A.; Sevov, S. C., *J. Am. Chem. Soc.* **2017**, *139*, 15176.
265. Perla, L. G.; Sevov, S. C., *Angew. Chem. Int. Ed.* **2016**, *55*, 6721.
266. Schrenk, C.; Schnepf, A., *Main Group Met. Chem.* **2013**, *36*, 161.
267. Schrenk, C.; Gerke, B.; Pöttgen, R.; Clayborne, A.; Schnepf, A., *Chem. Eur. J.* **2015**, *21*, 8222.
268. Schnepf, A. B.; Schrenk, C.; Kunz, T., *Angew. Chem. Int. Ed.* **2018**, *57*, 4088.
269. Henke, F.; Schenk, C.; Schnepf, A., *Dalton Trans.* **2011**, *40*, 6704.
270. Kasavajjula, U.; Wang, C.; Appleby, J. A., *J. Power Sources* **2007**, *163*, 1003.
271. Obrovacz, M. N.; Christensen, L., *Electrochem. Solid-State Lett.* **2004**, *7*, A93.

272. Zeilinger, M.; Baran, V.; van Wüllen, L.; Häussermann, U.; Fässler, T. F., *Chem. Mater.* **2013**, *25*, 4113.
273. Johnson, Q.; Smith, G. S.; Wood, D., *Acta Cryst.* **1965**, *18*, 131.
274. Axel, H.; Schäfer, H.; Weiss, A., *Z. Naturforsch., B: Anorg. Chem., Org. Chem.* **1966**, *21*, 115.
275. Kotina, I. M.; Kuryatkov, V. V.; Mosina, G. N.; Novikov, S. R.; Sorokin, L. M., *Fiz. Tverd. Tela* **1984**, *26*, 436.
276. Zeilinger, M.; Benson, D.; Häussermann, U.; Fässler, T. F., *Chem. Mater.* **2013**, *25*, 1960.
277. Gladyshevskii, E. I.; Oleksiv, G. I.; Krypyakevych, P. I., *Crystallogr. Rep.* **1964**, *9*, 269.
278. Toffoletti, L.; Kirchhain, H.; Landesfeind, J.; Klein, W.; van Wüllen, L.; Gasteiger, H. A.; Fässler, T. F., *Chem. Eur. J.* **2016**, *22*, 17635.
279. Eickhoff, H.; Toffoletti, L.; Klein, W.; Raudaschl-Sieber, G.; Fässler, T. F., *Inorg. Chem.* **2017**, *56*, 6688.
280. Strangmueller, S.; Eickhoff, H.; Müller, D.; Klein, W.; Raudaschl-Sieber, G.; Kirchhain, H.; Sedlmeier, C.; Baran, V.; Senyshyn, A.; Deringer, V. L.; van Wüllen, L.; Gasteiger, H. A.; Fässler, T. F., *J. Am. Chem. Soc.* **2019**, *141*, 14200.
281. Toffoletti, L., Synthesis and Characterization of Binary and Ternary Phases in the Li–Si–P System as New Materials for Li-ion Batteries, **2015**, *Chair of Inorganic Chemistry with Focus on Novel Materials*, Munich, Germany, TUM
282. Eickhoff, H.; Strangmüller, S.; Klein, W.; Kirchhain, H.; Dietrich, C.; Zeier, W. G.; van Wüllen, L.; Fässler, T. F., *Chem. Mater.* **2018**, *30*, 6440.
283. Dr. Henrick Eickhoff and Stefan Strangmüller, M. Sc., Chair of Inorganic Chemistry with Focus on Novel Materials, are working on the research of Li/Sn/P phases as potential battery materials.
284. Armatas, G. S.; Kanatzidis, M. G., *Science* **2006**, *313*, 817.
285. Sun, D.; Riley, A. E.; Cadby, A. J.; Richman, E. K.; Korlann, S. D.; Tolbert, S. H., *Nature* **2006**, *441*, 1126.
286. Armatas, G. S.; Kanatzidis, M. G., *Adv. Mater.* **2008**, *20*, 546.
287. Armatas, G. S.; Kanatzidis, M. G., *Nano Lett.* **2010**, *10*, 3330.
288. Ma, X.; Xu, F.; Atkins, T. M.; Goforth, A. M.; Neiner, D.; Navrotsky, A.; Kauzlarich, S. M., *Dalton Trans.* **2009**, 10250.
289. Nolan, B. M.; Henneberger, T.; Waibel, M.; Fässler, T. F.; Kauzlarich, S. M., *Inorg. Chem.* **2015**, *54*, 396.
290. Pelosi, M.; Tillard, M.; Zitoun, D., *J. Nanopart. Res.* **2013**, *15*, 1.
291. Mayer, K., Molecular Tetrel and Pentel Element Anions – Productive Source for Intermetalloid Clusters and Materials, **2018**, *Chair of Inorganic Chemistry with Focus on Novel Materials*, Munich, Germany, TUM
292. Grüttner, A.; Nesper, R.; von Schnering, H. G., *Angew. Chem.* **1982**, *94*, 933.
293. Schwarz, M.; Nesper, R.; von Schnering, H. G., *J. Less Common Met.* **1988**, *137*, 297.
294. Zeilinger, M.; Jantke, L.-A.; Scherf, L. M.; Kiefer, F. J.; Neubüser, G.; Kienle, L.; Karttunen, A. J.; Konar, S.; Häussermann, U.; Fässler, T. F., *Chem. Mater.* **2014**, *26*, 6603.
295. Kurakevych, O. O.; Le Godec, Y.; Crichton, W. A.; Strobel, T. A., *Energy Procedia* **2016**, *92*, 839.

296. Kurakevych, O. O.; Godec, Y. L.; Strobel, T. A.; Kim, D. Y.; Crichton, W. A.; Guignard, J., *Journal of Physics: Conference Series* **2017**, *950*, 042049.
297. Guerette, M.; Ward, M. D.; Lokshin, K. A.; Wong, A. T.; Zhang, H.; Stefanoski, S.; Kurakevych, O.; Le Godec, Y.; Juhl, S. J.; Alem, N.; Fei, Y.; Strobel, T. A., *Cryst. Growth Des.* **2018**, *18*, 7410.
298. Kurakevych, O. O.; Strobel, T. A.; Kim, D. Y.; Muramatsu, T.; Struzhkin, V. V., *Cryst. Growth Des.* **2013**, *13*, 303.
299. Kiefer, F.; Hlukhyi, V.; Karttunen, A. J.; Fässler, T. F.; Gold, C.; Scheidt, E.-W.; Scherer, W.; Nylen, J.; Häussermann, U., *J. Mater. Chem.* **2010**, *20*, 1780.
300. Zaikina, J. V.; Muthuswamy, E.; Lilova, K. I.; Gibbs, Z. M.; Zeilinger, M.; Snyder, G. J.; Fässler, T. F.; Navrotsky, A.; Kauzlarich, S. M., *Chem. Mater.* **2014**, *26*, 3263.
301. López-Cruz, E.; Cardona, M., *Solid State Commun.* **1983**, *45*, 787.
302. Conesa, J. C., *J. Phys. Chem. B* **2002**, *106*, 3402.
303. Scherf, L. M.; Hattendorff, J.; Buchberger, I.; Geier, S.; Gasteiger, H. A.; Fässler, T. F., *J. Mater. Chem.* **2017**, *5*, 11179.
304. Tang, Z.; Litvinchuk, A. P.; Gooch, M.; Guloy, A. M., *J. Am. Chem. Soc.* **2018**, *140*, 6785.
305. Courac, A.; Le Godec, Y.; Renero-Lecuna, C.; Moutaabbid, H.; Kumar, R.; Coelho-Diogo, C.; Gervais, C.; Portehault, D., *Inorg. Chem.* **2019**, *58*, 10822.
306. Korber, N.; Fleischmann, A., *J. Chem. Soc., Dalton Trans.* **2001**, 383.
307. Axel, H.; Schaefer, H.; Weiss, A., *Angew. Chem.* **1965**, *77*, 379.
308. Zeilinger, M.; Kurylyshyn, I. M.; Häussermann, U.; Fässler, T. F., *Chem. Mater.* **2013**, *25*, 4623-4632.
309. Chevrier, V. L.; Zwanziger, J. W.; Dahn, J. R., *J. Alloys Compd.* **2010**, *496*, 25.
310. Kuhn, A.; Dupke, S.; Kunze, M.; Puravankara, S.; Langer, T.; Pöttgen, R.; Winter, M.; Wiemhöfer, H.-D.; Eckert, H.; Heitjans, P., *J. Phys. Chem. C* **2014**, *118*, 28350-28360.
311. Schaefer, H.; Axel, H.; Menges, E.; Weiss, A., *Z. Naturforsch., B: Anorg. Chem., Org. Chem.* **1965**, *20*, 394.
312. Zeilinger, M.; Fässler, T. F., *Dalton Trans.* **2014**, *43*, 14959.
313. Kiefer, F.; Fässler, T. F., *Solid State Sci.* **2011**, *13*, 636-640.
314. Kiefer, F.; Fässler, T. F., *Solid State Sci.* **2011**, *13*, 636.
315. Frank, U.; Müller, W., *Z. Naturforsch., B: Anorg. Chem., Org. Chem.* **1975**, *30*, 313.
316. Hopf, V.; Müller, W.; Schäfer, H., *Z. Naturforsch., B: Anorg. Chem., Org. Chem.* **1972**, *27*, 1157.
317. Hopf, V.; Schaefer, H.; Weiss, A., *Z. Naturforsch., B: Anorg. Chem., Org. Chem.* **1970**, *25*, 653.
318. Menges, E.; Hopf, V.; Schaefer, H.; Weiss, A., *Z. Naturforsch., B: Anorg. Chem., Org. Chem.* **1969**, *24*, 1351.
319. Hansen, D. A.; Chang, L. J., *Acta Crystallogr. B* **1969**, *25*, 2392-2395.
320. Robert, F.; Lippens, P. E.; Fourcade, R.; Jumas, J.-C.; Gillot, F.; Morcrette, M.; Tarascon, J.-M., *Hyperfine Interact.* **2006**, *167*, 797-801.
321. Lupu, C.; Mao, J.-G.; Rabalais, J. W.; Guloy, A. M.; Richardson, J. W., *Inorg. Chem.* **2003**, *42*, 3765-3771.
322. Yin, F.; Su, X.; Li, Z.; Wang, J., *J. Alloys Compd.* **2005**, *393*, 105-108.
323. Gasior, W.; Moser, Z.; Zakulski, W., *J. Non-Cryst. Solids* **1996**, *205*, 379-382.

324. Dahn, J. R.; Courtney, I. A.; Mao, O., *Solid State Ion.* **1998**, *111*, 289-294.
325. Gladyshevskii, E. I.; Oleksiv, G. I.; Kripyakevich, P. I., *Sov. Phys. - Crystallogr.* **1964**, *9*, 269.
326. Frank, U.; Müller, W., *Z. Naturforsch.* **1975**, *30b*, 316-322.
327. Frank, U.; Müller, W.; Schäfer, H., *Z. Naturforsch.* **1975**, *30b*, 1-5.
328. Frank, U.; Müller, W.; Schäfer, H., *Z. Naturforsch.* **1975**, *30b*, 6-9.
329. Müller, W., *Z. Naturforsch.* **1974**, *29b*, 304-307.
330. Müller, W.; Schäfer, H., *Z. Naturforsch.* **1973**, *28b*, 246-248.
331. Copestake, J., *J. Non-Cryst. Solids* **1984**, *61-62*, 231.
332. Zhou, C., *J. Nucl. Mater.* **2016**, *477*, 95.
333. Zalkin, A.; Ramsey, W. J., *J. Phys. Chem. A* **1956**, *60*, 234.
334. Frigerio, N., *Nucl. Technol.* **1971**, *10*, 322.
335. Rollier, J., *Z. Kristallogr.* **1939**, *101*, 470.
336. Tkachenko, N. V.; Boldyrev, A., *Chemical Science* **2019**, *10*, 5761.
337. Wilson, W. L.; Rudolph, R. W.; Lohr, L. L.; Taylor, R. C.; Pyykko, P., *Inorg. Chem.* **1986**, *25*, 1535.
338. Slavik, H., Synthese und Charakterisierung von Doppelsalzen mit Clustern der Tetrelelemente, **2017**, *Chair of Inorganic Chemistry with Focus on Novel Materials*, Munich, Germany, TUM
339. Giebel, M., Investigation of Soluble Mixed Si-Ge Clusters and Sn-Bi Alloys for the Synthesis of Macroporous Thin Films, **2019**, *Chair of Inorganic Chemistry with Focus on Novel Materials*, Munich, Germany, TUM
340. Frank, U.; Müller, W., *Z. Naturforsch., B: Anorg. Chem., Org. Chem.* **1975**, *30*, 313.
341. Hopf, V.; Schäfer, H.; Weiss, A., *Z. Naturforsch., B: Anorg. Chem., Org. Chem.* **1970**, *25*, 653.
342. Thompson, H. S., *J. R. Agric. Soc. Engl.* **1850**, *11*, 68.
343. Way, J. T., *J. R. Agric. Soc. Engl.* **1850**, *11*, 313.
344. Adams, B. A.; Holmes, E. L., *J. Soc. Chem. Ind. London* **1935**, *54*, 1.
345. De Dardel, F.; Arden, T. V., Wiley-VCH: Weinheim, 2012; Vol. 19, p 474.
346. Mustafa, S.; Shah, K. H.; Naeem, A.; Ahmad, T.; Waseem, M., *Desalination* **2010**, *264*, 108.
347. Phipps, A.; Hume, D., *J. Am. Chem. Soc.* **1967**, *75*, 6348.
348. Klein, W.; Jansen, M., *Z. Naturforsch., B: Chem. Sci.* **1999**, *54b*, 1345.
349. Klein, W.; Armbruster, K.; Jansen, M., *Chem. Commun.* **1998**, 707.
350. Klein, W.; Jansen, M., *Z. Anorg. Allg. Chem.* **2000**, *626*, 947.
351. Klein, W.; Jansen, M., *Z. Naturforsch., B: Chem. Sci.* **2001**, *56b*, 287.
352. GmbH, S. A. I., ICP-OES-Analyzers Plasma Views: Axial, Radial, Dual, MultiView and New Dual Side-On, **2019**, 28.08.2019, <https://www.analytica-world.com/de/whitepaper/1126584/icp-oes-plasmabetrachtungs-techniken-im-vergleich-axial-radial-dual-multiview-und-das-neue-dual-side-on.html>.
353. PerkinElmer, ICP Optical Emission, **2019**, 28.08.2019, https://www.perkinelmer.com/CMSResources/Images/44-74835TCH_DualViewICP.pdf.
354. Shamsipur, M.; Madrakian, T., *J. Coord. Chem.* **2000**, *52*, 139.
355. Stenger, H.; Weller, F.; Dehnicke, K., *Z. Anorg. Allg. Chem.* **1991**, *606*, 109.
356. Ströbele, M.; Meyer, H.-J., *Z. Naturforsch., B: Chem. Sci.* **2001**, *56*, 1025.

357. Alizadeh, N., *Spectrochim. Acta, Part A* **2011**, 78, 488.
358. Zhang, H.; Wang, X.; Zhang, K.; Teo, B. K., *Inorg. Chem.* **1998**, 37, 3490.
359. Inokuchi, Y.; Nakatsuma, M.; Kida, M.; Ebata, T., *J. Phys. Chem. A* **2016**, 120, 6394.
360. Xu, J.; Wang, C.; Wang, T.; Wang, Y.; Kang, Q.; Liu, Y.; Tian, Y., *RSC Advances* **2018**, 8, 11528.
361. Chockla, A. M.; Korgel, B. A., *J. Mater. Chem.* **2009**, 19, 996.
362. Hüger, E.; Strauß, F.; Stahn, J.; Deubener, J.; Bruns, M.; Schmidt, H., *Sci. Rep.* **2018**, 8, 17607.
363. Fortner, J.; Yu, R. Q.; Lannin, J. S., *J. Vac. Sci. Technol., A* **1990**, 8, 3493.
364. Zaitseva, N.; Dai, Z. R.; Grant, C. D.; Harper, J.; Saw, C., *Chem. Mater.* **2007**, 19, 5174.
365. Olovsson, I.; Templeton, D. H., *Acta Cryst.* **1959**, 12, 832.
366. Xue, Z.; He, D.; Xie, X., *J. Mater. Chem. A* **2015**, 3, 19218.
367. Freitag, K. M.; Kirchhain, H.; Wüllen, L. v.; Nilges, T., *Inorg. Chem.* **2017**, 56, 2100.
368. Walke, P.; Freitag, K. M.; Kirchhain, H.; Kaiser, M.; van Wüllen, L.; Nilges, T., *Z. Anorg. Allg. Chem.* **2018**, 644, 1863.
369. Gadjourova, Z.; Martín y Marero, D.; Andersen, K. H.; Andreev, Y. G.; Bruce, P. G., *Chem. Mater.* **2001**, 13, 1282.
370. Arun, N.; Vasudevan, S.; Ramanathan, K. V., *J. Chem. Phys.* **2003**, 119, 2840.
371. Köster, T. K. J.; van Wüllen, L., *Solid State Ion.* **2008**, 178, 1879.
372. Yanai, N.; Uemura, T.; Horike, S.; Shimomura, S.; Kitagawa, S., *Chem. Commun.* **2011**, 47, 1722.
373. Taylor, B. R.; Kauzlarich, S. M.; Delgado, G. R.; Lee, H. W. H., *Chem. Mater.* **1999**, 11, 2493.
374. Gibson, N.; Shenderova, O.; Luo, T. J. M.; Moseenkov, S.; Bondar, V.; Puzyr, A.; Purtov, K.; Fitzgerald, Z.; Brenner, D. W., *Diamond Relat. Mater.* **2009**, 18, 620.
375. Liu, J.; Liang, C.; Tian, Z.; Zhang, S.; Shao, G., *Sci. Rep.* **2013**, 3, 1741.
376. Heinz, H.; Pramanik, C.; Heinz, O.; Ding, Y.; Mishra, R. K.; Marchon, D.; Flatt, R. J.; Estrela-Lopis, I.; Llop, J.; Moya, S.; Ziolo, R. F., *Surf. Sci. Rep.* **2017**, 72, 1.
377. Scharfe, S., Untersuchungen zur Reaktivität von Zintl-Anionen der Tetrele in Lösung, **2010**, Chair of Inorganic Chemistry with Focus on Novel Materials, Munich, Germany, TUM
378. Somer, M.; Aydemir, U.; Baitinger, M.; von Schnering, H. G., *Z. Anorg. Allg. Chem.* **2006**, 632, 1281.
379. Kliche, G.; von Schnering, H. G.; Schwarz, M., *Z. Anorg. Allg. Chem.* **1992**, 608, 131.
380. Laury, M. L.; Carlson, M. J.; Wilson, A. K., *J. Comput. Chem.* **2012**, 33, 2380.
381. Nolas, G. S.; Kendziora, C. A., *Phys. Rev. B* **2000**, 62, 7157.
382. Dong, J.; Sankey, O. F.; Ramachandran, G. K.; McMillan, P. F., *J. Appl. Phys.* **2000**, 87, 7726.
383. Myles, C. W.; Dong, J.; Sankey, O. F.; Kendziora, C. A.; Nolas, G. S., *Phys. Rev. B* **2002**, 65, 235208-1.
384. Olijnyk, H., *Phys. Rev. B* **1992**, 6589 - 6591.
385. Boyko, M., Poler Intermetallics at the Border Between Hume-Rothery and Zintl Phases Investigations in the Systems Alkali Metal - Tin with Late Transition and p-Block Metals,

2019, *Chair of Inorganic Chemistry with Focus on Novel Materials*, Munich, Germany, TUM

386. Fässler, T. F.; Witzel, B. J. L.; Klein, W.; Dums, J. V.; Boyko, M., *Angew. Chem. Int. Ed.* **2019**, *58*, 12908.
387. Franke, P.; Neuschütz, D., Co-Ge (Cobalt - Germanium). In *Binary Systems. Part 5: Binary Systems Supplement 1: Phase Diagrams, Phase Transition Data, Integral and Partial Quantities of Alloys*, Franke, P.; Neuschütz, D., Eds. Springer Berlin Heidelberg: Berlin, Heidelberg, 2007; p 1.
388. Devasagayaraj, A.; Achyutha Rao, S.; Periasamy, M., *J. Organomet. Chem.* **1991**, *403*, 387.
389. Hieber, W.; Mühlbauer, F.; Ehmann, E. A., *Ber. Dtsch. Chem. Ges.* **1932**, *65*, 1090.
390. Hammer, R.; Klein, H.-F., *Z. Naturforsch., B: Anorg. Chem., Org. Chem.* **1977**, *32*, 138.
391. Warnock, G. F.; Cooper, N. J., *Organometallics* **1989**, *8*, 1826.
392. Wolf, R.; Ehlers, A. W.; Slootweg, J. C.; Lutz, M.; Gudat, D.; Hunger, M.; Spek, A. L.; Lammertsma, K., *Angew. Chem. Int. Ed.* **2008**, *47*, 4584.
393. Malberg, J.; Bodensteiner, M.; Paul, D.; Wiegand, T.; Eckert, H.; Wolf, R., *Angew. Chem. Int. Ed.* **2014**, *53*, 2771.
394. Rödl, C.; Wolf, R., *Eur. J. Inorg. Chem.* **2016**, *2016*, 736.
395. Coburger, P.; Demeshko, S.; Rödl, C.; Hey-Hawkins, E.; Wolf, R., *Angew. Chem. Int. Ed.* **2017**, *56*, 15871.
396. Rödl, C.; Schwedtmann, K.; Weigand, J. J.; Wolf, R., *Chem. Eur. J.* **2019**, *25*, 6180.
397. Rödl, C.; Wolf, R., *Chem. Eur. J.* **2019**, *25*, 8332.
398. Schubert, K. P. H., *Z. Metallkd.* **1950**, *41*, 433.
399. Panday, P. K.; Schubert, K., *J. Less Common Met.* **1969**, *18*, 175.
400. Ellner, M., *J. Less Common Met.* **1976**, *48*, 21.
401. Takizawa, H.; Sato, T.; Endo, T.; Shimada, M., *J. Solid State Chem.* **1988**, *73*, 40.
402. Audebrand, N.; Ellner, M.; Mittemeijer, E. J., *Powder Diffr.* **2000**, *15*, 120.
403. Mayer, K.; Dums, J. V.; Klein, W.; Fässler, T. F., *Angew. Chem. Int. Ed.* **2017**, *56*, 15159.
404. Corella, J. A.; Thompson, R. L.; Cooper, N. J., *Angew. Chem. Int. Ed.* **1992**, *31*, 83.
405. Rosa, P.; Mézailles, N.; Ricard, L.; Mathey, F.; Le Floch, P.; Jean, Y., *Angew. Chem. Int. Ed.* **2001**, *40*, 1251.
406. Chan, A. S. C.; Shieh, H.-S.; Hill, J. R., *J. Organomet. Chem.* **1985**, *279*, 171.
407. García, M. P.; Jiménez, M. V.; Lahoz, F. J.; Oro, L. A., *Inorg. Chem.* **1995**, *34*, 2153.
408. Lang, A.; Jeitschko, W., *J. Mater. Chem.* **1996**, *6*, 1897.
409. Schubert, K.; Lukas, H. L.; Meissner, H. G.; Bhan, S., *Z. Metallkd.* **1959**, *50*, 534.
410. Nial, O., *Sven. Kem. Tidskr.* **1947**, *59*, 172.
411. Schubert, K.; Pfisterer, H., *Z. Metallkd.* **1950**, *41*, 433.
412. Benda, C. B.; Waibel, M.; Fässler, T. F., *Angew. Chem. Int. Ed.* **2015**, *54*, 365.
413. Ormeci, A.; Aydemir, U.; Somer, M., *Z. Anorg. Allg. Chem.* **2011**, *637*, 907.
414. Biltz, W., *Raumchemie der festen Stoffe*, Leopold Voss Verlag, Leipzig, **1934**.
415. Stone, A. J., *Inorg. Chem.* **1981**, *20*, 563.
416. Stone, A. J.; Alderton, M. J., *Inorg. Chem.* **1982**, *21*, 2297.
417. de Heer, W. A., *Rev. Mod. Phys.* **1993**, *65*, 611.
418. Knizia, G., *J. Chem. Theory Comput.* **2013**, *9*, 4834.

419. Lichtenberger, N.; Franzke, Y. J.; Massa, W.; Weigend, F.; Dehnen, S., *Chem. Eur. J.* **2018**, *24*, 12022.
420. Hirshfeld, F. L., *Theo. Chim. Acta.* **1977**, *44*, 129.
421. Reed, A. E.; Weinstock, R. B.; Weinhold, F. J., *Chem. Phys.* **1985**, *83*, 735.
422. Frischhut, S.; Bentlohner, M. M.; Fässler, T. F., *Eur. J. Org. Chem.* **2019**, *2019*, 3101.
423. MestrelabResearch, MestReNova, v10.0.2-15465, **2015**.
424. OriginLabCorp., OriginPro, Northampton, MA, v9.3.226, **2018**.
425. Sheldrick, G. M., *Acta Cryst.* **2008**, *64*, 112.
426. Spek, A. L., *Acta Crystallogr. Sect. D. Biol. Crystallogr.* **2009**, *65*, 148.
427. Crystal-Impact-GbR, Diamond, Bonn, Germany, v3.2k, **2014**.
428. Momma, K.; Izumi, F., *J. Appl. Crystallogr.* **2011**, *44*, 1272.
429. Kottke, T.; Stalke, D., *J. Appl. Crystallogr.* **1993**, *26*, 615.
430. STOE&CieGmbH, WinXPOW, Darmstadt, Germany, v3.0.2.5, **2011**.
431. Netzsch-GerätebauGmbH, PROTEUS Thermal Analysis V4.8.2, Selb, **2006**.
432. Frisch, M. J.; Trucks, G. W.; Schlegel, H. B.; Scuseria, G. E.; M. A. Robb, J. R. C., G. Scalmani, V. Barone, B. Mennucci, G. A. Petersson, H. Nakatsuji, M. Caricato, X. Li, H. P. Hratchian, A. F. Izmaylov, J. Bloino, G. Zheng, J. L. Sonnenberg, M. Hada, M. Ehara, K. Toyota, R. Fukuda, J. Hasegawa, M. Ishida, T. Nakajima, Y. Honda, O. Kitao, H. Nakai, T. Vreven, J. A. Montgomery Jr., J. E. Peralta, F. Ogliaro, M. Bearpark, J. J. Heyd, E. Brothers, K. N. Kudin, V. N. Staroverov, T. Keith, R. Kobayashi, J. Normand, K. Raghavachari, A. Rendell, J. C. Burant, S. S. Iyengar, J. Tomasi, M. Cossi, N. Rega, J. M. Millam, M. Klene, J. E. Knox, J. B. Cross, V. Bakken, C. Adamo, J. Jaramillo, R. Gomperts, R. E. Stratmann, O. Yazyev, A. J. Austin, R. Cammi, C. Pomelli, J. W. Ochterski, R. L. Martin, K. Morokuma, V. G. Zakrzewski, G. A. Voth, P. Salvador, J. J. Dannenberg, S. Dapprich, A. D. Daniels, O. Farkas, J. B. Foresman, J. V. Ortiz, J. Cioslowski, D. J. Fox, Gaussian09, Wallingford CT, **2009**.
433. Perdew, J. P.; Burke, K.; Ernzerhof, M., *Phys. Rev. Lett.* **1996**, *77*, 3865.
434. Andrae, D.; Häussermann, U.; Dolg, M.; Stoll, H.; Preuss, H., *Theo. Chim. Acta.* **1990**, *77*, 123.
435. Weigend, F.; Ahlrichs, R., *Phys. Chem. Chem. Phys.* **2005**, *7*, 3297.
436. Barone, V.; Cossi, M., *J. Phys. Chem. A* **1998**, *102*, 1995.
437. Weigend, F.; Häser, M.; Patzelt, H.; Ahlrichs, R., *Chem. Phys. Lett.* **1998**, *294*, 143.
438. Metz, B.; Stoll, H.; Dolg, M., *J. Chem. Phys.* **2000**, *113*, 2563.
439. Jmol, Jmol: an open-source Java viewer for chemical structures in 3D.
<http://www.jmol.org/>
440. Knizia, G.; Klein, J. E. M. N., *Angew. Chem. Int. Ed.* **2015**, *54*, 5518.
441. Geitner, F. S., Investigations on the Reactivity of Nine-Atomic Group 14 Element Zintl Anions in Solution, **2018**, *Chair of Inorganic Chemistry with Focus on Novel Materials*, Munich, Germany, TUM
442. Busmann, E., *Z. Anorg. Allg. Chem.* **1961**, *312*, 214.
443. Jette, E. R.; Foote, F., *Z. Kristallog. – Cryst. Mater.* **1935**, *92*, 313.
444. Ehbrecht, M.; Kohn, B.; Huisken, F.; Laguna, M. A.; Paillard, V., *Phys. Rev. B* **1997**, *56*, 6958.
445. Ott, H., *Z. Kristallog. – Cryst. Mater.* **1926**, *63*, 222.

446. Cortona, P., *Phys. Rev. B* **1992**, 46, 2008.
447. Peters, D.; Tenten, A.; Jacobs, H., *Z. Anorg. Allg. Chem.* **2002**, 628, 1521.
448. Theoretical pattern was refined by Dr. Viktor Hlukyy, Chair of Inorganic Chemistry with Focus on Novel Materials.
449. von Schnering, H. G.; Llanos, J.; Chang, J.-H.; Peters, K.; Peters, E. M.; Nesper, R., *Z. Kristallogr. - New Cryst. Struct.* **2005**, 220, 324.
450. Rudman, P. S., *J. Less Common Met.* **1965**, 9, 77.
451. Queneau, V.; Todorov, E.; Sevov, S. C., *J. Am. Chem. Soc.* **1998**, 120, 3263.
452. Schubert, K.; Pfisterer, H., *Z. Metallkd.* **1950**, 41, 433.
453. Baitinger, M.; von Schnering, H. G.; Grin, Y.; Kniep, R., *Z. Kristallogr. - New Cryst. Struct.* **1999**, 214, 453.
454. Schubert, K.; Pfisterer, H., *Z. Metallkd.* **1950**, 41, 433.
455. Wallbaum, H. J., *Z. Metallkd.* **1943**, 35, 200.
456. Hoch, C.; Roehr, C., *Z. Anorg. Allg. Chem.* **2002**, 628, 1541.
457. Straumanis, M. E.; Aka, E. Z., *J. Am. Chem. Soc.* **1951**, 73, 5643.
458. Hoch, C.; Wendorff, M.; Roehr, C., *J. Alloys Compd.* **2003**, 361, 206.
459. Rabadanov, M. K.; Ataev, M. B., *Crystallog. Rep.* **2002**, 47, 33.
460. Nowotny, H.; Bachmayer, K., *Monatsh. Chem.* **1950**, 81, 669.
461. Knoedler, H., *Acta Cryst.* **1957**, 10, 86.

9. List of publications

In order to maintain priority it should be noted that the following publications, containing data found in this dissertation, have been published prior to the release of this dissertation.

1. Metallocages for Metal Anions: Highly Charged $[\text{Co}@\text{Ge}_9]^{5-}$ and $[\text{Ru}@\text{Sn}_9]^{6-}$ Clusters Featuring Spherically Encapsulated Co^{1-} and Ru^{2-} Anions, B. J. L. Witzel, W. Klein, J. V. Dums, M. Boyko, T. F. Fässler, *Angew. Chem. Int. Ed.* **2019**, 58, 12908 – 12913.